CARDIFF
UNIVERSITY
PRIFYSGOL
CAERDYDD

Cardiff
Catalysis Institute
Sefydliad Catalysis
Caerdydd

Catalysts Design for Biomass Conversion

Fabian Morteo Flores

Supervisor:
Dr Alberto Roldan Martinez

A thesis is being submitted in partial fulfilment of the requirements for the degree of Doctor of Philosophy.

Cardiff University
School of Chemistry

April 2022

Abstract

The strong dependency on fossil fuels has generated environmental problems due to greenhouse gas emissions, causing a rise in average global temperature and governments' attention to using renewable energies to reduce the net carbon to zero. The study of biomass conversion as a renewable source fuel into bio-oil has increased in recent years due to its energy-efficient and widely available feedstock being one alternative in replacing fossil fuels and gas. However, using bio-oil as a fuel has significant disadvantages due to the high amount of oxygenated compounds present in the mixture, which causes an increase in viscosity and challenges the ignition in the engines. Therefore, a bio-oil upgrade must be used to remove the oxygen compounds before being used as a fuel. One option is the hydrodeoxygenation process, which requires high temperatures, hydrogen, and catalysts to remove oxygen in the form of water and produce free-oxygen fuel.

This thesis aims to study the selection of hydrodeoxygenation (HDO) catalysts, such as transition metals (TMs) and oxide supports, using DFT calculations. First, studies were carried out to explore the relationship between the electronic properties of thirteen TMs, Fe, Co, Ni, Cu, Mo, Ru, Rh, Pd, Ag, W, Ir, Pt and Au and their hydrogen/oxygen affinity. The results helped to create scaling relationships to select the most suitable metal catalysts to bind the biomass-derived compounds and break the C–O bonds. Second, the acid-base properties of five pristine and hydroxylated oxide surfaces, γ-Al_2O_3, CeO_2, MgO, β-SiO_2 and anatase-TiO_2, were investigated. This includes the interaction with model compounds derived from lignin, such as guaiacol, phenol, anisole, and catechol.

Third, the guaiacol's HDO mechanism is analysed on six TM catalysts based on the intermediate hydrogen/oxygen affinity, *Fe (110), Co (0001), Ni (111), Cu (111), Pd (111)* and *Pt (111)*. Three first main pathways were proposed to convert guaiacol to anisole (dihydroxylation), phenol (demethoxylation) and catechol (demethylation). The results confirmed that the demethylation pathway is the most accessible on Co, Ni, Cu, Pd, and Pt, following the route guaiacol → catechol → phenol → benzene. In contrast,

Fe (110) preferred the dehydroxylation (DHY) reaction pathway, following the guaiacol → anisole → benzene route. Finally, a microkinetic study was implemented to understand the catalytic process of the guaiacol HDO conversion on five metal surfaces, Co, Ni, Cu, Pd, and Pt. The study includes temperature-programmed reaction and rate order simulations. The results showed that Ni exhibits a fast-kinetic rate at 573 K and performs well in the deoxygenation and hydrogenation reactions compared to the other TM surfaces.

The impact of the results in this thesis provides a better understanding of the guaiacol HDO process. Moreover, the use of DFT calculations in the selection of metal catalysts, reaction mechanisms and microkinetic studies is a step forward to closing the gap between the theoretical and experimental studies, giving insight into the metal catalysts design from an atomistic perspective. This will help to understand the catalysts' performance and design of new materials promoting a circular and sustainable economy.

Acknowledgment

First, I would like to express my sincere gratitude to my supervisor Alberto Roldan Martinez. He was there to solve all my questions, guide me with any problem and give me immense support during this PhD journey. His happy personality and tremendous energy made our meetings more enjoyable. Second, I would like to thank CONACYT (Consejo Nacional de Ciencia y Tecnologia de Mexico) for funding my PhD in Cardiff and for the full support during my research career since my master's studies. Moreover, to the Cardiff Catalysis Institute and the Chemistry department for funding part of my research fees.

Furthermore, I also want to thank Supercomputing Wales, the Material Chemistry Consortium and the service provided by GW4 and the UK Met Office for the computational time provided on Hawk, Thomas, and Isambard, respectively. Finally, and not least, I would like to express a sincere gratitude to my thesis reviewers, who helped me to improve my thesis content. Thanks to Dr. Devis Di Tommaso, Dr. Jonathan Rourke and Prof Stuart Taylor

I also want to thank all the people who were with me during this PhD journey. First, the Computational Chemistry group, specifically Xiuyuan Lu, Max Quayle, Lara Kabalan and Maicon Delarmelina. Their talks and opinions about the study and life in Cardiff during this period made me feel welcome every time I was in the office. Second, the people from Mexico who were there to talk about life and the adulthood transition, including Brenda Godinez, Fausto Mayorga, Juan Gonzalez, Mayda Lam, Karla Parra, Yuridia Gomez, and Samanta Grimaldo. Third, to my friends and colleagues from Cardiff's Latin American and Spanish society. Moreover, I would like to express my gratitude to the Kelsey Family (Anthony, Jennifer, Kiera, Lee, and Wendy), who always made me feel at home in Llanelli.

Special gratitude to my parents and family, including my dad and mom (Esteban and Elsa), aunt (Angela), and wonderful sister Gabriela. They were there in every step of my studies and did not leave me alone at any moment. Finally, I would like to express my complete gratitude to my wonderful partner Christian, who was there when I was upset, happy and stressed. He has supported me in every step of this journey since I started in Bath. I do not have more words to thank you for all the support over these years.

Gracias a todos (Thanks to everyone)

Table of contents

1 Introduction

2 *Theoretical Background*

3 Biomass hydrodeoxygenation catalysts from atomistic activity descriptors

4 *The effect of pristine and hydroxylated oxides surfaces on the Guaiacol HDO process*

5 *Mechanism and trends of Guaiacol HDO on transition metal catalysts*

6 *Microkinetic study of Guaiacol HDO on transition metal catalysts*

7 *Conclusions and future work*

List of publications

The work described in this thesis have been published in the following papers:

1. **F. Morteo-Flores**, J. Engel, and A. Roldan (2019). “Biomass hydrodeoxygenation catalysts innovation from atomistic activity predictors” *Philosophical Transactions of the Royal Society A*, 378, 20200056. doi: 10.1098/rsta.2020.0056.

2. **F. Morteo-Flores** and A. Roldan (2021). “The effect of pristine and hydroxylated oxide surfaces on the guaiacol HDO process: A DFT study” *ChemPhysChem*, 23, e202100583. doi: 10.1002/cphc.202100583.

3. **F. Morteo-Flores** and A. Roldan (2022). “Mechanisms and trends of Guaiacol Hydrodeoxygenation on transition metal catalysts.” *Frontiers in Catalysis, 2:861364.* doi: 10.3389/fctls.2022.861364.

4. **F. Morteo-Flores** and A. Roldan: “Microkinetic study of guaiacol hydrodeoxygenation on transition metal catalysts.” *To be submitted*.

List of conferences

The work described in this thesis have been published in the following conferences:

1. **F. Morteo-Flores** and A. Roldan: "Scaling relations and computational catalyst design for HDO processes" *Midlands Computational Chemistry Meeting*, Loughborough, UK. 15th April 2019 (Poster).

2. **F. Morteo-Flores** and A. Roldan: *"Computational study of the properties of oxide supports for the Hydrodeoxygenation (HDO) of guaiacol (GUA)"* Cardiff Catalysis Institute conference. Cardiff, UK. 15-16th January 2020 (Poster).

3. **F. Morteo-Flores** and A. Roldan: "Scaling relationships and computational catalysts design for HDO Processes" *XVIII Symposium of Mexican studies and students in the UK*", Nottingham, UK. 1-2nd July 2020 (Poster).

4. **F. Morteo-Flores**: *"Computational study of the properties of clean and hydroxylated oxide surfaces for the Hydrodeoxygenation (HDO) of guaiacol (GUA)."* Multiscale modelling of Materials and molecules, Uppsala, Sweden (Online). 8th June 2021 (Poster).

5. **F. Morteo-Flores** and A. Roldan: **"***Selection of catalysts based on their electronic properties for HDO processes*" The Materials and Molecular Modelling (MMM) Hub++ Conference 2021, London, UK. 14-15th September 2021 (Flash presentation).

6. **F. Morteo-Flores** and A. Roldan: "*Mechanism of the Guaiacol Hydrodeoxygenation on transition metal catalysts"* 19th Annual Cardiff Chemistry Conference 2021, Cardiff, UK. 27th October 2021 (Poster).

List of abbreviations

a_o	Lattice parameter
A_o	Pre-exponential factor
ASE	Atomic Simulation Environment
bcc	body-centred cubic structure
BZ	Brillouin zone
B_o	Bulk modulus
C_B	Conduction band
CG	Conjugate gradients
CI-NEB	Climbing-image nudged elastic band method
DFT	Density functional theory
DFT-D3	It is a density functional theory dispersion correction with zero damping
DFT+U	Method combining a DFT for the description of the on-site Coulomb interactions.
DDO	Direct deoxygenation pathway
DHY	Dehydroxylation pathway
DM	Improved dimer method
DME	Demethylation pathway
DMO	Demethoxylation pathway
DOS	Density of state
E_a	Activation energy
E_{ads}	Adsorption energy
E_{coh}	Cohesive energy
ε_{CB}	Band centre of the conduction band
ε_d	d-band centre
ε_{VB}	Band centre of the valence band
E_{IS}	Initial state energy
E_F	Fermi level
E_{FS}	Final state energy

E_g	Bandgap
E_r	Reaction energy
E_{TS}	Transition state energy
fcc	face-centred cubic structure
GGA	Generalized gradient approximation
hcp	hexagonal close-packed structure
HDN	Hydrodenitrogenation process
HDO	Hydrodeoxygenation process
HDS	Hydrodesulfurization process
HGL	Hydrogenolysis pathway
IPCC	The Intergovernmental Panel on Climate Change
K_d	d-band kurtosis
KS	Kohn-Sham
LB	Long bridge site for (110) surface
LDA	Local density approximation
MAE	Mean absolute error
$\mathrm{M_iAE}$	Maximum absolute error
MPa	Mega pascal pressure unit
MPE	Mean percentage error
MP2	Second-order Møller-Plesset perturbation theory
ODE	Ordinary differential equation
PAW	Projector augmented-wave method
PBE	Generalized gradient approximation functional developed by Perdew, Burke and Ernzerhof
PES	Potential energy surface
PDOS	Projected density of states
RMSE	Root-mean-square deviation method
RPBE	A revised version of the PBE functional
SB	Short bridge site for (110) surface
S_d	d-band skewness
S_o	Sticking coefficient
TM	Transition metal
TPD	Temperature-programmed desorption

TS	Transition states
TSS	Transition state scaling
TSS-IS	Transition state scaling using the initial states
TSS-FS	Transition state scaling using the final states
TST	Transition state theory
USPP	Ultrasoft pseudopotentials
VASP	Vienna *Ab-initio* Simulation Package
V_B	Valence band
W_d	d-band width

List of Tables

List of Figures

1

Introduction

1.1 Society based on a circular economy

In the last few decades, a society based on a circular economy has grown against petroleum and natural gas, the long-established fuels of our sustainable future.[1] The strong dependency on fossil fuels has caused environmental problems due to greenhouse gas emissions, such as carbon dioxide and nitrous oxide, accelerating the rise in average global temperature. Human activities have warmed the world by 0.87 °C during 2006 – 2015 compared to pre-industrial times.[2] The Intergovernmental Panel on Climate Change (IPCC) published a report predicting a global warming increase of 1.5 °C between 2030 and 2052 if the current warming rate continues.[3] The objective of reducing emissions is to limit the mean global temperature below 2 °C, preferably at the limit increase to 1.5 °C, to mitigate the impacts of climate change such as hotter temperatures, severe storms and an increase in droughts. If no actions are taken to reduce greenhouse emissions, these can accelerate global warming by 3 °C or more by 2100.[4]

In terms of greenhouse gases, carbon dioxide (CO_2) accounts for about 80% of the total gas emissions derived from human activities.[5] CO_2 is presented in the atmosphere as part of the earth's carbon cycle. Still, the continuous combustion of fossil fuels to produce electricity and energy for transportation has altered the carbon cycle by emitting more carbon dioxide into the atmosphere.[6] Therefore, one of the main goals of using new renewable energies is to reduce the net carbon to zero.[7] In 2021, the United Kingdom (UK) government introduced a climate change target to reduce the volume of emissions by 78% by 2035.[8] This is a substantial step in the process to accomplish a net-zero target by 2050. Therefore, the government needs to take action to accelerate the transition of clean energy and net-zero emissions.[9]

Climate change and the use of materials are closely linked. A circular economy relies on the maximisation of resources where no waste occurs. In this context, biomass in the form of lignocellulosic is significant to the circular economy in terms of material products and energy provision.[10, 11] The European Commission (EC) implemented a new Circular Economy action plan, whose main goal is to keep resources in use for as long as possible and cut waste and production.[12] Renewable biomass is a desirable substitute for fossil fuels whereby waste biomass forms new resources, thus reducing and limiting the consumption of natural resources in a sustainable practice.[13]

Biomass is categorised into several materials: degraded land, agriculture, forest, and animal residues. Biomass can be converted into biofuels via a thermochemical and biochemical process.[14] The first generation of biofuels was derived from food sources such as corn and wheat. Although these sources are easy to collect, there is an ethical debate on using this kind of biomass due to the lack of food in different countries. This biofuel generation has other markets, and there is not enough food to feed the world population.[15] Most research has focused on a second generation of biofuels produced from agricultural and wood residues, which needs to be used responsibly to avoid using any land to make food.[16] The use of the second generation of biofuels has significantly impacted environmental concerns, reducing greenhouse emissions, specifically carbon dioxide. Although the environmental benefits of the second biomass generation are abundant, such as environmental performance, better energy efficiency and the widely available feedstocks, it still needs to reach an affordable commercial scale.[17] The future of biofuel production may rely upon the second generation, but further investigations need to be done to deal with the worldwide demand as an alternative to fossil fuels' dependency.

This chapter introduces the challenges in biomass conversion, including the different technologies and the selection of catalytic materials for biofuel upgrading. ***Figure 1.1*** shows the conversion routes for the lignocellulosic biomass conversion to biofuel. Among the different thermochemical processes, the pyrolysis method, specifically fast pyrolysis, is the most economically feasible method for biomass conversion into bio-oil, giving high production of liquid fuels and low char content.

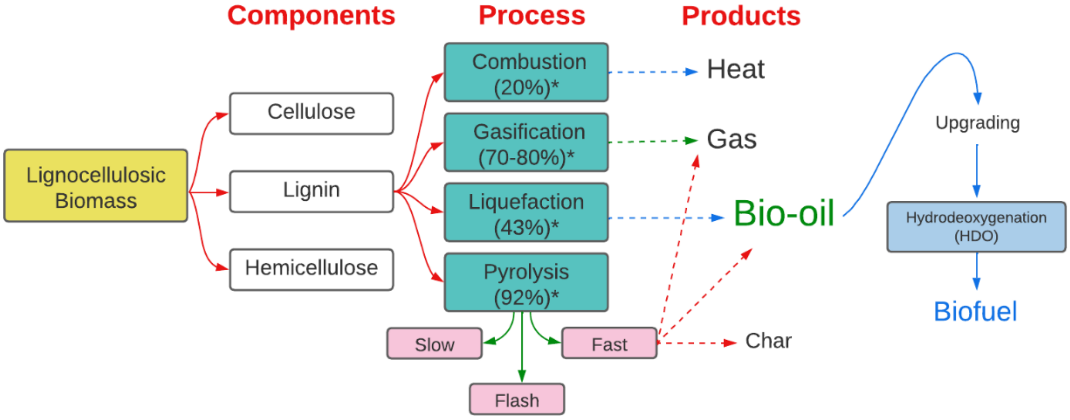

Figure 1.1. *Lignocellulosic biomass conversion using different conversion processes. The asterisk refers to the process efficiency.*

1.2 Lignocellulosic biomass

Lignocellulosic biomass (generally known as biomass) is a dry organic material not used for food. Usually, it is agricultural waste, where trees and grass crops are the primary producers (approximately 64% of the terrestrial biomass) for this kind of biomass to produce a liquid product.[18, 19] This liquid product is denominated as bio-oil, a complex mixture of organic fuel, which is a promising feedstock to replace conventional fuels for power generation due to the easy way to store and transport compared to gaseous products.[20] The lignocellulosic biomass contains three major components: cellulose (40 – 60 wt.%), hemicellulose (10 – 40 wt.%) and lignin (10 – 25 wt.%), ***Figure 1.2***.[21] Cellulose is an organic crystalline compound, which is the primary constituent of the cell wall of green plants. It consists of glucose units linked via β-(1,4) glycosidic bonds, and it is used to produce paper type materials. The second component is the hemicellulose, which cross-links with either cellulose or lignin, reinforcing the cell wall. This component is an amorphous biopolymer that contains a family of approximately 500 – 3000 sugar monomer units such as pentoses (e.g. arabinose and xylose) and hexoses (e.g. glucose, galactose) components. In contrast with cellulose, hemicellulose is less used due to its structural diversity and the difficulty to hydrolyse pentose units.[18] The third and essential component of biomass is lignin. This component is a family of a three-dimensional non-crystalline compound based on 4-hydroxyphenyl propanoids. Lignin has the function to hold the cellulose fibrils together, hindering their removal and providing rigidity and strength to the plant cell walls. At the moment, due to its complexity, bio-oil production from lignocellulosic biomass is inefficient, expensive, and challenging to generate.[22]

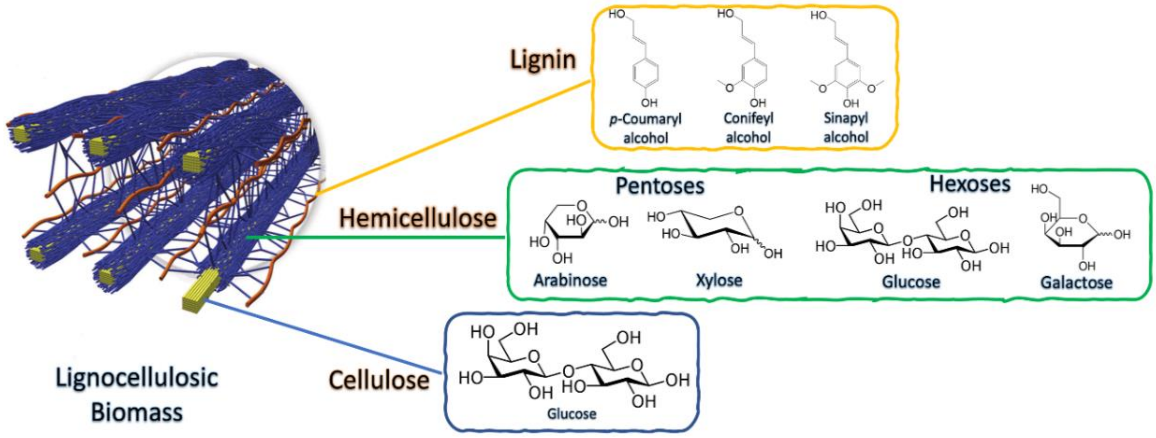

Figure 1.2. *Structure of lignocellulosic biomass with their three main components (i) Cellulose, (ii) Hemicellulose and (iii) Lignin.*

1.3 Lignin properties.

Lignin is the most resistant to biological degradation among the three components of lignocellulosic biomass because of its high energy content.[23] Moreover, lignin is the only biomass component based on aromatic units, contributing to the production of transportation fuels. Its aromatic structure form more cyclic compounds, which generate more energy in the combustion compared to hemicellulose and cellulose.[24] Understanding the lignin composition and properties is fundamental to manipulating and providing new bio-oil production strategies. The resistance of lignin to degradation is due to its interlinked structure. As a result, only 2% of the lignin is used commercially, while the rest is burned, emitting a high amount of greenhouse gases. The lignin has a high molecular weight of around 800 – 900 carbon atoms, while fuel production requires between 6 – 20 atoms.[25] For this reason, the lignin must be cleaved into small molecules.

Lignin consists of three different aromatic units: *p*-hydroxyphenyl (H), guaiacyl (G) and syringyl (S). They result from the phenylpropane units polymerisation, considered the primary building blocks of lignin (also called monolignols units), ***Figure 1.3***.[26-28] These compounds differ in the number of methoxy, hydroxyl and carboxyl groups, being the aromatic ring a common element.[29] Their composition varies depending on the type of biomass and the lignin content. For example, there are two types of lignin: softwood and hardwood. The main difference is that softwood lignin comprises a significant proportion of guaiacyl and a minor number of p-hydroxyphenyl units. In contrast, hardwood lignin contains guaiacyl and syringyl units in equal proportions.[30] These monomers are linked by several ether linkages (C–O bonds), e.g. α–O–4, 4–O–5 in ***Figure 1.3***. The β–O–4 ether bond linkage is the most predominant between the monomers (≈ 40 – 60% of all linkages), whereas the rest are C–C inter-unit linkages.[31] Analyses have revealed that β-ether bonds are readily cleaved at a low range of temperatures (< 300 °C); however, C–C type linkages are stable during lignin depolymerisation because of the strong carbon-carbon bond strength.[32] The α–O–4 type linkages are the weakest bond energy in lignin (between 1.73 – 2.6 eV), whereas the bond dissociation energy for the β–O–4 is higher than 2.6 eV.[33] Therefore, preparing aromatic compounds from lignin via β–O–4 cleavage is a promising strategy.[34] A series of methods have been used to fragment the lignin into bio-oil small pieces, such as hydrolysis, pyrolysis and reductive depolymerisation.

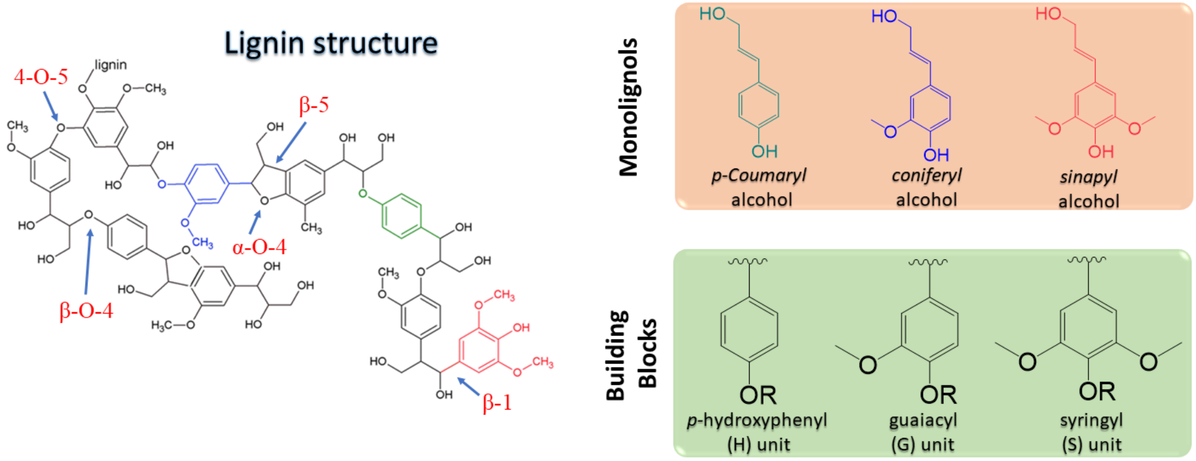

Figure 1.3. *Lignin structure with its chemical monolignols with the corresponding building blocks. Adapted from Ref* [35, 36].

1.4 Biomass conversion

This section discusses the lignin conversion methods into bio-oil. Several thermochemical processes such as (i) combustion, (ii) gasification, (iii) pyrolysis and (iv) direct liquefaction are used to get condensable vapours and solid chemical products at temperatures higher than 200 °C. From these condensable vapours, bio-oil can be obtained and upgraded into biofuels.

The combustion method is an exothermic process that uses a high range of temperatures (800 – 1200 °C) with enough oxygen to oxidise the feed biomass, producing heat. One disadvantage of this process is its efficiency (around 20%), also making it a pollution producer.[37] Gasification is a thermal process characterised by biomass conversion at high temperatures (800 – 1200 °C) with a limited oxygen environment, making the combustion an incomplete process. The products of this process are a combustible gas called syngas (mixture of carbon monoxide, carbon dioxide and hydrogen) and small quantities of char (an unconverted organic residue, mainly carbon and ash).[38] The main aim of biomass gasification is the production of low heating value syngas (4 – 6 MJ/m^3), which can be burned to produce heat and steam to produce electricity, and it can be used as a fuel gas in internal combustion engine for power production.[39] Pyrolysis is a thermal degradation method that operates at mid-high temperatures (350 – 800 °C) under an inert atmosphere (argon or nitrogen gas flow) with a pressure between 0.1 – 0.5 MPa in the absence of oxygen to convert lignin into oil (bio-oil), syngas and char in a short time.[40] The first stage of pyrolysis comprises the combination of combustion and gasification processes, making it a non-independent technology.[37]

The direct liquefaction process is similar to pyrolysis because both yield liquid fuels as a final product, but the latter uses high pressure (5 – 20 MPa) and a low-temperature range (200 – 350 °C) and catalysts.[41] The main difference between pyrolysis and direct liquefaction methods is the maximum bio-oil yield; for pyrolysis (specifically fast-pyrolysis), 62.6 wt.% of bio-oil is recovered with 25.7 wt.% and 11.7 wt.% of syngas and char, whereas the maximum bio-oil yield for the direct liquefaction is 47.0 wt.%. Moreover, the gas formed in the direct liquefaction is composed of CO_2, whereas the gas from pyrolysis is a syngas with a higher market.[42] This makes the pyrolysis technology a good alternative in producing bio-oil.

1.4.1 Pyrolysis

The pyrolysis process is classified into three categories: (i) slow pyrolysis, (ii) fast pyrolysis, and (iii) flash pyrolysis. This classification is based on their operation conditions such as temperature, residence time (time at which the reactant is inside the reactor) and heating rate used, which affect the composition of the final products. Slow or conventional pyrolysis uses a mid-range of temperatures (550 – 950 °C) with a long residence time (10 – 100 min) and a low rate of heating (1 °C/s). Fast pyrolysis is carried out at mid-high temperature (between 850 – 1250 °C), but with a short residence time (0.5 – 5 s) and a high heating rate (10 – 200 °C/s). Finally, flash pyrolysis is characterised by high temperatures (between 1050 – 1300 °C) with a short residence time and a very high heating rate of 0.5 s and 1000 °C/s.[43-45]

Slow pyrolysis and flash pyrolysis have different disadvantages. Slow pyrolysis is not suitable to yield bio-oil (~ 30 wt.%) due to moderate temperatures, which provokes an increase in char production (~ 35 wt.%). Moreover, it agglomerates and forms large particles causing corrosion problems and blocking the engine's valves, impacting the ignition process.[46, 47] On the contrary, flash pyrolysis presents high bio-oil yields with a conversion of up to 70 wt.%. However, this process requires that the size of the biomass material be the smallest possible (< 0.2 mm); otherwise, this will provoke thermal instability and corrosiveness of the oil directly promoted for the short residence time.[37, 48] In contrast, fast pyrolysis uses high heating rates, mid-high range of temperatures and short residence time, which allows the rapid cooling of vapours and aerosol, increasing the bio-oil yield (50 wt.%). Moreover, this process yields a low amount of char (20 wt.%) compared to slow pyrolysis.[37, 49] The fast pyrolysis of biomass has different temperature stages. First, the biomass structure decomposes initially at 100 °C. After this, cellulose and hemicellulose start disintegrating at low temperatures: 260 °C and 360 °C, respectively. In contrast, lignin is more resistant, provoking that its decomposition occurs at very high temperatures (≈ 900 °C).[50] At 500 °C occurs the maximum conversion for the biomass, with a high yield of liquid bio-oil (65 wt.%). Moreover, there are char and gaseous species production (15 wt.% and 13 wt.%). The decrease in char production is due to the second decomposition stage of the char at high temperatures.[51] However, the increase of temperature promotes a second cracking of the biomass, producing CO and methane, which is proportional to the gas production. Therefore, mid-high temperatures will give the highest bio-oil yield with a low product yield of char and gases. The basic performance of the fast pyrolysis and removal of char is seen in ***Figure 1.4***.

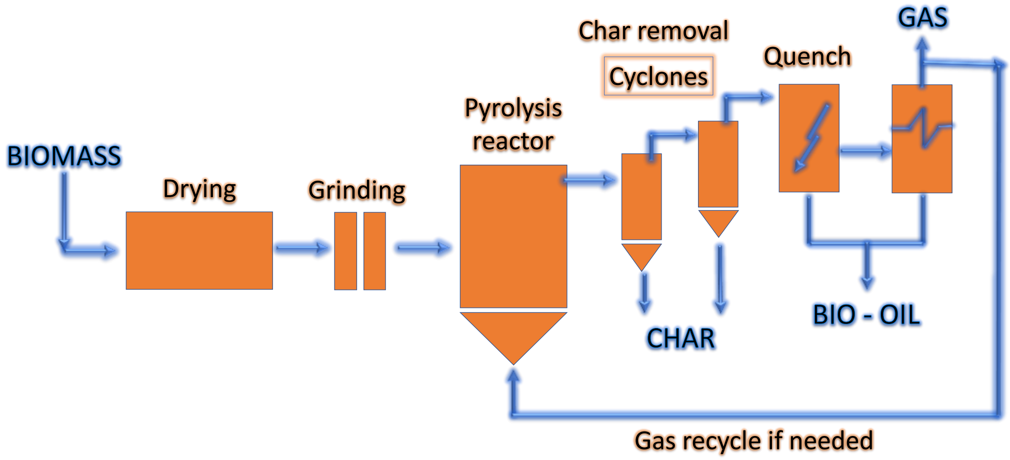

Figure 1.4. *Fast pyrolysis process to obtain bio-oil as a final product. Reproduced from Meier et al.*[52]

1.5 Bio-oil

Bio-oil is a dark brown liquid from biomass fast-pyrolysis, which can be used as a green fuel with benefits to the environment. As a result of the fast pyrolysis non-equilibrium reaction, bio-oils chemical composition change over time to achieve thermodynamic equilibrium, raising its viscosity rate.[53] Therefore, bio-oils need to be cooled quickly after being produced and stored at low temperature to avoid an increase in viscosity.[54]

This bio-oil is a mixture of compounds of different molecular sizes divided into water-soluble (high-polarity components) and water-insoluble (low-polarity compounds) fractions.[55] The water-soluble fraction involves carbohydrates and monofunctional hydrocarbons.[56] Whereas the water-insoluble fraction contains compounds derived from the lignin component with an average molecular weight between 370 – 1000 g/mol. These compounds are composed mainly by lignin subunits (i.e. hydroxyphenyl, guaiacyl, and syringyl), representing more than 200 different species depending on the type of biomass (35 – 60 wt.% of all components). The more predominant compounds are the phenolics and alkylated phenols such as ethers, aldehydes, phenols and alcohols.[57]

The high number of oxygenated compounds present in the mixture creates considerable differences between the properties of bio-oils and conventional hydrocarbon fuels. Among the disadvantage of the raw bio-oils are lower energy density, immiscibility with hydrocarbon fuels (but soluble in polar solvents), and low boiling point temperature (< 100 °C). The high acidity of bio-oils (pH ≈ 2.7) makes the liquid very corrosive at high temperatures. The presence of alcohol compounds causes an increase in viscosity (35 – 100 cP) related to the molecular weight of the bio-oil, which leads to a poor performance during fuel combustion.[53, 58] Finally, it is challenging to ignite bio-oils due to their water content.

Moreover, the cetane number (parameter to express the ignition quality in fuel) is impossible to measure accurately because bio-oils cannot be ignited in traditional engines. In some cases, experiments can be carried out to measures based on extrapolation results (cetane number = 5.6) compared to fossil fuels (diesel cetane number = 48).[58, 59] The low cetane value means that the ignition will take a long period before combustion. Therefore, the poor quality of the bio-oil makes its use impossible as a green and renewable fuel replacement for fossil fuels. Namely, upgrading must be carried out to reduce the disadvantages and increase the bio-oil quality to offer a near-future energy solution.

1.5.1 Bio-oil upgrading

There are two main methods to improve the quality of bio-oils, also known as catalytic upgrading, due to the use of catalysts: (i) zeolite cracking and (ii) hydrodeoxygenation (HDO), also called hydrotreatment. The catalytic upgrading of bio-oils is a challenging reaction because of the diversity of compounds forming the oil, and the different reactions involved, such as cracking, carbonylation, decarboxylation, hydrocracking, hydrodeoxygenation, hydrogenation and polymerization, which take place with both methods, i.e. zeolite cracking and HDO.[60]

Zeolite cracking is a method that uses inorganic porous materials such as HZSM-5 and ZSM-5 as catalysts to produce aromatic hydrocarbons, where the oxygen is removed as carbon dioxide. One of the disadvantages of this process is the production of a considerable amount of coke deposition at high temperatures due to the high acidity of the zeolites.[61] Hydrodeoxygenation (HDO) has shown high efficiency in reducing the oxygen compounds using various catalysts, low-temperature conditions and keeping the carbon number in the products.[62] One disadvantage is the high hydrogen consumption, which makes this process not affordable in terms of costs. A good understanding of this process is necessary to know the different HDO reaction pathways, operating conditions, making the process cost-effective and competitive.[63]

1.6 Hydrodeoxygenation (HDO)

Hydrotreatment is the variety of catalytic hydrogenation processes whose primary purpose is to remove heteroatoms, e.g. sulphur, nitrogen, oxygen, and metals, with minimal cracking of the carbonaceous compounds. Other names have been used for different reactions, such as hydrodesulfurization (removal of sulphur), hydrodenitrogenation (removal of nitrogen) and hydrodeoxygenation (removal of oxygen).[64] Both hydrodesulfurization (HDS) and hydrodenitrogenation (HDN) are used in fossil fuels such as gasoline and diesel to reduce hazardous emissions of sulphur dioxide and NO_x.[65] Although the hydrodeoxygenation (HDO) co-occurs with the HDS and HDN reactions, sulphur and nitrogen compounds are negligible for the bio-oil due to the minimal content (< 0.1 wt.%) in comparison with the oxygen compounds (> 40 wt.%). Therefore, the use of HDO is predominant for upgrading bio-oil to use as conventional fuels.

Hydrodeoxygenation requires a mid-range of temperatures and high pressure (400 °C and 20 MPa, respectively), while a complete conversion of oxygenated compounds into hydrocarbons is at 600 °C.[66] This process is conducted in the presence of catalysts and molecular hydrogen as a reducing source. The molecular hydrogen spontaneously dissociates into atoms with transition metals due to its low energy barrier (< 0.1 eV).[67] The co-adsorbed H promotes the C–O bond scission (deoxygenation reaction), releasing the oxygen in the form of water. Meanwhile, hydrogen saturates the dangling bond of the molecule, creating compounds free of oxygen; this process is illustrated in *Eq. 1.1.* [41, 68 69]

$$R - OH + H_2 \rightarrow R - H + H_2O \qquad \text{Eq. 1.1}$$

Two-stage operating treatments of the HDO process have been proposed according to the different reaction conditions to achieve the desired bio-oil conversions and obtain good quality biofuel.[70] The first stage, denominated as the stabilisation stage, is performed at 250 °C, where the reactor is stabilised with a constant pressure (10 MPa). In this stage, primary reactants such as ethers and methoxy phenols are converted into phenols. Ketones and carboxylic acids groups are present in low content, giving a stabilised oil product. The second stage, denominated as deep HDO, takes place at 350 °C with high pressure of H_2 (> 14 MPa). In this stage, furans and phenols convert into oxygen-free products, decreasing the oxygen from 48 to 0.5 wt.%, improving the heating value up to 46 MJ/kg.[71]

1.6.1 Model compounds

As discussed, bio-oils present a considerable amount of oxygen, where phenolic molecules are predominant. Guaiacol and substituted guaiacol compounds are the most common phenolic monomer (≈ 2 wt.% for straw lignin and 3 wt.% for grass lignin). Whereas syringol and alkylphenols groups represent almost 1.5 wt.% of the bio-oil. In general, all the compounds share a common factor, the presence of methoxy ($-OCH_3$) and hydroxy ($-OH$) groups.[72]

Due to the wide variety of lignin phenolic units, it is common to employ model compounds in experimental studies to reduce the complexity of the upgrading process. Information on the reaction mechanisms is fundamental to guide and design the catalysts and reaction conditions. Different publications have used a variety of model compounds as a strategy to understand the chemistry and explore the insights for upgrading real pyrolysis bio-oils. Guaiacol (1-hydroxy-2-methoxy benzene) has been used as a primary model compound for the HDO process.[73-76] This is because the molecule contains two types of O−functional groups, methoxy and hydroxy groups, connected to an aromatic ring (***Figure 1.5***).[73-78] The importance of hydroxyl and methoxy groups in model compounds is due to the predominant existence of C–O–C and C–C linkages in lignin and bio-oils. Although C–C bonds are easily cleaved, C–O bonds represent a real challenge due to a high bond dissociation energy.[79] Moreover, guaiacol produces different products through the HDO process, such as anisole [74, 80-82], catechol [83, 84] and phenol. Phenol is the most desirable product in the guaiacol conversion due to its low H_2 consumption into benzene, making the process cost-effective.[85-89]

Different catalysts such as supported transition metals play an essential role in the HDO. A deep understanding of the selection and preparation of catalysts needs to be carried out based on understanding the HDO process and optimisation of the reaction parameters for upgrading bio-oils.[90]

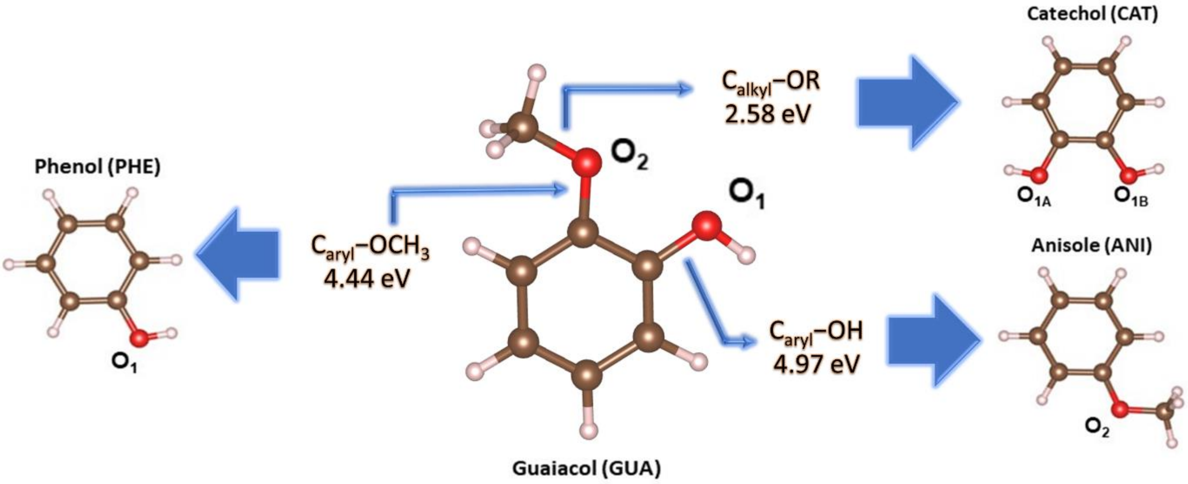

Figure 1.5*. Model compounds resulting from the lignin fast-pyrolysis. Bond dissociation energies indicated in eV obtained from ref [91].*

1.7 Catalysts for HDO processes

Catalysts are materials that accelerate the reaction rate without being consumed or being part of the final product. Catalysts enable industrial processes in a cost-effectively manner. Generally, catalysts can be classified into (i) homogeneous, (ii) heterogeneous, and (iii) enzymatic catalysts.

In homogeneous catalysts, the reactant and the catalyst are in the same phase; the most common form are metal complexes in solutions. These catalysts have several advantages, such as a high degree of interaction between the catalyst and the reactant; they are usually more selective than heterogeneous catalysts. However, the separation of the product can be challenging. In some cases, the catalyst is not removed from the product; this is a disadvantage for industrial-scale processes, making them not economically and commercially unfeasible.[92] Proteins catalyse most biological reactions; these proteins act as enzymes, increasing the rate of all chemical reactions within cells. Therefore, these enzymes act as biological catalysts. In the absence of these enzymatic catalysts, the biochemical reactions could take years to occur under low range of temperature and pressure conditions. Therefore, enzyme catalysts can accelerate the reactions to a fraction of seconds. [93]

In heterogeneous catalysts, the catalyst phase is different from the reactants or products. For example, solid catalysts can react with reactants that are in liquid or gas phase. Over the last years, the development of efficient heterogeneous catalysts for HDO processes with model compounds has increased substantially, offering some advantages in preparation, recovery, stability, regeneration and low toxicity.[94] Moreover, heterogenous catalysts enable the control of specific properties, such as the selectivity of the products and maximising the conversion of the compounds.[95] In these catalysts, the molecule (adsorbate) binds to the catalyst (adsorbent); this process is denominated adsorption, which leads to the reaction. Then, the product splits from the adsorbent in a process denominated desorption. Transition metals are used as catalysts because they lend or withdraw electrons due to their partially filled *d* orbitals, enabling electrons to form chemical bonds with the reactant.[96] The metal particles are unstable, and they sinter at high temperatures. Therefore, the support role is essential in heterogeneous catalysts because they increase the surface area and stabilise the nanoparticles.[97, 98]

In order to design efficient catalysts for the HDO, it is necessary to identify the different types of metals and compare them in terms of activity, cost, and selectivity. Catalysts need to be bifunctional to adsorb oxy compounds and activate molecular hydrogen, promoting the C−O bond scission and hydrogenation. The role of the active phase, specifically metal, and supports is unclear. However, some authors propose that the role of the support is the adsorption of oxy compounds. Whereas the metal phase is responsible for the activation of hydrogen. However, some metals with oxyphilic behaviour have shown activity to deoxygenated model compounds.[99] Therefore, the selection of the metal needs to be based on the activation of hydrogen and affinity for O atoms.[100]

1.7.1 Metal sites

The selection of a suitable metal catalyst for the HDO is based on the degree of strength between the oxy compounds and the metal.[101] Sabatier's principle states that an optimal catalyst needs to bind the hydrogen atom and oxy compounds in an intermediate strength, not too strong or weak, to form hydrocarbon products, as shown in *Eq. 1.1*. The metals that bind molecules too weakly cannot overcome the activation barrier.[102] In contrast, a strong interaction will not be able to desorb the products. The selection of metals is required to find an appropriate balance between hydrogenation and deoxygenation in the hydrodeoxygenation processes.[103, 104]

Many metals have been evaluated as supported catalysts for the HDO, e.g. Ru, Rh, Pd, Ag, Ir, Pt, Au, Fe, Co, Ni, Cu, Mo, and W.[105] Noble metals such as Pd, Pt and Rh have demonstrated an improvement in hydrocarbon production, maximising the oxygen removal from bio-fuels.[106] Moreover, their reaction selectivity drives into cyclohexane, methoxy cyclohexane and aromatic hydrocarbon products. Pd and Pt-based catalysts have demonstrated high efficiency on different supports, e.g. SiO_2, γ-Al_2O_3, MgO and C, improving the deoxygenation capabilities and reducing the amount of H_2 required, i.e. showing better hydrogenation activity at low temperatures.[103, 107] One of the biggest challenges for noble metals is their availability and cost, resulting in an expensive small-scale production.[108]

Non-noble metals such as Ni has emerged as replacement candidate due to their low cost and excellent HDO conversion performance of model compounds (***Table 1.1***). As an active metal, Ni has been limited to low temperatures for the high production of aromatic products to avoid ring opening. For example, Ni/TiO_2 (anatase) and Ni/MgO catalysts have converted the guaiacol HDO at low temperatures, yielding cyclohexanol and phenol, respectively.[109, 110] Moreover, using Ni on SiO_2-ZrO_2 for the phenol conversion produces alkanes and aromatic hydrocarbons (54.9% and 7.8%, respectively), which are responsible for the increase in the octane number, which measures the ability of a fuel to resist detonation in a combustion engine.[89, 111] Alloy catalysts such as NiMo and CoMo have been employed in industrial processes for many years due to the catalytic synergy between these two elements, giving good results in treating petroleum in the hydrodesulfurization process (HDS).[70] Their use in the HDO process has also offered effective removal of oxygen. The role of cobalt in alloy catalysts, such as NiCo alloy, facilitates the reduction and dispersion of nickel on the support, improving the HDO yield substantially compared to the Ni and Co monometallic catalysts.[111] The addition of less expensive oxyphilic metals (strong affinity for oxygen) in bimetallic catalysts, such as Fe, Mo and W, has received significant attention due to increased oxygen removal and more selection of desirable products as benzene.[112-115]

Table 1.1. *Hydrodeoxygenation of guaiacol over heterogeneous catalysts. T, P, and Conv corresponds to temperature, pressure, and conversion, respectively.*

Metal	Support	Metal (wt.%)	T (°C)	Time (h)	P (MPa)	Conv (%)	Products / selectivity (%)	ref
Rh	ZrO_2	3	100	5	8	98.9	1 methyl-1,2-cyclohexanediol (75%)	116
Pd		3	100	5	8	13.7	Cyclohexanol (40%)	
Pt		3	100	5	8	10	Cyclohexanol (65%)	
Ni	MgO	20	160	4	4.0	99.6	Cyclohexanol (98%) Phenol (0.87%)	109
Pt	Al_2O_3	1	180	5	5	56	Methoxycyclohexanol (72%)	117
Pt	CeO_2	1	180	5	5	30	Methoxycyclohexanol (89%)	
Pt	a-TiO_2	1	180	5	5	33	Methoxycyclohexanol (65%)	
Ni	γ-Al_2O_3	20	200	8	5	78	Cyclohexanol (40%)	118
Co		20	200	8	5	85	Cyclohexanol (45%)	
NiCo		Ni (5) Co (15)	200	8	5	100	Cyclohexanol (45%) Methanol (8%)	
Ni	SiO_2	60	220	--	2	99	Cyclohexane (70%) Methoxycyclohexanol (20%)	110
Ni	TiO_2	60	220	--	2	99	Methoxycyclohexanol (20%) Cyclohexanol (60%)	
Pt	SiO_2	1	250	3	10	30	Cyclohexane (13%) Octanol (40%)	119
Pt		5	250	3	10	54	Methoxycyclohexanol (42%)	
Pd	a-TiO_2 (anatase)	5	260	--	3	100	Cyclohexane (62%) Benzene (18%)	120

Pd	r-TiO_2 (rutile)	5	260	--	3	83	Methoxycyclohexanol (40%) Cyclohexane (40%)	
Pd	Al_2O_3	5	300	3	0.1	70	Catechol (100%)	74
Ni	γ-Al_2O_3	20	300	1	0.1	100	Benzene (50%) Cyclohexanone (35%)	113
Co	Unsupported - Metal powder	--	300	1	0.1	20	1,2-Cyclohexanediol (33%), phenol (22.6%)	
Ni		--	300	1	0.1	51.3	Phenol (35%) Cyclohexanol (32%)	
Fe		--	300	1	0.1	11.8	Benzene (37.53%) 1,2-Benzenediol (24%)	
Pt	γ-Al_2O_3	1	300	6	0.14	93	Phenol (26%) Catechol (51%)	121
Pt	MgO	1	300	6	0.14	70	Phenol (51%) Catechol (25%)	
Ni	Al_2O_3	8	300	4	4	100	Cyclohexane (75%)	122
	CeO_2	8	300	4	4	100	Cyclohexane (45%) Cyclohexanol (40%)	
	a-TiO_2	8	300	4	4	60	Phenol (50%)	
	Unsupported – Metal particles	8	300	4	4	93	Cyclohexane (30%) Cyclohexanol (22%)	
Ni	γ-Al_2O_3	35	300	4	1	80	Cyclohexane (45%) Phenol (16%)	123
Co		35	300	4	1	95	Cyclohexane (20%), cyclohexene (30%), phenol (8%)	
NiCo 1:2		Ni (5.6) Co (10.6)	300	4	1	100	Cyclohexane (55%) Benzene (30%) Phenol (10%)	
NiCu	γ-Al_2O_3	Ni (14.1) Cu (5.7)	320	1	17	80.3	Cyclohexane (55%) Benzene (<5%)	75
Ni	SiO_2	55.4	320	1	17	97.5	Cyclohexane (63.9%) Benzene (16.4%)	
Cu	Carbon	5	350	--	4	3.6	Phenol (33.3%), catechol (33.1%)	109
Ni		5	350	--	4	30.7	Benzene (11.7%), phenol (5.8%), methoxyl cyclohexanone (26%)	
Pd		1	350	--	4	15.5	Methoxylcyclohexane (26.7%), benzene (15.3%), catechol (4.0%)	
Ru		1	350	--	4	34.2	Benzene (34.2%) Phenol (19.7%), and cyclohexanone (22%)	
Co	Al-MCM-41	10	400	1	0.1	90	Phenol (33%) Methane (13%)	111
Fe	SiO_2	17	400	2.5	0.1	100	Methane (40%) Phenol (30%)	114

1.7.2 Oxide supports

There are two main aspects to be considered in the choice of oxide supports for an HDO catalyst: (i) negligible carbon precipitation upon bio-oils complete reduction, which is related to low surface acidity, and (ii) the ability to activate oxy-compounds facilitating their selective reduction.[124-126] The support characteristics are related to the catalytic properties such as activity, selectivity and distribution of active phases.[127] Thus, to innovate and develop cost-effective HDO catalysts, one must understand the effect of the support under reaction conditions.

Oxides are a diverse class of materials widely used as supports due to their easy preparation, stability, and cheap cost.[128] They are formed by metal and oxygen ions (denominated as cations and anions, respectively). Cations are responsible for the acidity, denominated as Lewis's acidity (electron acceptor), whereas oxygen ions behave as electron donors, and they are responsible for the basicity, denominated as Lewis basicity.[129] Typical oxide supports are classified in (i) oxides of main group elements such as MgO, Al_2O_3 and SiO_2, (ii) transition metals such as TiO_2, and (iii) and rare-earth metals such as CeO_2, see ***Figure 1.6***.[126]

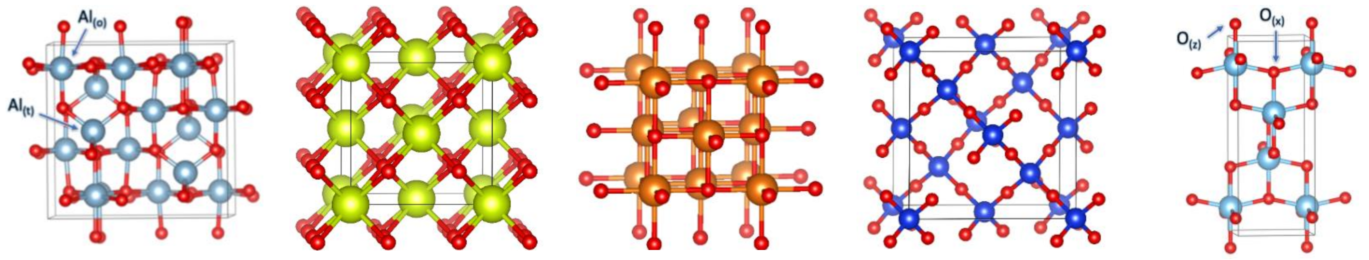

a) γ-Al_2O_3 **b) CeO_2** **c) MgO** **d) β-SiO_2** **e) a-TiO_2**

Figure 1.6. *Bulk structure of a) Digne model γ-Al_2O_3, b) CeO_2, c) MgO, d) β-cristobalite SiO_2, and e) TiO_2 anatase. $O_{(x)}$ and $O_{(z)}$ represent the position of the O atom concerning Ti, whereas $Al_{(o)}$ and $Al_{(t)}$ are octahedral and tetrahedral Al atoms.*

1.7.2.1 *Alumina (γ-Al_2O_3)*

Alumina has a variety of metastable structures depending on the calcination temperatures: from boehmite Al_2O_3 → γ-Al_2O_3 → δ-Al_2O_3 → θ-Al_2O_3 until the most stable at high-temperature α-Al_2O_3 (corundum), where γ-Al_2O_3 is made at temperatures between 500 and 1000 °C.[130] γ-Al_2O_3 is the most widely used for catalyst applications due to its high thermal stability (> 1200 °C), mechanical strength and high surface area. Moreover, it is inexpensive to produce, and it has amphoteric properties.[131, 132] The γ-Al_2O_3 structure has been described as a spinel cubic-closed arrangement, similar to $MgAl_2O_4$ spinel. In the spinel structure, Al cations occupy the octahedral and tetrahedral sites of the lattice with a ratio of 2/3 metal-oxygen. However, the structural properties of the surface are less understood as the positions of the Al^{3+} cations are not well known.[133]

Several research groups have investigated the γ-alumina structure using theoretical DFT calculations.[132] One of the most widely accepted simulation models was studied by Digne *et al*.[133] The model indicates a non-spinel model is more stable than a defective traditional spinel structure. This non-spinel model is not crystallographic perfect because it includes eight units of Al_2O_3, which cannot reproduce the complexity of the physical material. Moreover, the model presents a tetragonal distortion, lattice ratio (c/a), bulk modulus and % of Al in tetrahedral sites similar to experimental data of γ-alumina. It is a structure compatible with periodic DFT calculations; therefore, it provides an excellent, accurate and optimised surface structure under realistic temperature and pressure conditions.[133]

One of the essential characteristics of γ-Al_2O_3 is its acid/base properties. This is due to the presence of Lewis acid sites and Brønsted acidity (Lewis basicity) on the surface with similar strength, classifying the oxide as an amphoteric material.[134] A highly acid-base centre is observed on the three-fold coordinated Al (Al_{3c}) site, which is found only on the (110) surface, being this facet the most predominant on the surface with a 70% of γ-Al_2O_3 particles area, whereas the *(100)* and *(111)* facets correspond to the 30% remaining.[135, 136] The γ-Al_2O_3 is the most important support HDO due to its excellent performance for activating phenolic compounds.[88, 137-142] Although γ-Al_2O_3 gives a good performance, there are reports of coke formation (material with a high carbon content and impurities) in the conversion of guaiacol in bath reaction conditions.[143] This leads to the deactivation of the catalyst, decreasing its lifetime and reducing hydrocarbon production because the active sites are covered on the catalysts, blocking catalyst pores.[144] Therefore, different alternatives of oxide support need to be analysed to use instead of alumina with excellent performance in the HDO process.

1.7.2.2 Cerium oxide (CeO_2)

Cerium oxide (CeO_2) is a semiconductor material, which contains rare-earth with a cubic fluorite structure (*Fm3m*).[145] Its crystalline bulk consists of four Ce atoms in a cubic lattice placed in the centre (Ce_{7c}) and eight O atoms per unit cell occupying the tetrahedral lattice sites.[146]

One of the characteristics of ceria is the transition from Ce^{4+} to Ce^{3+} states, forming oxygen vacancies, although it can alternate between these states depending on the conditions.[147] This support has been used in different applications such as carbon monoxide oxidation, [148] nitrogen oxide reduction, [149] and automobile three-way catalytic converters.[150] The use of oxygen vacancies enhances the adsorption and activation of oxy compounds, promoting catalytic performance.[151] Li *et al*.[152] studied the HDO of guaiacol over Fe catalysts supported on several oxide materials, including ceria. Fe/CeO_2 demonstrated less coke formation than Fe/SiO_2 and Fe/Al_2O_3. Moreover, it shows higher guaiacol conversion and selectivity to phenol (56 wt.%) with no presence of catechol compared to Fe/MgO and Fe/SiO_2. They concluded that a support with redox properties gives, as a result, good activity. However, high iron loading on CeO_2 forms Fe_3C phases, which is related to severe deactivation. The latter statement could be associated with the low surface area of CeO_2 (63 m^2/g).[147] Therefore, CeO_2 is a good candidate for HDO due to its weak basic behaviour, low coke formation and redox performance, which may facilitate the C−O bond scission.[153]

1.7.2.3 Magnesium oxide (MgO)

Magnesium oxide (MgO) is an insulator oxide with a rock-salt structure composed of a very electropositive cation (Mg^{2+}) surrounded O^{2-} ions.[154] Its crystal structure belongs to the group *Fm3m* and contains one formula unit per primitive cell based on a Mg^{2+} with a neighbour O^{2-} atom.[155, 156] This support is classified as basic support due to its behaviour with aqueous solutions.[157] Due to its dielectric resistance and excellent optical transparency, MgO is used in different applications, such as optoelectronics and electrochemical biosensors.[158-160] MgO has been used as catalytic support due to its highly reactive defect sites (defects with oxygen atoms missing) at the surface, which are responsible for the catalytic activity of this support because it can be interpreted as a 5-centred bond.[161] Kulichenko *et al*.[162] studied the periodic defects on the *MgO (100)* surface and which periodicity of the defect leads is responsible for the significant increase in the catalytic activity by the growth of active sites.

Meanwhile, the use of MgO as support in hydrodeoxygenation processes has been extended recently. Yang *et al*.[163] studied the CoMo and CoMoP supported. The basic support promotes the dispersion of metal species over the support and makes the catalyst resistant to coke deposition. In contrast, Kaluza *et al*.[164] observed a low activity of the HDO of octanoic acid using NiMo catalysts supported on the same material. This low activity and selectivity provoke the molecule conversion toward the hydrodecarbonylation pathway, which is the least wanted due to the formation of CO/CO_2. This was observed due to the hydration of the catalysts. Hence, MgO support can inhibit coke formation, solving one of the problems of amphoteric material like Al_2O_3. However, the hydration of the support can decrease the ability to adsorb oxy compounds.

1.7.2.4 Silica oxide (SiO_2)

Silicon dioxide (SiO_2), or silica, is an oxide support whose basic structure is formed with a SiO_4 tetrahedral unit, a Si_{4c} at the centre and O_{2c} atoms at the corner ordered in the *Fd3m* cubic structure.[165-167] Its textural properties, such as a large surface area (300 m^2/g), make it an excellent adsorbent. The silica exists in different crystalline forms such as quartz (α, β), cristobalite (α, β) and stishovite.[168] Many works have identified the β-cristobalite as the model which represents the most abundant silica surface.[169-171] Several research works have demonstrated that OH groups (hydroxyl) are bound with Si atoms on the surface, denominated as silanol groups (≡Si-OH).[169] This is due to the water produced during calcination of silica gel saturates the Si dangling bonds. Different types of surface hydroxylation have been identified: (i) vicinal, (ii) isolated and (iii) geminal groups, represented in ***Figure 1.7***. Two single silanol groups attached to different silicon atoms are close to hydrogen bonds in the vicinal group. In the isolated group, the silicon atom has three bonds into the bulk structure, and the fourth bond is attached to a single −OH group. In contrast, the geminal group consists of two hydroxyl groups attached to one silicon atom.[172] The geminal group is suitable for the *(100)* facet, allowing them to interact through hydrogen bonding.[171] Silica has a broad of applications, such as hydrogenation,[173] microelectronics, [174] and glass industries.[175]

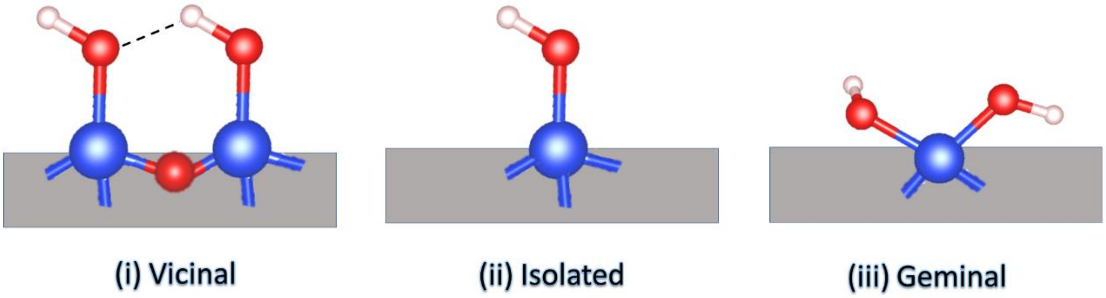

***Figure 1.7**. Schematic representations of (i) vicinal, (ii) isolated and (iii) geminal types of silanol groups encountered at silica surfaces. Colour code: O, H and Si atoms are represented in red, white, and blue, respectively.*

SiO_2 has been widely investigated for HDO processes. Shin-Kuan *et al*.[176] studied the HDO of guaiacol over Ni_2P-supported catalysts, where Al_2O_3, SiO_2 and ZrO_2 served as supports. The results indicated that Ni_2P/SiO_2 promoted the guaiacol conversion into phenol compared to Al_2O_3 and ZrO_2, which facilitated the conversion into catechol. Moreover, it was found that Ni_2P/SiO_2 did not produce coke at high temperatures. Jin *et al*.[177] studied the catalytic HDO of anisole over Ni supported on SiO_2. They confirmed that Ni/SiO_2 deoxygenation process depends on the temperature. Moreover, the material demonstrated the presence of weak acidic −OH sites on the surface, promoting the dispersion of the active phase and favouring the adsorption with O atoms, enhancing its ability in the C−O bond cleavage. Therefore, weak acidic sites and low coke production make SiO_2 a suitable candidate to examine in the HDO reactions.

1.7.2.5 Titanium oxide (TiO_2)

Titanium oxide (TiO_2) is a semiconductor oxide material which exists in a number of crystalline forms where the most important are: (i) anatase, (ii) rutile and (iii) brookite. However, most of the research focuses on the anatase, rutile and P25 forms. Lu *et al*.[120] studied the HDO of guaiacol on Pd catalysts supported on TiO_2 (anatase, rutile and P25). The results showed that the catalysts have a high ability to scission the C−O; due to partially reduced titanium species (Ti^{3+}). Moreover, anatase TiO_2 gave the highest HDO activity of guaiacol at 260 °C (conversion = 100%) than rutile TiO_2 under the same conditions (conversion = 80%). The crystal structure of the bulk TiO_2 unit cell for the anatase phase (a-TiO_2) contains four TiO_2 units (12 atoms). Ti atoms are in octahedral coordination with eight O atoms, provoking inequivalent distances between Ti−O bonds in the structure (long and short bonds).[178]

Due to its optical and electronic properties, it is one of the most suitable catalysts for applications related to solar cells [179], CO_2 photoreduction [180, 181] and hydrogen production.[182] However, this oxide has some limitations, such as a small surface area and low molecular adsorption ability, giving, as a result, low interaction with the oxy molecules. Although, the incorporation of −OH species on the surface tends to facilitate the adsorption of oxy compounds.[183] The use of TiO_2 has been widely investigated for HDO processes. He *et al*.[184] studied the HDO of acetic acid on Pt catalyst (1 wt.%) supported on ZrO_2, CeO_2 and TiO_2. The results indicated that Pt/TiO_2 meets the requirements for ethane production, such as intermediate metal-oxygen bond strength, dissociation of hydrogen and best selectivity. The Pt/TiO_2 acidity is responsible for promoting ethanol dehydration and re-hydrogenation to produce ethane compared with the other catalysts. Zhang *et al*.[122] investigated the HDO of guaiacol on Ni catalysts supported on anatase Al_2O_3, TiO_2, and ZrO_2 supports. The outcomes revealed a high selectivity to phenolic compounds on Ni/TiO_2 (< 1.5 wt.%), whereas saturated hydrocarbons were the main products for the other supports.

1.8 Objectives of the thesis

Effective selection of catalysts requires new technology development where new tools such as DFT calculations will play a significant role. Therefore, this thesis aims to provide a computational study on heterogeneous catalysts for biofuel upgrading to contribute to the design of stable materials for bio-oil upgrading, promoting a circular and sustainable economy.

Chapter 3 aims to analyse the correlation between relevant adsorption energies of the HDO process and electronic properties of thirteen metal surfaces, evaluating their viability as descriptors for the catalytic activity. Using statistical tools such as violin plot and linear regression will increase the accuracy with respect to the descriptors and the interaction with hydrogen and oxygen atoms.

Chapter 4 aims to examine the acid and base properties of five clean and hydroxylated oxide surfaces and their interaction with model compounds derived from the lignin pyrolysis process. In *Chapter 5*, the optimal metal surfaces found in Chapter 3 will be studied to provide atomistic details on the guaiacol HDO mechanism. Different reaction schemes based on the guaiacol C−O bond scission, i.e. (i) C_{aryl}−OH, (ii) C_{aryl}−OCH_3 and (iii) C_{alkyl}−O, are proposed as the first stage of the hydrogenation process. The different C−O cleave energies will be linked through the reaction energy profile, which will rationalise the catalyst's performance and accelerates the design of new catalysts.

Finally, *Chapter 6* aims to create a microkinetic model to understand the guaiacol's HDO conversion from a thermodynamic and kinetic point of view. This study will allow us to analyse the catalyst performance under different temperature conditions, providing a close relationship between experimental and theoretical studies.

1.9 References

1. S. Shafiee and E. Topal, *Energy policy*, 2009, **37**, 181-189.
2. F. A. Malla, A. Mushtaq, S. A. Bandh, I. Qayoom and A. T. Hoang, in *Climate Change*, Springer, 2022, pp. 1-20.
3. M. Allen, et al., presented in part at Intergovernmental Panel on Climate Change, Geneva, CH, 2019
4. World Energy Outlook 2020, https://www.iea.org/reports/world-energy-outlook-2020, (accessed December 2021).
5. Global emissions, https://www.c2es.org/content/international-emissions/, (accessed December, 2021).
6. CO_2 and greenhouse gas emissions, https://ourworldindata.org/co2-and-other-greenhouse-gas-emissions, (accessed August 2020).
7. J. Deutch, *Joule*, 2020, **4**, 2237-2240.
8. H. Fekete, et al., *Renewable and Sustainable Energy Reviews*, 2021, **137**, 110602.
9. J. Rosenow, R. Lowes, O. Broad, G. Hawker, J. Wu, M. Qadrdan and R. Gross, *The pathway to net zero heating in the UK*, UK Energy Research Centre, 2020.
10. J. H. Clark, T. J. Farmer, L. Herrero-Davila and J. Sherwood, *Green Chemistry*, 2016, **18**, 3914-3934.

11. E. Commission, *Communication from the Commission to the European Parliament, the Council, the European Economic and Social Committee and the Committee of the Regions*, Youth Opportunities Initiative, 2011.
12. Z. Wysokińska, *Comparative Economic Research*, 2016, **19**, 57-73.
13. J. Sherwood, *Bioresource Technology*, 2020, **300**, 122755.
14. M. Akia, F. Yazdani, E. Motaee, D. Han and H. Arandiyan, *Biofuel Research Journal*, 2014, **1**, 16-25.
15. R. A. Lee and J.-M. Lavoie, *Animal Frontiers*, 2013, **3**, 6-11.
16. S. C. Bhatia, in *Advanced Renewable Energy Systems*, ed. S. C. Bhatia, Woodhead Publishing India, 2014, pp. 403-425.
17. S. T. Inc, *Second generation biofuels: A review from a market barrier perspective*, IEA Bioenergy, Delta, CA, 2006.
18. A. Yousuf, D. Pirozzi and F. Sannino, in *Lignocellulosic Biomass to Liquid Biofuels*, eds. A. Yousuf, D. Pirozzi and F. Sannino, Academic Press, 2020, pp. 1-15.
19. T. Umezawa, *Phytochemistry Reviews*, 2018, **17**, 1305-1327.
20. M. K. Lam, C. G. Khoo and K. T. Lee, in *Biofuels from Algae (Second Edition)*, Elsevier, 2019, pp. 475-506.
21. A. Yousuf, *Waste Management*, 2012, **32**, 2061-2067.
22. B. A. Simmons, D. Loqué and J. Ralph, *Current Opinion in Plant Biology*, 2010, **13**, 312-319.
23. K. Tekin, S. Karagöz and S. Bektaş, *Renewable and Sustainable Energy Reviews*, 2014, **40**, 673-687.
24. M. M. Ambursa, J. C. Juan, Y. Yahaya, Y. H. Taufiq-Yap, Y.-C. Lin and H. V. Lee, *Renewable and Sustainable Energy Reviews*, 2021, **138**, 110667.
25. J. Zakzeski, P. C. A. Bruijnincx, A. L. Jongerius and B. M. Weckhuysen, *Chemical Reviews*, 2010, **110**, 3552-3599.
26. A. R. Kakroodi and M. Sain, in *Lignin in Polymer Composites*, eds. O. Faruk and M. Sain, William Andrew Publishing, 2016, pp. 195-206.
27. H. E. Desch and J. M. Dinwoodie, *Timber: structure, properties, conversion and use*, Macmillan International Higher Education, 2016.
28. F. G. Calvo-Flores, J. A. Dobado, J. Isac-García and F. J. Martín-Martínez, *Lignin and lignans as renewable raw materials: chemistry, technology and applications*, John Wiley & Sons, 2015.
29. S. Guadix-Montero and M. Sankar, *Topics in Catalysis*, 2018, **61**, 183-198.
30. N. N. Deshavath, V. D. Veeranki and V. V. Goud, in *Sustainable Bioenergy*, eds. M. Rai and A. P. Ingle, Elsevier, 2019, pp. 1-19.
31. Y. Zhang, F. Huo, Y. Wang, Y. Xia, X. Tan, S. Zhang and H. He, *Frontiers in chemistry*, 2019, **7**, 78.
32. H. Kawamoto, *Journal of Wood Science*, 2017, **63**, 117-132.
33. Z. Jiang, H. Zhang, T. He, X. Lv, J. Yi, J. Li and C. Hu, *Green chemistry*, 2016, **18**, 4109-4115.
34. R. Rinaldi, R. Jastrzebski, M. T. Clough, J. Ralph, M. Kennema, P. C. Bruijnincx and B. M. Weckhuysen, *Angewandte Chemie International Edition*, 2016, **55**, 8164-8215.

35. S. Schoenherr, M. Ebrahimi and P. Czermak, *Lignin-Trends and Applications*, 2018.
36. X. Wang, M. Arai, Q. Wu, C. Zhang and F. Zhao, *Green Chemistry*, 2020, **22**, 8140-8168.
37. M. I. Jahirul, M. G. Rasul, A. A. Chowdhury and N. Ashwath, *Energies*, 2012, **5**, 4952-5001.
38. Z. E. Zadeh, A. Abdulkhani, O. Aboelazayem and B. Saha, *Processes*, 2020, **8**, 799.
39. M. Balat, *Energy Sources, Part A: Recovery, Utilization, and Environmental Effects*, 2009, **31**, 516-526.
40. C. Z. Zaman, K. Pal, W. A. Yehye, S. Sagadevan, S. T. Shah, G. A. Adebisi and R. Johan, *Pyrolysis; IntechOpen: Rijeka, Croatia*, 2017, 1.
41. V. Piemonte, M. Capocelli, G. Orticello and L. Di Paola, in *Membrane Technologies for Biorefining*, Woodhead Publishing, 2016, pp. 263-287.
42. N. Doassans-Carrère, J.-H. Ferrasse, O. Boutin, G. Mauviel and J. Lédé, *Energy & Fuels*, 2014, **28**, 5103-5111.
43. C. R. Lohri, D. Sweeney and H. M. Rajabu, *Carbonizing urban biowaste for low-cost char production in developing countries*, Swiss Federal Institute of Aquatic Science and Technology, 2015.
44. Y. Zhang, et al., in *Sustainable Resource Recovery and Zero Waste Approaches*, Elsevier, 2019, pp. 193-206.
45. H. Yang, R. Yan, H. Chen, D. H. Lee, D. T. Liang and C. Zheng, *Fuel processing technology*, 2006, **87**, 935-942.
46. A. Hilal DemirbaŞ, *Energy sources*, 2005, **27**, 1367-1373.
47. A. Javaid, T. Ryan, G. Berg, X. Pan, T. Vispute, S. R. Bhatia, G. W. Huber and D. M. Ford, *Journal of Membrane Science*, 2010, **363**, 120-127.
48. L. Li, J. S. Rowbotham, H. Christopher Greenwell and P. W. Dyer, in *New and Future Developments in Catalysis*, Elsevier, Amsterdam, NL, 2013, pp. 173-208.
49. A. Patel, B. Agrawal and B. R. Rawal, *Energy Sources, Part A: Recovery, Utilization, and Environmental Effects*, 2020, **42**, 1649-1661.
50. H. Yang, R. Yan, H. Chen, D. H. Lee and C. Zheng, *Fuel*, 2007, **86**, 1781-1788.
51. P. A. Horne and P. T. Williams, *Fuel*, 1996, **75**, 1051-1059.
52. D. Meier, B. Van De Beld, A. V. Bridgwater, D. C. Elliott, A. Oasmaa and F. Preto, *Renewable and Sustainable Energy Reviews*, 2013, **20**, 619-641.
53. Q. Zhang, J. Chang, T. Wang and Y. Xu, *Energy conversion and management*, 2007, **48**, 87-92.
54. J. P. Diebold, *A review of the chemical and physical mechanisms of the storage stability of fast pyrolysis bio-oils*, National Renewable Energy Laboratory, Colorado, US, 2000.
55. T. Ba, A. Chaala, M. Garcia-Perez, D. Rodrigue and C. Roy, *Energy & Fuels*, 2004, **18**, 704-712.
56. H. Duan, et al., *Nature Communications*, 2017, **8**, 591.
57. A. Pattiya, in *Direct Thermochemical Liquefaction for Energy Applications*, ed. L. Rosendahl, Woodhead Publishing, 2018, pp. 3-28.

58. Q. Lu, W.-Z. Li and X.-F. Zhu, *Energy Conversion and Management*, 2009, **50**, 1376-1383.
59. M. Ikura, M. Stanciulescu and E. Hogan, *Biomass and bioenergy*, 2003, **24**, 221-232.
60. P. M. Mortensen, J.-D. Grunwaldt, P. A. Jensen, K. Knudsen and A. D. Jensen, *Applied Catalysis A: General*, 2011, **407**, 1-19.
61. N. M. Basir, N. A. M. Jamil and H. Hamdan, *Nanomaterials and Nanotechnology*, 2021, **11**, 1847980420981536.
62. W. Jin, L. Pastor Pérez, D. Shen, A. Sepúlveda-Escribano, S. Gu and T. Ramirez Reina, *ChemCatChem*, 2019, **11(3)**, 924-960.
63. A. Bakhtyari, M. A. Makarem and M. R. Rahimpour, in *Bioenergy Systems for the Future*, Woodhead Publishing, 2017, pp. 87-148.
64. B. Zhang and D. Seddon, *Hydroprocessing catalysts and processes: the challenges for biofuels production*, World Scientific, 2018.
65. G. H. Cedeño, R. Silva-Rodrigo, A. Guevara-Lara, J. A. Melo-Banda, A. I. Reyes de la Torre, F. Morteo Flores and A. Castillo-Mares, *Catalysis Today*, 2016, **271**, 64-79.
66. P. M. Mortensen, J. D. Grunwaldt, P. A. Jensen, K. G. Knudsen and A. D. Jensen, *Applied Catalysis A: General*, 2011, **407**, 1-19.
67. K. Christmann, in *Encyclopedia of Interfacial Chemistry*, Elsevier, Oxford, 2018, pp. 213-220.
68. D. R. Aireddy and K. Ding, *ACS Catalysis*, 2022, **12**, 4707-4723.
69. K. Christmann, *Surface Science Reports*, 1988, **9**, 1-163.
70. E. Furimsky, *Applied Catalysis A: General*, 2000, **199**, 147-190.
71. X. Xu, C. Zhang, Y. Liu, Y. Zhai and R. Zhang, *Chemosphere*, 2013, **93**, 652-660.
72. P. J. de Wild, W. J. J. Huijgen and H. J. Heeres, *Journal of Analytical and Applied Pyrolysis*, 2012, **93**, 95-103.
73. D. Laurenti, P. Afanasiev and C. Geantet, *Applied Catalysis B: Environmental*, 2011, **101**, 239-245.
74. H. Zhao, D. Li, P. Bui and S. Oyama, *Applied Catalysis A: General*, 2011, **391**, 305-310.
75. M. Bykova, D. Y. Ermakov, V. Kaichev, O. Bulavchenko, A. Saraev, M. Y. Lebedev and V. Yakovlev, *Applied Catalysis B: Environmental*, 2012, **113**, 296-307.
76. X. Zhang, T. Wang, L. Ma, Q. Zhang, Y. Yu and Q. Liu, *Catalysis Communications*, 2013, **33**, 15-19.
77. H. Lee, H. Kim, M. J. Yu, C. H. Ko, J.-K. Jeon, J. Jae, S. H. Park, S.-C. Jung and Y.-K. Park, *Scientific reports*, 2016, **6**, 1-8.
78. J. Sun, A. M. Karim, H. Zhang, L. Kovarik, X. S. Li, A. J. Hensley, J.-S. McEwen and Y. Wang, *Journal of catalysis*, 2013, **306**, 47-57.
79. H. Fang, J. Zheng, X. Luo, J. Du, A. Roldan, S. Leoni and Y. Yuan, *Applied Catalysis A: General*, 2017, **529**, 20-31.
80. S. J. Hurff and M. T. Klein, *Industrial & engineering chemistry fundamentals*, 1983, **22**, 426-430.

81. Z. Yu, Y. Wang, Z. Sun, X. Li, A. Wang, D. M. Camaioni and J. A. Lercher, *Green chemistry*, 2018, **20**, 609-619.
82. K. Kirkwood and S. D. Jackson, *Catalysts*, 2020, **10**, 584.
83. C. Zhang, C. Jia, Y. Cao, Y. Yao, S. Xie, S. Zhang and H. Lin, *Green Chemistry*, 2019, **21**, 1668-1679.
84. W.-S. Lee, Z. Wang, R. J. Wu and A. Bhan, *Journal of Catalysis*, 2014, **319**, 44-53.
85. S. Boullosa-Eiras, R. Lødeng, H. Bergem, M. Stöcker, L. Hannevold and E. A. Blekkan, *Catalysis Today*, 2014, **223**, 44-53.
86. S. Echeandia, P. Arias, V. Barrio, B. Pawelec and J. Fierro, *Applied Catalysis B: Environmental*, 2010, **101**, 1-12.
87. B. Yoosuk, D. Tumnantong and P. Prasassarakich, *Chemical engineering science*, 2012, **79**, 1-7.
88. E.-M. Ryymin, M. L. Honkela, T.-R. Viljava and A. O. I. Krause, *Applied Catalysis A: General*, 2010, **389**, 114-121.
89. X. Zhang, Q. Zhang, T. Wang, L. Ma, Y. Yu and L. Chen, *Bioresource technology*, 2013, **134**, 73-80.
90. L. Chen, J. Xin, L. Ni, H. Dong, D. Yan, X. Lu and S. Zhang, *Green Chemistry*, 2016, **18**, 2341-2352.
91. K. Agrawal, A. M. Verma and N. Kishore, *ChemistrySelect*, 2019, **4**, 6013-6025.
92. D. J. Cole-Hamilton, *Science*, 2003, **299**, 1702-1706.
93. The Central Role of Enzymes as Biological Catalysts, https://www.ncbi.nlm.nih.gov/books/NBK9921/, (accessed December 2021).
94. N. Tran, Y. Uemura, T. Trinh and A. Ramli, *Processes*, 2021, **9**, 430.
95. J. A. Melero, J. Iglesias, G. Morales and M. Paniagua, in *Handbook of Biofuels Production (Second Edition)*, Woodhead Publishing, 2016, pp. 359-388.
96. M. Melchionna, P. Fornasiero and M. Cargnello, in *Studies in Surface Science and Catalysis*, eds. P. Fornasiero and M. Cargnello, Elsevier, 2017, vol. 177, pp. 1-56.
97. F. Broglia, L. Rimoldi, D. Meroni, S. De Vecchi, M. Morbidelli and S. Ardizzone, *Fuel*, 2019, **243**, 501-508.
98. C. A. Teles, R. C. Rabelo-Neto, N. Duong, J. Quiroz, P. H. Camargo, G. Jacobs, D. E. Resasco and F. B. Noronha, *Applied Catalysis B: Environmental*, 2020, **277**, 119238.
99. E. Kordouli, B. Pawelec, C. Kordulis, A. Lycourghiotis and J. Fierro, *Applied Catalysis B: Environmental*, 2018, **238**, 147-160.
100. X. Wang, M. Arai, Q. Wu, C. Zhang and F. Zhao, *Green Chemistry*, 2020, **22**, 8140-8168.
101. H. Ooka, J. Huang and K. S. Exner, *Frontiers in Energy Research*, 2021, **9**.
102. S. Eijsbouts, *Applied Catalysis A: General*, 1997, **158**, 53-92.
103. L. Wang, C. Li, S. Jin, W. Li and C. Liang, *Catalysis letters*, 2014, **144**, 809-816.
104. A. J. Medford, A. Vojvodic, J. S. Hummelshøj, J. Voss, F. Abild-Pedersen, F. Studt, T. Bligaard, A. Nilsson and J. K. Nørskov, *Journal of Catalysis*, 2015, **328**, 36-42.
105. H. Wu, C. Feng, L. Zhang, J. Zhang and D. P. Wilkinson, *Electrochemical Energy Reviews*, 2021, **4(3)**, 473-507.

106. A. S. Ouedraogo and P. R. Bhoi, *Journal of Cleaner Production*, 2020, **253**, 119957.
107. A. J. Foster, P. T. M. Do and R. F. Lobo, *Topics in Catalysis*, 2012, **55**, 118-128.
108. Z. He and X. Wang, *Catalysis for sustainable energy*, 2012, **1**, 28-52.
109. J. Long, S. Shu, Q. Wu, Z. Yuan, T. Wang, Y. Xu, X. Zhang, Q. Zhang and L. Ma, *Energy Conversion and Management*, 2015, **105**, 570-577.
110. M. Lu, Y. Sun, P. Zhang, J. Zhu, M. Li, Y. Shan, J. Shen and C. Song, *Industrial & Engineering Chemistry Research*, 2019, **58**, 1513-1524.
111. N. Tran, Y. Uemura, S. Chowdhury and A. Ramli, *Applied Catalysis A: General*, 2016, **512**, 93-100.
112. R. Nava, B. Pawelec, P. Castaño, M. Álvarez-Galván, C. Loricera and J. Fierro, *Applied Catalysis B: Environmental*, 2009, **92**, 154-167.
113. L. Tai, B. De Caprariis, P. De Filippis, R. Hamidi and M. Scarsella, *Chemical Engineering Transactions*, 2021, **86**, 85-90.
114. R. N. Olcese, M. Bettahar, D. Petitjean, B. Malaman, F. Giovanella and A. Dufour, *Applied Catalysis B: Environmental*, 2012, **115-116**, 63-73.
115. J. Zhang, C. Zhao, C. Li, S. Li, C.-W. Tsang and C. Liang, *Catalysis Science & Technology*, 2020, **10**, 2948-2960.
116. A. Gutierrez, R. K. Kaila, M. L. Honkela, R. Slioor and A. O. I. Krause, *Catalysis today*, 2009, **147**, 239-246.
117. M. Hellinger, H. W. P. Carvalho, S. Baier, D. Wang, W. Kleist and J.-D. Grunwaldt, *Applied Catalysis A: General*, 2015, **490**, 181-192.
118. M. Zhou, J. Ye, P. Liu, J. Xu and J. Jiang, *ACS Sustainable Chemistry & Engineering*, 2017, **5**, 8824-8835.
119. M. Hellinger, S. Baier, P. M. Mortensen, W. Kleist, A. D. Jensen and J.-D. Grunwaldt, *Catalysts*, 2015, **5**, 1152-1166.
120. M. Lu, H. Du, B. Wei, J. Zhu, M. Li, Y. Shan and C. Song, *Energy & Fuels*, 2017, **31**, 10858-10865.
121. T. Nimmanwudipong, C. Aydin, J. Lu, R. C. Runnebaum, K. C. Brodwater, N. D. Browning, D. E. Block and B. C. Gates, *Catalysis letters*, 2012, **142**, 1190-1196.
122. X. Zhang, P. Yan, B. Zhao, K. Liu, M. C. Kung, H. H. Kung, S. Chen and Z. C. Zhang, *ACS Catalysis*, 2019, **9**, 3551-3563.
123. D. Raikwar, S. Majumdar and D. Shee, *Molecular Catalysis*, 2021, **499**, 111290.
124. A. Coumans and E. Hensen, *Catalysis Today*, 2017, **298**, 181-189.
125. R. Pentcheva, W. Moritz, J. Rundgren, S. Frank, D. Schrupp and M. Scheffler, *Surface Science*, 2008, **602**, 1299-1305.
126. J. Engel, S. Francis and A. Roldan, *Physical Chemistry Chemical Physics*, 2019, **21**, 19011-19025.
127. J. Lee, E. J. Jang and J. H. Kwak, *Journal of Catalysis*, 2017, **345**, 135-148.
128. P. Somasundaran, *Encyclopedia of surface and colloid science*, CRC press, Florida, US, 2015.
129. I. Chorkendorff and J. W. Niemantsverdriet, *Concepts of modern catalysis and kinetics*, Wiley-VCH, Weinheim, DE, 2017.
130. G. Paglia, C. E. Buckley, A. L. Rohl, R. D. Hart, K. Winter, A. J. Studer, B. A. Hunter and J. V. Hanna, *Chemistry of Materials*, 2004, **16**, 220-236.

131. B. Sathyaseelan, I. Baskaran and K. Sivakumar, *Soft nanoscience letters*, 2013, **2013**.
132. R. Prins, *Journal of Catalysis*, 2020, **392**, 336-346.
133. M. Digne, P. Sautet, P. Raybaud, P. Euzen and H. Toulhoat, *Journal of Catalysis*, 2004, **226**, 54-68.
134. M. Trueba and S. P. Trasatti, *European journal of inorganic chemistry*, 2005, **2005**, 3393-3403.
135. J. Gu, J. Wang and J. Leszczynski, *ACS Omega*, 2018, **3**, 1881-1888.
136. P. Nortier, P. Fourre, A. M. Saad, O. Saur and J. Lavalley, *Applied Catalysis*, 1990, **61**, 141-160.
137. T. Samadhi, S. Subagjo, K. R. Lismana and K. Fuadi, *Journal of Engineering and Technological Sciences* 2011, **43**, 113-126.
138. A. Y. Bunch and U. S. Ozkan, *Journal of catalysis*, 2002, **206**, 177-187.
139. T.-R. Viljava, S. Komulainen, T. Selvam and A. Krause, in *Studies in surface science and catalysis*, Elsevier, 1999, vol. 127, pp. 145-152.
140. T.-R. Viljava, R. Komulainen and A. Krause, *Catalysis Today*, 2000, **60**, 83-92.
141. E. Laurent and B. Delmon, *Journal of Catalysis*, 1994, **146**, 281-291.
142. O. Şenol, T.-R. Viljava and A. Krause, *Catalysis Today*, 2005, **106**, 186-189.
143. E. Laurent and B. Delmon, *Applied Catalysis A: General*, 1994, **709**, 77-96.
144. S. Cheng, L. Wei, X. Zhao and J. Julson, *Catalysts*, 2016, **6**, 195.
145. E. Kusmierek, *Catalysts*, 2020, **10**, 1435.
146. M. Nolan, S. Grigoleit, D. C. Sayle, S. C. Parker and G. W. Watson, *Surface Science*, 2005, **576**, 217-229.
147. S. M. Schimming, O. D. LaMont, M. König, A. K. Rogers, A. D. D'Amico, M. M. Yung and C. Sievers, *ChemSusChem*, 2015, **8**, 2073-2083.
148. S. Dey and G. C. Dhal, *Materials Science for Energy Technologies*, 2020, **3**, 6-24.
149. X. Chen, S. Gao, H. Wang, Y. Liu and Z. Wu, *Catalysis Communications*, 2011, **14**, 1-5.
150. S. Rood, S. Eslava, A. Manigrasso and C. Bannister, *Proceedings of the Institution of Mechanical Engineers, Part D: Journal of Automobile Engineering*, 2020, **234**, 936-949.
151. S. Cao, et al., *Nano Energy*, 2020, **67**, 104287.
152. C. Li, Y. Nakagawa, M. Tamura, A. Nakayama and K. Tomishige, *ACS Catalysis*, 2020, **10**, 14624-14639.
153. P. M. Mortensen, J.-D. Grunwaldt, P. A. Jensen and A. D. Jensen, *ACS Catalysis*, 2013, **3**, 1774-1785.
154. E. A. Elkhalifa and H. B. Friedrich, *Arabian Journal of Chemistry*, 2018, **11**, 1154-1159.
155. R. Evarestov and A. Bandura, *International journal of quantum chemistry*, 2004, **100**, 452-459.
156. D.-N. Zhang, L. Zhao, J.-F. Wang and Y.-L. Li, *Surface Review and Letters*, 2015, **22**, 1550037.
157. Acid-base Behavior of the Oxides, http://www.chemguide.co.uk/, (accessed December 2021).
158. T. Blasco and J. L. Nieto, *Applied Catalysis A: General*, 1997, **157**, 117-142.

159. Q. M. Jebur, A. Hashim and M. A. Habeeb, *Transactions on Electrical and Electronic Materials*, 2019, **20**, 334-343.
160. S. Abinaya, H. P. Kavitha, M. Prakash and A. Muthukrishnaraj, *Sustainable Chemistry and Pharmacy*, 2021, **19**, 100368.
161. I. A. Popov, E. Jimenez-Izal, A. N. Alexandrova and A. I. Boldyrev, *The Journal of Physical Chemistry C*, 2018, **122**, 11933-11937.
162. M. Kulichenko, N. Fedik, D. Steglenko, R. M. Minyaev, V. I. Minkin and A. I. Boldyrev, *Chemical Physics*, 2020, **532**, 110680.
163. Y. Yang, A. Gilbert and C. C. Xu, *Applied Catalysis A: General*, 2009, **360**, 242-249.
164. L. Kaluža, J. Karban and D. Gulková, *Reaction Kinetics, Mechanisms and Catalysis*, 2019, **127**, 887-902.
165. G. L. Tan, M. F. Lemon and R. H. French, *Journal of the American Ceramic Society*, 2003, **86**, 1885-1892.
166. T. Demuth, Y. Jeanvoine, J. Hafner and J. Angyan, *Journal of Physics: Condensed Matter*, 1999, **11**, 3833.
167. C. Arasa, P. Gamallo and R. Sayós, *The Journal of Physical Chemistry B*, 2005, **109**, 14954-14964.
168. R. B. Sosman, *Phases of silica*, Rutgers University Press, New Jersey, US, 1965.
169. L. Zhuravlev, *Colloids and Surfaces A: Physicochemical and Engineering Aspects*, 2000, **173**, 1-38.
170. X. Rozanska, F. Delbecq and P. Sautet, *Physical Chemistry Chemical Physics*, 2010, **12**, 14930-14940.
171. I.-S. Chuang and G. E. Maciel, *The Journal of Physical Chemistry B*, 1997, **101**, 3052-3064.
172. in *Studies in Surface Science and Catalysis*, eds. E. F. Vansant, P. Van Der Voort and K. C. Vrancken, Elsevier, 1995, vol. 93, pp. 59-77.
173. C. H. Lin, S. C. Lee and Y. F. Chen, *Applied physics letters*, 1993, **63**, 902-904.
174. H. S. Lee, A. S. Lee, K.-Y. Baek and S. S. Hwang, in *Dielectric Material*, ed. M. A. Silaghi, InTechOpen, Rijeka, Croatia, 2012, p. 59.
175. K. Burrows and V. Fthenakis, *Solar Energy Materials and Solar Cells*, 2015, **132**, 455-459.
176. S.-K. Wu, P.-C. Lai, Y.-C. Lin, H.-P. Wan, H.-T. Lee and Y.-H. Chang, *ACS Sustainable Chemistry & Engineering*, 2013, **1**, 349-358.
177. S. Jin, Z. Xiao, C. Li, X. Chen, L. Wang, J. Xing, W. Li and C. Liang, *Catalysis Today*, 2014, **234**, 125-132.
178. S. Singh and M. N. Tripathi, *Pramana*, 2017, **89**, 5.
179. J. H. Bang and P. V. Kamat, *Advanced Functional Materials*, 2010, **20**, 1970-1976.
180. O. Ola and M. M. Maroto-Valer, *Journal of Photochemistry and Photobiology C: Photochemistry Reviews*, 2015, **24**, 16-42.
181. J. Low, B. Cheng and J. Yu, *Applied Surface Science*, 2017, **392**, 658-686.
182. V. Jovic, W.-T. Chen, D. Sun-Waterhouse, M. G. Blackford, H. Idriss and G. I. Waterhouse, *Journal of Catalysis*, 2013, **305**, 307-317.

183. N. Muhd Julkapli, S. Bagheri and S. Bee Abd Hamid, *The Scientific World Journal*, 2014, **2014**.
184. Z. He and X. Wang, *Journal of Energy Chemistry*, 2013, **22**, 883-894.

2

Theoretical Background

2.1 Molecular properties of materials

It is well known that the properties of a material formed by a collection of atoms can be understood from variations in the energy upon distortion of the atom's structure. This is a complex task when researchers try to apply the fundamental laws of nature to a system of interest, such as molecules. Quantum mechanics is a basic chemistry theory that describes the nature's physical properties at the scale of atoms. In quantum mechanics, objects exist in a haze of probability; they have a certain chance of being at any point. Applying quantum mechanics to a chemical system is known as quantum chemistry, which deals with developing theories that describe particles' motion in a system and their application in chemical processes.[1] Chemical structure and reactivity involve the interaction of many particles, such as electron interaction, but solving the many-body problems is not generally easy. Therefore, quantum chemistry tries to reduce many-body systems to an approximate effective one-particle system which are numerically easy to know the materials' electronic and physical properties. This chapter discusses the theory and methods behind the simulation employed in the biomass HDO process on transition metals and oxide supports in this thesis. Density functional theory has been selected as a technique that can provide electronic structure information about the different catalytic systems using the Vienna Ab-initio Simulation Package (VASP).

2.2 The Schrödinger Equation

Erwin Schrödinger proposed in 1926 the quantum mechanics model of the hydrogen atom, where the electrons are treated as waves. He defined a basic equation to describe the energy of the system denominated as *Schrödinger equation*, *Eq. 2.1*.

$$\hat{H}\Psi = E\Psi \qquad \text{Eq. 2.1}$$

Where $\hat{H}$ is the Hamiltonian operator corresponding to the system energy, which consists of *M* and *N* (nuclei and electrons of the system, respectively), and the wavefunction, Ψ, which contains all information about the system. Finally, E is the numerical value of the total energy of the state described by Ψ. $\hat{H}$ is a differential operator associated with the sum of the system's kinetic and potential energies, as expressed in *Eq. 2.2.*

$$\hat{H} = -\frac{1}{2}\sum_{i=1}^{N}\nabla_i^2 - \sum_{A=1}^{M}\frac{1}{2M_A}\nabla_A^2 - \sum_{i=1}^{N}\sum_{A=1}^{M}\frac{Z_A}{r_{iA}} + \sum_{i=1}^{N-1}\sum_{j>i}^{N}\frac{1}{r_{ij}} + \sum_{A=1}^{M-1}\sum_{B>A}^{M}\frac{Z_A Z_B}{R_{AB}} \qquad \text{Eq. 2.2}$$

Eq. 2.2 is expressed in atomic units where *A* and *B* are defined as the nuclei (*M*), while *i* and *j* denote the system's electrons (*N*). M_A is the mass of nucleus *A*, Z_A and Z_B are the atomic number of nucleus *A* and *B*, respectively. *R* and r are the distance between the A_{nuclei} - B_{nuclei} and i_{electron} - j_{electron}, respectively. The first two terms in *Eq. 2.2* describe the kinetic energy of the electrons and nuclei ($\hat{T}_e$ and $\hat{T}_N$). Simultaneously, the operator ∇^2 (denominated Laplace) is the sum of the second derivatives concerning the three cartesian coordinates for electrons or nuclei. The remaining terms represent the Coulomb attraction between the nuclei and the electrons, the repulsive potential between electron-electron and nucleus-nucleus interaction ($\hat{V}_{Ne}$, $\hat{V}_{ee}$, and $\hat{V}_{NN}$, respectively).

The nuclei move much slower than the electrons because the atomic nuclei are much heavier (more than 1800 times the mass of an electron). As a result, the electrons are considering moving around fixed nuclei. Therefore, it is common to use the *Born-Oppenheimer approximation*, which assumes the separation of the nuclei and electrons to describe the electrons' motions. For a given collection of electrons in a set of nuclei fields, it is necessary to find the lowest energy configuration (called the ground state) of the electrons. As the nuclei do not move, the nuclei terms' repulsive potential and kinetic energy are eliminated in *Eq. 2.3*, resulting in a simple equation (denominated as electronic Hamiltonian), which describes the motion of electrons.

$$\hat{H}_{elec} = -\frac{1}{2}\sum_{i=1}^{N}\nabla_i^2 - \sum_{i=1}^{N}\sum_{A=1}^{M}\frac{z_A}{r_{iA}} + \sum_{i=1}^{N-1}\sum_{j>1}^{N}\frac{1}{r_{ij}} = \hat{T}_e + \hat{V}_{Ne} + \hat{V}_{ee} \qquad \text{Eq. 2.3}$$

2.3 Density Functional Theory (DFT)

The Schrödinger equation is solved for systems with a single electron. For large systems, approximative numerical solutions need to be obtained. An alternative for treating the many-electron problem is provided by the density functional theory (DFT). In DFT, the term density refers to the electron density, $\rho\,(r)$, of the system, which is used instead of the wavefunction.

2.3.1 Hohenberg-Kohn theorems

Hohenberg and Kohn presented two mathematical theorems in 1964. These fundamental theorems represent the major pillars on which the modern-day density functional theory is based. They demonstrated that for each system, the energy is a functional of its electronic density. The *first Hohenberg-Kohn theorem* states that "the ground state electron density", $\Psi(\rho_o)$, and the ground state wavefunction, Ψ_o, from the Schrödinger equation can be used as a full description of the ground state of the system"; in other words $\Psi_o = \Psi(\rho_o)$.[2] This enables the ground state energy to be expressed as a functional of the ground state density, $F[\Psi(\rho_o)]$.

The first Hohenberg-Kohn theorem proves that the ground state density is enough to obtain all properties of interest. Still, this theorem says nothing if a specific density is the ground state density. The *second Hohenberg-Kohn theorem* states that "the electron density that minimises the energy of the overall function is the true electron density, which corresponds to the full solution of the Schrödinger equation".[3] If the true functional form is known, it is possible to minimise the energy by varying the electron density to find the ground state density. When the ground state density is known, all the properties can be obtained.[4]

2.3.2 Kohn-Sham Equations

Although Hohenberg-Kohn theorems can give a solid idea about the modern DFT, Kohn-Sham (1965) provided a practical form to find the proper electron density, $\rho(r)$. In this idea, the electron density can be solved involving a set of equations (Kohn-Sham equations), where each equation only involves a single electron wave function equation.[4, 5] The Kohn-Sham (KS) equations have the following form, *Eq. 2.4*.

$$\left[-\frac{1}{2}\nabla^2 + V_{ext}(r) + V_H(r) + V_{XC}(r)\right] \cdot \phi_i(r) = \varepsilon_i \cdot \phi_i(r) \qquad \textit{Eq. 2.4}$$

As the solution of the KS equations is a single electron wavefunction, which depends on only three variables, $\phi_i(r)$, the equation is apparently similar as *Eq. 2.1*. Where ε_i represents the energy of the Kohn-Sham orbital (ϕ_i). The first three terms represent three external potentials, where the particles are non-interacting among them. The first potential is the external Coulomb potential, V_{ext}, which describes the interaction between an electron and a collection of nuclei. V_H denominated as Hartree potential, describes the Coulomb repulsion between the electrons. Finally, the third potential, V_{XC}, which is the central idea of the KS equations is based on the exchange-correlation potential. This potential contained all the interactions which are not considered in the other potentials.

2.3.3 Exchange correlation functionals

The fundamental aim of DFT is to obtain the ground state energy of the Schrödinger equation of a many-body problem. Whereas the electron density obtained by the Kohn-Sham equations is possible, the approximations of the wavefunctions are inaccurate. The DFT theorems demonstrated that the correct answer could be obtained if a good functional is chosen. As the exchange-correlation potential, V_{XC}, contains all the interactions and the quantum mechanical effects, this can be obtained from the derivative of the exchange-correlation functional (E_{XC}) with respect to the electron density, *Eq. 2.5.*

$$V_{XC}(r) = \frac{\delta E_{XC}(r)}{\delta \rho(r)}$$ *Eq. 2.5*

The actual form of the E_{XC} is unknown, so it is necessary to find a way to use an approximation for this function. There are two approximations to calculate E_{XC}: (i) The local density approximation (LDA) and (ii) the generalized gradient approximation (GGA).[6]

2.3.3.1 Local density approximation (LDA)

The local density approximation (LDA) describes the atomic structure, and vibrational properties for a wide range of system. In LDA, the E_{XC} is given by *Eq. 2.6.*

$$E_{XC}^{LDA} = \int d^3r \, \rho(r) \, \epsilon_{XC}^{unif}\big(\rho(r)\big)$$ *Eq. 2.6*

Where ϵ_{XC}^{unif} is the exchange-correlation energy per electron of a uniform electron gas. The LDA approximation*, Eq. 2.6,* assumes that the density can be treated locally as a uniform electron gas, and the exchange-correlation energy in the system is the same at each point. This means that in a molecule with many electrons, the density changes slowly over the molecule, e.g. heavy metallic atoms. However, this is not true for molecules where the electron density is not uniform. Moreover, the electron spin densities are not equal. This restricts the use of the LDA approximation, making consistent errors and provoking energetic failures. Therefore, LDA is not accurate enough to describe the energetics of chemical reactions with considerable precision.[7]

2.3.3.2 The generalized gradient approximation (GGA)

In the search for improving the *xc* functional, generalized gradient approximation (GGA) emerged as an important advance to include the electron density gradient, $\nabla\rho(r)$. GGA considers the inhomogeneity of the electron density providing a better description of the electronic system.[8] The GGA E_{XC} is given by *Eq, 2.7.*

$$E_{XC}^{GGA} = \int d^3r\, f\,(\rho(r), \nabla\rho\,(r)) \qquad \textit{Eq. 2.7}$$

Whereas ϵ_{XC}^{unif} is unique in LDA, the function *f* in GGA is not, and many different forms can be suggested.[4] Although the GGA approximation has more physical information, it is not necessarily more accurate. For example, GGA approximation allows improving the representation of localised bonds, although the energy of unoccupied orbitals is minimised, and the adsorption energy values can be exaggerated.

Different E_{XC}^{GGA} functional approximations have been observed favouring higher accuracy and approximation to experimental data. Perdew-Burke-Ernzerhof (PBE) is one of the most used GGA exchange-correlation functional because it has good accuracy for systems such as molecules with metal surfaces, bulk and surface materials.[6, 9-11] Efforts have been put to develop new GGA functionals with better numerical performance to be applied to a wide range of chemical reactions and systems. Another version of the PBE functional, RPBE, has been suggested, which keeps the same features of the PBE functional but use a minimum number of parameters.[12] Both PBE and RPBE follow the same construction logic and physical criteria.[13] RPBE aims to improve the total atomic energies, reducing the maximum and mean absolute error of PBE. However, a general exchange-correlation functional that gives exact calculations of a system's ground state energy is still missing.[9]

2.4 DFT calculations

DFT is a technique to describe atomistic models' electronic, structural, and vibrational properties. It is necessary to solve the Kohn-Sham equations using a computer to cast the problem finely. The Vienna ab initio simulation package (VASP) is an efficient DFT code to study 3D systems with periodic boundary conditions developed by Georg Kresse, Jürgen Furthmuller and Jürgen Hafner.[14] The selection of VASP for DFT calculations for this study over different simulation packages is because VASP is a more efficient and user-friendly package for DTF codes and has clear guidance. Moreover, VASP is usually much quicker for Kohn-Sham calculations and has more post-DFT corrections options than Quantum Expresso and CASTEP.[15] Therefore, VASP will be used for the calculations of the materials for this thesis

VASP proved to be very useful for investigating numerous chemical applications involving electronic systems.[16-19] Therefore, *section 2.4* describes how DFT calculations using VASP help predict fundamental properties such as crystal structure, geometric properties and vibrational frequencies for the different materials studied in this work.

2.4.1 Unit cell

The quantum mechanics approach solves the many-body problem; however, the electrons inside a solid are not the only obstacle to solve for a system. It is necessary to define the location of the atoms in a crystal of a metal. A crystal can be described in terms of a lattice, which is a group of ordered points (denominated as lattice points) that describe the crystal form. This lattice is composed of a repeated small unit in three dimensions called "the unit cell". The lattice is defined by translation vectors, which mathematical expression is described in *Eq. 2.9.*

$$R = n_1 a + n_2 b + n_3 c \qquad \textit{Eq. 2.8}$$

Where n_1, n_2, and n_3 are the integers, and a, b and c are the lattice vectors along the principal directions of the unit cell (called as lattice constants) separated by three angles (α, β, γ), ***Figure 2.1***.[20, 21]

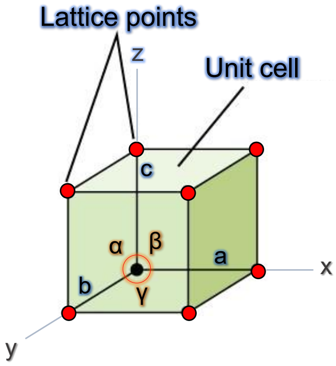

Figure 2.1. *Illustration representing the relationship between the crystal lattice and the unit cell.*

The possible shapes of bulk unit cells are limited by considering that the periodic repetition of the unit cell must not have voids. When the lattice can fill the 3D space periodically repeating without leaving gaps, these are called Bravais lattices (named after Auguste Bravais). Bravais determined that there are 14 distinct lattices in 3D that are grouped into seven lattice systems: orthorhombic (4), cubic (3), tetragonal (2), monoclinic (2), hexagonal, trigonal, and triclinic.[22] Although the composition of a crystal is known, it is not a complete description of the location of the atoms in the material.[23]

2.4.2 Reciprocal space

Reciprocal space (also called *k-space*) is an imaginary space where the reciprocal vectors lie on the real space (space applied for crystals). To describe the reciprocal space, it is necessary to think of any crystal having two lattice vectors (one real and the other reciprocal). The mathematical description of the reciprocal lattice construction can be generated by three reciprocal lattice vectors $b_1, b_2, b_3,$ where the unit cell of the reciprocal lattice is called as Brillouin zone (BZ). K-points are sampling points in the first Brillouin zone (also called as Wigner-Seitz primitive cell) of the material because it is the closest to the origin (0,0,0) (called the gamma point).[24]

In practical calculations, a finite number of k-points to sample the Brillouin zone is fundamental in order to find the electronic ground state. To build the mesh of k-points in the BZ, the Monkhorst-Pack grid method is used. This technique uses a rectangular grid of points of three dimensions (M_x, M_y, M_z), spaced equally through the whole BZ. Basically, the larger the grid dimensions, the more accurate the sampling will be.[25] A convergence test can establish the appropriate size to calculate the dimensions of the grid with a computational time cost. This is the importance of making converge test and how reciprocal space is related in DFT calculations.

2.4.3 Bloch's Theorem

The crystals are represented by periodic boundary conditions, where the system is enclosed in a unit cell. However, there are extended systems, such as molecular simulations in chemical applications, where the unit cell is not large enough. Therefore, it is necessary to define an infinite periodic system and apply DFT calculations for the electrons in the periodic cell.[26] Bloch's theorem applies for the wavefunctions of free electrons (Ψ_k) inside a crystal, which can be described as plane-waves for a periodic cell part (u_k), which has the same periodicity character as the crystal, where $u_k\ (r + R) = u_k(r)$. The electron wavefunctions in the form of *Eq. 2.9* are denominated as Bloch functions.

$$\Psi_k(r) = e^{(ik\cdot r)} \cdot u_k(r) \qquad \textit{Eq. 2.9}$$

The subscript k indicates continuous wavevectors that are confined to the first BZ of the reciprocal lattice. Bloch's theorem aims to use the periodicity of a crystal to reduce the number of one-electron wavefunctions to be calculated in the crystal's unit cell. Therefore, the periodic part of the wavefunction can be written in form of *Eq. 2.10.*[27]

$$u_k(r) = \sum_{G} C_G \cdot e^{(iG\cdot r)} \qquad \textit{Eq. 2.10}$$

C_G can be explained as plane-wave coefficients, where G denotes the reciprocal lattice vectors. This means that the combination of two equations: *Eq. 2.9* and *2.10* gives *Eq. 2.11.* Each wavefunction is written as the sum of plane-waves, where C_{k+G} are plane-waves coefficients which describes the wavefunction.

$$\Psi_k(r) = \sum_{K+G} C_{k+G} + e^{i(k+G)r} \qquad \textit{Eq. 2.11}$$

Eq. 2.11 evaluates the solution at a single point in the reciprocal space. In general, Bloch's theorem allows the calculation of a finite number of electronic wavefunctions for an infinite system. As a result, there are an endless number of k-points for each electron. The wavefunctions at each k-point are now expressed in terms of plane-wave basis set. This means that the plane-waves $(k + G)$ coefficient has a kinetic energy. The number of plane-waves can be represented by a cut-off, where E_{cut} is the maximum kinetic energy of the plane-waves and determines the size of the basis set. The higher the cut-off energy, the more accurate the wavefunction representation. When the calculations are performed, it is necessary to be careful in selecting plane-waves cut-off and k-points. Calculation convergence needs to be done to find accuracy in searching the ground energy of the systems and optimised computational cost.

2.4.4 Dispersion forces

Dispersion forces, such as Van der Waals interactions, can be described as the attraction forces between atoms and molecules that are not directly bonded to each other. Modern DFT only describes the electron correlation effects in ground state molecules but does not correctly describe long-range electronic correlation effects. Different correction schemes have been developed to fix this problem, which is indispensable for the chemical accuracy in DFT calculations. One of the proposed correction schemes is the second order Møller-Plesset perturbation theory (MP2), which is cheaper because of its computational simplicity. However, binding energies are overestimated in π-π interactions and underestimate intermolecular distances.[28] Moreover, MP2 would be computationally demanding for calculations reported in this thesis. One of the most successful methods used to calculate these interactions is the DFT-D, where the general form for the dispersion energy is described in *Eq. 2.12.*

$$E_{disp}^{DFT-D} = -\frac{1}{2}\sum_{A\neq B}\sum_{n} s_n \frac{C_n^{AB}}{R_{AB}^{n}} f_{damp}(R_{AB}) \qquad \textit{Eq. 2.12}$$

Eq. 2.12 denotes the sum of all-atom pairs in the system. C_n^{AB} and R_{AB} represent the averaged dispersion coefficient (*n* describes the order, *n* = 6, 8, 10…) and the internuclear distance for an atom pair (*AB*). s_n is the goal scaling factor, which can be used to adjust the correction to the repulsive behaviour of the chosen exchange-correlation DFT. Finally, f_{damp} is the damping function, which determines the short-range behaviour of the dispersion correction. The damping function is essential in all DFT-D methods because it helps electron correlation effects at intermediate distances. Although this function has been criticised because it has a strong influence on the results due to the specific choice of its parameters to determine the steepness of the function.[29] Therefore, the new DFT-D (DFT-D3) version has a zero-damping function.[30]

DFT-D3 has been validated for its good performance for the interaction in small and large systems in the gas phase, including all periodic table elements.[29] This new version is numerically more stable, including accurate simulations with standard functional, being an accurate tool for theoretical application in chemistry.

2.4.5 Pseudopotentials

The core electrons have a more negligible effect on the properties of the solid because they are tightly bound to the nucleus. In contrast, the valance electrons are outer shell electrons that participate in chemical bonding. Therefore, it is essential to know the description of the atom's core electrons to reduce the number of plane-waves using pseudopotentials. The use of the pseudopotential is based on the energetic interaction of core and valence electrons. This means that the atomic core electrons are replaced by an effective potential (pseudopotential).

The wavefunctions for valence electrons are replaced by pseudo wavefunctions, which reproduce the all-electron calculations' energy levels. This will reduce computational time without missing the effect provided between the interaction of core and valence electrons.[31] The pseudopotential approach is that the electronic structure changes associated with the bonds only occur outside the atomic core regions. Therefore, removing the core regions should not affect the bonding of the system. This result in low plane-waves representing the orbitals, and more speed and a lower memory will be used.[26] Pseudopotentials that require high cut-off energies are denominated as hard, while more computationally efficient pseudopotentials with low cut-off energies are soft.

It is essential to reduce the number of plane-waves in the wavefunction expansion, this is related to the softness of the pseudopotential. Vanderbilt (1990) developed ultrasoft pseudopotentials (USPP); these are smoother and require lower cut-off energies than alternative approaches.[32] Vanderbilt's approach was adopted widely, especially for *3d* TMs saving computer time and improve accuracy. However, the use of many parameters results in extensive tests to describe the wavefunctions accurately; this made the construction of this pseudopotential difficult. Likewise, for materials with a great electronegativity difference and significant magnetic moments, the USPP looks more problematic, with low accuracy.

Blöchl (1994) developed a method to solve these disadvantages, denominated as Projector augmented-wave method (PAW).[33] The construction of PAW datasets is easier because the PAW method works directly with all-electrons wavefunctions and potentials without compromising its efficiency. The PAW approach is to transform true all-electron wavefunction into pseudo wavefunctions as expressed in *Eq. 2.13.*

$$\Psi\,(r) = \widetilde{\Psi}\,(r) + \sum_i \left(\phi_i(r) - \widetilde{\phi}_\imath(r)\right) \langle P_i | \widetilde{\Psi}\,(r) \rangle \qquad \text{Eq. 2.13}$$

Where Ψ and $\widetilde{\Psi}$ are the wavefunction and the pseudo wavefunction, respectively. ϕ_i, $\widetilde{\phi}_\imath$, P_i are the set of all electron partial-waves, pseudo partial-waves, and a projector function, respectively. The partial-waves are chosen to be the solutions of the Schrödinger equation for an isolated atom, and these are equal to the all-electron partial-waves. This method uses the frozen core approximation (the core electrons are frozen), this means that core states are not affected by the ion's environment. The use of PAW is easy to implement in programs because it can handle strong magnetic moments and significant electronegativity differences with high precision.[34]

2.5 DFT calculations of surfaces

2.5.1 Bulk properties

The modelling of surfaces of a periodic crystal has increased due to its importance in different areas, such as catalysis, energy, and material science. The modelling can provide crucial insight into reactive species and the relation between electronic and physical properties of the materials.[35] To study the different materials, e.g. transition metal and oxide supports, a slab needs to be created to study the surface applying periodic boundary conditions.[36] First, it is necessary to specify the crystal structure properties of the bulk, in this case, the lattice parameter (a_O).[37] To calculate a_O values of pure metals, it is necessary to test different values representing the construction and expansion of the unit lattice. Other bulk properties to compare with experimental results are bulk modulus, formation energy and cohesive energy. The material's equilibrium bulk modulus (B_O) explains the material's ability to compress with the change in pressure per atom. In other words, a material with a large bulk modulus is difficult to compress; in contrast, a material with a small bulk modulus is easy to compress.

$$B_O = V\left(\frac{d^2E}{dV^2}\right) \qquad \textit{Eq. 2.14}$$

$$E_{coh} = E_{atom} - \frac{E_{bulk}}{n} \qquad \textit{Eq. 2.15}$$

The bulk modulus of a material is defined using *Eq. 2.14*. Where V is the total ground state energy as a function of the volume, and B_O is evaluated at the minimum of the volume function (V).[38] Another parameter is the cohesive energy (E_{coh}), which is the energy that must be applied to a compound to separate its constituents into free isolated atoms. This is one of the parameters used to understand the nature of chemical bonding, which is calculated using *Eq. 2.15*. In *Eq. 2.15*, E_{atom} and E_{bulk} are the energies of the isolated metal atom in a vacuum and the bulk containing n atoms, respectively. If the values are larger positive, the chemical bonding within the solid is stronger.[39]

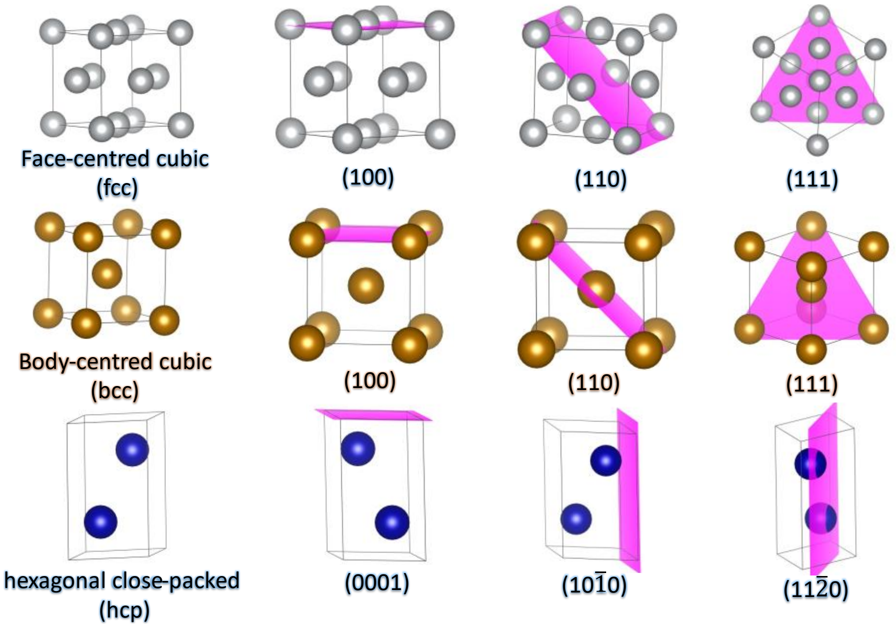

Figure 2.2. *Most common crystal structures for transition metals (i) fcc, (ii) bcc and (iii) hcp. Different planes are represented for each system: for fcc and bcc (111), (100) and (100), and for hcp (0001),* $(10\bar{1}0)$ *and* $(10\bar{2}0)$*.*

The crystal structure explained in *section 2.4.1* is based on the meaning of the simple cubic crystal. Still, most of the elements of the periodic table, in specific transition metals, exist in three different structures: (i) face-centred cubic (fcc), (ii) body-centred cubic and (iii) hexagonal close-packed (hcp). The fcc structure has atoms located in each corner and one centred in each face in the unit cell. The bcc structure has atoms at each corner and one atom in the unit cell centre. While the hcp structure is a regular hexagon structure, this structure has three layers of atoms, having two lattice parameters: *a* and *c*, representing the side and height parameters of the system, respectively, ***Figure 2.2***.

2.5.2 Slab model

The standard structure used to calculate the surface properties is denominated as “slab”, which is created by the cleavage along some plane in the crystal bulk material. The orientation of the plane is represented by indices formed by three numbers in parentheses as *(hlk)*, e.g. *(110), (111), (100)*, denominated as Miller indices.[40] These indices indicate the directions of the surface crystallographic planes. The slab is formed by a finite number of atomic layers, exposing the surface of interest to be modelled, where a large vacuum along the z-direction separates periodic images.[41] The vacuum distance should be as larger as possible to avoid interaction between the adjacent slabs, ***Figure 2.3***.[42] The work required to split the bulk and form the surface is related to the stability of the material.[43] The surface energy *(γ)* is defined as the energy required per unit area to cleave the bulk.[44]

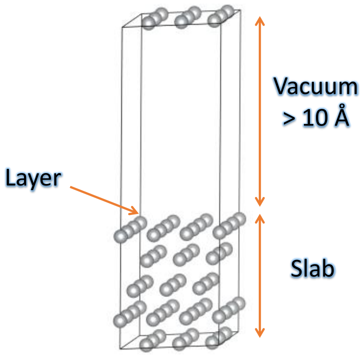

Figure 2.3*. Representation of a slab model of Ni exposing the (111) surface. The slab is composed by five atomic layers with a vacuum size > 10 Å.*

The surface energy is calculated using *Eq. 2.16* from the total energy of the relaxed slab (E_{slab}^{relax}), the unrelaxed frozen bulk-terminated slab (E_{slab}^{fix}), the number of atoms of the slab (n), the energy per atom of the bulk material (E_{bulk}) and A is the area of the newly generated surfaces.[45, 46] The surface energy is expressed as J m^{-2} (1 eV Å^{-2} = 16.02 J m^{-2}).

$$\gamma = \frac{E_{slab}^{relax} - nE_{bulk}}{A} - \frac{E_{slab}^{fix} - nE_{bulk}}{2A} \qquad \text{Eq. 2.16}$$

2.6 Electronic properties

Materials can be classified as metals, semiconductors, or insulators based on the possible energies for an electron in the material, ***Figure 2.4***. A practical way to differentiate the material is to plot the electron energies using the density of states (DOS). First, it is essential to describe the theory behind the behaviour of the electrons inside a metal solid called the band theory.

2.6.1 Band theory

Electrons of a single atom occupy atomic orbitals, and each orbital has a discrete energy. When many atoms are brought together to form a solid, their atomic orbitals overlap. Their discrete energies are perturbed, and each energy splits into levels. Since the number of atoms of a solid is large, the number of orbitals is significant in a tight space. Therefore, the energy of the levels is so close together that they form a continuous band denominated as an energy band. These energy bands will not be the same; the electrons in the collection of individual atoms occupy a band denominated as valence band (V_B). This band is a bonding band filled with electrons, mostly by the outermost electrons. Meanwhile, the anti-bonding band is denominated as conduction band (C_B), an empty band of electrons mainly because the inner electron orbitals do not overlap considerably.[47]

There is a way to group these bands in a given energy interval using the density of states (DOS). The DOS is a mathematical function representing the number of the different states occupied by the system at a particular energy level. The DOS can sketch the electronic properties information involving any material; therefore, it is possible to decompose the DOS into specific orbitals, e.g. *s, p, d* orbitals; this is called projected density of states (PDOS). The integral of this projection up to the Fermi level gives the total electron density. The importance of the DOS at *0 K* is to classify the material into metals, semiconductors, and insulators.[48] There is a difference between the representation of the electronic properties of metals, semiconductors and insulators.

2.6.1.1 DOS of transition metals

The behaviour of the *d*-orbital is characteristic of the transition metals (TMs), where the metals have the valance and the conduction band overlapping, making the band filled with the valence electrons up to the Fermi level. The DOS of transition metals are smooth curves because of the overlap between the *d*-orbital; the *d* states are more localised on the atoms forming a band filled to a certain degree. In contrast, the overlap of *s*- and *p*- orbitals is less significant because these are delocalised. As a result, the *sp*-orbitals form a band that behaves as an almost free electron gas that spreads over the metal, giving a wide band.[49]

2.6.1.2 DOS of semiconductors and insulators

According to the band theory, the semiconductors and insulators act differently from transition metals. A forbidden band separates the valence and conduction band; this is denominated as a bandgap. The bandgap (E_g) is a block of energy with no electrons, and it is not covered by any band between the highest occupied state and the lowest unoccupied state in the V_B and C_B, respectively.[50] The difference between semiconductors and insulators is the E_g size. The E_g of the semiconductor is small, which allows the movement of electrons from V_B to C_B. In contrast, the E_g of the insulators is a wide bandgap, making the crossing of electrons from V_B to C_B almost impossible.

The DOS of the semiconductors and insulators is the same where the valence band is below the Fermi level (E_F). For the oxides, the electronic states of the valence band are dominated by the *O-2p* states, which are close to the Fermi level. In contrast, the C_B is mainly composed of the cation's empty *s* and *p* states. Oxides are good insulators such as γ-Al_2O_3, CeO_2 and MgO and SiO_2 because their V_B is fully occupied with e^-, making them chemically inactive because the e^- cannot move between the atoms.

These oxides can be modified to improve their interaction with molecules through different processes, such as the hydroxylation process.[49]

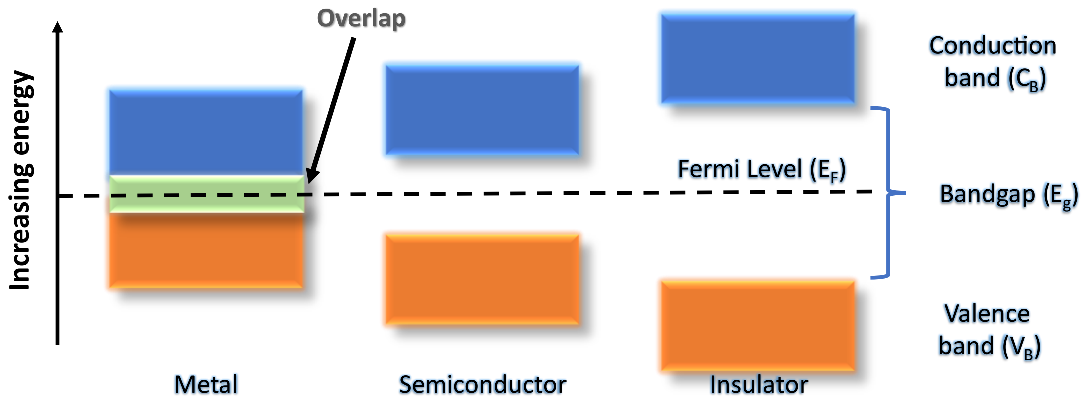

Figure 2.4. *Schematic representation of the band theory of solids.*

2.6.2 Descriptors

The main reactivity for transition metal catalysts has focussed on the behaviour of the electronic properties of the *d states*, which describes the interaction between the metal and the adsorbate. Different descriptors can be obtained from the DOS that work as a reactivity trend model to describe the catalytic activity. These descriptors are divided into primary and secondary features. The primary descriptors are derived from the electronic properties, e.g. d-band centre (ε_d), d-band width (W_d), work function (ϕ), d-band skewness (S_d), and kurtosis (K_d). At the same time, the second features are extracted from the periodic table, e.g. ionization potential, electron affinity and Pauling electronegativity.[51] Because descriptors are often simple to calculate; extensive screening studies can be carried out efficiently over various materials, accelerating the catalyst innovation.[52-54]

2.6.2.1 d-band centre

Hammer and Nørskov introduced the d-band centre (ε_d) parameter. The ε_d measures the interaction strength between the metal and the adsorbate concerning the electronic properties, in this case, the *d-band*.[55, 56] When the metal *d*-orbitals hybridise with the adsorbate's bonding orbitals, two states are created: bonding and antibonding. The location of the d-band centre considers the bond strength between the metal and the adsorbate concerning the degree of filling of the bonding and the antibonding states with respect to the Fermi Level, ***Figure 2.5***.[57] If the antibonding orbital from the hybridization between metal and atom (e.g. oxygen atom) is further away from the Fermi level and has lower electron occupancy, this creates stronger bonding between the metal and the atom (M – O bond).[58] Therefore, a more substantial upward shift, more significant possibility of forming emptier antibonding states, leading to a stronger interaction with the adsorbate. In other words, a higher d-band centre results in stronger bonds.[59, 60] This is because the position of the d-band centre is closer to the Fermi level.

2.6.2.2 d-band width

Vojvodic *et al*.[61] proposed a modification of the d-band model introducing the d-band width (W_d) descriptor in the bonding of metal surfaces, $\varepsilon_d^W = \varepsilon_d + W_d/2$. The new energy descriptor induced variations in bond strength, which were not captured by the simple d-band centre.[62] The use of these parameters captures the effect of the d-electrons and the interaction with the adsorbate introducing a refined energy descriptor with ε_d *and* W_d.[63] Thus, the narrower the bandwidth, the higher the occupation of this d-band is.[64]

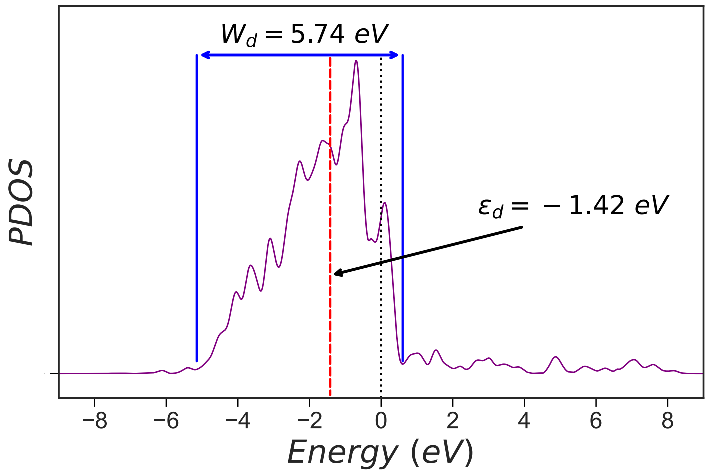

Figure 2.5. *Projected density of states (PDOS) for Ni (111) surface. Dotted black line at zero energy indicates the E_F. The perpendicular dashed red line indicates the d-band centre (ε_d), and the blue upper frame gives the d-band width (W_d). The ε_d is defined as the d-state energy cutting through the middle of all the d-states and it is obtained by halving the integral of the d-band (Eq. 2.17).*

The d-band centre (ε_d) and d-band width (W_d) are obtained from the projected density of states (DOS) on the *d* states, ***Figure 2.5***, where these parameters can be described by their power moment (μ_n). The first moment (ε_d), which describes the distribution's average energy, is shown in *Eq. 2.17*. Where $\rho(\varepsilon)$ represents the density of states distribution, ε is the d-band's energies. Meanwhile, the *nth* centre moment (μ_n) is shown in *Eq. 2.18*. The W_d (second moment) is four times the square root of the width of the distribution relative to the d-band centre, $4\sqrt{\mu_2}$.[65] Other descriptors from the d-band to use are the d-band skewness (S_d) and d-band kurtosis (K_d) represented by the third and fourth moment, respectively. These descriptors are based on the measure of the symmetry and heavy or light tails of the d-band distribution, being defined as $\mu_3/\mu_2^{3/2}$ and μ_4/μ_2^2, respectively.[66]

$$\varepsilon_d = \frac{\int_{-\infty}^{\infty} \varepsilon\rho(\varepsilon)\, d\varepsilon}{\int_{-\infty}^{\infty} \rho(\varepsilon)\, d\varepsilon} \qquad \textit{Eq. 2.17}$$

$$\mu_n = \frac{\int_{-\infty}^{\infty} (\varepsilon - \varepsilon_d)^n \rho(\varepsilon)\, d\varepsilon}{\int_{-\infty}^{\infty} \rho(\varepsilon)\, d\varepsilon}, n = 0, 1, 2, 3, 4 \qquad \textit{Eq. 2.18}$$

2.6.2.3 Work function

The work function (ϕ) is another helpful parameter of great importance to describe the electronic properties of the metal. This descriptor defines the minimum energy needed to remove an electron from a solid initially at the Fermi level (E_F) to take it to the vacuum level, ***Figure 2.6***. The weakest bound electrons in a solid are the electrons at the Fermi level, and the vacuum level (E^{vac}) is the energy level where the e⁻ are not bound. Still, they are free to move in any direction.[67] Therefore, the work function equals the difference between the vacuum and Fermi level, *Eq. 2.19.*

$$\phi = E^{vac} - E_F \qquad \textit{Eq. 2.19}$$

Several works have used the ϕ as a descriptor to understand the catalytic activity. Łosiewicz *et al*.[68] investigated the activity of different metals in the hydrogen electro-evolution exchange current using the work function as an activity descriptor, proving that the catalytic activity is a periodic function of their atomic numbers. Likewise, Shen *et al.*[69] used ϕ as an additional descriptor along with the d-band centre to improve the predicting accuracy and understand the catalytic properties in oxygen reduction reactions.

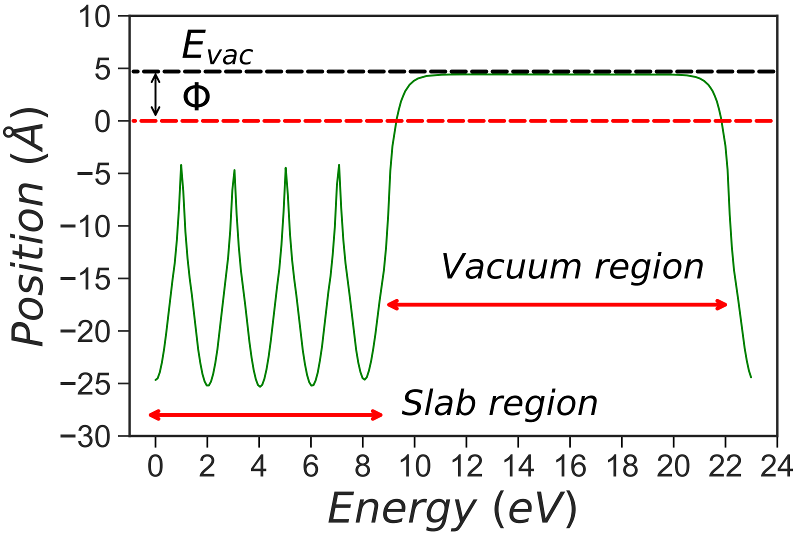

Figure 2.6. *Calculated work function (ϕ) of surface along the z-direction perpendicular to the slab. Parallel red dashed line indicates the E_F*

2.6.3 Bader charge analysis

For some systems, the atomic charges are calculated to determine the interaction of atoms or molecules (e.g. H atom on γ-Al_2O_3). The aim is to calculate the electronic charges of individual atoms in the system, but this calculation is not an easy task because many atoms are in a system. Richard Bader proposed a theory (denominated theory of Atoms in Molecules) to divide the molecule into atoms, and each atom is described by a volume (called Bader volume) based on the charge density.[70] Each volume contains a single maximum charge density separated from other volumes by surfaces (denominated zero flux surfaces). These surfaces have a minimum charge density perpendicular to the surface. In other words, in a molecular system, when the charge density reaches a minimum, the atoms are separated from each other.

In a system, the charge density inside the volume is a good approximation of the total electronic charge of an atom. Because it gives information on the chemical bonding and the bond strength of an atom, making it accessible for computational calculations.[71] In this work, Bader charge analysis was used to measure the level of interaction (charge transfer) between a single atom (e.g. H and O atom) and the surface (oxide surfaces).

2.7 Molecular geometry optimisation

The DFT calculations study any material (e.g. surface, molecules) at *0 K* because the material is relaxed with a minimum energy at this temperature. It is essential for any chemical process to describe the energy of a set of atoms (r) as a function of the position, being $E(r)$ the minimum energy (or local minimum). The first thing to do is to find the geometry optimization; this optimisation refers to the process of finding the minimum energy where the coordinates of a set of atoms are in an equilibrium position in a 3-D arrangement.

This energy is known as potential energy, and the graphical relationship is denominated as potential energy surface (PES). This local minimum is the first derivative of the energy with respect to the atom's position (*Eq. 2.20*), where the negative of this gradient is the force and whose result is zero. Although this stationary point (atom's position) could also be a maximum or a saddle point, therefore, one needs to examine the second derivative of the PES concerning the geometry to discover it.

$$\nabla E = \partial E / \partial \mathrm{r} \qquad \textit{Eq. 2.20}$$

2.7.1 Vibrational frequencies

The frequencies are related to the bond strength of the molecule (stronger bonds require more energy to stretch). Thus, the frequency could be explained as a function of atoms comprising the bond, where the movement of the atoms gives a frequency denominated as vibrational mode.[72] Vibrational frequencies play an essential role in geometry optimisation because they describe the PES curvature to predict the atoms' favourable position when these deviate from the minimum.[73]

The second derivative determines the nature of the turning points on the PES. This test will tell if the point is a local minimum, maximum or a saddle point, where all the points will have a zero gradient (first derivative). The point will be a maximum when the second derivative has negative vibrational frequencies and a minimum when positive vibration frequencies appear. However, if there are positive vibrational frequencies with one or more negative (imaginary) vibrational frequencies, this will be a saddle point, ***Figure 2.7***.[74]

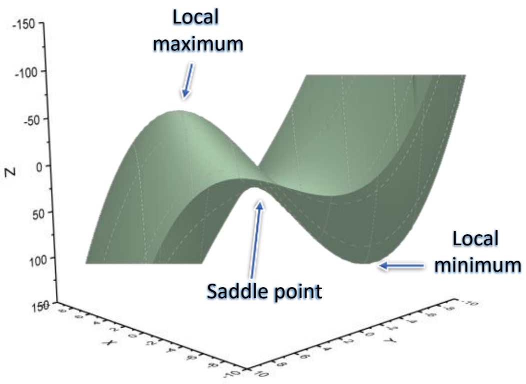

Figure 2.7. *3D representation of the changes in energy that occur as a function of atomic coordinates.*

2.7.2 Transition states

The energy profile can be described as a chemical reaction model, which represents an energetic pathway along the reaction coordinate, illustrating the kinetic and thermodynamic events of the reaction. The reaction coordinate represents the reaction progress following a path that connects the minimum points such as the reactants (initial state) and products (final state), ***Figure 2.8***.[75]

This path passes through a saddle point between the initial and the final states; this point is typically called a transition state. These transition states (TS) are based on the transition state theory (TST), which assumes an activation complex at the top of the energy barrier (highest energy of the chemical reaction). This energy barrier is the minimum energy required for the reaction to occur, which can only proceed in the forward direction. Therefore, a transition state is an intermediate between the reactant and products, describing the activation energy (E_a) of the elementary chemical reactions and the stability of the product.[76]

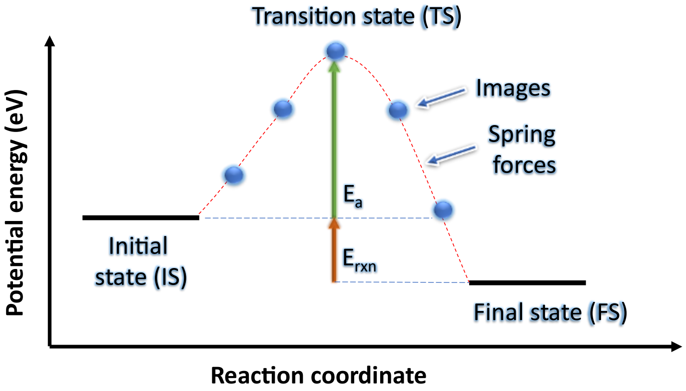

Figure 2.8. *Schematic representation of a reaction path computed with the Nudged elastic band (NEB) method.*

There are different methods to find the TS in an energy path, such as the nudged elastic band (NEB). The NEB is a method that tries to find a saddle point, creating a trajectory with a chain of images (replicas) of the system. Each image finds the lowest energy possible, maintaining an equal distance with the neighbour image. This optimisation is done by adding spring interactions between the adjacent images to ensure the continuity of the path.[77, 78] One characteristic of this method is a force projection ensuring that the spring forces do not obstruct elastic band convergence to the minimum energy path. These forces control the space of the images along the band. Although the NEB method is helpful, it only gives a discrete representation of the minimum energy path where the saddle point needs to be obtained by interpolation. A new modification of this method denominated climbing image Nudged elastic band (CI-NEB), drives the highest energy to the saddle point. The image with the highest energy is identified, and this image does not feel the spring forces along the band. Instead, the image tries to maximize its energy along the band, and when the image converges, this will be similar to the saddle point.[78]

When a very complex system with a significant number of atoms is studied, the computational cost increases considerably; therefore, a new way of finding saddle points is needed. The dimer method (DM) is less computationally demanding to find the transition states because it only uses two system images to create one image (dimer image).[79] These two images (or two replicas) have the exact *3N* coordinates, but a distance separates these. The dimer's energy and force are evaluated with the sum of energies and the average of the forces of the two images. This method moves the dimer uphill on the PES, where the dimer is rotated along the lowest curvature mode, this movement will bring it to the saddle point, and its energy is minimized. Therefore, the saddle point will be a maximum point along the lowest curvature mode. These aspects make it feasible to search transition states with less computational effort.

2.8 DFT+U method

DFT is a convenient tool to predict the properties of different materials. However, it is not accurately acceptable in predicting electronic properties for some reducible semiconductors, e.g. CeO_2, TiO_2. The accurate description of electronic structure is primordial for predicting electronic properties (i.e. bandgap); one alternative to relieve this problem is the so-called Hubbard model correction. The main approach of this model is to treat the strong Coulomb interaction of localised electrons, such as *d* and *f* electrons, which DFT-GGA does not correctly describe. Therefore, these electrons cannot move between atoms freely, and they prefer to jump from one to another. The Hubbard model can include the “on-site repulsion” from the Coulomb repulsion of electrons of the same atomic orbitals.[80]

To describe the strength of the on-site interactions, the method introduces some parameters such as U (on-site Coulomb term, Hubbard parameter) and J (site enhance term). This method can be introduced in the DFT calculations using the (i) Liechtenstein or (ii) Dudarev schemes. The Liechtenstein method introduced the U and J as independent terms. In contrast, the Dudarev scheme joins them in a single parameter $U_{eff} = U - J$ for the Coulomb interaction.[81, 82] The implementation of the DFT+U requires a great understanding of the approximation to provide great accuracy in the calculations.[83] To include the U correction can accurately predict intermolecular interaction and improve the description of the physical and electronic properties of the material with a considerably low computational cost.

One example of using the DFT+U method is on CeO_2 where the typical DFT calculations fail to provide accuracy in the localization of the Ce-*f* states in the reducible CeO_2 oxide system. During the formation of oxygen vacancies, one oxygen is removed from the lattice site, leaving two electrons behind, and splitting the Ce-*4f* band into two occupied and unoccupied bands. These electrons are concentrated on the empty *f state* in Ce^{4+}. In the DOS description, the Ce-*4f* unoccupied band is merged with the Ce-*5d* band in the conduction band.[84, 85] The DFT+U model has been used in several theoretical studies for the ceria system to provide consistency in treating reduced cerium ions. Moreover, it provides the localization of the *Ce-4f* unoccupied band, improving the band gap calculation.[86-88] However, one of the disadvantages of the Hubbard method is that it fails to predict systems' properties with more delocalized electrons, such as metals.

2.9 Microkinetic Modelling

The design of catalysts relies not only on understanding the electronic and physical properties but also on the rate of the chemical reactions. Although this is easy to get in experimental studies, theoretical works can give future predictions in the catalytic design.[89] Kinetic studies help describe the rate of a chemical reaction and find a reaction mechanism that explains how the reactants react to the final product. Moreover, it also predicts the system performance as a function of temperature, pressure, and time conditions. The kinetics of the processes depend on the reactor employed; there are two types of reactors: batch and flow reactor. Batch reactors are widely used in industry to produce fine chemicals. To start the process, the reactor is filled with reactants, which are gradually converted into products. These reactions occur either exothermically or endothermically; therefore, the reaction rate and the concentration of all participants in the reaction vary with time. In contrast, flow reactors are used in large-scale industrial processes. In this reactor, the reactants are continuously fed into the reactor at a constant rate, and the products appear at the outlet. These reactors operate under steady-state conditions, where the reaction and concentration rates become independent of time.[49] However, batch reactors help to conduct operating conditions studies and generate kinetic data more efficiently and economically than other reactors.[90] Therefore, our study will focus on the batch reactor.

A microkinetic model is a convenient tool for consolidating essential information about the catalytic process, intermediates, and products, closing the gap between simulation and experiments. This allows an estimation of the contribution of each elementary step to the overall rate under realistic reaction conditions.[91] However, its main drawback is that the energy barriers of each elementary step must be known. This problem can be solved by density functional theory (DFT), which offers a good agreement with experiments.[92] On the other hand, complex reaction networks are challenging to rationalise only from DFT reaction profiles, and its coupling with the microkinetic model leads to a multiscale tool providing a robust understanding of the system.[93]

2.9.1 Reaction mechanism

The formulation of the reaction mechanism is the first step to create a microkinetic model. This mechanism is a sequence of elementary steps where chemical change occurs and the catalyst is not altered. The reaction mechanism generally includes adsorption of reactants, surface reaction or transformation, and desorption of products. There are two reaction mechanisms (i) Langmuir-Hinshelwood and (ii) Eley-Rideal reaction.

Langmuir-Hinshelwood reaction assumes that all species are adsorbed and accommodate on the surface before they take part in any reaction. Therefore, species react in the chemisorbed state on the surface, e.g. $N^* + H^* \rightleftharpoons NH^*$. In contrast, the Eley-Rideal mechanism assumes that one of the reactants reacts directly out of the gas phase, without being accommodated at the surface, e.g. $C_2H_4 + O^* \rightleftharpoons C_2H_4O^*$. In this case, the reaction of A + B, being B, a gas-phase molecule, approaches the surface and react with chemisorbed A* without being adsorbed. A catalytic reaction proceeds through one of these two mechanisms, impacting the kinetic description. However, in elementary steps, the Eley-Rideal mechanism does not require free sites to react to write the catalytic reaction between A and B. Both catalytic reaction mechanisms have an important implication for the kinetic description. However, the Eley-Rideal mechanism is extremely rare for hydrodeoxygenation because several experiments have found that H_2 and model compounds (such as guaiacol) are adsorbed on the catalyst surface before the reaction occurs.[94, 95] Therefore, Langmuir-Hinshelwood will be used to develop the microkinetic model for this study.[96]

2.9.2 Transition state theory (TST)

Henry Eyring, Meredith Evans, and Michael Polanyi (1935) developed a helpful and straightforward theory to determine the rate of a reaction at equilibrium, denominated as transition state theory (TST). The TST is based on an "active complex", which is the transition state between the reactants and products. The highest energy characterises this complex along the reaction coordinate, where reacting molecules are activated to the transition state by collisions with surrounding molecules.[97]

If the reaction is the dissociation of a diatomic molecule, the stretching vibration between these two atoms in the molecule will weaken the bond between them. Where the rate of reaction from the transition state to the product is taken as the frequency of the reaction coordinate. According to the TST, the rate constant (k) of each surface elementary step can be calculated with *Eq. 2.21.*

$$k = A_o \exp\left(\frac{-\Delta G^{\neq}}{k_B T}\right) = \frac{k_B T}{h}\frac{q_{TS}}{q_{IS}} \exp\left(\frac{-\Delta G^{\neq}}{k_B T}\right) \qquad \textit{Eq. 2.21}$$

Here A_o is the pre-exponential factor, $\Delta G^{\neq}$ is the activation free energy of the reaction, k_B is the Boltzmann constant, h is the plank's constant, T is the temperature and q_{TS} and q_{IS} are the partition functions of the transition and initial states, respectively. The partition functions are introduction in the *section 2.9.3*.

2.9.3 Vibrational energies and partition functions

The kinetic energy of atomic motion can be divided into contributions such as translation, rotation, and vibration. The vibrational states are essential for explaining the molecular structure because vibrations contain all the chemical energy available. The calculation of the vibrational frequency of a molecule helps to discover the contribution of the vibrational energy to the total energy of the molecule. Moreover, if the moment of inertia and vibrational energy is known, translation and the rotation contributions to the total energy can be obtained.[98]

Partition function (q) is the critical feature that allows estimating all thermodynamics functions of the molecule and atoms in elementary reaction steps. Total partition function (Q) is considered as the product of the partition functions. In other words, Q is the product of the contributions from translational (q_{trans}), rotational (q_{rot}), vibrational (q_{vib}), electronic (q_{elec}) energies for a gas molecule, *Eq. 2.22*.[99]

$$Q = q_{trans} \cdot q_{rot} \cdot q_{vib} \cdot q_{elec} \cdot q_{nucl} \qquad \textit{Eq. 2.22}$$

Where q_{trans} is the partition function for the translational, q_{elec}, q_{nucl}, are the partitions functions related to the electrons and the nuclei of the atoms. The rotational partition function (q_{rot}) is related to the number of rotational degrees of freedom of the species. Finally, vibrational partition function (q_{vib}) is related to the vibrational contributions of the species.

2.9.3.1 Translational partition function

When a particle of mass (m) moves in one dimension (x) over a line of length (l) with a velocity, the coordinates available for this particle can be divided into small cells each of size (h), which is the Planck's constant. This is the translational partition function (q_{trans}) for any particle, where the 2D-translational partition function for a free molecule is derived by *Eq. 2.23.*

$$q_{trans}^{2D}(A,T) = \left(\frac{2\pi m k_B T}{h^2}\right) A_{cat} \qquad \textit{Eq. 2.23}$$

Where A_{cat} is the average area of one active site on a catalyst. The 3D-translational partition function for a molecule is calculated using *Eq. 2.24*, where V is the volume of the domain.

$$q_{trans}^{3D} = V * \frac{(2\pi m k_B T)^{3/2}}{h^3} \qquad \textit{Eq. 2.24}$$

2.9.3.2 Rotational partition function

The rotational partition function (q_{rot}) is related to the number of rotational degrees of freedom that a species has. The rotational partition function for a free molecule is calculated using two equations, depending on its symmetry and linear type (*Eq. 2.25 and 2.26*). For larger molecules, the inertial moments along the principal axes need to be considered.

$$q_{rot}^{linear} = \frac{1}{\sigma}\left(\frac{8\pi^2 I k_B T}{h^2}\right) \qquad \textit{Eq. 2.25}$$

$$q_{rot}^{non-linear} = \frac{1}{\sigma}\left(\frac{8\pi^2 k_B T}{h^2}\right)^{3/2} \sqrt{\pi I_a I_b I_c} \qquad \textit{Eq. 2.26}$$

Where σ is the symmetry factor and I is the moment of inertia defined in Eq. 2.27.

$$I = \mu r^2 \qquad \textit{Eq. 2.27}$$

Where the μ is the reduced mass of the atoms in the molecule and r_i is its distance from the rotation axis to the centre of mass. For a homonuclear or a symmetric linear molecule, the factor σ is equals 2, while for a heteronuclear molecule is 1. This symmetry factor can be estimated directly from the symmetry of the molecule.

2.9.3.3 Vibrational partition function

The vibrational partition function (q_{vib}) is related to natural vibration modes obtained through frequency calculations. The q_{vib} of a system is written in *Eq. 2.28*.

$$q_{vib} = \prod_{i=1}^{N} \frac{1}{1 - e^{-hv_i/k_B T}} \qquad \textit{Eq. 2.28}$$

Where i is a specific vibrational mode and N is the number of vibrations. The vibrational partition function in the gas phase, q_{vib}^{gas}, is also calculated using *Eq. 2.28* for $3N_i - 6$

and $3N_i - 5$ vibrational degrees of freedom for a non-linear and linear molecule in the gas phase, respectively, and N_i is the number of atoms in the molecule.

2.9.3.4 Electronic and nuclear partition function

The electronic partition function is related to the molecule's electronic ground state since the energy separation between excited states is very large compared with k_BT. Meanwhile, the nuclear partition function does not contribute to the partition function and can be taken as unity. Usually, the electronic systems are in a singlet electronic state, and the nuclear partition function is unity, e.g. q_{elec} and q_{nucl} are equal constant 1. After the total partition function (Q) is known for each elementary step, it is possible to build a microkinetic model to describe the system's reaction.

Many thermodynamical variables can be obtained from the partition functions, such as entropy (S), specific heat at constant pressure (C_p), enthalpy (H) and free energy (G), using *Eq. 2.29 – 2.33.*

$$S = k_B \ln(Q) + k_B T \left(\frac{\partial \ln Q}{\partial T}\right)_{N,V} \qquad \textit{Eq. 2.29}$$

$$C_p = T\left(\frac{\partial S}{\partial T}\right)_P \qquad \textit{Eq. 2.30}$$

The enthalpy (H) is the combination of the energy calculated by DFT (E_{DFT}) and the zero-point energy (ZPE). This energy considers the vibration energy that exists at 0 K and is calculated using *Eq. 2.31.*

$$ZPE = \sum \frac{1}{2} hv \qquad \textit{Eq. 2.31}$$

$$H = E_{DFT} + ZPE + \int_0^T C_P \, dT \qquad \textit{Eq. 2.32}$$

$$G = H - TS \qquad \textit{Eq. 2.33}$$

2.10 References

1. F. A. Bischoff, in *Advances in Quantum Chemistry*, Academic Press, 2019, vol. 79, pp. 3-52.
2. C. C. M. Rindt and S. V. Gaastra-Nedea, in *Advances in Thermal Energy Storage Systems*, Woodhead Publishing, 2015, pp. 375-415.
3. D. Sholl and J. A. Steckel, *Density functional theory: a practical introduction*, John Wiley & Sons, New Jersey, US, 2011.
4. S. Kurth, M. A. L. Marques and E. K. U. Gross, in *Encyclopedia of Condensed Matter Physics*, Elsevier, Oxford, UK, 2005, pp. 395-402.
5. L. Piela, in *Ideas of Quantum Chemistry*, Elsevier, Amsterdam, Netherlands, 2007, pp. 567-614.
6. P. Ziesche, S. Kurth and J. P. Perdew, *Computational Materials Science*, 1998, **11**, 122-127.
7. K. Burke, J. P. Perdew and M. Ernzerhof, *The Journal of Chemical Physics*, 1998, **109**, 3760-3771.
8. K. Burke, J. P. Perdew and M. Ernzerhof, *International journal of quantum chemistry*, 1997, **61**, 287-293.
9. L. Vega, J. Ruvireta, F. Viñes and F. Illas, *Journal of Chemical Theory and Computation*, 2018, **14**, 395-403.
10. J. P. Perdew, K. Burke and M. Ernzerhof, *Physical review letters*, 1996, **77**, 3865.
11. M. Ernzerhof and G. E. Scuseria, *The Journal of chemical physics*, 1999, **110**, 5029-5036.
12. C. Adamo and V. Barone, *The Journal of chemical physics*, 2002, **116**, 5933-5940.
13. B. Hammer, L. B. Hansen and J. K. Nørskov, *Physical Review B*, 1999, **59**, 7413.
14. G. Sun, J. Kürti, P. Rajczy, M. Kertesz, J. Hafner and G. Kresse, *Journal of Molecular Structure: THEOCHEM*, 2003, **624**, 37-45.
15. J. Hafner, *Computer Physics Communications*, 2007, **177**, 6-13.
16. J. Hafner, *Computer physics communications*, 2007, **177**, 6-13.
17. D. Santos-Carballal, A. Roldan, R. Grau-Crespo and N. H. de Leeuw, *Physical Chemistry Chemical Physics*, 2014, **16**, 21082-21097.
18. J. Engel, S. Francis and A. Roldan, *Physical Chemistry Chemical Physics*, 2019, **21**, 19011-19025.
19. J. Engel, E. Schwartz, C. R. A. Catlow and A. Roldan, *Journal of Materials Chemistry A*, 2020, **8**, 15695-15705.
20. D. Kirsh and A. Kupriyanov, presented in part at Proceedings of Information Technology and Nanotechnology (ITNT-2015), 2015
21. W. Massa, *Crystal structure determination*, Springer, Berlin, DE, 2013.
22. P. Kratzer and J. Neugebauer, *Frontiers in chemistry*, 2019, **7**, 106.
23. R. A. Dunlap, *Crystalline structure*, Morgan & Claypool Publishers, California, US, 2018.

24. P. K. Misra, in *Physics of Condensed Matter*, ed. P. K. Misra, Academic Press, Boston, US, 2012, pp. 1-35.
25. H. J. Monkhorst and J. D. Pack, *Physical review B*, 1976, **13**, 5188.
26. E. J. Bylaska, in *Annual Reports in Computational Chemistry*, Elsevier, 2017, vol. 13, pp. 185-228.
27. J. M. Martínez-Duart, R. J. Martín-Palma and F. Agulló-Rueda, *Survey of Solid State Physics*, Elsevier, Amsterdam, NL, 2006.
28. S. Grimme, *Journal of computational chemistry*, 2004, **25**, 1463-1473.
29. S. Grimme, J. Antony, S. Ehrlich and H. Krieg, *The Journal of chemical physics*, 2010, **132**, 154104.
30. J. Moellmann and S. Grimme, *The Journal of Physical Chemistry C*, 2014, **118**, 7615-7621.
31. G. L. Gutsev, in *Advances in Quantum Chemistry*, Academic Press, 1998, vol. 29, ch. 137-157, pp. 137-157.
32. G. Srivastava and D. Weaire, *Advances in Physics*, 1987, **36**, 463-517.
33. P. E. Blöchl, *Physical review B*, 1994, **50**, 17953.
34. G. Kresse and D. Joubert, *Physical Review B*, 1999, **59**, 1758.
35. J. P. Janet, Q. Zhao, E. I. Ioannidis and H. J. Kulik, *Molecular Simulation*, 2017, **43**, 327-345.
36. W. Sun and G. Ceder, *Surface Science*, 2013, **617**, 53-59.
37. M. F. Horstemeyer, *Integrated Computational Materials Engineering (ICME) for metals: using multiscale modeling to invigorate engineering design with science*, John Wiley & Sons, New Jersey, US, 2012.
38. R. Gaudoin and W. M. C. Foulkes, *Physical Review B*, 2002, **66**, 052104.
39. P. Janthon, S. Luo, S. M. Kozlov, F. Vines, J. Limtrakul, D. G. Truhlar and F. Illas, *Journal of chemical theory and computation*, 2014, **10**, 3832-3839.
40. M. Ohring, in *Engineering Materials Science*, ed. M. Ohring, Academic Press, San Diego, US, 1995, pp. 1-11.
41. P. Fornasiero and M. Cargnello, *Morphological, Compositional, and Shape Control of Materials for Catalysis*, Elsevier, 2017.
42. W. C. Sun, Gerbrand, *Surface Science*, 2013, **617**, 53-59.
43. J. Wang and S.-Q. Wang, *Surface Science*, 2014, **630**, 216-224.
44. R. W. Balluffi, S. Allen and W. C. Carter, *Kinetics of materials*, John Wiley & Sons, Hoboken, New Jersey, 2005.
45. J. R. dos Santos Politi, F. Viñes, J. A. Rodriguez and F. Illas, *Physical Chemistry Chemical Physics*, 2013, **15**, 12617-12625.
46. H. W. Hugosson, O. Eriksson, U. Jansson, A. V. Ruban, P. Souvatzis and I. Abrikosov, *Surface science*, 2004, **557**, 243-254.
47. S. A. Holgate, *Understanding solid state physics*, CRC Press, Florida, US, 2021.
48. R. Hoffmann, *Solids and surfaces: a chemist's view of bonding in extended structures*, John Wiley & Sons, 2021.
49. I. Chorkendorff and J. W. Niemantsverdriet, *Concepts of modern catalysis and kinetics*, Wiley-VCH, Weinheim, DE, 2017.
50. Band gap, https://www.britannica.com/science/band-gap, (accessed 1 June 2021).
51. Z. Li, X. Ma and H. Xin, *Catalysis Today*, 2017, **280**, 232-238.

52. F. Abild-Pedersen, J. Greeley, F. Studt, J. Rossmeisl, T. Munter, P. G. Moses, E. Skulason, T. Bligaard and J. K. Nørskov, *Physical review letters*, 2007, **99**, 016105.
53. D. Loffreda, F. Delbecq, F. Vigné and P. Sautet, *Journal of the American Chemical Society*, 2006, **128**, 1316-1323.
54. R. A. Van Santen, M. Neurock and S. G. Shetty, *Chemical reviews*, 2009, **110**, 2005-2048.
55. A. Pérez-Mendoza and R. Ribadeneira, in *Density Functional Theory*, IntechOpen, 2018.
56. B. Hammer and J. Nørskov, *Surface Science*, 1995, **343**, 211-220.
57. S. Bhattacharjee, U. V. Waghmare and S.-C. Lee, *Scientific reports*, 2016, **6**, 35916.
58. J. Greeley and J. K. Nørskov, *Surface science*, 2005, **592**, 104-111.
59. B. Hammer and J. K. Norskov, *Nature*, 1995, **376**, 238-240.
60. A. Medford, A. Vojvodic, J. Hummelshøj, J. Voss, F. Abild-Pedersen, F. Studt, T. Bligaard, A. Nilsson and J. Nørskov, *Journal of Catalysis*, 2015, **328**.
61. A. Vojvodic, J. Nørskov and F. Abild-Pedersen, *Topics in catalysis*, 2014, **57**, 25-32.
62. D. Pettifor, *Journal of Physics C: Solid State Physics*, 1970, **3**, 367.
63. P. Pankajakshan, S. Sanyal, O. E. de Noord, I. Bhattacharya, A. Bhattacharyya and U. Waghmare, *Chemistry of Materials*, 2017, **29**, 4190-4201.
64. E. N. Economou, *The physics of solids: essentials and beyond*, Springer Science & Business Media, Berlin, DE, 2010.
65. A. Vojvodic, J. Nørskov and F. Abild-Pedersen, *Topics in catalysis*, 2014, **57**, 25-32.
66. H. Xin, A. Vojvodic, J. Voss, J. K. Nørskov and F. Abild-Pedersen, *Physical Review B*, 2014, **89**, 115114.
67. A. Kahn, *Materials Horizons*, 2016, **3**, 7-10.
68. B. Łosiewicz, M. Popczyk, I. Napłoszek and A. Budniok, presented in part at Solid State Phenomena, 2015
69. X. Shen, Y. Pan, B. Liu, J. Yang, J. Zeng and Z. Peng, *Physical Chemistry Chemical Physics*, 2017, **19**, 12628-12632.
70. W. Tang, E. Sanville and G. Henkelman, *Journal of Physics: Condensed Matter*, 2009, **21**, 084204.
71. G. Henkelman, A. Arnaldsson and H. Jónsson, *Computational Materials Science*, 2006, **36**, 354-360.
72. J. D. Kubicki and H. D. Watts, *Minerals*, 2019, **9**, 141.
73. H. Nakata, D. G. Fedorov, F. Zahariev, M. W. Schmidt, K. Kitaura, M. S. Gordon and S. Nakamura, *The Journal of chemical physics*, 2015, **142**, 124101.
74. Y. Saad, J. R. Chelikowsky and S. M. Shontz, *SIAM review*, 2010, **52**, 3-54.
75. G. L. Errol, *Springer, New York*, 2011, **43**, 44-45.
76. F. Jensen, *Introduction to computational chemistry*, John wiley & sons, New Jersey, US, 2017.
77. G. Henkelman and H. Jónsson, *The Journal of chemical physics*, 2000, **113**, 9978-9985.

78. G. Henkelman, B. P. Uberuaga and H. Jónsson, *The Journal of chemical physics*, 2000, **113**, 9901-9904.
79. G. Henkelman and H. Jónsson, *The Journal of chemical physics*, 1999, **111**, 7010-7022.
80. S. A. Tolba, K. M. Gameel, B. A. Ali, H. A. Almossalami and N. K. Allam, *Density Functional Calculations-Recent Progresses of Theory and Application*, 2018, 3-30.
81. A. Liechtenstein, V. I. Anisimov and J. Zaanen, *Physical Review B*, 1995, **52**, R5467.
82. S. Dudarev, G. Botton, S. Savrasov, C. Humphreys and A. Sutton, *Physical Review B*, 1998, **57**, 1505.
83. S. A. Tolba, K. M. Gameel, B. A. Ali, H. A. Almossalami and N. K. Allam, *Density Functional Calculations: Recent Progresses of Theory and Application*, 2018, **1**.
84. J. Kullgren, C. W. M. Castleton, C. Müller, D. M. Ramo and K. Hermansson, *The Journal of Chemical Physics*, 2010, **132**, 054110.
85. L. J. Bennett and G. Jones, *Physical Chemistry Chemical Physics*, 2014, **16**, 21032-21038.
86. F. Esch, S. Fabris, L. Zhou, T. Montini, C. Africh, P. Fornasiero, G. Comelli and R. Rosei, *Science*, 2005, **309**, 752-755.
87. D. Lu and P. Liu, *The Journal of chemical physics*, 2014, **140**, 084101.
88. A. Peles, *Journal of Materials Science*, 2012, **47**, 7542-7548.
89. A. H. Motagamwala and J. A. Dumesic, *Chemical Reviews*, 2021, **121**, 1049-1076.
90. A. K. Noriega, A. Tirado, C. Méndez, G. Marroquín and J. Ancheyta, *Chinese Journal of Chemical Engineering*, 2020, **28**, 1670-1683.
91. J. K. Nørskov, F. Studt, F. Abild-Pedersen and T. Bligaard, *Fundamental concepts in heterogeneous catalysis*, John Wiley & Sons, 2014.
92. J. K. Nørskov, F. Abild-Pedersen, F. Studt and T. Bligaard, *Proceedings of the National Academy of Sciences*, 2011, **108**, 937-943.
93. M. Rellán-Piñeiro and N. López, *ACS Sustainable Chemistry & Engineering*, 2018, **6**, 16169-16178.
94. L. Zhou and A. Lawal, *Applied Catalysis A: General*, 2017, **532**, 40-49.
95. R. V. Chaudhari, A. Torres, X. Jin and B. Subramaniam, *Industrial & Engineering Chemistry Research*, 2013, **52**, 15226-15243.
96. A. Behroozsarand and A. N. Pour, *Journal of Natural Gas Science and Engineering*, 2014, **20**, 99-108.
97. E. Mavroudakis, D. Cuccato and D. Moscatelli, in *Computational Quantum Chemistry*, ed. M. Soroush, Elsevier, 2019, pp. 47-98.
98. V. P. Gupta, in *Principles and Applications of Quantum Chemistry*, ed. V. P. Gupta, Academic Press, Boston, 2016, pp. 247-289.
99. A. L. Cooksy, in *Mathematical Physics in Theoretical Chemistry*, eds. S. M. Blinder and J. E. House, Elsevier, 2019, pp. 161-187.

3

Biomass hydrodeoxygenation catalysts from atomistic activity descriptors

3.1 Introduction

As shown by many previous reports, transition metals (TMs) such as Fe [1, 2], Co [3, 4], Ni [5-7], Cu [5, 8], Mo [9-11], Ru [12, 13], Rh [3, 14], Pd [15-18], W [19], Pt [17, 20-22] are highly active catalysts in the HDO reaction. However, these catalysts also show high activity for the hydrogenation of aromatic rings leading to less-desirable saturated products; furthermore, most of these catalysts rapidly deactivate due to coking.[23, 24] A complete understanding of the HDO process on the catalysts is needed to design new selective and durable materials. Several computational studies provided insights into the HDO reaction, but the search for understanding the relationship between activity, selectivity, and the catalysts' properties is still ongoing.[25-30]

The catalytic activity of supported metal catalysts depends on structural features (e.g. particle size and shape), structure and nature of the support, and the intrinsic properties of the metal atoms. It is beneficial to have a thermodynamically feasible pathway with low activation barriers for the desired reaction and weak binding of the products on the catalyst to prevent site inhibition for an efficient catalytic turnover. Commonly, linear Brønsted-Evans-Polanyi (BEP) relationships can be found between the activation and the adsorption energies, which may lead to volcano relations between adsorptions strength and catalytic activity (Sabatier principle).[31-33] Similar to the BEP, the scaling relationships are graphical constructions illustrating the correlation between adsorption energies with oxygenated species and properties of the catalysts, e.g. transition metal surfaces.[34] Basic geometric and electronic properties of the catalytic surfaces, which control the activation energies for the elementary surface reaction, can be used as descriptors of the catalytic activity.[35-37]

Because descriptors are often simple to calculate; extensive screening studies can be carried out efficiently over various materials, accelerating the catalyst innovation.[34, 38, 39]

Chapter 3 explores the relationship between 13 TMs, e.g. Fe, Co, Ni, Cu, Mo, Ru, Rh, Pd, Ag, W, Ir, Pt and Au, and their affinity for hydrogen and oxygen, using density functional theory (DFT) calculations. The relation of these parameters will define the trends of the hydrodeoxygenation (HDO) process on biomass-derived compounds.

3.2 Computational details

3.2.1 Bulk calculation details

It is essential to study the bulk structure through a series of convergence performances to investigate the surface properties of the metals and the adsorption process.[40] Among the different GGA-functionals, PBE is selected due to its reliable description of the hydrogen bonding, which is crucial for determining metal surfaces in the HDO process, giving a good description for periodic DFT calculations of metallic systems.[41] In recent years, RPBE-GGA functional has received attention due to its ability to predict adsorption energies in heterogeneous catalytic reactions, where RPBE performs very well for chemisorption in a set of experimental energies for adsorption reactions.[42] Therefore, this study selects these two GGA-functional to determine the electronic properties and adsorption energies with hydrogen and oxygen.

In this study, groups 6 (Mo, W), 8 (Fe, Ru), 9 (Co, Rh, Ir), 10 (Ni, Pd, Pt), and 11 (Cu, Ag, Au) metals were considered as potential catalysts for the HDO process. All calculations were performed with the Vienna Ab initio Simulation Package (VASP) [43], using two types of GGA functionals within the density functional theory (DFT): (i) the standard version of the Perdew-Burke-Ernzerhof (PBE) exchange functional and (ii) the revised version (RPBE).[44, 45] The core electrons were described using the Projected Augmented Wave (PAW) formalism.[46] Long-range interactions were added using Grimme's empirical dispersion correction DFT-D3.[47]

The number of k-points was sampled with a Monkhorst-Pack grid for bulk calculations.[48] ***Figure 3.1 (a)*** represents the convergence calculation for Ni bulk, where the energy varies considerably as the number of k-points changes and the computational time increases. When the number of k-points is more significant than > 13, the total energy reaches a plateau, indicating that the 13 x 13 x 13 k-points is enough to have a well-converged result and a reasonable computational cost. The cut-off energy for Ni bulk is calculated as an example to find the well-converged energy. **Figure 3.1 (b)** shows the plot with the cut-off energy against the energy per atom for the Ni bulk, in which 450 eV is enough to converge.

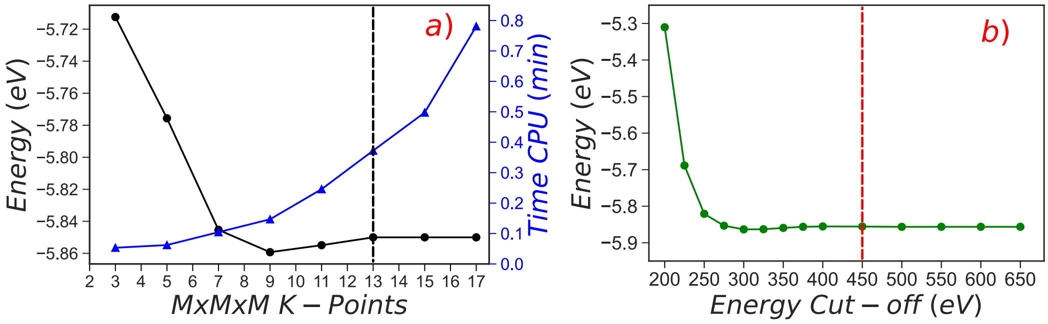

Figure 3.1. *Converged studies for the (a) k-points and (b) cut-off energy for Ni bulk*

The calculations of bulk properties (*Eq. 2.14 and 2.15*), e.g. lattice parameter (a_o), bulk modulus (B_o), and cohesive energy (E_{coh}), play a crucial role in validating and helping to understand mechanical properties of the materials. To describe the performance of each GGA-functional (PBE, RPBE), the accuracy of a_o, B_o, and E_{coh} was analysed against the experimental values. ***Table 3.1*** summarised the bulk parameters for 13 metallic elements with three different structures (fcc, bcc, and hcp) for the GGA-functional based on statistical analysis to identify the best functional to use in this study: (i) MAE (mean absolute error) and (ii) MPE (Mean percentage error). All the data is in good agreement with experiment values, and there are no systematic errors observable in the two functional methods, ***Figure 3.2***.[49]

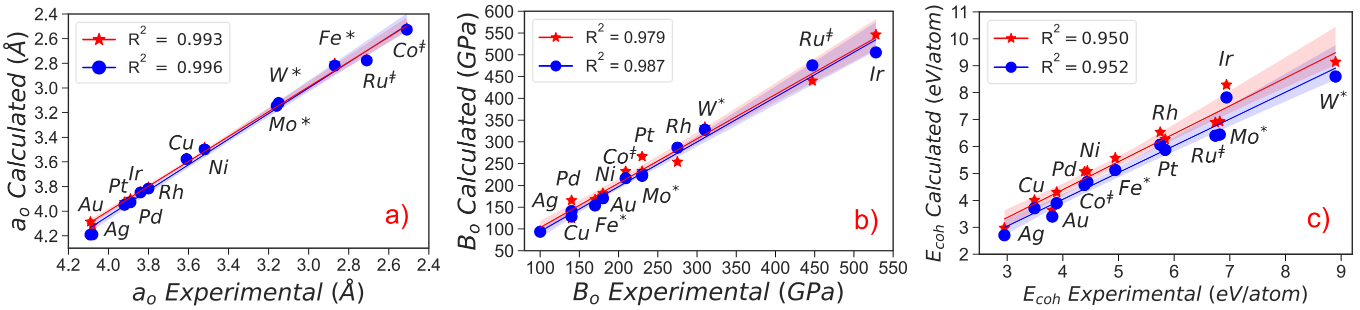

Figure 3.2. *Calculated results for (a) lattice parameter, a_o, (b) bulk modulus, B_o, and (c) cohesive energy, E_{coh} for GGA (PBE and RPBE) functional with their respective experimental values. GGA-PBE and RPBE are represented in red and blue colours, respectively. * and ‡ correspond to bcc and hcp metal structures.*

Table 3.1. *Mean absolute error (MAE) and mean percentage error (MPE) of the GGA-functional (PBE and RPBE) calculated values compared to experimental ones for 13 metallic elements.*

	PBE						RPBE					
	MAE			MPE			MAE			MPE		
	a_o (Å)	B_o (GPa)	E_{coh} (eV/a)*	a_o (%)	B_o (%)	E_{coh} (%)	a_o (Å)	B_o (GPa)	E_{coh} (eV/a)*	a_o (%)	B_o (%)	E_{coh} (%)
Ni	0.04	2.0	0.65	−1.0%	−1.1%	−14.6%	0.02	9.7	0.24	0.6%	5.4%	−5.5%
Cu	0.04	15.4	0.52	−1.1%	11.0%	−14.8%	0.03	11.7	0.22	0.9%	8.4%	−6.2%
Rh	0.01	21.0	0.78	0.1%	7.6%	−13.6%	0.02	11.8	0.32	−0.4%	−4.3%	−5.5%
Pd	0.01	25.7	0.42	0.3%	−18.3%	−10.6%	0.04	1.1	0.01	−1.0%	−0.8%	−0.2%
Ag	0.04	5.2	0.02	−0.1%	5.2%	−0.8%	0.10	6.4	0.25	−2.5%	6.4%	8.3%
Ir	0.01	18.2	1.35	0.1%	−3.4%	−19.5%	0.01	22.6	0.88	−0.2%	4.3%	−12.7%
Pt	0.01	36.4	0.43	0.2%	−15.8%	−7.4%	0.03	5.5	0.03	−0.7%	2.4%	−0.6%
Au	0.03	3.8	0.17	0.8%	2.1%	4.6%	0.11	9.3	0.41	−2.7%	5.2%	10.9%
Fe‡	0.07	2.3	0.63	−2.5%	1.3%	−12.8%	0.05	16.1	0.19	1.8%	9.5%	−3.8%
Mo‡	0.03	2.4	0.11	−0.9%	−1.0%	−1.6%	0.03	7.9	0.38	0.9%	3.5%	5.5%
W‡	0.02	23.9	0.24	−0.5%	−7.7%	−2.7%	0.02	17.9	0.30	0.5%	−5.8%	3.4%
Co^{+}	0.01	23.5	0.68	0.2%	−11.2%	−15.4%	0.02	7.5	0.19	−0.7%	−3.6%	−4.2%
Ru^{+}	0.06	6.8	0.15	2.0%	1.5%	−2.3%	0.07	28.8	0.34	−2.5%	−6.4%	5.0%
	0.02	14.3	0.47	−0.2%	−2.3%	−8.6%	0.04	12.0	0.29	−0.5%	1.9%	−0.4%

* E_{coh} is in eV/atom units, ‡ These metals have a bcc structure, $^{+}$ These metals have a hcp structure

Bulk calculations showed that the RPBE modelled the bulk properties slightly better than the PBE functional with a small range of error in comparison with the experimental values. B_o and E_{coh} present the most considerable difference between the two GGA-functional compared to a_o. This statement is supported by the MPE, where PBE showed an error of −2.3% and −8.6% for B_o and E_{coh}, respectively, whereas, for RPBE, the error is less significant (1.9% and −0.4%).[50] The main difference is seen in the cohesive energy, where metallic elements such as Ir, Co, Ni and Cu present the highest % of error compared with the experimental values for PBE (MPE: −19.5%, −15.4%, −14.8%, and −14.6%, respectively). The use of statistical methods supports the selection of RPBE as the functional with minor errors in the studies. Therefore, RPBE will be used to systematically study the surface and adsorption with H and O species.

3.2.2 Surface calculation details

Slab models of their low index surfaces were generated with the Atomic Simulation Environment (ASE) based on optimised bulk lattice parameters.[51] The setup of our slab models was based on benchmarking calculations on *Ni (111), Ni (110), and Ni (100)*. ***Figure 3.3*** shows the variations in surface energy with the number of metal atom layers, vacuum thickness, the number of relaxed layers, and the number of k-points for the three Ni surfaces. The results help to build the slab model for each surface.

Based on previous studies (*section 3.2.1*), spin-polarized density functional theory (DFT) calculations were carried out using VASP (Vienna Ab initio Software Package) code to systematically study the hydrogen and oxygen adsorption on a wide range of TM surfaces. The exchange and correlation contributions were calculated using the revised functional of Perdew-Burke-Ernzerhof (RPBE). A kinetic energy cut-off of 550 eV was defined for the valence electron plane-wave basis set.[44] The incorporation of dipole corrections is due to eliminating the error induced by the artificial electrostatic interaction between the surface dipole moments of repeated slabs.[52] Therefore, dipole corrections were employed perpendicular to the metal surfaces upon hydrogen/oxygen adsorption

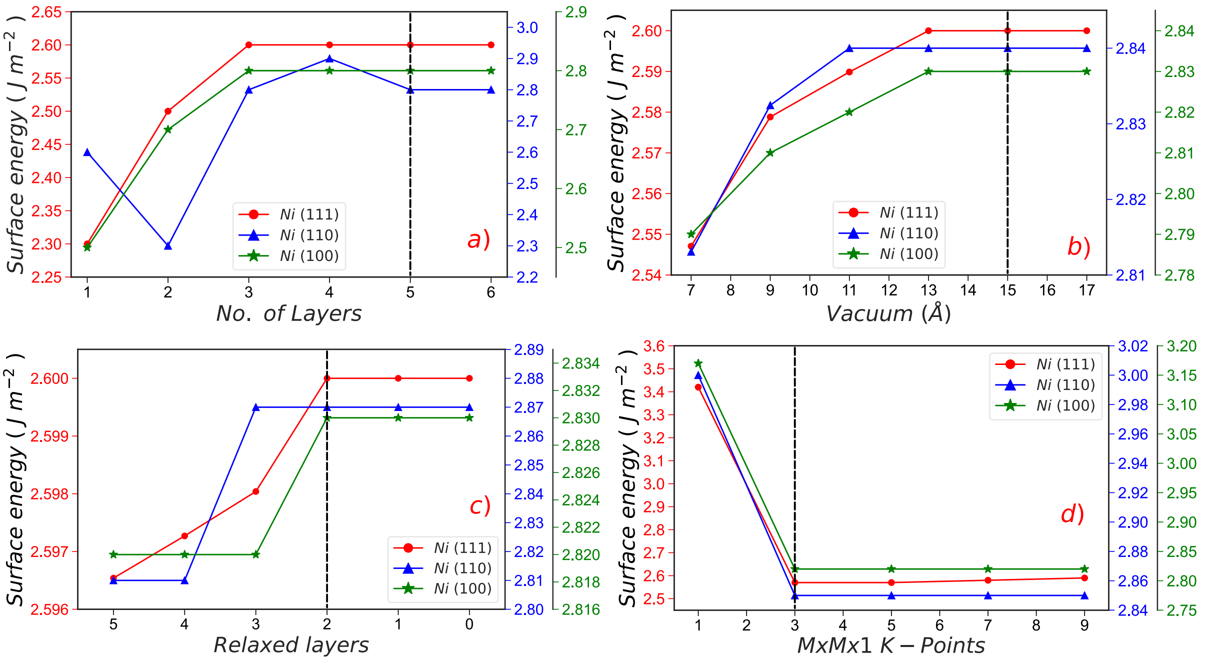

Figure 3.3. *Variation of surface energy of (a) number of layers, (b) vacuum thickness, (c) relaxed layers, and (d) number of k-points of fcc-Ni (111), (110), and (100).*

Each slab model consists of five atomic layers, where the top two were relaxed, and the bottom three layers were fixed to their bulk positions. A vacuum of 15 Å along the z-axis was added to avoid any interaction with the periodic images. The Brillouin zone was sampled with a Monkhorst-Pack 3 x 3 x 1 k-point grid for surface calculations. Isolated molecules were placed in a 20 x 20 x 20 Å box to avoid interactions with their periodic image. The selection of low-index terminations is because they proved to be the most stable surfaces in experimental investigations during chemical reactions compared to high-index surfaces.[53] Therefore, in this work, *(100)*, *(110)*, and *(111)* surfaces were chosen for the metals with fcc and bcc structure, and the *(0001)*, *(10$\bar{1}$0)* and *(11$\bar{2}$0)* surfaces for hcp metals.

The results were summarised on metals optimisation from the bulk-like slab in ***Table 3.2***. They contain information regarding the areas and atomic layers distances along the z-axis and slab magnetisations.

Table 3.2. *Properties of the clean surfaces of (111), (110), (100) fcc, bcc and (0001) for hcp. Δd_{12} and Δd_{23} are the lattice spacing between the first and second layer and between the second and third layer, respectively. M_s is the local magnetic moment per metal atom, and A is the surface area in $Å^2$*

	(111)				(110)				(100)			
	Δd_{12} (%)	Δd_{23} (%)	M_s (μ_B)	A ($Å^2$)	Δd_{12} (%)	Δd_{23} (%)	M_s (μ_B)	A ($Å^2$)	Δd_{12} (%)	Δd_{23} (%)	M_s (μ_B)	A ($Å^2$)
Ni	0.01	0.00	0.61 0.69*	47.58	−0.08	0.05	0.68 0.70*	77.69	−0.01	0.01	0.64 0.64*	54.94
Cu	0.02	0.00	0.00	49.93	−0.05	0.04	0.00	81.54	0.01	0.02	0.00	57.65
Rh	−0.01	−0.01	0.00	56.76	−0.11	0.05	0.01	92.68	−0.03	0.01	0.00	65.54
Pd	0.02	0.00	0.00	60.20	−0.06	0.05	0.00	98.31	0.02	0.00	0.00	69.52
Ag	0.02	0.00	0.00	68.29	−0.03	0.04	0.00	111.51	0.04	0.02	0.00	78.85
Ir	−0.01	0.00	0.00	57.58	−0.13	0.06	0.00	94.02	−0.04	0.01	0.00	66.48
Pt	0.02	−0.01	0.00	60.87	−0.12	0.08	0.00	99.40	0.00	0.00	0.00	70.29
Au	0.09	0.03	0.00	66.19	−0.03	0.12	0.00	108.08	0.08	0.05	0.00	76.43
Fe‡	1.37	11.88	2.65 2.48*	123.26	1.54	0.87	2.34 2.48*	50.32	0.84	4.80	2.64 2.70*	71.16
Mo‡	−0.13	−0.25	0.00	152.34	−0.04	0.01	0.00	62.19	−0.10	0.04	0.00	87.95
W‡	−0.11	−0.23	0.00	154.23	−0.02	0.01	0.00	62.96	−0.09	0.03	0.10	89.04
	(0001)				($10\bar{1}0$)				($11\bar{2}0$)			
Co	−0.03	0.00	1.61 1.66*	48.62	−5.37	−1.17	1.53* 1.85*	48.62	11.73	13.5	1.55 1.85*	69.60
Ru	−0.03	0.01	0.00	57.01	2.97	4.82	0.06	47.10	2.19	6.47	0.07	81.60

‡ These materials have a bcc structure. * Experimental [54-56]

3.2.3 Surface characterisation

Different descriptors, e.g. surface energy, work function, d-band centre, d-band width, d-band skewness, and d-band kurtosis, were selected to study the electronic/geometry properties of the clean surfaces and correlate with the H and O adsorption. The surface energy (γ), work function (ϕ) of the metal surfaces were calculated using *Eq. 2.16 and 2.19*. The d-band centre (ε_d) is defined as the energy d-state cutting through the middle of all the d-states, and it is obtained by halving the integral of the d-band, *section 2.6.2*. To get the d-band width (W_d), the band was normalised using the Gaussian curve fitting in Origin to find the best fit for the series of energy states. Based on the rectangular band model approximation, the difference between the lowest energy (W_1) and the highest energy states (W_2) was taken within the region $W_d = W_2 - W_1$, ***Figure 2.5***.[57]

Whereas the d-band skewness (S_d) and d-band kurtosis (K_d) are based on the measure of symmetry and heavy or light tails of the distribution of the d-band, *Eq. 2.18*.[58]

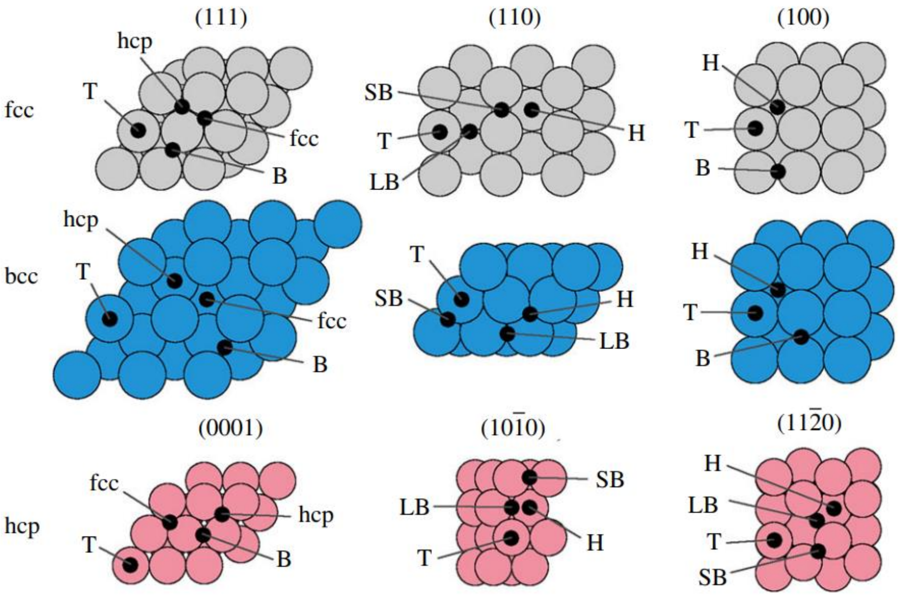

Figure 3.4. *Schematic representations of the different adsorption sites on the (111), (110), and (100) surfaces of Ag (fcc) and W (bcc) and (0001), $(10\bar{1}0)$, and $(11\bar{2}0)$ surfaces of Co (hcp); T: ontop; B: bridge; SB: short bridge; LB: long bridge; H: hollow; fcc: hollow position over atom of the second layer; hcp: hollow position over the hollow position in the second layer.*

To study the adsorption of hydrogen and oxygen atoms at these adsorption sites, the respective atom was placed at 1.5 Å over the top layer of the surface and fully relaxed. To calculate the gas phase energies of hydrogen and oxygen, the molecules were placed in a sufficiently large box to avoid spurious interactions with the periodic cells.[59] Inequivalent adsorption sites on the TMs were investigated for the adsorption of hydrogen and oxygen, ***Figure 3.4***. For the fcc metals, these are on top (T), bridge (B), hollow fcc (fcc), and hollow hcp (hcp) on the *(111)* surface; on top (T), short bridge (SB), long bridge (LB), and hollow (H) on the *(110)* surface and on top, bridge, and hollow on the *(100)* surface. The hollow fcc positions are located over a hollow position of the first subsurface layer, while the hollow hcp positions are over a metal atom of the second layer. For the bcc metals, the sites are on top (T), bridge (B), hollow fcc, and hollow hcp on the *(111)* surface, on top (T), short bridge (SB), long bridge (LB), and hollow on the *(110)* surface and on top (T), bridge (B), and hollow (H) on the *(100)* surface. On the *(0001)* surface of the hcp metals, the sites are on top (T), bridge (B), hollow fcc, and hollow hcp positions.[60] For *(10$\bar{1}$0)* and *(11$\bar{2}$0),* the sites are on top, short bridge (SB), long bridge (LB) and hollow.[61] The adsorption energies (E_{ads}) were calculated with *Eq. 3.1*, where the $E_{ads/slab}$ is the energy of the adsorbate on the slab, and n is the number of atoms. Whereas E_{slab} and $E_{adsorbate}$ are the energies of the clean surface and the free adsorbate (H_2 and O_2), respectively.

$$E_{ads} = E_{ads/slab} - \left(E_{slab} + \frac{n}{2}E_{adsorbate}\right) \qquad \textit{Eq. 3.1}$$

Normalisation (z-score) is a strategy to transform the data to have a mean of zero and a standard deviation of one, allowing to compare and evaluate the accuracy of the descriptors. The z-score is obtained with *Eq. 3.2*, where x_i is the original data, $\bar{x}$ is the sample mean, and s is the sample standard deviation. The violin plot can visualise this z-score, which compares different data sets using standardized tables.

$$z = \frac{x_i - \bar{x}}{s} \qquad \textit{Eq. 3.2}$$

3.3 Results and discussion

3.3.1 Descriptors

3.3.1.1 Surface energy

The surfaces energies were calculated for *(111)*, *(110)*, and *(100)* fcc surfaces (Ni, Cu, Rh, Pd, Ag, Ir, Pt and Au), bcc metals (Fe, Mo, and W) and *(0001)*, *(10$\bar{1}$0)*, and *(*11$\bar{2}$0*)* surfaces for the hcp metals (Co and Ru), ***Figure 3.5***. The values obtained agree with experimental values from previous works with a mean absolute percentage error of 6.5%.[62] The *(111)* surfaces are the most stable surfaces of the fcc metals due to the high atomic coordination of the surface atoms compared to the *(110)* and *(100)* surfaces. This is in line with previous computational results from Wang *et al*.[63] and Vitos *et al.*[64] obtained with non-spin polarised PBE calculations and LMTO calculations, respectively.

The results indicate higher stability of the *(100)* surface compared to the *(110)* surface for all group 10 and 11 and Ir, whereas the results of Vitos *et al.*[64] suggest that the *(110)* surfaces are more stable for Ni and Pd, and Ir. The calculated values have a trend with the decrease in the coordination number of the surface layer atoms from *(111)* (CN: 9) to *(100)* (CN: 8) and *(110)* (CN: 7). Interestingly, the *(110)* surface of Rh is predicted to be slightly more stable ($\gamma = 0.02$ J m^{-2}) than the *(100)* surface. In contrast, both Vitos *et al.* and Wang *et al.* reported the opposite ordering with a slight separation of 0.10 and 0.08 J m^{-2}. The *(110)* surfaces of group 6 (Mo and W) are calculated to be the most stable, followed by the *(111)* and *(100)* surfaces, in agreement with previous reports.[64]

For the bcc metals (Fe, Mo, and W), the coordination number of the top layer atoms is not a good indicator of the surface energy as the small difference in distance to the first and second neighbours does not correctly reflect the density of the packing at the surface. Moreover, the *(0001)* surfaces of the hcp metals Co and Ru are the most stable surfaces for these metals, which agrees with previous reports.[64, 65] The next most stable surfaces are, in both cases, the *($10\bar{1}0$)* followed by the *($11\bar{2}0$)* surface. This reflects the decrease in the coordination number of the surface atoms from 9 for the *(0001)* to 8 for the *($10\bar{1}0$)* and 7 for the *($11\bar{2}0$)* surface. The deviations from the mentioned literature values arise from the different computational methodologies, which emphasise the need for a systematic recalculation of the surface energies.

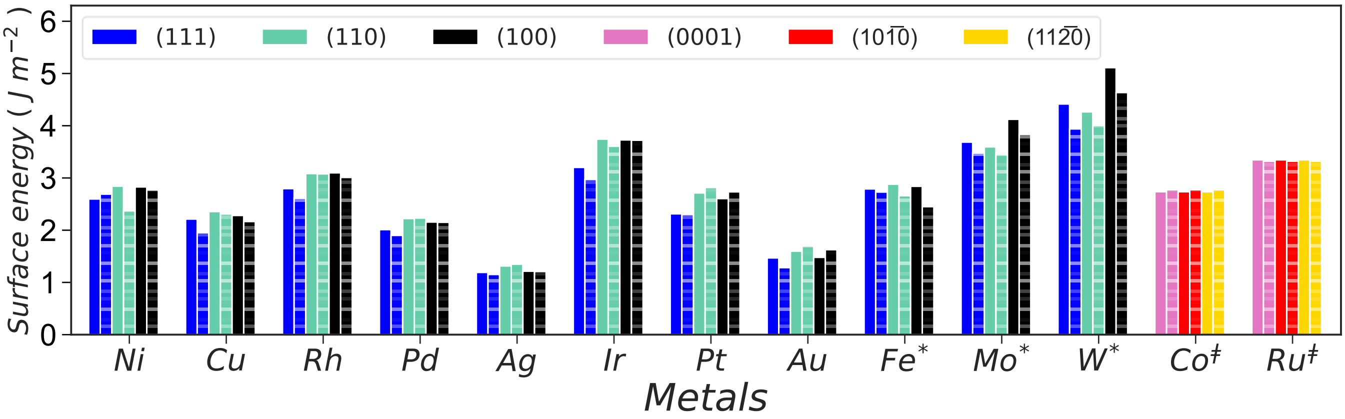

***Figure 3.5**. Surface energies of the investigated metal surfaces. The solid bars represent the calculated values, whereas the dashed bars represent previous computational results.[63, 64, 66-74]. * and ‡ correspond to bcc and hcp metal structures.*

High surface energies are related to surface instability and high chemical reactivity. In general, a decrease in surface energy is seen with an increasing group number within a period. The surfaces of Ag and Au show the lowest surface energies (1.47 J m^{-2} and 1.19 J m^{-2}, respectively), which reflects their general low reactivity. This means that the interaction between the absorbent (e.g. H or O atom) and the transition metal will be small, provoking high activation barrier and endothermic behaviour. In contrast, the more reactive early transition metals Mo and W have significantly higher values (3.69 J m^{-2} and 4.42 J m^{-2}, respectively); however, this high reactivity will produce a substantial interaction between the absorbent and the TM, and problems in the desorption of products. Therefore, both extremes will lead to a weak catalytic activity according to the Sabatier principle.[31-33]

3.3.1.2 Work function

The work function (ϕ) for all investigated metal surfaces is shown in ***Figure 3.6***. The calculated values of the surfaces present a mean absolute percentage error of 4.7% with respect to the experimental values.[63, 75] The work function depends on the exposed metal facet, which suggests that the more stable the surface is, the higher the work function becomes. This trend can be confirmed for the fcc metals, where the work function values are in the following order *(111) > (100) > (110)* for the respective metals.

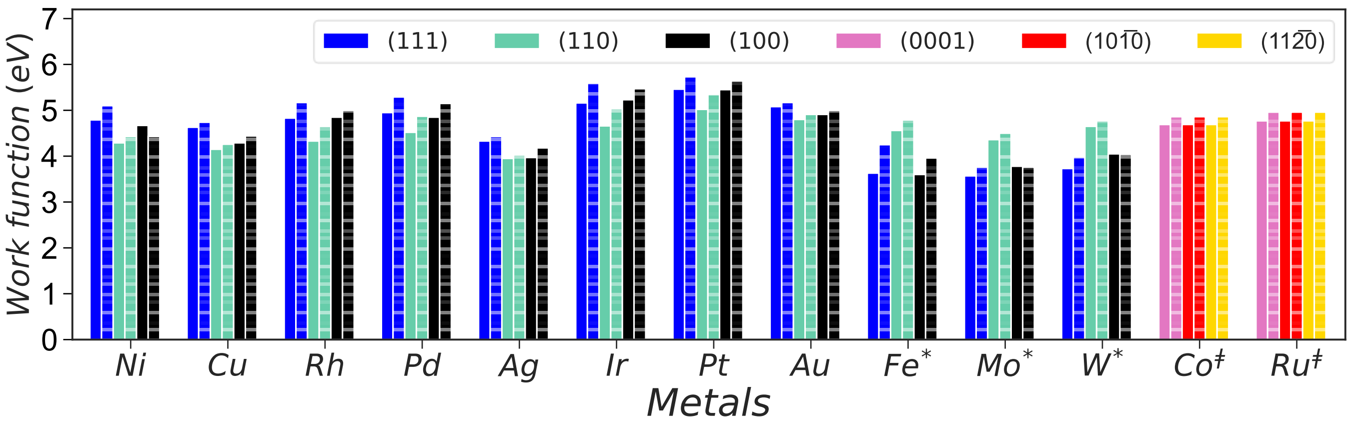

***Figure 3.6**. Work function (ϕ) of the investigated metal surfaces. The solid bars represent the calculated values, whereas the dashed bars represent previous experimental results.[63, 75]. * and ‡ correspond to bcc and hcp metal structures.*

The same sequence can be seen for the bcc metals, where the most stable facet (110) has the highest work function. High work function means that the electrons cannot escape easily from the surface because it has a low probability that the surface is exposed to the vacuum.[63] Therefore, the described trend between work function and surface energy is only valid for surfaces of the same metal, and no correlation can be found for the surfaces of different metals.[76] Pt and Ir show the overall highest work function, so it can be concluded that these metals accumulate electron density at the surface. In contrast, Mo, Fe and W present the lowest work function being poor in electron density at the surfaces.[77, 78]

3.3.1.3 d-band properties

The calculated values for d-band properties such as d-band centre (ε_d), width (W_d), skewness (S_d) and kurtosis (K_d) of all metal surfaces are summarised under study as a heatmap in ***Figure 3.7 (a − d)***, respectively.

Various computational studies have also calculated the herein reported d-band properties. The estimated d-band centre (ε_d) values present a mean absolute percentage error of 12.6% with respect to previous works. Whereas there is generally good agreement with the literature values, the moderate deviation of the percentage error found for the surfaces is due to a considerable difference between Fe, Pt and Pd (21.3% of mean absolute percentage error). The substantial percentage of error between previous computational studies and the d-band centre and d-band width calculated in this work is due to the different GGA pseudopotentials and calculation methods used to obtain the d-band centre in previous studies. Therefore, studies with the same GGA-functional should give low error values with d-band parameters calculated in this work.

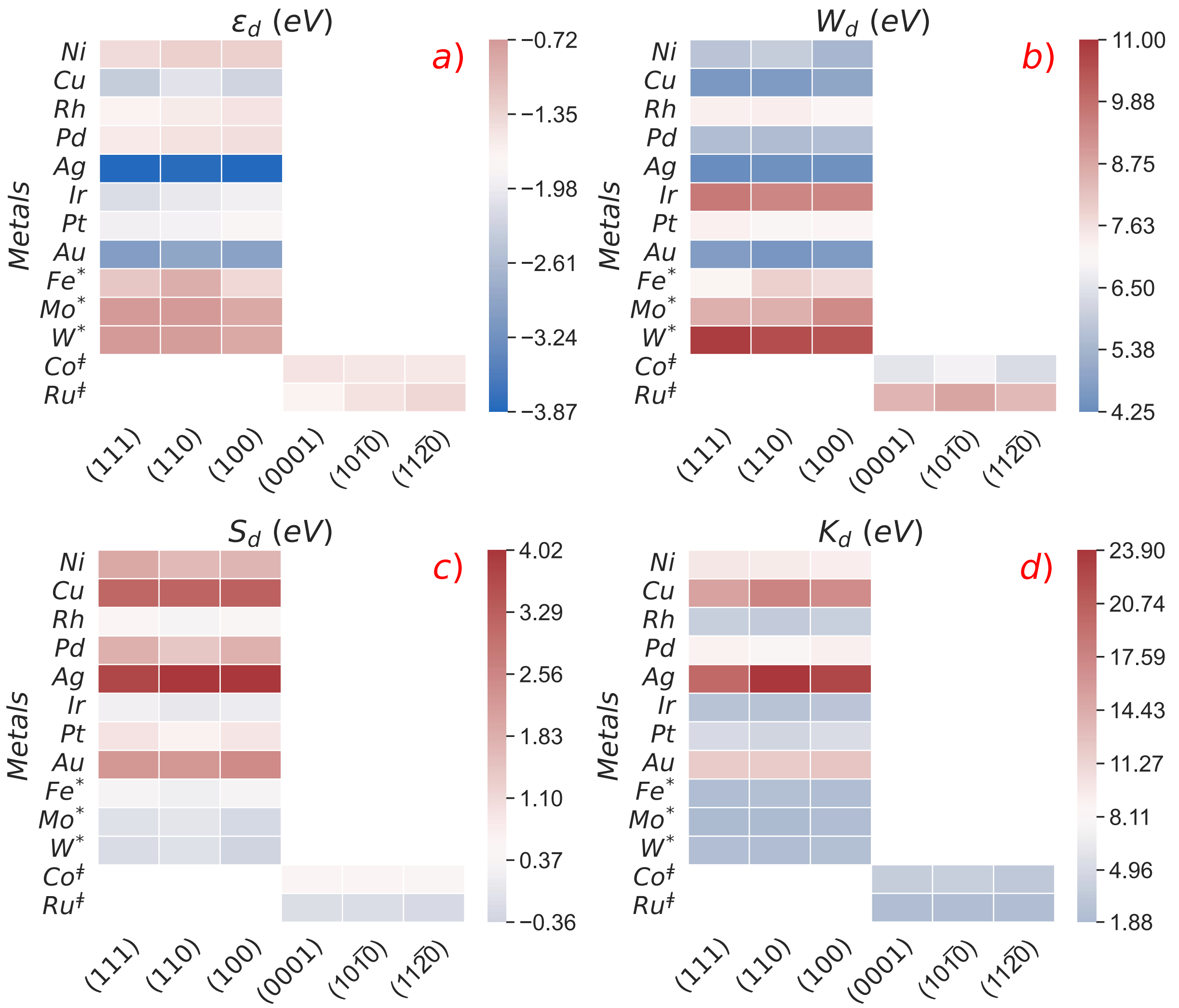

Figure 3.7. *Heatmap of (a) d-band centre (ε_d), (b) d-band width (W_d), (c) d-band skewness (S_d) and (d) d-band kurtosis (K_d) (in eV) on (111), (110), (100) fcc and bcc and (0001), (10$\bar{1}$0), and (11$\bar{2}$0) hcp surfaces. Smaller values are given by red colour in the plot. Values are within the range from –3.88 to –0.72 eV for ε_d, 4.25 to 11.0 eV for W_d, –0.36 to 4.02 eV for S_d and 1.80 to 23.90 eV for K_d. * and ‡ correspond to bcc and hcp metal structures.*

A detailed comparison to previous computational works for ε_d and W_d can be found in ***Table 3.3***. As expected, the values of the d-band centres of the most stable surfaces generally become more negative within a period with the increase of atomic number due to the increased filling of the d-band except for the group 10 (Ni, Pd, Pt). The d-band centre of the group 9 (Co, Rh, Ir) is closer to the Fermi energy than the neighbouring group 8 (Fe, Ru, Os) and group 10 metals. For example, the d-band centre of Fe (111) was calculated as −1.20 eV, while the ones of Co (0001) and Ni (111) are −1.50 eV and −1.42 eV, respectively.

Table 3.3. *d-band centre (ε_d) and d-band width (W_d) values for the (111), (110), (100) fcc and bcc surfaces and for the (0001), ($10\bar{1}0$), ($11\bar{2}0$) hcp surfaces.*

	(111)				*(110)*				*(100)*			
	ε_d		W_d		ε_d		W_d		ε_d		W_d	
	This work	*Other works* [79]	This work	*Other works* [79]	This work	*Other works* [79-81]	This work	*Other works* [79]	This work	*Other works* [79-81]	This work	*Other works* [79]
Ni	−1.42	−1.59	5.74	4.72	−1.30	−1.56	5.95	4.72	−1.30	−1.56	5.43	4.72
Cu	−2.37	−2.46	4.55	3.67	−2.07	−2.52	4.67	3.67	−2.26	−2.52	4.98	3.67
Rh	−1.69	−2.10	7.31	7.42	−1.57	−1.73	7.34	7.42	−1.51	−1.73	7.12	7.42
Pd	−1.56	−1.78	5.59	4.51	−1.48	−1.81	5.53	4.51	−1.45	−1.81	5.61	4.51
Ag	−3.85	−4.04	4.27	3.46	−3.82	−4.10	4.36	3.46	−3.87	−4.10	4.35	3.46
Ir	−2.15	−2.95	9.66	8.92	−2.01	−2.11	9.39	8.92	−1.94	−2.11	9.39	8.92
Pt	−1.92	−2.42	7.29	6.51	−1.89	−2.25	7.07	6.51	−1.77	−2.25	7.13	6.51
Au	−3.05	−3.36	4.69	5.08	−2.91	−3.33	4.50	5.08	−2.97	−3.33	4.65	5.08
Fe‡	−1.20	−0.90	7.16	6.18	−0.93	−0.84	7.94	6.18	−1.38	−0.90	7.71	6.18
Mo‡	−0.72	−0.99	8.55	9.26	−0.73	−0.90	8.56	9.26	−0.87	−0.99	9.31	9.26
W‡	−0.72	−0.77	10.89	11.81	−0.75	−0.77	10.55	11.81	−0.88	−0.77	10.37	11.81
	(0001)				*($10\bar{1}0$)*				*($11\bar{2}0$)*			
Co	−1.50	−1.50	6.54	6.09	−1.52	−1.48	6.85	6.09	−1.55	−1.48	6.33	6.09
Ru	−1.68	−1.95	8.49	8.29	−1.48	−1.45	8.78	8.29	−1.36	−1.45	8.36	8.29

‡ These materials have a bcc structure.

Such behaviour was previously described for Ru-Rh-Pd and Os-Ir-Pt.[79, 81] The reason for this could be the change in crystal structure from one metal to the next, which could influence the location of the d-band centre, as shown by the results. For the fcc metals (except for Ag), the *(111)* surfaces are the most negative d-band centres, which exhibit the highest coordination number. Still, there is no clear correlation between these properties. The d-band centre follows the ordering *(111)* < *(100)* < *(110)* for Cu and Au, and *(111)* < *(110)* < *(100)* for Rh, Ir, and Pt. For Ni, both the *(110)* and *(100)* surfaces have the same d-band centre values. Ag's lowest d-band centre can be found for the (100) surface, but the overall variation between the surfaces is only 0.05 eV. In the case of the bcc structures, Fe *(110)*, Mo and W, *(111)* and *(110)*, have the lowest d-band centre.

There is no relationship either with the most stable surface or the highest coordination number. Whereas Fe, Mo, and W *(100)* showed the highest d-band centre being *Mo (100)* and *W (100)* the least stable surfaces. For hcp structures, the *(0001)* surfaces are the most stable with the highest coordination number and have the lowest d-band centre in comparison with $(10\bar{1}0)$ and $(11\bar{2}0)$ surfaces of the same metals. There is no apparent connection to the coordination number of the surface atoms visible for fcc surfaces. A higher ε_d corresponds to a lower filling of the antibonding states, provoking a strong binding between the metal and adsorbates. This suggests that Au and Ag will be less reactive than Mo and W, ***Figure 3.7 (a)***. The W_d computational values calculated were compared with Vojvodic *et al*.[79], resulting in a mean absolute percentage error of 11.7%. This reflects that the method based on the rectangular band model approximation, in which the W_d is obtained as the difference between the lowest and highest energy states, does not give considerably different results to those obtained using the second moment of the electronic density of states in previous works.[57] W_d did not show a link with the ε_d values calculated; this is caused by an independent relationship between the filling of d-band with these two descriptors similar to ref [82].

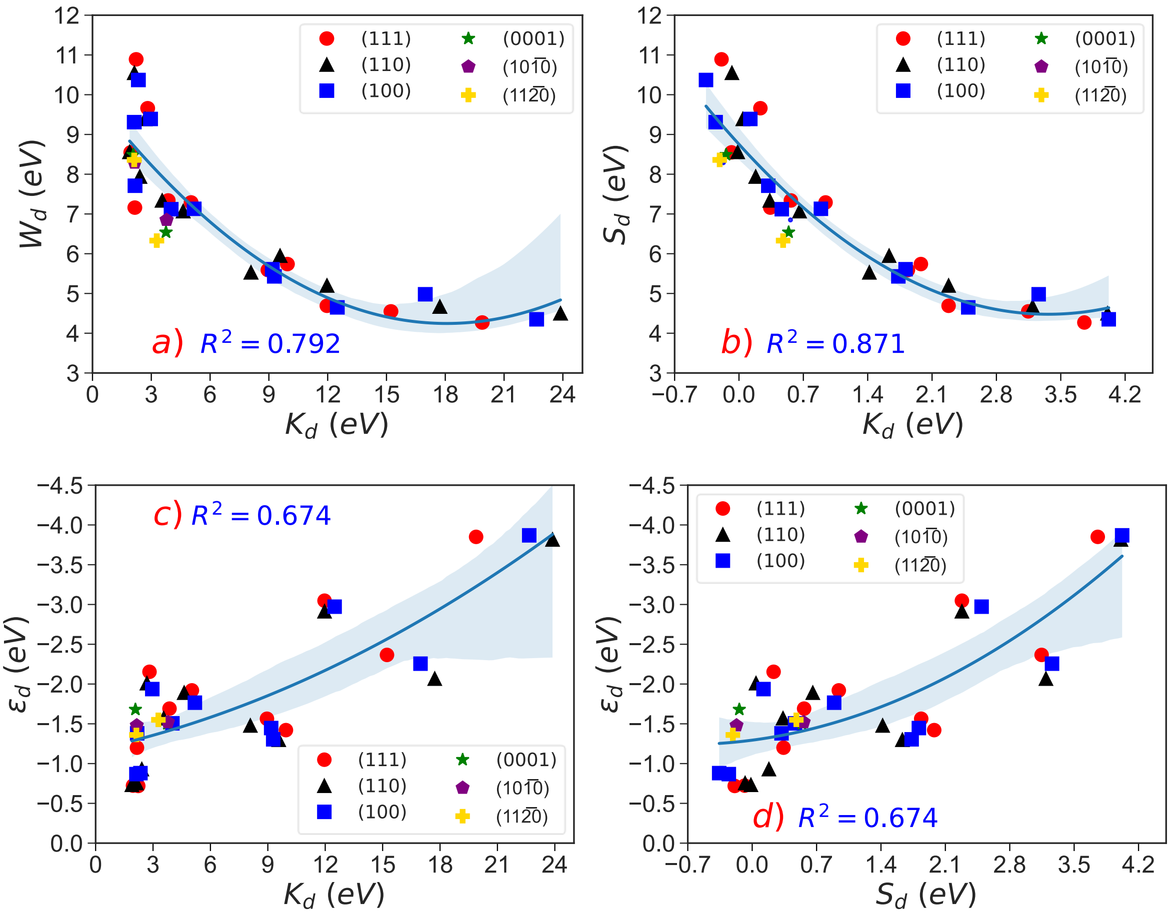

__Figure 3.8__. Polynomial regression with different descriptors (a) W_d and K_d, (b) W_d and S_d, (c) ε_d and K_d, and (d) ε_d and S_d.

However, W_d presents a good relationship with K_d and S_d (R^2: 0.792 and 0.871, respectively). The trend shows that the K_d and S_d values decrease with the increase of W_d, ***Figure 3.8 (a − b).*** K_d measures the spread of the d-band, in which lower values means that the d-band is broader and a more positive ε_d, while S_d measures the symmetry of the d-band. Positive S_d values indicate that the distribution of the states is more concentrated on the left side of the band, and its d-band centre is far away from the E_F. Hence, significant positive S_d values mean a narrow d-band and a more negative high d-band. However, there is a good correlation degree with the ε_d (R^2: 0.674 for K_d and S_d), the highest degree correlation with the d-band width means the lack of relationship with W_d and ε_d, ***Figure 3.8 (c − d)*****.**

3.3.2 Hydrogen and oxygen adsorption

3.3.2.1 Hydrogen adsorption

The hydrogen adsorption energies are summarised in a heatmap, ***Figure 3.9***, illustrating the dependence on the facet and the adsorption site. The calculated values of the hydrogen adsorption in different surfaces are in good agreement with several reports using different facets with five atomic layers. Although, there are differences in the affinity between dissimilar metals and hydrogen.[54] In some cases, the most favourable sites are different due to using other computational methodologies and hydrogen coverage.[83-85]

The most favourable adsorption sites on the *(111)* surfaces are on hollow-hcp sites for Ni, Cu, Pd and Ag surfaces. The adsorption on the *(110)* surface is preferably on bridge sites (SB or LB) for the fcc metals except for Pt, where the top site is slightly favoured. All fcc metals show the most substantial adsorption on hollow (Ni, Cu, and Ag) and bridge (Pt, Pd, Au, Rh, and Ir) sites on the *(100)* surfaces, being the Ag *(100)* surface with the least difference between both sites (> 0.05 eV) similar to ref [86]. The bcc metals Mo and W show only for the *(100)* surface a common most stable adsorption site (bridge) except for Fe, where the hollow is slightly favoured over the bridge sites; these results are similar to Ferrin *et al*.[54]

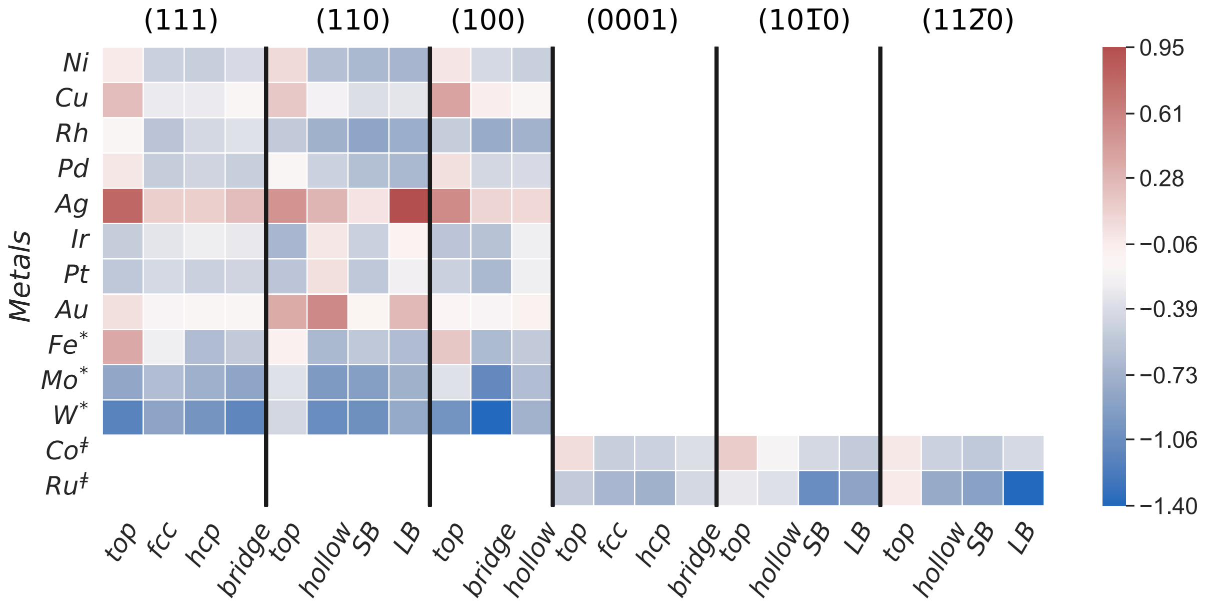

Figure 3.9. *Heatmap of hydrogen adsorption energies (E_{ads}); values within the range from –1.40 eV to 0.95 eV. * and ‡ correspond to bcc and hcp metal structures.*

On the *(111)* surface, the calculations suggest the hollow-hcp (Fe), bridge (Mo), and top (W) are the most stable sites, while the top position has the lowest adsorption energy on Fe *(110)*, Mo *(110)* and W *(110)*. The most stable adsorption on the *(0001)* surfaces of the hcp metals Co and Ru are on hollow hcp. The adsorption on the bridge sites (SB or LB) for *(10$\bar{1}$0)* and *(11$\bar{2}$0)* hcp surfaces is preferred, while the top position is least favourably. In general, the *(100)* surfaces of the fcc and bcc metals (except Au, Pt, Mo, and W) bind stronger to the hydrogen than the other facets.

However, there is no clear trend for ordering the adsorption energies on the *(110)* and *(111)* surfaces. The weakest adsorption of hydrogen can be found on the *(111)* surface for Pt, Mo, Ir and Fe; and on the *(110)* surface for Au and W. Interestingly, the results indicate that the *(100)* surface of Ni, Cu, Pd, Ag, and Rh has the weakest interaction with H. Moreover, the results show that the *(10$\bar{1}$0)* and *(11$\bar{2}$0)* surfaces of the hcp metals have a weak interaction with hydrogen compared to the *(0001)* surface. On all surfaces, except Ag *(111)*, the adsorption energies are negative, which means that the chemisorption of atomic hydrogen is energetically favoured.

3.3.2.2 Oxygen adsorption

The oxygen adsorption energies were summarised in a heatmap, ***Figure 3.10***, which illustrates the dependence on the facet and adsorption site. The most favourable adsorption site is on the hollow site of the *(111)* surfaces of all the fcc metals except on Pt and Ir, which is on the *(111)* top site. All the fcc showed the most exothermic adsorption site in the short-bridge sites (SB) of the *(110)* surface except for Cu and Ag, which the O prefers the hollow site with a slight difference compared to the short-bridge site.

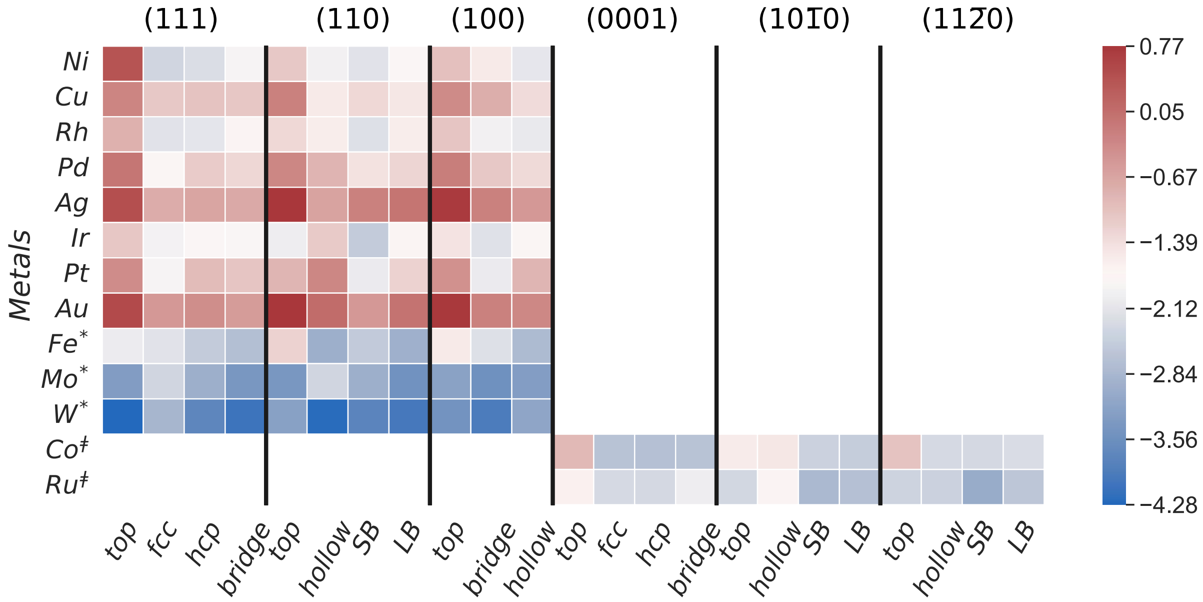

Figure 3.10. *Heatmap of oxygen adsorption energies (E_{ads}); only values within range from −4.28 eV to 0.77 eV. * and ‡ correspond to bcc and hcp metal structures.*

The bcc metals have a substantial affinity for oxygen showing strong interaction. Fe prefers on the hollow site, same as the H adsorption; Mo prefers on the *(100)* bridge site, while the strongest adsorption for W takes place on top of the *(111)* surface. Like hydrogen, the most stable oxygen adsorption site on the *(0001)* surface of the hcp metals is on the hollow hcp. For *$(10\bar{1}0)$* and *$(11\bar{2}0)$* surfaces, the oxygen prefers both Co and Ru bridge sites. In agreement with previous reports, bcc metals have a strong oxyphilic character [87-90], which may facilitate the direct cleavage of C─O bonds but will require elevated temperatures to release the oxygenated compounds. The different behaviour of these facets opens the possibility of nanoparticles engineering where the right ratio between desired facets may enhance the catalytic activity and selectivity towards specific products.

3.3.3 Scaling relationships

To maximise the predictive character of this study, the trends in hydro- and oxophilicity were analysed by exploring several relationships between the adsorption energies and surface descriptors described above. Combining the metals and surfaces explored, more than 39 values were normalised, leading to a violin plot enhancing the comparison and rationalisation.

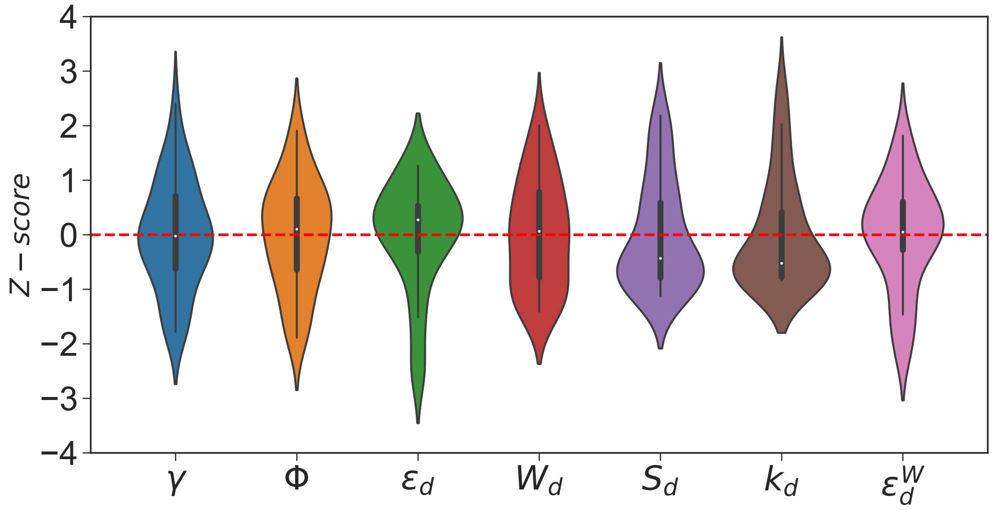

Figure 3.11. *Violin plots of the descriptors surface energy (γ), work function (ϕ), d-band centre (ε_d), d-band width (W_d), d-band skewness (S_d), d-band kurtosis (K_d) and d-band width modification (ε_d^W) of the TMs candidates. The white circle inside the violin plot represents the median value.*

The violin plot, ***Figure 3.11***, represents the statistical distribution of the normalised descriptors, which is convenient for comparing them. This plot will help visualise the entire data distribution and analyse linear relationships. The more normal distributed, e.g. symmetrical shape with a wide belly curved around zero, is the data, the more likely a linear trendline (and a higher degree of correlation) with respect to the hydrogen and oxygen adsorption. The white dot in the centre of the violin plot identifies the median of the results of each descriptor, which is an approximation of the mean and ensures that the extreme high or low values do not alter the mean estimation.[82] The data distribution shows a bell-shaped curve (Gaussian curve) within the z-score range of −4 to 4, where the mean dominates the position of the centre, i.e. the median and the mean are equal.[36] The data related to the work function (ϕ) and d-band centre (ε_d), second and third violin, falls right on the mean, although the position is not in the centre, which is determined by the peak of the curve. The d-band width violin presents an elongated distribution without a well-defined peak around the mean, indicating a lack of symmetry in the data and, therefore, a weak linear trend. Both the d-band skewness (S_d) and kurtosis (K_d) show the belly-shape curve in one extreme; this is related to a log-normal distribution, in which the data is more skewed in one part. This will give a better logarithmic trend with the H and O adsorption energies than a linear trend.

The first and the last violin plots, surface energy (γ) and d-band width modification ($\varepsilon_d^W = \varepsilon_d + W_d/2$) descriptors, have a defined curve peak falling right to the mean.[79] Moreover, their broad sections are remarkably concentrated around the median value, close to zero, showing that the data is symmetrically around the mean. This means that these descriptors are within one standard deviation of the mean. Therefore, there is a high probability to fit in a linear trend with the dataset with a high degree of correlation.[91]

Table 3.4. *Linear regression model results for dependent (H_{ads} and O_{ads}) and independent (descriptors) variables. b and m represent the Y-intercept and the slope of each relationship, respectively, and R^2 is the regression coefficient to describe the association of two variables.*

	H_{ads}			O_{ads}		
	b	**m**	**R^2**	**b**	**m**	**R^2**
γ	−0.333	0.368	0.885	−1.005	0.703	0.852
ϕ	0.122	−1.122	0.035	0.705	−5.315	0.123
ε_d	−0.339	−1.175	0.766	−1.038	−3.983	0.757
W_d	−0.146	0.453	0.763	−0.449	1.003	0.755
S_d	0.215	−0.814	0.764	0.629	−2.846	0.691
K_d	0.043	−0.879	0.687	0.125	−3.028	0.613
ε_d^W	−0.187	−0.250	0.911	−0.574	−1.149	0.902

The violin plot facilitates the identification of descriptors based on the information from ***Figure 3.11***. Scaling relationships between the descriptors and the adsorption energies of the most stable sites are represented with details of the slope, intercept, and R^2 are seen in ***Tables 3.4 − 3.5***. Inset in these figures, the corresponding (multiple) correlation coefficients (R^2) are used as a statistical test to measure the association between the two variables, i.e. descriptors and adsorption energy.[92] As close to one is R^2, the better is the fitting and stronger the relationship between variables. It was demonstrated that adding a second descriptor increases the species' chemical properties and affinity accuracy. Multiple linear regression models were used ($Y_{calc} = \beta_0 + \beta_1\phi$ (or $\beta_1\gamma$) $+ \beta_2\varepsilon_d^W$), combining different descriptors, e.g. γ, ϕ, ε_d, and W_d.

Table 3.5 shows the details for the fitting. These present a substantial improvement in accuracy correlating both adsorption energies with the combination of ε_d^W with different descriptors ($R^2 = 0.919$ and 0.907 for γ and $R^2 = 0.913$ and 0.946 for the ϕ). It proves that the electron transfer (represented by ϕ) between the adsorbent, TM surface and the band hybridisation (represented by ε_d^W) can occur simultaneously during the adsorption process.[93]

Table 3.5. *Multiple linear regression model results for dependent (H_{ads} and O_{ads}) and independent (descriptors) variables. β_0 is the Y-intercept; and β_1 and β_2 are the slope for the explanatory variables, and R^2 is the regression coefficient measure to describe the association of the variables.*

	H_{ads}				O_{ads}			
	β_0	**β_1**	**β_2**	**R^2**	**β_0**	**β_1**	**β_2**	**R^2**
ϕ, ε_d	−1.263	0.020	−0.337	0.767	−5.731	0.405	−0.995	0.796
ϕ, ε_d^W	−0.388	0.030	−0.186	0.913	−3.127	0.431	−0.555	0.946
γ, ε_d^W	−0.097	−0.079	−0.147	0.919	−0.746	−0.207	−0.468	0.907

Moreover, it was demonstrated that the electronic properties control the catalytic activity and the stability of the structure related to the measure of the number of bonds broken to form a new surface is a good factor to take into account in the material selection.

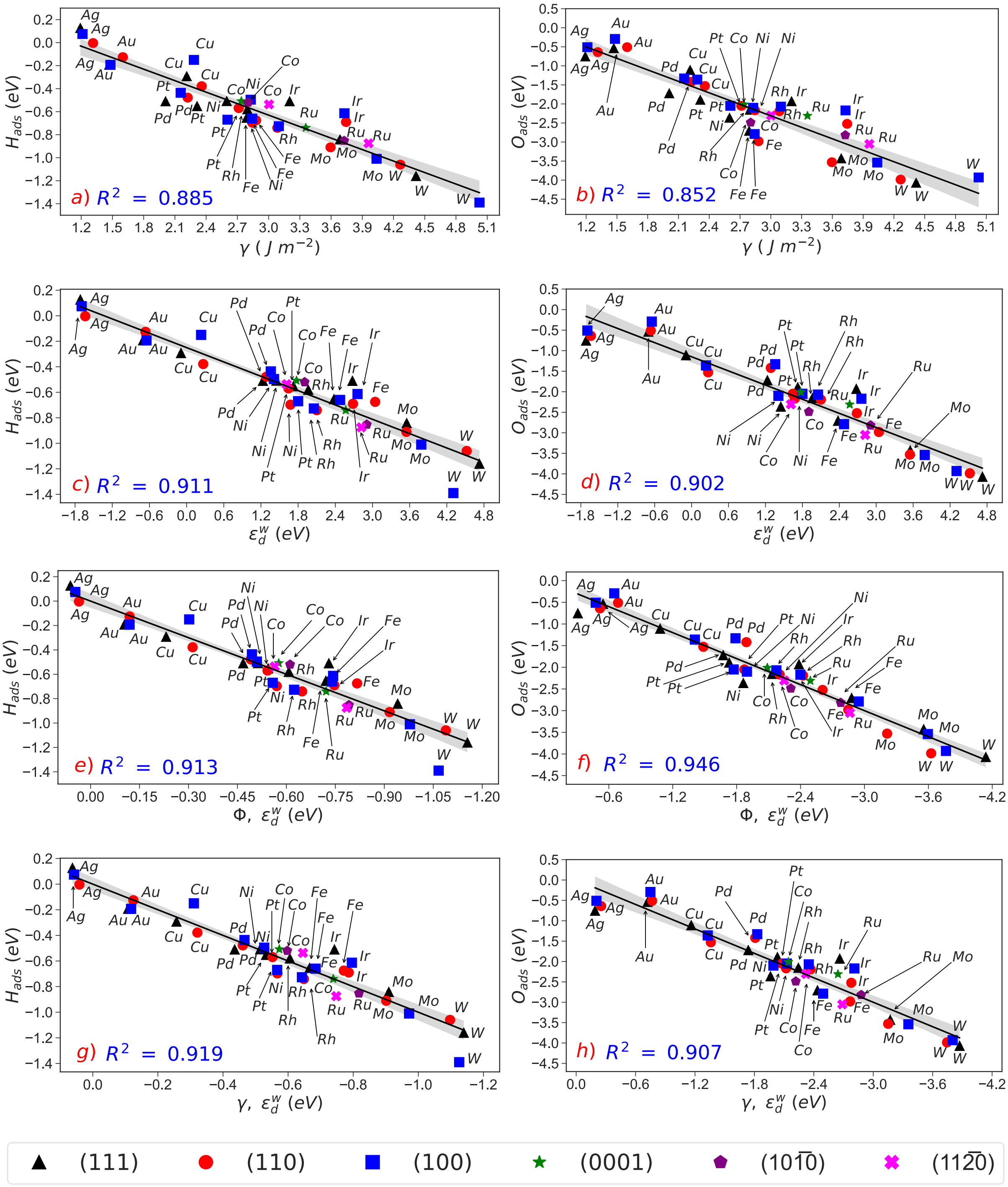

Figure 3.12. *Scaling relationships between (a-b) surface energy, γ (c-d) d-band width modification, ε_d^W, (e-f) work function, ϕ, with the d-band width modification, ε_d^W, and (g-h) surface energy, γ, with the d-band width modification, ε_d^W for H and O adsorption energies. Simple (a-d) and multiple (e-h) linear regression coefficients (R^2) are inset.*

The charge of H and O on such metal surfaces is quite different, and the small magnitude of the fitting parameter β_1 for H adsorption compared to the O adsorption reflects the low influence of the electron transfer for the H adsorption. The results herein discussed metals hydrogen and oxygen affinities and based on Sabatier's principle [31-33], the selection of monometallic HDO was catalysts was rationalised. The scaling relationships with ε_d^W, $\varepsilon_d^W + \gamma$ and $\varepsilon_d^W + \phi$ indicates that Ag and Au have weak affinities for H and O, contrarily to Mo, W, and Ru, which is too strong, ***Figure 3.12***. Cu, Pd and Pt are considered intermediate weak adsorption energies, while Fe, Rh and Co have intermediate strong adsorption energies. The three models point to Ni as metal catalysts with intermediate affinities for hydrogen and oxygen (neither too strong nor too weak). This outcome is a good agreement with several studies which use Ni as part of metal catalysts such as monometallic, bimetallic supported in hydrogenation and deoxygenation process of biomass derivates with good results.[94-96]

3.4 Chapter conclusion

In this chapter, the creation of scaling relationships using H and O's adsorption energies on the surfaces was analysed using GGA-RPBE. The descriptors were evaluated with the violin plot normalising the data. The surface energy (γ) and the d-band width modification ε_d^W showed a normal distribution, making them more likely to fit in a linear regression. This hypothesis was confirmed using these two descriptors in the scaling relationship giving a high R^2 correlation (greater than 0.85) in both H and O species, providing high accuracy in selecting metal surfaces. This concludes that the ε_d descriptor is not a universal parameter to describe the interactions with the d-band, and modifications need to be made to improve the accuracy in the selection of materials. In the three models studied ($\gamma + \varepsilon_d^W$ and $\phi + \varepsilon_d^W$), Ni is the metal with intermediate affinities for H and O. Therefore, it has good properties for the hydrogenation of oxygenated reactions along the HDO process.

This result is in good agreement with multiple investigations using this metal as monometallic and as a part of bimetallic catalysts supported on different materials. Moreover, the best results were obtained by combining the descriptors of work function and d-band properties. Ultimately, these results help build a robust screening methodology for catalytic materials and shed light on the chemical properties that influence the adsorption and catalytic process.

3.5 References

1. A. J. Hensley, Y. Wang and J.-S. McEwen, *ACS Catalysis*, 2015, **5**, 523-536.
2. A. J. Hensley, Y. Wang and J.-S. McEwen, *Surface Science*, 2016, **648**, 227-235.
3. Y.-C. Lin, C.-L. Li, H.-P. Wan, H.-T. Lee and C.-F. Liu, *Energy & Fuels*, 2011, **25**, 890-896.
4. T.-R. Viljava, R. Komulainen and A. Krause, *Catalysis Today*, 2000, **60**, 83-92.
5. S. Sitthisa and D. E. Resasco, *Catalysis letters*, 2011, **141**, 784-791.
6. S. Jin, Z. Xiao, C. Li, X. Chen, L. Wang, J. Xing, W. Li and C. Liang, *Catalysis Today*, 2014, **234**, 125-132.
7. J. Chang, T. Danuthai, S. Dewiyanti, C. Wang and A. Borgna, *ChemCatChem*, 2013, **5**, 3041-3049.
8. A. Dongil, B. Bachiller-Baeza, I. Rodriguez-Ramos, J. Fierro and N. Escalona, *RSC advances*, 2016, **6**, 26658-26667.
9. M. K. Huuska, *Polyhedron*, 1986, **5**, 233-236.
10. Y. Romero, F. Richard and S. Brunet, *Applied Catalysis B: Environmental*, 2010, **98**, 213-223.
11. T. Prasomsri, M. Shetty, K. Murugappan and Y. Román-Leshkov, *Energy & Environmental Science*, 2014, **7**, 2660-2669.
12. D. C. Elliott and T. R. Hart, *Energy & Fuels*, 2009, **23**, 631-637.
13. S. Boonyasuwat, T. Omotoso, D. E. Resasco and S. P. Crossley, *Catalysis letters*, 2013, **143**, 783-791.
14. A. Gutierrez, R. K. Kaila, M. L. Honkela, R. Slioor and A. O. I. Krause, *Catalysis Today*, 2009, **147**, 239-246.
15. D. Prochazkova, P. Zámostný, M. Bejblova, L. Červený and J. Čejka, *Applied Catalysis A: General*, 2007, **332**, 56-64.
16. C. Zhao, J. He, A. A. Lemonidou, X. Li and J. A. Lercher, *Journal of Catalysis*, 2011, **280**, 8-16.
17. D. Gao, C. Schweitzer, H. T. Hwang and A. Varma, *Industrial & Engineering Chemistry Research*, 2014, **53**, 18658-18667.
18. Y. Hong, H. Zhang, J. Sun, K. M. Ayman, A. J. R. Hensley, M. Gu, M. H. Engelhard, J.-S. McEwen and Y. Wang, *ACS Catalysis*, 2014, **4**, 3335-3345.
19. H. Fang, A. Roldan, C. Tian, Y. Zheng, X. Duan, K. Chen, L. Ye, S. Leoni and Y. Yuan, *Journal of Catalysis*, 2019, **369**, 283-295.
20. Z. He and X. Wang, presented in part at Abstracts of papers of the American Chemical Society, 2012
21. B. Peng, C. Zhao, I. Mejía-Centeno, G. A. Fuentes, A. Jentys and J. A. Lercher, *Catalysis Today*, 2012, **183**, 3-9.
22. J. Lu, S. Behtash, O. Mamun and A. Heyden, *ACS Catalysis*, 2015, **5**, 2423-2435.
23. D. Shi, L. Arroyo-Ramírez and J. M. Vohs, *Journal of catalysis*, 2016, **340**, 219-226.
24. A. Gutierrez, R. Kaila, M. Honkela, R. Slioor and A. Krause, *Catalysis Today*, 2009, **147**, 239-246.

25. K. Lee, G. H. Gu, C. A. Mullen, A. A. Boateng and D. G. Vlachos, *ChemSusChem*, 2015, **8**, 315-322.
26. J. Lu, S. Behtash, O. Mamun and A. Heyden, *ACS Catalysis*, 2015, **5**, 2423-2435.
27. C. Dupont, R. Lemeur, A. Daudin and P. Raybaud, *Journal of catalysis*, 2011, **279**, 276-286.
28. J.-S. Moon, E.-G. Kim and Y.-K. Lee, *Journal of catalysis*, 2014, **311**, 144-152.
29. A. M. Verma and N. Kishore, *Molecular Simulation*, 2017, **43**, 141-153.
30. J. Zhang, B. Fidalgo, D. Shen, X. Zhang and S. Gu, *Molecular Catalysis*, 2018, **454**, 30-37.
31. A. J. Medford, A. Vojvodic, J. S. Hummelshøj, J. Voss, F. Abild-Pedersen, F. Studt, T. Bligaard, A. Nilsson and J. K. Nørskov, *Journal of Catalysis*, 2015, **328**, 36-42.
32. M. Che, *Catalysis today*, 2013, **218**, 162-171.
33. J. K. Nørskov, et al., *Journal of catalysis*, 2002, **209**, 275-278.
34. F. Abild-Pedersen, J. Greeley, F. Studt, J. Rossmeisl, T. Munter, P. G. Moses, E. Skulason, T. Bligaard and J. K. Nørskov, *Physical review letters*, 2007, **99**, 016105.
35. F. Calle-Vallejo, M. T. Koper and A. S. Bandarenka, *Chemical Society Reviews*, 2013, **42**, 5210-5230.
36. L. M. Ghiringhelli, J. Vybiral, S. V. Levchenko, C. Draxl and M. Scheffler, *Physical review letters*, 2015, **114**, 105503.
37. Z. Li, X. Ma and H. Xin, *Catalysis Today*, 2017, **280**, 232-238.
38. D. Loffreda, F. Delbecq, F. Vigné and P. Sautet, *Journal of the American Chemical Society*, 2006, **128**, 1316-1323.
39. R. A. Van Santen, M. Neurock and S. G. Shetty, *Chemical reviews*, 2009, **110**, 2005-2048.
40. E. Ziambaras and E. Schröder, *Physical Review B*, 2003, **68**, 064112.
41. K. Tonigold and A. Groß, *Journal of computational chemistry*, 2012, **33**, 695-701.
42. A. J. Hensley, K. Ghale, C. Rieg, T. Dang, E. Anderst, F. Studt, C. T. Campbell, J.-S. McEwen and Y. Xu, *The Journal of Physical Chemistry C*, 2017, **121**, 4937-4945.
43. G. Kresse and J. Furthmüller, *Computational materials science*, 1996, **6**, 15-50.
44. J. P. Perdew, K. Burke and M. Ernzerhof, *Physical review letters*, 1996, **77**, 3865.
45. B. Hammer, L. B. Hansen and J. K. Nørskov, *Physical Review B*, 1999, **59**, 7413.
46. P. E. Blöchl, *Physical review B*, 1994, **50**, 17953.
47. S. Grimme, J. Antony, S. Ehrlich and H. Krieg, *The Journal of chemical physics*, 2010, **132**, 154104.
48. H. J. Monkhorst and J. D. Pack, *Physical review B*, 1976, **13**, 5188.
49. M. G. Quesne, A. Roldan, N. H. de Leeuw and C. R. A. Catlow, *Physical Chemistry Chemical Physics*, 2018, **20**, 6905-6916.
50. P. Janthon, S. M. Kozlov, F. Vines, J. Limtrakul and F. Illas, *Journal of chemical theory and computation*, 2013, **9**, 1631-1640.

51. A. H. Larsen, et al., *Journal of Physics: Condensed Matter*, 2017, **29**, 273002.
52. L. Bengtsson, *Physical Review B*, 1999, **59**, 12301.
53. W. Sun and G. Ceder, *Surface Science*, 2018, **669**, 50-56.
54. P. Ferrin, S. Kandoi, A. U. Nilekar and M. Mavrikakis, *Surface Science*, 2012, **606**, 679-689.
55. H. Krakauer, A. J. Freeman and E. Wimmer, *Physical Review B*, 1983, **28**, 610-623.
56. S. Blügel and G. Bihlmayer, in *Handbook of Magnetism and Advanced Magnetic Materials*, 2005.
57. S. Miller, C. Dsilva and J. R. Kitchin, in *Catalysis: Volume 24*, The Royal Society of Chemistry, 2012, vol. 24, pp. 83-115.
58. H. Xin, A. Vojvodic, J. Voss, J. K. Nørskov and F. Abild-Pedersen, *Physical Review B*, 2014, **89**, 115114.
59. L. Zhang, W. Goddard and S. Jiang, *The Journal of chemical physics*, 2002, **117(5)**, 7342-7349.
60. X. F. Shang, Y. W. Wang, X. M. Tao and M. Q. Tan, *Advanced Materials Research*, 2012, **571**, 48-55.
61. L. Vega, J. Ruvireta, F. Viñes and F. Illas, *Journal of Chemical Theory and Computation*, 2018, **14**, 395-403.
62. M. J. Spencer, A. Hung, I. K. Snook and I. Yarovsky, *Surface Science*, 2002, **513**, 389-398.
63. J. Wang and S.-Q. Wang, *Surface Science*, 2014, **630**, 216-224.
64. L. Vitos, A. Ruban, H. L. Skriver and J. Kollar, *Surface science*, 1998, **411**, 186-202.
65. J.-M. Zhang, D.-D. Wang and K.-W. Xu, *Applied Surface Science*, 2006, **253**, 2018-2024.
66. N. E. Singh-Miller and N. Marzari, *Physical Review B*, 2009, **80**, 235407.
67. F. R. De Boer, W. Mattens, R. Boom, A. Miedema and A. Niessen, *Cohesion in metals*, Amsterdam, NL, 1988.
68. F. Mittendorfer, A. Eichler and J. Hafner, *Surface Science*, 1999, **423**, 1-11.
69. K. Mills and Y. Su, *International Materials Reviews*, 2006, **51**, 329-351.
70. E. Aghemenloh, J. O. A. Idiodi and S. O. Azi, *Computational Materials Science*, 2009, **46**, 524-530.
71. M. Methfessel, D. Hennig and M. Scheffler, *Physical Review B*, 1992, **46**, 4816.
72. V. Zólyomi, L. Vitos, S. Kwon and J. Kollár, *Journal of Physics: Condensed Matter*, 2009, **21**, 095007.
73. H. L. Skriver and N. Rosengaard, *Physical Review B*, 1992, **46**, 7157.
74. W. Tyson and W. Miller, *Surface Science*, 1977, **62**, 267-276.
75. R. Tran, Z. Xu, B. Radhakrishnan, D. Winston, W. Sun, K. A. Persson and S. P. Ong, *Scientific data*, 2016, **3**, 160080.
76. A. Y. Lozovoi and A. Alavi, *Physical Review B*, 2003, **68**, 245416.
77. H. Wolfschmidt, O. Paschos and U. Stimming, in *Fuel cell science: theory, fundamentals, and biocatalysis*, John Wiley & Sons, Inc. Hoboken, NJ, USA, 2010, pp. 1-70.
78. S. Srinivasan, in *Fuel Cells*, Springer, 2006, pp. 27-92.

79. A. Vojvodic, J. Nørskov and F. Abild-Pedersen, *Topics in catalysis*, 2014, **57**, 25-32.
80. J. Greeley, *Annual review of chemical and biomolecular engineering*, 2016, **7**, 605-635.
81. I. Takigawa, K.-i. Shimizu, K. Tsuda and S. Takakusagi, *RSC advances*, 2016, **6**, 52587-52595.
82. P. Pankajakshan, S. Sanyal, O. E. de Noord, I. Bhattacharya, A. Bhattacharyya and U. Waghmare, *Chemistry of Materials*, 2017, **29**, 4190-4201.
83. D. F. Johnson and E. A. Carter, *Journal of Materials Research*, 2010, **25**, 315-327.
84. C. Liu, L. Zhu, X. Wen, Y. Yang, Y.-W. Li and H. Jiao, *Surface Science*, 2020, **692**, 121514.
85. P. van Helden, J.-A. van den Berg and C. J. Weststrate, *ACS Catalysis*, 2012, **2**, 1097-1107.
86. A. Eichler, J. Hafner and G. Kresse, *Surface Review and Letters*, 1997, **4**, 1297-1303.
87. K. Yao, Z. Yuan, S. Jin, Q. Chi, B. Liu, R. Huang and Z. Zhang, *Green Chemistry*, 2020, **22**, 39-43.
88. A. Lalsare, A. Sivri, R. Egan, R. J. Vukmanovich, C. E. Dumitrescu and J. Hu, *Chemical Engineering Journal*, 2020, **385**, 123783.
89. R. N. Olcese, M. Bettahar, D. Petitjean, B. Malaman, F. Giovanella and A. Dufour, *Applied Catalysis B: Environmental*, 2012, **115-116**, 63-73.
90. S. Echeandia, P. Arias, V. Barrio, B. Pawelec and J. Fierro, *Applied Catalysis B: Environmental*, 2010, **101**, 1-12.
91. J. L. Hintze and R. D. Nelson, *The American Statistician*, 1998, **52**, 181-184.
92. Y. Nanba and M. Koyama, *The Journal of Physical Chemistry C*, 2019, **123**, 28114-28122.
93. X. Shen, Y. Pan, B. Liu, J. Yang, J. Zeng and Z. Peng, *Physical Chemistry Chemical Physics*, 2017, **19**, 12628-12632.
94. Y. Nakagawa and K. Tomishige, *Catalysis Communications*, 2010, **12**, 154-156.
95. M. Stanković, J. Krstić, M. Gabrovska, V. Radonjić, D. Nikolova, D. Lončarević and D. Jovanović, *New Advances in Hydrogenation Processes: Fundamentals and Applications*, 2017, 131.
96. K. A. Resende, A. H. Braga, F. B. Noronha and C. E. Hori, *Applied Catalysis B: Environmental*, 2019, **245**, 100-113.

4

The effect of pristine and hydroxylated oxides surfaces on the Guaiacol HDO process

4.1 Introduction

Different catalytic materials have been studied to improve HDO efficiency. Supported transition metals have received substantial attention due to their oxyphilic characteristics.[1, 2] Normally, nanoparticles are synthesized with a support. The support advantages include improving the dispersion of nanoparticles, enhanced surface areas, and increased stability against deactivation processes.[3] Oxides are the most employed materials to use as a support due to their easy preparation, stability, and accessible cost. Among common catalysts' supports, γ-Al_2O_3 is one of the most widely used in the HDO due to its excellent performance in activating phenolic compounds.[4-11] However, γ-Al_2O_3 transforms into boehmite under hydrothermal conditions, leading to coke deposition.[12] The same for most stable alumina forms such as α-alumina, which demonstrates its low reduction to coke deposition.[13]

Alternatively, oxide supports such as MgO [14-17], CeO_2 [18-22], SiO_2 [23-27], and TiO_2 anatase [28-30] have been studied based on their acid-base properties and reducibility. These oxide surfaces are hydroxylated in contact with water molecules under room temperature and pressure. The dissociation of water molecules forms the hydroxyl groups on metal oxides, releasing protons (H^+) and hydroxide ions (OH^-). The transference of electrons creates two types of hydroxyl groups. The hydroxide ion (OH^-) is bonded to the exposed metal ions (cation) from the oxide surfaces forming a terminal hydroxyl, OH (I). Meanwhile, the H^+ sticks to the surface oxygen (anion), creating a bridging hydroxyl, OH (II).[31, 32]

Chapter 4 analyses the structure and electronic properties of clean and hydroxylated oxides' surfaces, such as γ-Al_2O_3, CeO_2, MgO, β-SiO_2 and TiO_2 anatase and their interaction with model compounds. The compounds are guaiacol, anisole, catechol, phenol, and benzene, which are derived from the lignin pyrolysis process.

4.2 Computational details

Spin-polarised density functional theory (DFT) at 0 K using the Vienna Ab initio Simulation Package (VASP) was carried out to investigate the interaction of phenolic compounds with clean and hydroxylated oxides surfaces.[33] The exchange and correlation contributions were calculated using the generalised gradient approximation (GGA) with the revised functional of Perdew-Burke-Ernzerhof (RPBE).[1] The core electrons were described using the Projected Augmented Wave (PAW) formalism.[34] Dispersion interactions were added using the zero damping Grimme's dispersion correction DFT-D3.[35]

Dipole correction was used perpendicular to the surfaces of the oxides upon molecular adsorptions. The conjugate gradient convergence criteria threshold was 0.03 eV $Å^{-1}$ for the ionic and 10^{-5} eV for the electronic. DFT+U method was applied for the CeO_2 oxide surface to describe the localisation of *4f* orbitals using the Liechtenstein method.[36] Parameters for DFT+U method were set to 4 eV (U_{eff}), which replicates the reduction of CeO_2 with J =1 eV and U = 5 eV.[2]

4.2.1 Bulk calculation details

Preliminary test calculations were performed for five oxide supports: γ-Al_2O_3, CeO_2, MgO, β-SiO_2 and anatase TiO_2 (a-TiO_2), bulk structures can be seen in ***Figure 1.6*** to obtain the best computational setting, such as k-points and cut-off energy.[37, 38] The Digne model was chosen for simulating the γ-Al_2O_3 structure.[39] CeO_2 bulk has a cubic fluorite structure (*Fm3m* crystal structure), in which four Ce atoms are located in a cubic lattice placed in the centre (Ce_{7c}), and the O atoms occupy the tetrahedral lattice sites.[40]

MgO belongs to the group *Fm3m* and contains one formula unit per primitive cell based on an Mg^{2+} with a neighbour O^{2-} atom.[41, 42] For SiO_2, the β-cristobalite structure was selected using a simple cubic formed with SiO_4 tetrahedral units, i.e. a Si_{4c} at the centre and O_{2c} atoms at the corner ordered in the *Fd3m* cubic structure.[43, 44] Bulk TiO_2 unit cell for the anatase phase (a-TiO_2) contains four TiO_2 units (12 atoms) where Ti atoms are in octahedral coordination, provoking inequivalent distances between Ti−O bonds in the structure (long and short bonds).[45] An optimised number of k-points using the method of Monkhorst-Pack was set to 13 x 13 x 13 k-point grid, and a kinetic energy cut-off of 550 eV was defined for the valence electron plane-wave basis set, ***Figure 4.1 (a − b)***.

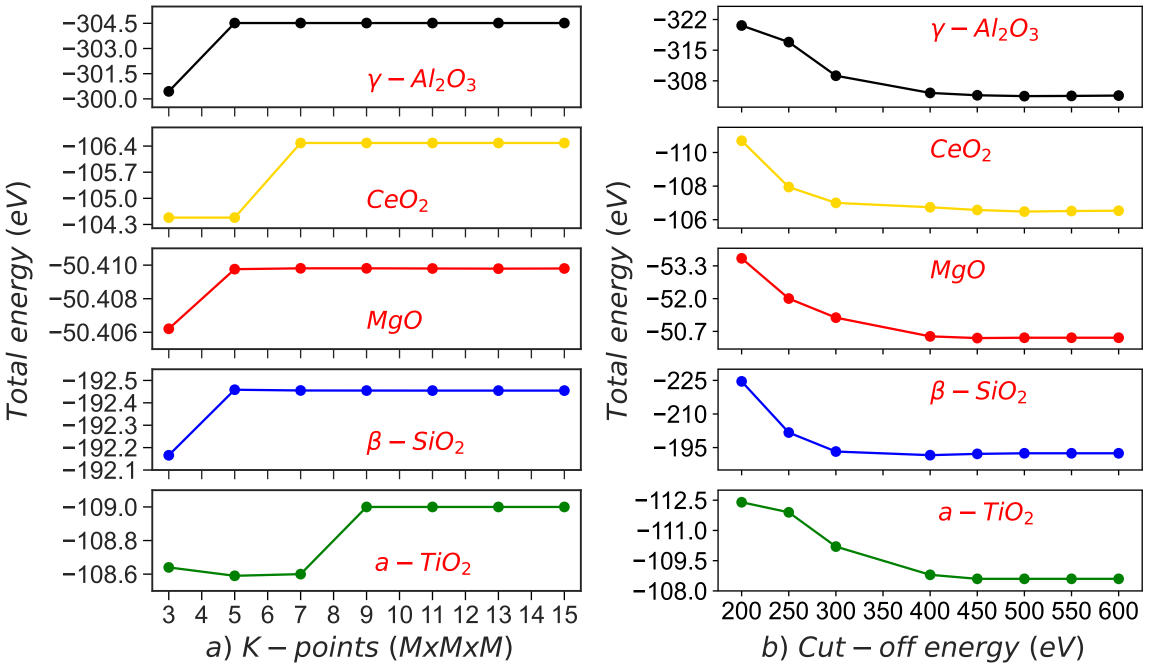

Figure 4.1. *The convergence of total energy (a) K-points and b) cut-off energy of the bulk structures*

Based on the previous tests, calculations were performed to get the optimised lattice parameters for the materials. ***Table 4.1*** shows the optimised lattice parameter (a_o, Å) for the oxide bulk structures. The structure properties, such as geometry and distances between atoms (metal-oxygen, oxygen-oxygen), were compared with other available theoretical works performed using GGA with PBE functional with a small error margin.

***Table 4.1**. a) Lattice parameters and b) M−O and O−O distances (in Å) properties for the bulk structures of oxide surfaces obtained in the present work with available theoretical values.*

		a_o (Å)	d_{M-O} (Å)$^+$	d_{o-o} (Å)
γ-Al_2O_3	This work	a = 5.57, c = 8.069	$Al_{(o)}$ = 1.91, $Al_{(t)}$ = 1.76	2.62
	Other theor. works	a = 5.66 ^{46}, c= 8.08 ^{47}	$Al_{(o)}$ = 1.94 ^{48}, $Al_{(t)}$ = 1.78 ^{48}	2.70
	Error (%)	a =1.63%, c = 0.14%	$Al_{(o)}$ = 1.55%, $Al_{(t)}$ = 1.12%	2.96%
CeO_2	This work	5.47	2.37	2.73
	Other theor. works	5.45 ^{49}	2.36 ^{50}	2.70 ^{44}
	Error (%)	0.37%	0.34%	1.11%
MgO	This work	4.22	2.10	2.98
	Other theor. works	4.21 ^{51}	2.13 ^{52}	2.70 ^{44}
	Error (%)	0.17%	1.22%	9.39%
β-SiO_2	This work	7.47	1.62	2.64
	Other theor. works	7.45 ^{44}	1.61 ^{44}	2.70 ^{44}
	Error (%)	0.23%	0.25%	2.19%
a-TiO_2	This work	a = b = 3.83, c = 9.62	$O_{(x)}$ =1.96, $O_{(z)}$ = 2.00	d_{M-M} = 3.83
	Other theor. works	a = b = 3.79 ^{53}, c = 9.74	$O_{(x)}$ = 1.94 ^{53}, $O_{(z)}$ = 2.00	d_{M-M} = 3.82 ^{53}
	Error (%)	a = b = 1.08%, c = 1.20 %	$O_{(x)}$ = 0.75%, $O_{(z)}$ = 0.25%	d_{M-M} = 0.18 %

+ $O_{(x)}$ and $O_{(z)}$ represent the position of the O atom concerning Ti, whereas Al(o) and Al(t) are octahedral and tetrahedral Al atoms.

* d_{M-O}, d_{O-O}, d_{M-M} = Metal (M) and oxygen (O) distances, oxygen - oxygen and metal - metal, respectively.

4.2.2 Surface calculation details

Slab models of low index surfaces were generated with the METADISE code, [54] where the *(100)*, *(110)*, *(101)*, and *(111)* planes for the oxides' surfaces were chosen. These slabs were built upon the convergence of surface energy (γ) as a function of slab thickness, vacuum, k-points and the number of atomic layers relaxed, ***Figure 4.2***. γ-Al_2O_3 was modelled with a four-layer slab, *p(2 x 2),* with 32 Al and 48 O atoms (surface area = 81.2 Å^2); for CeO_2, the oxygen-terminated three-layers surface was selected with three atoms layers each, *p(4 x 4)* with 32 Ce and 64 O atoms (surface area = 207.3 Å^2). MgO was modelled with a four-layer slab, *p(2 x 2)* of 32 Mg and 32 O atoms (surface area = 70.9 Å^2). For β-SiO_2, a four-layer oxygen terminated slab, *p(4 x 4)* with 64 Si and 128 O atoms (surface area = 223.2 Å^2), was chosen. Finally, for a-TiO_2, a four-layer oxygen terminated slab was selected, *p(3 x 3),* with 48 Ti and 92 O atoms (surface area = 118.9 Å^2). A Γ-centred 3 x 3 x 1 k-points grid sampled the Brillouin zone of these slabs and a vacuum thickness of 15 Å. Isolated molecules were placed in a 20 x 20 x 20 Å^3 box to avoid interactions with their periodic images.

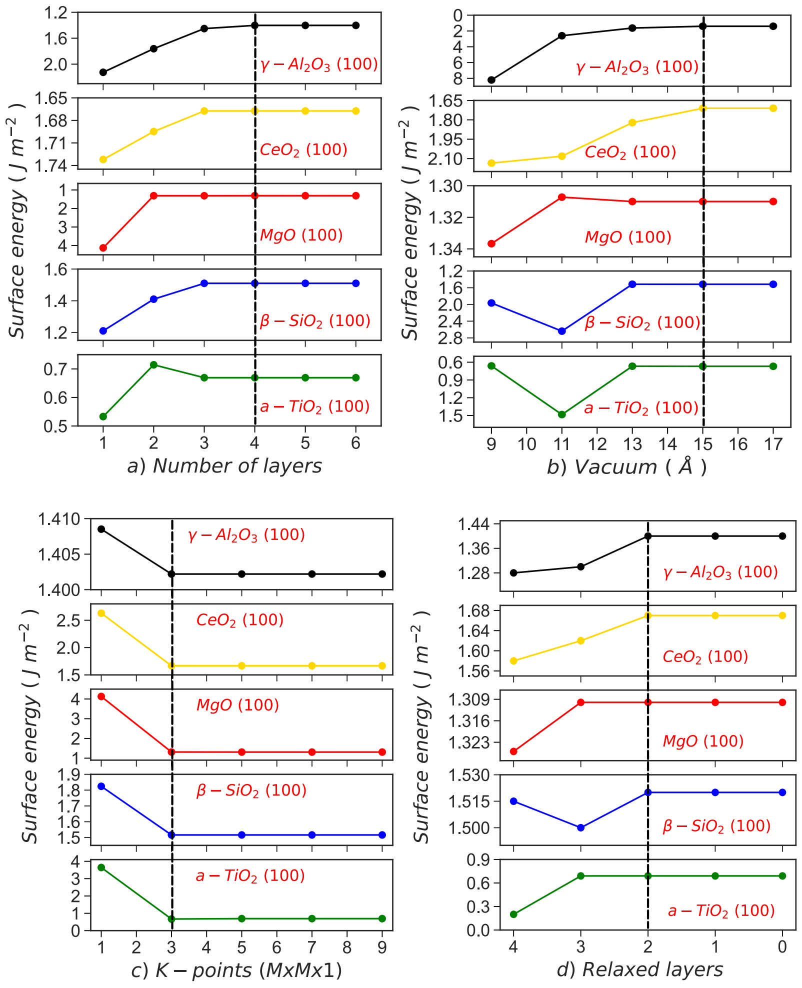

Figure 4.2. *Variation of the surface energy of (a) number of layers, (b) vacuum thickness, (c) number of k-points and (d) number of relaxed layers for γ-Al_2O_3, CeO_2, MgO, β-SiO_2, and a-TiO_2 (100) facet.*

4.3 Results and discussion

4.3.1 Slab calculation and atomic geometries of clean surfaces

Table 4.2 shows the surface energy (γ) for each clean oxide surface calculated using *Eq. 2.16.* The surface energy trend for *γ-Al_2O_3* is *(100) < (110) < (101) < (111)* similar to previous reports.[47, 55] Although the *(100)* facet is the most stable, the *(110)* is commonly selected to represent the γ-Al_2O_3 reactivity based on experimental studies confirming it to be the predominant surface, which covers ~83% of the total surface area.[55-57] The trends of surface energy for the other oxide surfaces are as follows: for CeO_2 *(111) < (110) = (101) < (100)*, for *MgO (100) < (110) = (101) < (111)*, for *β*-SiO_2 *(100) < (101) < (110) < (111)* where O-terminated slab is more stable than Si−terminated slab, and for *a*-TiO_2 *(101) < (100) < (110) < (111)* Miller indices. These results match with those found in previous studies.[58-61]

Table 4.2. *Calculated oxide support surface energies in J m*$^{-2}$

(hkl)	*γ*-Al_2O_3	CeO_2	*MgO*	*β*-SiO_2	*a*-TiO_2
(111)	1.85	0.57	3.91	2.43	1.78
(110)	1.63	0.87	2.62	2.17	1.17
(100)	1.40	1.67	1.31	1.52	0.69
(101)	1.75	0.87	2.62	1.67	0.61

γ-Al_2O_3 *(110)* consists of three- and four-fold coordinated Al atoms (Al_{3c} and Al_{4c}) and two- and three−fold coordinated O atoms (O_{2c} and O_{3c}). It should be noted that the Al_{3c} site exists only on the *(110)* surface, and it is the most acidic site. The lower the Al atom coordination is, the stronger its Lewis acidity.[47, 55, 62] Although the presence of three-coordinated Al atoms is not observed in experimental studies, Al_{3c} is expected based on the bulk structure. DFT studies have confirmed that *γ*-Al_2O_3 *(110)* undergoes a spontaneous reconstruction of the truncated bulk, where Al_{3c} is observed in the first subsurface layer. This spontaneous reconstruction explains the experimental observation where Al_{3c} is not found on γ-Al_2O_3 surfaces.[63]

The O-terminated CeO_2 *(111)* surface exposes three-fold coordinated O atoms with seven-fold coordinated Ce atoms (O_{3c}, Ce_{7c}, respectively).[64] *MgO (100)* surface is a flat terrace exposing O and Mg atoms with five-fold coordination each.[42, 65] *β*-SiO_2 *(100)* cleaved bulk contains three-fold Si coordination (Si_{3c}) and one-coordinated non-bridging O atoms (O_{1c}) at the topmost layer. Finally, the *a*-TiO_2 *(101)* surface has five-fold coordination of Ti atoms (Ti_{5c}) and two- and three-fold coordinated O atoms (O_{2c} and O_{3c}). The representative slab surfaces for each oxide surface are shown in ***Figure 4.3.***

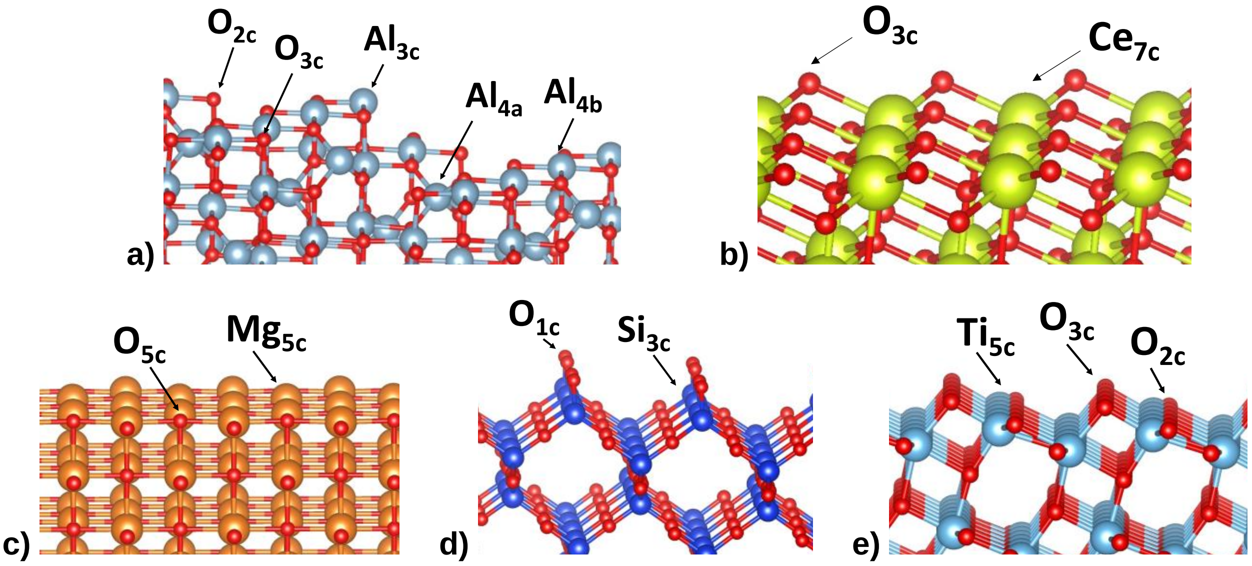

Figure 4.3. *Side view of clean surfaces of a) γ-Al_2O_3 (110), b) CeO_2 (111), c) MgO (100) d) β-SiO_2 (100) cleaved bulk, and e) a-TiO_2 (101). O atoms are represented in red colour and Al, Ce, Mg, Si and Ti metal atoms are represented in blue, yellow, orange, dark blue and light blue respectively. Surface sites are labelled, including their coordination as a subscript.*

4.3.1.1 Electronic properties of clean surfaces

The density of states (DOS) and projected density of states (PDOS) were employed aligned to the Fermi energy to represent the electronic structure of the oxide bulk and surfaces, ***Figures 4.4*** and ***4.5,*** respectively.

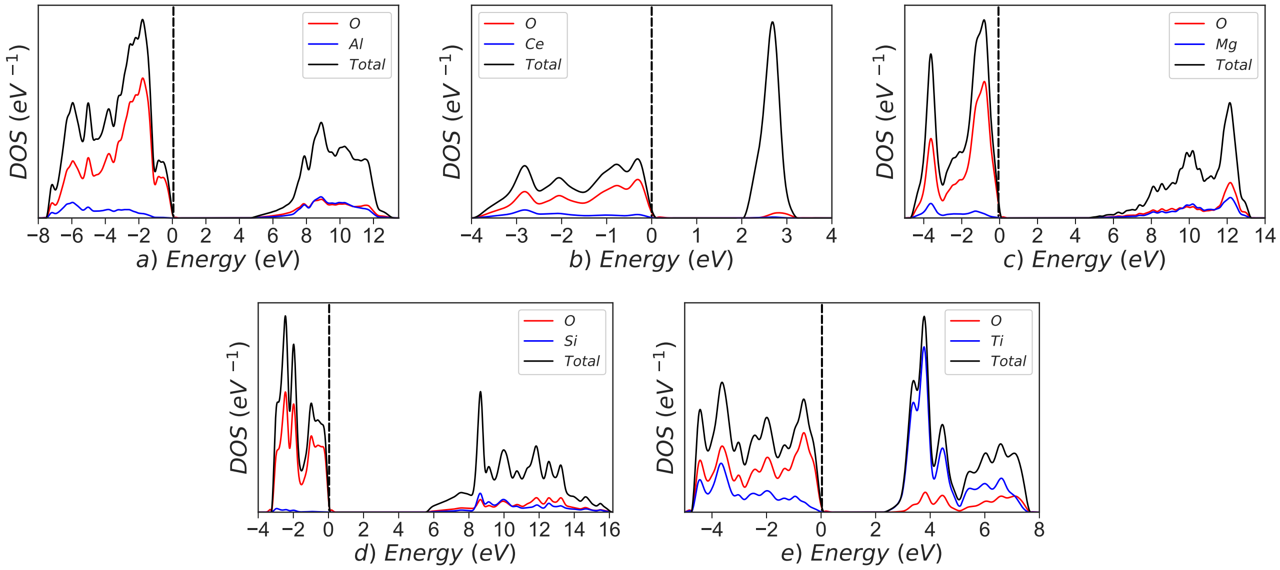

***Figure 4.4**. DOS and projected DOS for oxide bulks a) γ-Al_2O_3, b) CeO_2, c) MgO, d) β-SiO_2, and e) a-TiO_2. DOS are given in eV^{-1}.*

The DOS and PDOS show two distinctive regions typical of an oxide material: valence band (V_B) and conduction band (C_B). The valence bands (below 0 eV) of these oxides are mainly composed of *O-2p* states, which slightly hybridise with the states of metals. In contrast, the unoccupied metal orbitals form the conduction band.

In *γ-Al_2O_3 (110)*, the *O-2p* states dominate the valence band region, whereas the C_B region is mainly composed of the O−Al antibonding orbitals, as shown in ***Figure 4.5 (a)***. The small bands between V_B and C_B correspond to the unoccupied surface dangling bonds. The resulting electronic structure is very similar to the one found by Yazdanmehr *et al.*[66] The high degree of hybridisation on the γ-Al_2O_3 oxide indicates a specific covalent character.[47] In the O−terminated *CeO_2 (111),* the V_B region is composed of the hybridisation between O-*2p*, *Ce-5d* and *4f* states. The structure's main characteristic is the prominent peak in the C_B region formed by the localised empty *Ce-4f* states with a small contribution of *O-2p* states, indicating antibonding character.[67] The PDOS shows a significant contribution of Ce to the V_B region, indicating a not completely ionic character.[68]

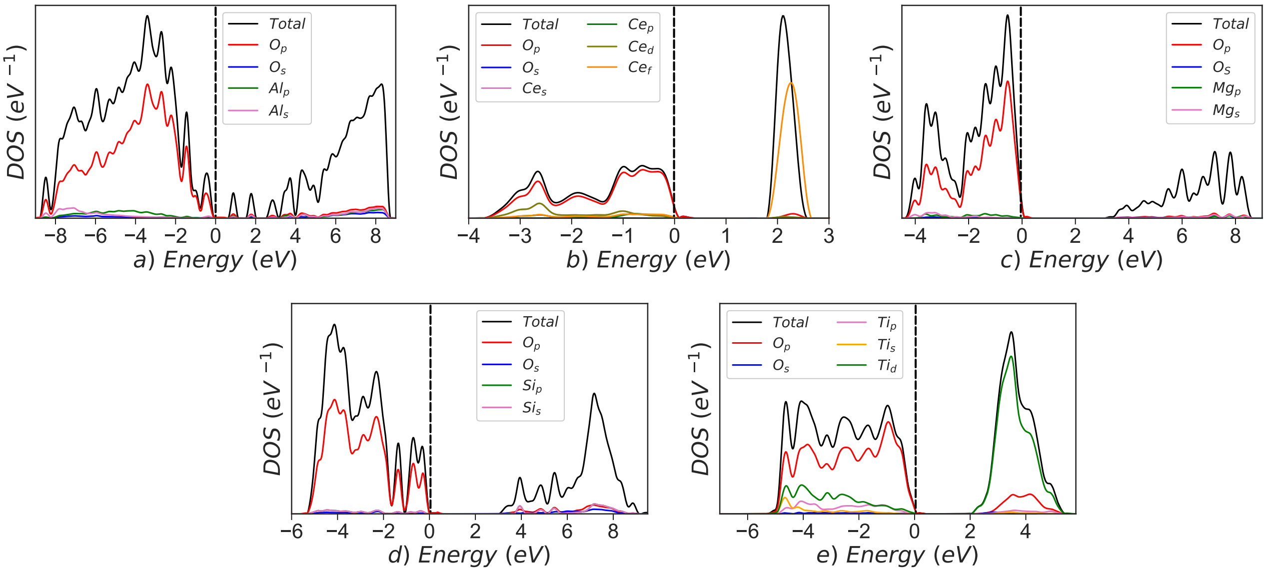

Figure 4.5. *DOS and projected DOS for the most stable clean surfaces: a) γ-Al_2O_3 (110), b) CeO_2 (111), c) MgO (100), d) β-SiO_2 (100), and e) a-TiO_2 (101).*

In the PDOS of *MgO (100),* the V_B region is predominated by *O-2p* states with small *Mg-2p* and *3s* states contributions. Small bands in the C_B region are composed mainly of *Mg-3s* states,[69] showing that the material is primarily ionic.[70] The *β-SiO_2 (100)*−DOS has a V_B region formed by the *Si-3p* and *3s* and *O-2p* states. The dangling bonds of the surface split the *O-2p* states creating two peaks close to the bandgap due to remaining unbonded oxygen atoms (electron lone pair).[61] The contributions of *Si-3p* states in the occupied region compared to *O-2p* states indicate that the material has a covalent character. The DOS of *a-*TiO_2 *(101)* shows a strong hybridisation in the V_B region composed of *O-2p* and *Ti-3d* orbitals; this indicates a strong interaction between Ti and O with a band width of approximately 5.0 eV. In contrast, the C_B region comprises unfilled *Ti-3d* states containing a significant contribution of *O-2p* and *2s* states. This material presents a considerable covalent behaviour; previous works have similar results.[71]

In good agreement with benchmark values, the bandgap (E_g) for *γ-*Al_2O_3 *(110)* [72], CeO_2 *(111)* [2], *MgO (100)* [2], β-SiO_2 *(100)* [61], and a-TiO_2 *(101)* [73, 74] surfaces is 3.76 eV, 1.88 eV, 3.45 eV, 2.90 eV, and 2.09 eV respectively, ***Table 4.3***. The main differences between the bulk and surface electronic structures are related to the oxygen electron dangling bonds at the surface, which causes a decrease in the bandgap's size.[42] Although the DOS analysis gives information about the characteristics of the material. Further research needs to be done to clarify the relationship between their acid/base properties and compounds in HDO processes.

Table 4.3*. Calculated and theoretical values of bandgaps (E_g) for bulk and surfaces of oxide surfaces.*

	Bulk, E_g (eV)		Surface, E_g (eV)	
	This work	**Theoretical works**	**This work**	**Theoretical works**
γ-Al_2O_3 *(110)*	4.88	4.13-6.19 [72]	3.76	3.96 [72]
CeO_2 *(111)*	2.02	1.88 [75]	1.88	2.10 [2]
MgO (100)	4.92	4.80 [76]	3.45	3.30 [2]
β-SiO_2 *(100)*	5.64	5.66-5.90 [75, 77]	2.90	2.41 [61]
a-TiO_2 *(101)*	2.50	2.60 [53]	2.09	2.12-2.14 [73, 74]

Note: Calculations from Refs [2, 53, 76, 77, 66, 73, and 74] were conducted at the GGA-PBE level of theory
Calculation from Ref [72] was conducted at the GGA-PW91 level of theory.

4.3.1.2 Hydrogen and oxygen adsorption on clean surfaces

Simulation of the O and H adsorption on clean surfaces was conducted to evaluate the possibility of variations in the HDO conditions and the degree of interaction between the metal cation of clean surfaces and oxygenated compounds compared to hydroxylated surfaces. Different adsorption sites have been considered, including top-oxygen (T_1), top-metal (T_2), bridge (B), and hollow (H), ***Figure 4.6.*** For γ-Al_2O_3 (110), two inequivalent top-oxygen sites were found: T_{1a} (O_{2c}) and T_{1b} (O_{3c}), and three top-metal sites: T_{2a} (Al_{4a}), T_{2b} (Al_{4b}) and T_{3c} (Al_{3c}). For a-TiO_2 (101), there are also two different top-oxygen sites: T_{1a} (O_{2c}) and T_{1b} (O_{3c}), and two bridge sites: B_1 (Ti−O_{2c}) and B_2 (Ti−O_{3c}). The hydrogen and oxygen adsorption energies (E_{ads}) were calculated using *Eq. 3.1*. ***Table 4.4*** contains the information about the adsorption sites on each surface. Bader charge analysis method was employed to measure the charge transfer between the surface and the adsorbed atom.

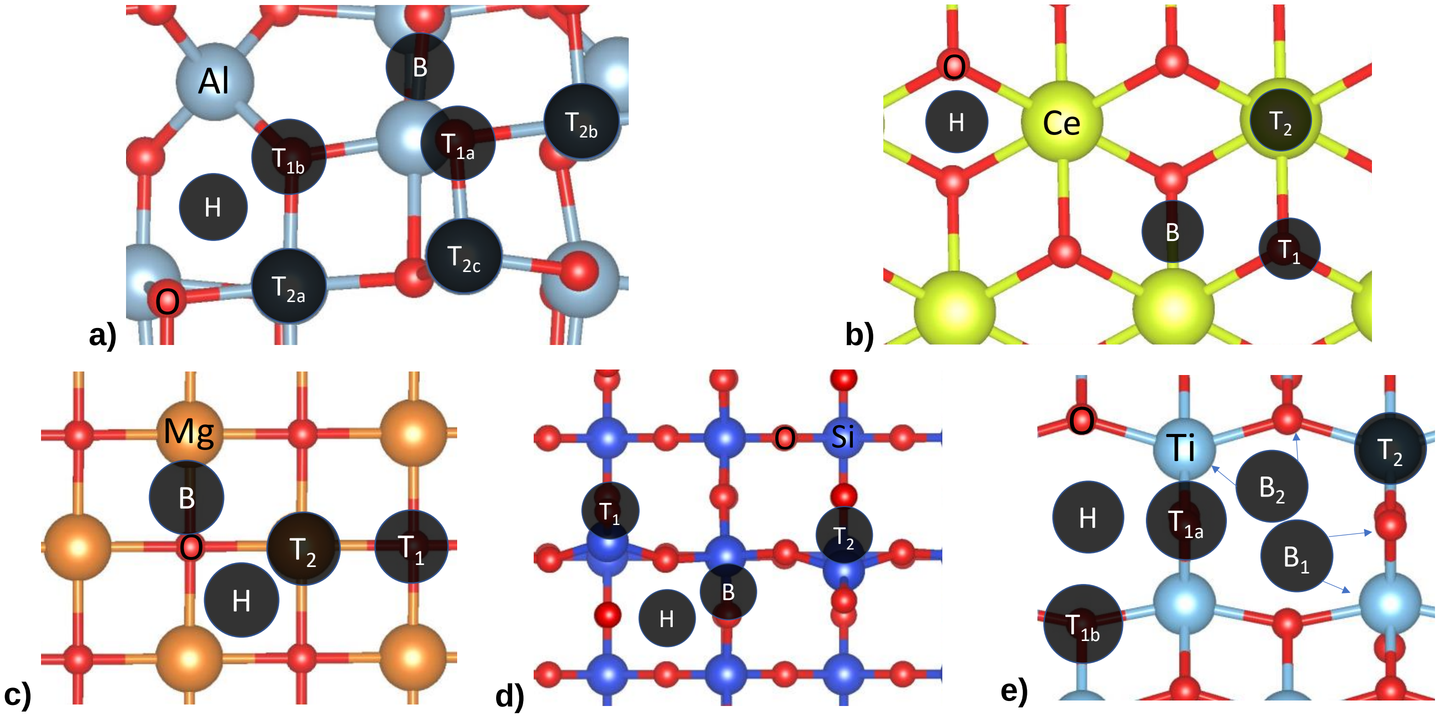

Figure 4.6*. Top view of the a) γ-Al_2O_3 (110), b) CeO_2 (111), c) MgO (100), d) β-SiO_2 (100), and e) a-TiO_2 (110) slab models. The adsorption sites are indicated with a black circle labelled as hollow (H), bridge (B), and top (T) adsorption sites. Colour code: O atom is represented in red colour and Al, Ce, Mg, Si and Ti metals atoms are represented in blue, yellow, orange, dark blue and light blue, respectively.*

Table 4.4. *Calculated hydrogen and oxygen adsorption energies (E_{ads}), Bader charge analysis (q) and distance between hydrogen / oxygen - surface (d) for the oxide surfaces.*

		H_{ads}				O_{ads}			
		T_1 (O)†	*T_2 (M)†*	*B (M-O)*	*H*	*T_1 (O)†*	*T_2 (M)†*	*B (M-O)*	*H*
γ-Al_2O_3 (110)	*E_{ads} (eV)*	−1.31, T_{1a} −0.60, T_{1b}	2.15, T_{2a} 1.42, T_{2b} 0.13, T_{2c}	−0.66	2.20	- - - ** T_{1a} - - - ** T_{1b}	−0.39, T_{2a} −2.02, T_{2b} −2.30, T_{2c}	−1.11	−0.09
	q |e⁻|	0.70, T_{1a} 0.67, T_{1b}	−0.64, T_{2a} −0.29, T_{2b} −0.06, T_{2c}	0.61	−0.95	- - - ** T_{1a} - - - ** T_{1b}	−0.59, T_{2a} −1.18, T_{2b} −1.41, T_{2c}	−0.48	−0.43
	d (Å)	0.97, T_{1a} 0.97, T_{1b}	1.60, T_{2a} 1.61, T_{2b} 1.58, T_{2c}	1.78	1.00	- - - ** T_{1a} - - - ** T_{1b}	1.87, T_{2a} 1.88, T_{2b} 1.76, T_{2c}	1.60	1.88
CeO_2 (111)	*E_{ads} (eV)*	−1.15	2.20	−0.47	−0.79	- - - **	−1.42	−1.41	−1.44
	q |e⁻|	0.60	0.02	0.58	0.61	- - - **	−0.47	−0.46	−0.52
	d (Å)	0.97	2.95	0.99	0.99	- - - **	1.90	1.40	1.32
MgO (100)	*E_{ads} (eV)*	−0.16	2.16	−0.08	−0.07	−0.96	0.40	−0.57	−0.23
	q |e⁻|	0.63	0.64	−0.20	0.64	−0.74	−0.27	−0.69	−0.71
	d (Å)	1.33	2.32	2.11	1.51	1.53	2.01	1.61	2.05
β-SiO_2 (100)	*E_{ads} (eV)*	−1.00	- - - **	−0.81	0.63	0.50	- - - **	−0.48	0.27
	q |e⁻|	0.66	- - - **	0.69	−0.59	0.01	- - - **	−0.75	−0.23
	d (Å)	0.97	- - - **	1.06	1.49	1.35	- - - **	1.64	1.85
a-TiO_2 (101)	*E_{ads} (eV)*	−0.10, T_{1a} 0.69, T_{1b}	2.18	2.22, B_1 2.19, B_2	2.26	0.14, T_{1a} 0.47, T_{1b}	0.28	−0.96, B_1 −0.50, B_2	0.56
	q |e⁻|	0.07, T_{1a} 0.05, T_{1b}	−0.34	0.02, B_1 −0.03, B_2	0.02	−0.32, T_{1a} −0.39, T_{1b}	−0.39	−0.34, B_1 −0.36, B_2	−0.36
	d (Å)	0.97, T_{1a} 0.98, T_{1b}	2.52	2.49, B_1 2.41, B_2	2.48	1.33, T_{1a} 1.50, T_{1b}	1.50	1.44, B_1 1.35, B_2	1.95

† T_1 (O) = Interaction between the hydrogen/oxygen atom and the oxygen atom from the surface. T_2 (M) = Interaction between the hydrogen/oxygen atom and the metal atom from the surface.

** Not available.

On *γ-Al_2O_3 (110)*, the H atom interacts preferably with the T_{1a} (O_{2c}) and T_{1b} (O_{3c}) with an E_{ads} = −1.31 eV and −0.60 eV, respectively. The charge transfer between O−H can be around 0.67 to 0.70 e⁻ concluding that the oxygen is protonated with a bond distance of 0.97 Å, showing a high affinity to the oxygen of the surface to create a hydroxyl bond.[78] The interaction between the hydrogen atom and T_{2c} (Al_{3c}) is more favourable (E_{ads} = 0.13 eV) than the other Al sites such as T_{2a} (Al_{4a}) and T_{2b} (Al_{4b}) due to their electronic properties (E_{ads} = 2.15 eV and 1.42 eV, respectively).[46, 79] For oxygen adsorption, it can be seen that it prefers the Al sites T_{2c} (Al_{3c}) with an E_{ads} = −2.30 eV. This strong interaction is due to the overlap between the *O-2p* states and the *Al-3p* states of the surface.[318] Other adsorption sites are weaker due to the repulsion of neighbouring oxygens. There is a downward charge transfer trend, with T_{2c} (Al_{3c}) site being the highest at q = −1.41 e^-, followed by T_{2b} (Al_{4b}) > T_{2a} (Al_{4a}) > bridge > and eventually the hollow site being the lowest at q = −0.43 e^-. Hence, the adsorption energy increases, as does the charge transfer from the surface to the oxygen.

On *CeO_2 (111)*, the hydrogen atom interacts more strongly with the top-oxygen site, T_1 (O) site, with an E_{ads} = −1.15 eV and a charge transfer of 0.60 e^-. In contrast, the Ce atom presents a repulsion effect with the hydrogen (E_{ads} = 2.20 eV, q = 0.02 e^-). This confirms that the strong interaction of the H atom to bind the oxygen of the surface would favour the formation of an O−H bond (hydroxyl group) with a bond distance of 0.97 Å, in good agreement with previous works.[80, 81] On the other hand, the oxygen adsorption takes place on the T_2 (Ce) site (E_{ads} = −1.42 eV) with a charge transfer of −0.47 e^- as found previously and on the hollow site (E_{ads} = −1.44 eV, q = −0.52 e^-).[82] This can be useful for molecules with two oxygen atoms such as catechol and guaiacol due to the Ce atoms are exposed outward in the *(111)* facet.

On *MgO (100)*, the H atom shows preferable adsorption on top of surface−O, T_1 (O) site, with an adsorption energy of −0.16 eV, leading to O−H formation. The charge transfer between the H atom and the T_1 (O) site is 0.63 e^- in agreement with previous studies.[83, 84] Similarly, O atom preferably adsorbs on the T_1 (O) site with a strong interaction with an E_{ads} = −0.96 eV. This interaction results in a peroxide ion (O_2^{2-}) donation with a good overlapping between both of the *2p* orbitals with a charge transfer of −0.74 e^-.[85, 86]

On *β-SiO_2 (100)*, the structure's geometry favours the hydrogen adsorption on O sites with an E_{ads} of −1.00 eV at a distance of 0.97 Å. These results agree with previous studies that demonstrate the strong attraction of hydrogen onto the O atom of the material due to the hydrophilic behaviour of the structure.[87] For the oxygen adsorption, the O atom presents a strong interaction on bridge site (B) with an E_{ads} = −0.48 eV (with a charge transfer of −0.75 e^-). These results show that a reconstruction of the surface is possible because the oxygen atom can interact with the unbonded Si atom of the surface to create a geminal silanol (Si−OH). On *a-TiO_2 (101)*, the results show that the H atom interacts weekly with the *a-TiO_2 (101)* surface being the T_{1a} (O_{2c}) site the most favourable adsorption (E_{ads} = −0.10 eV) compared to the T_{1b} (O_{3c}) with an E_{ads} = 0.69 eV, similar to other works.[88, 89]

Similarly, five adsorption sites were studied for oxygen adsorption, indicating that the bridge site (Ti_{5c}−O_{2c}) is the most favourable with an E_{ads} = −0.96 eV (q = −0.34 e^-). These results demonstrate that the oxygen atom will be adsorbed when it interacts with the O and Ti atoms of the surface at the same time, which coincides with a previous study.[90] According to Sabatier's principle, weak interaction between the surface's site and the oxygenated compounds, e.g. guaiacol, catechol, anisole, phenol, does not facilitate the removal of the O from the model compounds. Following this guide, oxide surfaces with a strong O-affinity would facilitate the HDO process.[91] Hence, based on our previous results, the HDO performance order should follow the oxygen adsorption energies, i.e. γ-Al_2O_3 > CeO_2 > a-TiO_2 ≈ MgO > β-SiO_2. However, the accessibility of the sites according to the surface morphology and steric hindrance should also be considered.

4.3.2 Hydroxylated surfaces

The hydroxylation of oxide surfaces is achieved by the dissociation of water molecules on them. The OH is bonded to a cationic site, forming a terminal hydroxyl OH (I), whereas the hydrogen sticks to the surface oxygen, creating a bridging hydroxyl, OH (II), ***Figure 4.7 (a − c, e)***.[92, 93] Instead of OH (II), the β-SiO_2 *(100)* surface contains two silanols on each Si (geminal silanol HO−Si−OH) with a bond length between 0.96 Å and 0.98 Å, ***Figure 4.7 (d).***[94]

The concentration of hydroxyl groups on the surface (hydroxyl coverage) is determined by the operating HDO temperature (573 K − 673 K) and the H_2O pressure. The hydroxyl coverage on *γ-Al_2O_3 (110)* covers from 3.0 OH·nm^{-2} to 11.8 OH·nm^{-2} at a temperature between 500 and 1000 K.[95] The lowest hydroxyl coverage (3.0 OH·nm^{-2}) makes the surface highly acidic because of the unsaturated Al_{3c} site.[47, 96-98] For *CeO_2 (111)*, the most stable structure for the *(111)* facet has a concentration of hydroxyl groups close to 4.0 OH·nm^{-2}.[99] *MgO (100)* hydroxylation in normal conditions is minimal due to its low hydrophilicity, i.e. water adsorption occurs at very low temperatures.[100] The opposite is on β-SiO_2, which hydroxylates during its synthesis at around 4.0 – 4.9 OH·nm^{-2}.[101] The hydroxyl coverage on *a-TiO_2 (101)* may reach 7 OH·nm^{-2}.[102] ***Table 4.5*** summarises the OH coverage investigated for the five surfaces and provides bond distances and angles registered between the surface and the OH groups.

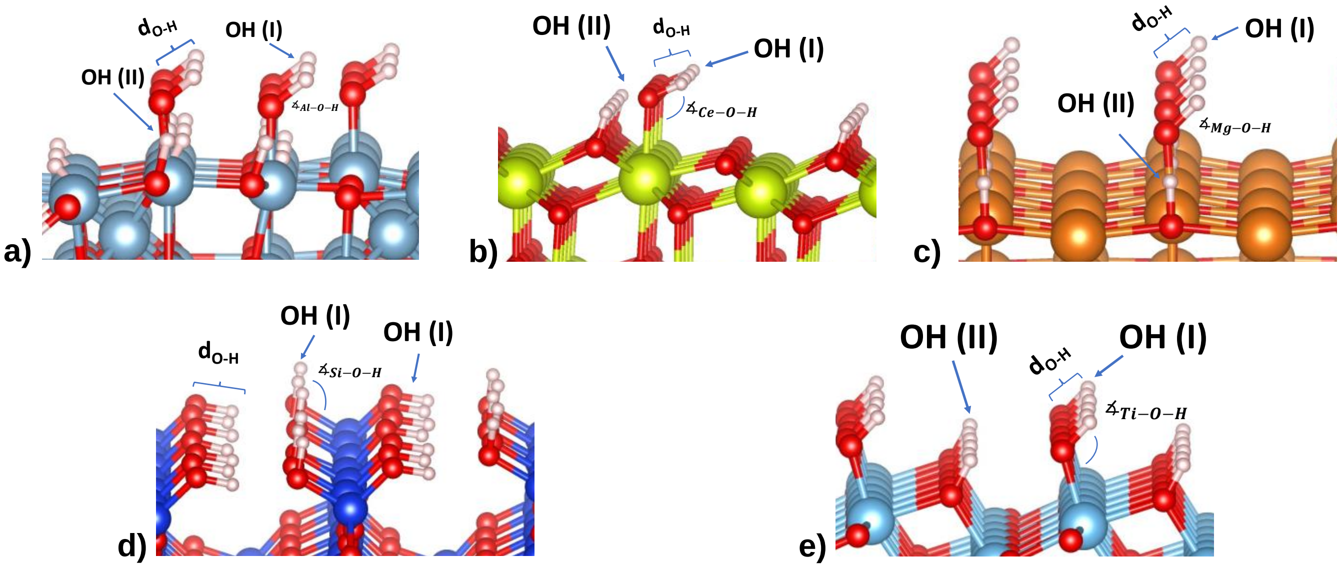

Figure 4.7. *Schematic side views of the hydroxylated surfaces, where OH (I) corresponds to a terminal hydroxyl group and OH (II) a bridging hydroxyl group for a) γ-Al_2O_3 (110), b) CeO_2 (111), c) MgO (100), and e) a-TiO_2 (101). d) β-SiO_2 (100) contains two geminal silanol OH (I). Colour code: O, H, Al, Ce, Mg, Si and Ti atoms are represented in red, white, blue, yellow, orange, dark blue and light blue colour, respectively.*

Table 4.5. *Calculated hydroxyl coverages, bond distances (d), and angle (∡) for the most stable hydroxylated surface configurations.*

		γ-Al_2O_3 (110)	*CeO_2 (111)*	*MgO (100)*	*β-SiO_2 (100)*	*a-TiO_2 (101)*
OH (nm^{-2})		6.15	3.85	5.64	3.59	5.05
OH (I)	*d_{M-O} (Å)*	1.82	2.26	1.87	1.67	1.88
	d_{O-H} (Å)	0.97	0.97	0.97	0.97	0.97
	$∡_{M-O-H}$ (°)	113.4	126.4	127.4	112.7	119.8
OH (II)	*d_{M-O} (Å)*	1.91	2.37	2.11	1.63	2.04
	d_{O-H} (Å)	1.03	0.98	1.02	0.98	0.97
	$∡_{M-O-H}$ (°)	106.5	108.9	95.0	123.2	118.4

d_{M-O} (Å) = Bond distance between metal and oxygen. d_{O-H} (Å) = Bond distance between oxygen and hydrogen. $∡_{M-O-H}$ (°) = angle between metal, oxygen, and hydrogen.

4.3.2.1 Electronic properties of hydroxylated surfaces

Figure 4.8 shows the hydroxylated surfaces' DOS and PDOS at the coverages summarised in ***Table 4.5***. The appearance of new states in the V_B region compared with clean surfaces results from the OH groups partially saturating the surface's dangling bonds. Both C_B and V_B slightly change their relative position due to the O_{2c} and H bonding, which provokes an enlargement of the bands, becoming wider than on clean surfaces.[103]

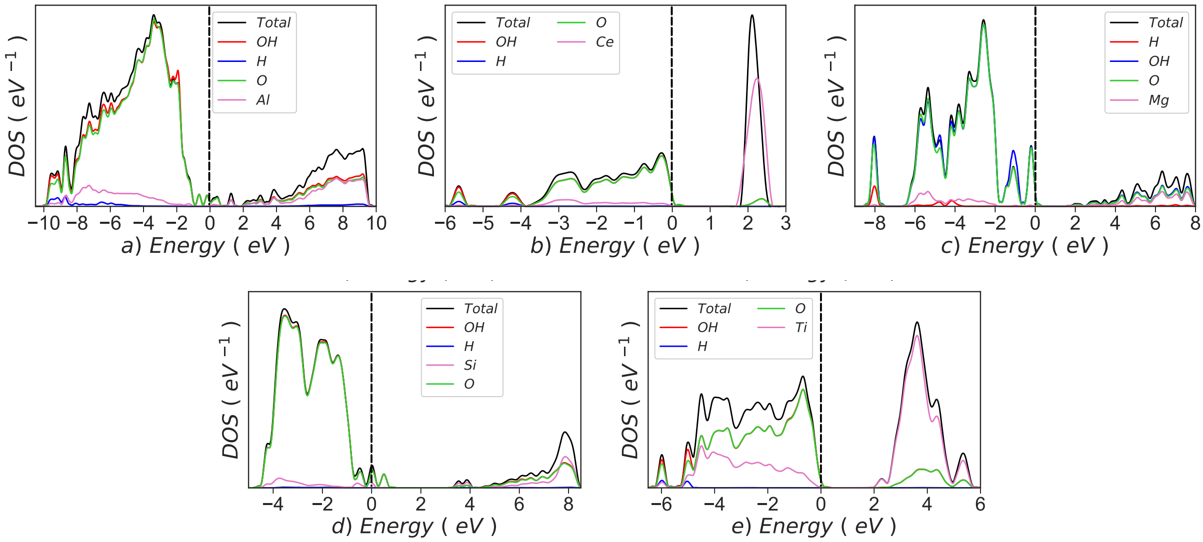

Figure 4.8. *DOS and projected DOS on the metal, OH (I) and OH (II) for the hydroxylated surfaces: a) γ-Al_2O_3 (110), b) CeO_2 (111), c) MgO (100), d) β-SiO_2 (100), and e) a-TiO_2 (101).*

The electronic structure indicates a change in the ionicity degree of the hydroxylated *γ-Al_2O_3 (110), CeO_2 (111), β-SiO_2 (100) and a-TiO_2 (101)* surfaces. The metal contributions to the V_B region suffer an upshift in energy, provoking an increase in the ionicity behaviour and a decrease in Lewis acidity. The protonation of the surfaces' O also shifted the position of the *O-2p* states. The computational model allowed us to simulate the *MgO (100)* hydroxylation, which provokes the valence band edge to increase and reduce its bandgap.

The two prominent peaks localised close to the Fermi level cause the Mg−O states to move towards lower energies and to decrease the degree of ionicity compared with the clean surface. The interaction of OH ions with Mg cations evokes MgOH groups' generation, leading to a significant downshift of energy in Mg orbitals and an increase of acidity.[104, 105] As expected, *β-SiO₂ (100)* hydroxylation stabilises the structure and reduces the number of dangling bonds at the surface.[106]

4.3.3 Lewis acid−base descriptor

A common feature between oxide surfaces is their acid−base properties, i.e. the metal cation acts as a Lewis acid site (electron acceptor) and the oxygen as a Lewis base site (electron donor). The overall acidity depends on the polarisation power of the cation and the anion.[107] From the PDOS analysis of the unoccupied and occupied bands, one can derive the Lewis acidity (from the metal's states) and Lewis basicity (*O-2p* states) to understand the oxygen and cation role in the oxide's reactivity. The V_B and C_B band centre (ε), defined in *Eq. 4.1* and *4.2* are proposed as Lewis acidity and basicity descriptors. The ε_{VB} and ε_{CB} are the band centre of the valence and conduction band, respectively, E_F is the Fermi energy, and $\rho(\varepsilon)$ is the projected electronic density of state distribution on the orbitals of interest, i.e. *p, d, or f.*[96, 108, 109]

$$\varepsilon_{VB} = \frac{\int_{-\infty}^{E_F} \varepsilon \cdot \rho(\varepsilon)\, d\varepsilon}{\int_{-\infty}^{E_F} \rho(\varepsilon)\, d\varepsilon} \qquad \textit{Eq. 4.1} \qquad \varepsilon_{CB} = \frac{\int_{E_F}^{\infty} \varepsilon \cdot \rho(\varepsilon)\, d\varepsilon}{\int_{E_F}^{\infty} \rho(\varepsilon)\, d\varepsilon} \qquad \textit{Eq. 4.2}$$

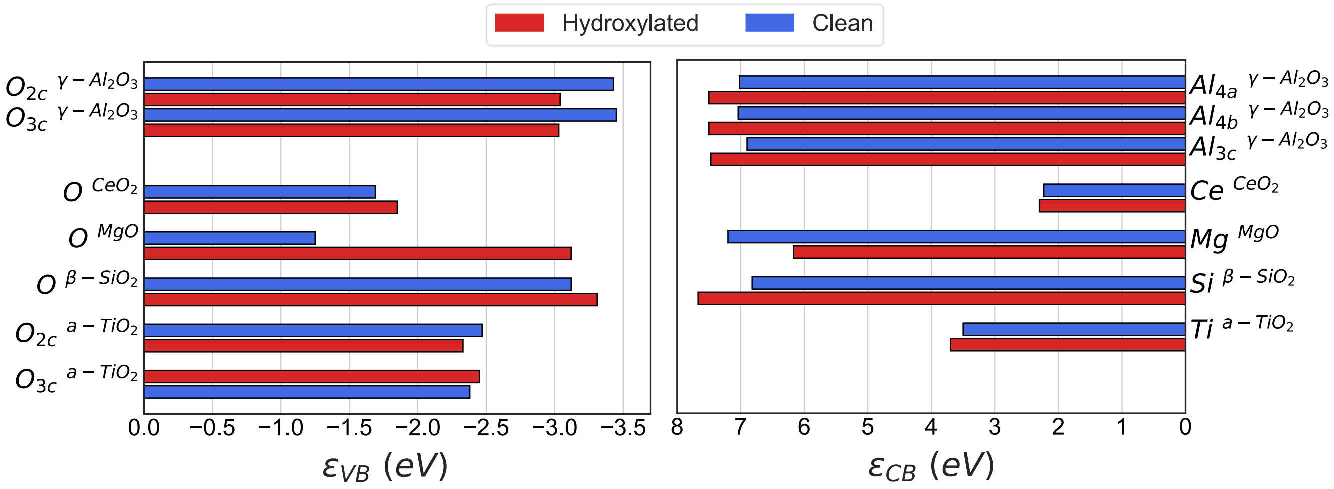

Figure 4.9. *Band centres (ε) of the occupied (V_B, left) and unoccupied states (C_B, right) of the oxide surfaces in this study.*

The ε_{VB} and ε_{CB} collected from the projected band centres were summarised in ***Figure 4.9***. The ε_{CB} of the clean surfaces follow the order MgO > γ-Al_2O_3 > β-SiO_2 > a-TiO_2 > CeO_2. However, the presence of *d* and *f* orbitals of Ti and Ce cation affects their ionic covalent character, as reported by Bordes-Richard *et al.*[110], and trends including all these oxides cannot be made. Comparing the Lewis acidity of the *sp* oxides, e.g. MgO, γ-Al_2O_3 and β-SiO_2, it is possible to categorise β-SiO_2 as an acid (ε_{CB} = 6.82 eV), γ-Al_2O_3 as an amphoteric (ε_{CB} = 6.90 eV), and MgO as a base oxide (ε_{CB} = 7.20 eV). These results show that the lower the ε_{CB} band centre, the higher the Lewis acidity. This reactivity agrees with the results from H and O adsorptions.[96, 109] The surfaces' basicity is directly related to the *2p* orbitals of the oxygen anion (ε_{VB}). The ε_{VB} of the clean surfaces follow the order MgO > CeO_2 > a-TiO_2 > β-SiO_2 > γ-Al_2O_3. According to these results, MgO has the highest Lewis basicity (ε_{VB} = −1.25 eV), and γ-Al_2O_3 has the lowest (ε_{VB} = −3.45 eV), showing a distinct relation between these results and the Lewis acidity from the ε_{CB} results.

The surface hydroxylation impacts the Lewis acidity and basicity of the materials. Al_{3c} site in γ-Al_2O_3 increases the energy of the conduction band with an $\Delta\varepsilon_{CB}$ = 0.57 eV (Δε, difference between the hydroxylated and clean surface, ***Table 4.6***), provoking a decrease in the Lewis acidity. Contrarily, upon surface hydroxylation, the Lewis basicity of O atoms increases due to the oxygen V_B upshift. On hydroxylated *MgO (100)*, the interaction between the OH and Mg atoms causes an increase in the Lewis acidity strength ($\Delta\varepsilon_{CB}$ = −1.03 eV) due to the decrease of the band centre (ε_{CB} = 6.17 eV). The band centre of the protonated O increases (ε_{VB} = −3.12 eV), reducing the basicity of the surface ($\Delta\varepsilon_{VB}$ = −1.87 eV).

Table 4.6. *Difference of band centre (Δε) between clean and hydroxylated oxide surfaces for the unoccupied (V_B) and occupied regions (C_B).*

	Sites	*Hydro* ε_{CB} *(eV)*	*Clean* ε_{CB} *(eV)*	$\Delta\varepsilon_{CB}$ *(eV)*	*Sites*	*Hydro* ε_{VB} *(eV)*	*Clean* ε_{VB} *(eV)*	$\Delta\varepsilon_{VB}$ *(eV)*
γ-Al_2O_3 (110)	Al_{4a}	7.50	7.02	0.48	O_{2c}	−3.04	−3.43	0.39
	Al_{4b}	7.50	7.04	0.46	O_{3c}	−3.03	−3.45	0.42
	Al_{3c}	7.47	6.90	0.57				
CeO_2 (111)	Ce	2.30	2.23	0.07	O	−1.85	−1.69	−0.16
MgO (100)	Mg	6.17	7.20	−1.03	O	−3.12	−1.25	−1.87
β-SiO_2 (100)	Si	7.67	6.82	0.85	O	−3.31	−3.12	−0.19
a-TiO_2 (101)	Ti	3.70	3.50	0.20	O_{2c}	−2.33	−2.47	0.14
					O_{3c}	−2.38	−2.45	0.07

Similar trends are for CeO_2 and a-TiO_2 with an $\Delta\varepsilon_{CB}$ = 0.07 and 0.20 eV, respectively. However, the surface protonation is different between these surfaces. The hydroxylation of CeO_2 produces a downshift in energy in O orbitals ($\Delta\varepsilon_{VB}$ = −0.16 eV), resulting in a decrease in the Lewis basicity linked with the cation's polarisation strength. On a-TiO_2, the surface hydroxylation increases the Lewis basicity on the O_{2c} site compared to the O_{3c} site. For instance, on γ-Al_2O_3, a medium hydroxylation coverage decreases the Lewis acidity of Al sites and increases the O atoms' basicity, similar results found by Wischert *et al.*[96] The hydroxylation of *β-SiO_2 (100)* surface also decreases its acidity ($\Delta\varepsilon_{CB}$ = 0.85 eV) and basicity ($\Delta\varepsilon_{VB}$ = −0.19 eV) character due to the interaction of a Lewis acid-base pair (OH^- and H^+). However, the surface geometry impacts the reactivity because of their anion termination and lesser polarisation power than clean surfaces.[32]

4.3.4 Molecular adsorption on clean oxide surfaces

Four lignol models were brought represented in ***Figure 1.5***, e.g. guaiacol, catechol, phenol, anisole**,** in addition to benzene as a possible product of the HDO close to four clean structures, γ-Al_2O_3 *(110)*, CeO_2 *(111)*, MgO *(100)*, and a-TiO_2 *(101)*. Clean β-SiO_2 *(100)* was not included as it is always hydroxylated. Three different molecular adsorption geometries were optimised for the lignol models according to the angle between the ring plane and the surface (90°, 45°, 0°). Guaiacol adsorption at three geometry modes is shown as an example on the clean oxide surfaces ***Table 4.7***

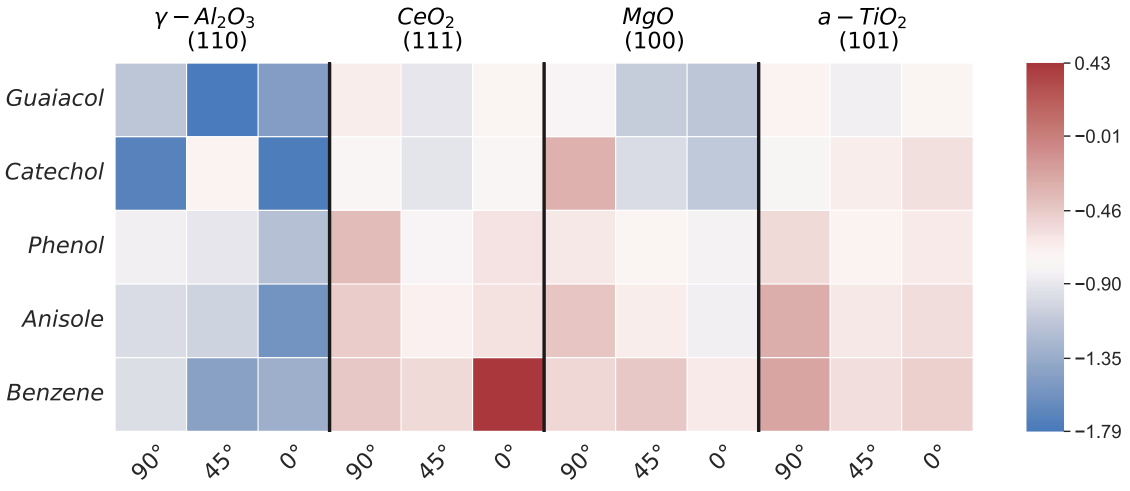

Figure 4.10. *Calculated adsorption energy (E_{ads}) of guaiacol, catechol, phenol, anisole, and benzene at different geometries modes for clean oxide surfaces*

The molecules were placed according to our previous oxygen adsorption results, i.e. favouring the stronger affinity between the cation of the surface and the molecular oxygen group. A heatmap in ***Figure 4.10*** summarises the interaction energies results of the adsorption of the five compounds.

Table 4.7. *Illustrations corresponding to the guaiacol adsorption on clean oxide surfaces at i) 90°, ii) 45° and iii) 0° geometries modes.*

	i) 90°	*ii) 45°*	*iii) 0°*
γ-Al_2O_3 (110)	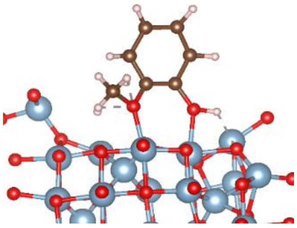	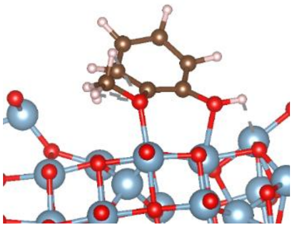	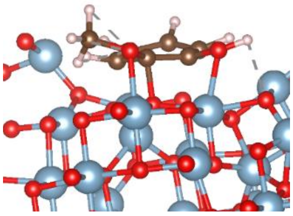
CeO_2 (111)		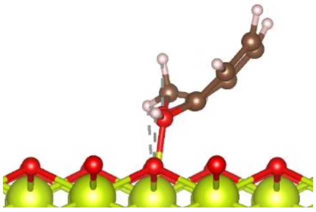	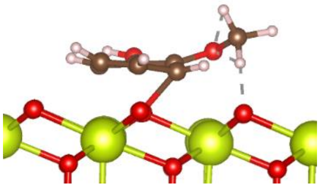
MgO (100)	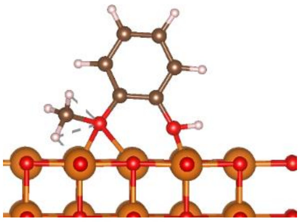	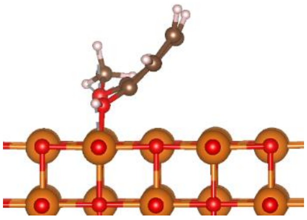	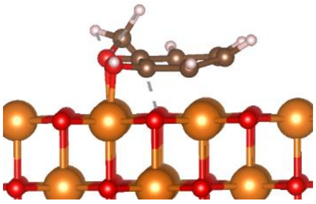
a-TiO_2 (101)	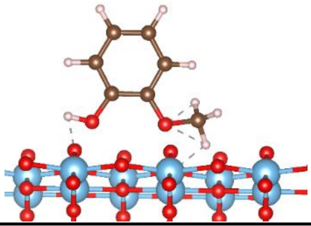	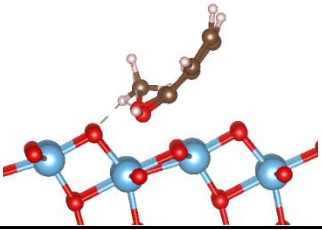	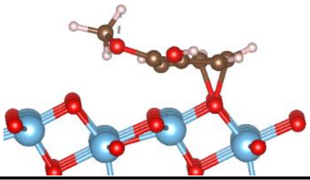

The most favourable geometry modes for each molecule are included in ***Table 4.8.*** On *γ-Al_2O_3 (110)*, the flat orientation is preferred (at 0°) except for guaiacol and benzene, in which 45° orientation is 0.31 eV and 0.12 eV more favourable than the flat one. The surface of MgO preferably adsorbs the compounds parallel to the surface as it facilitates the interaction with the π-conjugated orbitals of the molecule, which is more relevant than the interaction with the oxo groups. The O-termination on *CeO_2 (111)* and *a-TiO_2 (101)* structures prevents the interaction with the molecular oxo-groups, an effect seen with the weak atomic oxygen interaction. On *CeO_2 (111)*, the 45°

arrangement is the most favourable for all the compounds. It is the same on *a-*TiO_2 *(101)* surface except for catechol, in which OH groups favour the perpendicular orientation. Although both groups were placed (hydroxy and methoxy groups) closer to the cation atom at the surface, the methoxy group interacts weakly with the metal site, suggesting that the hydroxyl group is more accessible than the methoxy.[111, 112] The five compounds followed an adsorption strength trend (more negative) *γ-*Al_2O_3 *(110) > MgO (100) >* CeO_2 *(111) > a-*TiO_2 *(101).*

Table 4.8. *Calculated adsorption energies (E_{ads}), distance molecular oxygen-surface (d) and Bader charge (q) for the most favourable geometries modes on the clean oxide surfaces.*

		γ-Al_2O_3 *(110)*	CeO_2 *(111)*	*MgO (100)*	*a-*TiO_2 *(101)*
Guaiacol	*Initial angle (°)*	45°	45°	0°	45°
	E_{ads} *(eV)*	−1.78	−0.91	−1.14	−0.85
	d-O_1 *(−OH) (Å)*	1.93	1.89	1.74	2.18
	d-O_2 *(−*OCH_3*) (Å)*	2.10	1.91	1.98	2.31
	q |e^-|	0.17	0.02	1.32	0.61
Catechol	*Initial angle (°)*	0°	45°	0°	90°
	E_{ads} *(eV)*	−1.75	−0.92	−1.12	−0.80
	d-O_{1A} *(−OH) (Å)*	2.04	2.02	1.76	2.03
	d-O_{1B} *(−OH) (Å)*	1.68	2.21	1.72	1.86
	q |e^-|	0.47	0.31	0.45	0.16
Phenol	*Initial angle (°)*	0°	45°	0°	45°
	E_{ads} *(eV)*	−1.19	−0.79	−0.82	−0.71
	d-O_1 *(−OH) (Å)*	1.68	1.79	1.60	2.03
	q |e^-|	0.49	0.02	0.16	0.53
Anisole	*Initial angle (°)*	0°	45°	0°	45°
	E_{ads} *(eV)*	−1.56	−0.69	−0.85	−0.63
	d-O_2 *(−*OCH_3*) (Å)*	2.07	1.62	2.05	2.23
	q |e^-|	0.34	0.03	0.24	0.42
Benzene	*Initial angle (°)*	45°	45°	0°	45°
	E_{ads} *(eV)*	−1.45	−0.55	−0.64	−0.58
	q |e^-|	0.06	0.02	0.12	0.02

4.3.5 Molecular adsorption on hydroxylated surfaces

The adsorptions of lignin derivates on hydroxylated surfaces were carried out by placing the compounds nearby one of the surface hydroxyl groups, OH (I), and a neighbouring cation atom, similarly to the initial geometry on the clean surfaces***. Table 4.9*** shows the guaiacol adsorption on the hydroxylated oxide surfaces at three geometry modes as an example of the study realised for the four lignin models, including benzene.

Table 4.9. *Illustrations corresponding to the guaiacol adsorption on hydroxylated oxide surfaces at i) 90°, ii) 45° and iii) 0° geometries modes.*

	i) 90°	*ii) 45°*	*iii) 0°*
γ-Al_2O_3 (110)	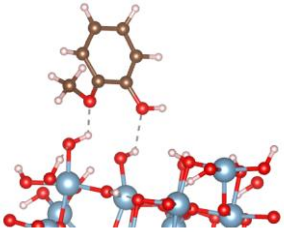	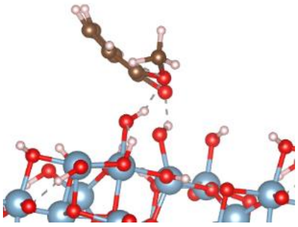	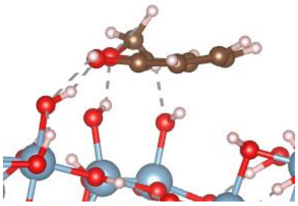
CeO_2 (111)	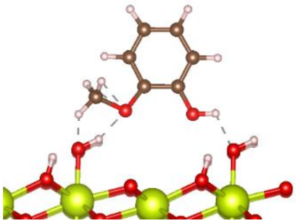	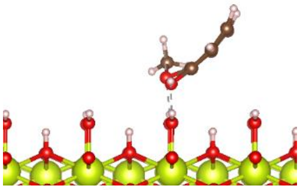	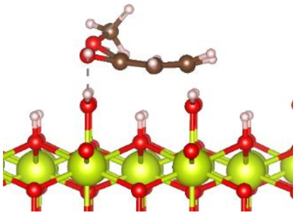
MgO (100)	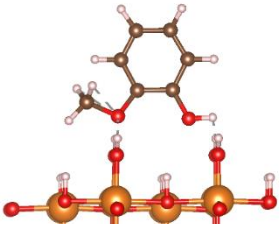	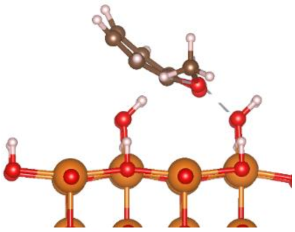	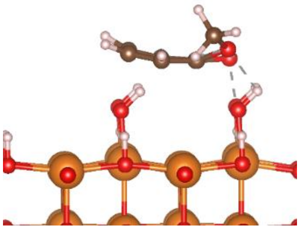
β-SiO_2 (100)	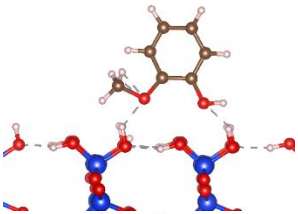	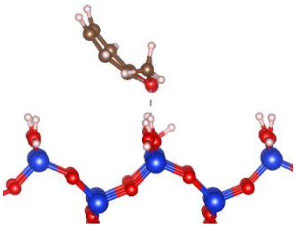	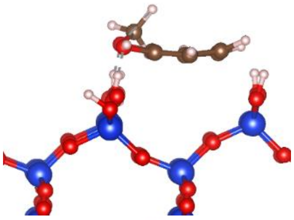
a-TiO_2 (101)	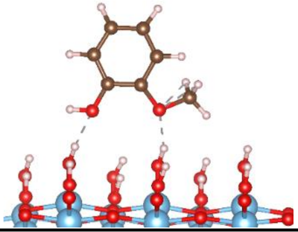	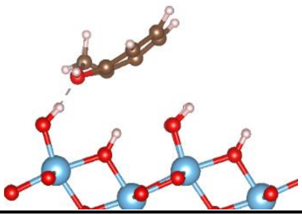	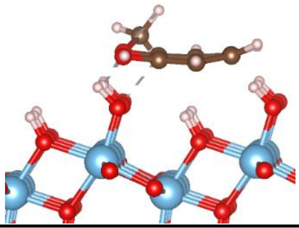

Figure 4.11 summarises the interaction energies depending on the compound’s initial orientations (90°, 45°, 0°). Whereas ***Table 4.10*** shows the properties of the most favourable adsorption modes on the hydroxylated surfaces. The majority of the compounds prefer absorbing parallel to the oxide surfaces rather than perpendicular (90°), which maximises the interaction with the hydroxyl groups on the surface. Indeed, structures such as catechol have established a strong affinity for hydrophilic surfaces because of their capacity to establish hydrogen bonds. Different experimental studies have confirmed the involvement of hydrogen bonding between the oxy-compounds and the hydroxyl groups from the surface.[113, 114]

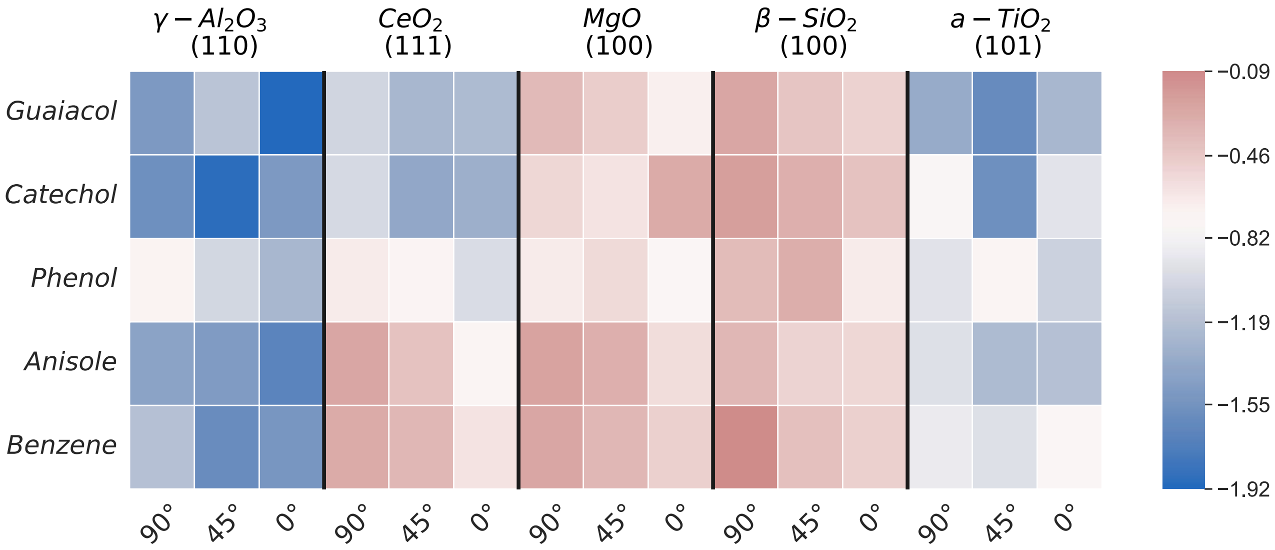

Figure 4.11. *Calculated adsorption energy (E_{ads}) of guaiacol, catechol, phenol, anisole and benzene at different geometry modes for hydroxylated oxide surfaces.*

For *γ-Al_2O_3 (110)*, the model compounds’ interaction with hydroxylated surfaces is slightly more favourable than with clean surfaces, although both expose the Al_{3c} site. Increasing O atoms’ basicity upon hydroxylated ($\Delta\varepsilon_{VB}$ = 0.42 eV) creates new Al−O pairs with more labile than clean surfaces. Hence, guaiacol presents a stronger interaction with the hydroxylated γ-Al_2O_3 at 0° (E_{ads} = −1.91 eV) compared to the pristine surface at 45° (E_{ads} = −1.78 eV). The most notable increase is with anisole, strengthening the interaction between the hydroxylated surface and the molecule by around 8.3% (E_{ads} = −1.69 eV) rather than the clean surface. These results are similar to previous studies, concluding that the OH and H’s distribution over the clean surface does not block Al sites and strengthen the hydrogen bonds with the π−system of the oxy-compounds.[96, 115]

Similar results were found for *CeO_2 (111)*, where the compounds' interactions with the hydroxylated CeO_2 are slightly stronger than the pristine surface (by ~ 19%). These results suggest that incorporating OH and H on CeO_2 improves the interaction at low hydroxyl coverage with a minimal decrease in acidity ($\Delta\varepsilon_{CB}$ = 0.07 eV) and a moderate reduction of basicity ($\Delta\varepsilon_{VB}$ = −0.16 eV). All the compounds prefer the parallel orientation with the surface except for guaiacol and catechol, which remain at 45°.

Table 4.10. *Calculated adsorption energies (E_{ads}), distance molecular oxygen-surface (d) and Bader charge (q) for the most favourable geometries modes for the hydroxylated oxide surfaces.*

		γ-Al_2O_3 (110)	*CeO_2 (111)*	*MgO (100)*	*β-SiO_2 (100)*	*a-TiO_2 (101)*
Guaiacol	*Initial angle (°)*	0°	45°	0°	0°	45°
	E_{ads} (eV)	−1.91	−1.26	−0.69	−0.51	−1.62
	d-O_1 (−OH) (Å)	2.51	1.60	1.57	2.21	2.12
	d-O_2 (−OCH_3) (Å)	2.30	2.30	2.38	2.22	1.95
	q $\|e^-\|$	0.92	0.60	0.60	0.54	0.64
Catechol	*Initial angle (°)*	45°	45°	45°	0°	45°
	E_{ads} (eV)	−1.89	−1.38	−0.61	−0.42	−1.59
	d-O_{1A} (−OH) (Å)	1.78	1.67	1.63	2.26	1.63
	d-O_{1B} (−OH) (Å)	1.89	1.65	1.51	2.11	1.97
	q $\|e^-\|$	0.30	0.31	0.69	0.57	0.15
Phenol	*Initial angle (°)*	0°	0°	0°	0°	0°
	E_{ads} (eV)	−1.26	−0.98	−0.75	−0.65	−1.05
	d-O_1 (−OH) (Å)	2.04	1.52	1.51	1.87	1.93
	q $\|e^-\|$	0.32	0.48	0.27	0.40	0.63
Anisole	*Initial angle (°)*	0°	0°	0°	0°	45°
	E_{ads} (eV)	−1.69	−0.74	−0.57	−0.54	−1.23
	d-O_2 (−OCH_3) (Å)	2.02	2.28	2.24	1.94	2.18
	q $\|e^-\|$	0.27	0.08	0.14	0.58	0.40
Benzene	*Initial angle (°)*	45°	0°	0°	0°	45°
	E_{ads} (eV)	−1.61	−0.61	−0.50	−0.50	−0.96
	q $\|e^-\|$	0.39	0.04	0.06	0.84	0.32

The most dramatic increases in interaction with the oxy-compounds are seen for hydroxylated *a-TiO₂ (101)*. Like CeO_2, the hydroxylated a-TiO_2 did not show a considerable difference in the acid/base properties. Its Lewis acid strength decreases ($\Delta\varepsilon_{CB}$ = 0.20 eV), and its Lewis basicity increases ($\Delta\varepsilon_{VB}$ = 0.14 eV). These results suggest that *Ti-d* orbitals metal oxide's interaction with HOMO from the molecule is stronger than *p* oxides. For example, anisole has the highest adsorption orientation at 45° (E_{ads} = −1.23 eV), indicating that the methoxy group interacts strongly with the surface shown in previous studies.[116] The lack of trends between charge transfer and adsorption energy suggests that the surface terminal hydroxyl groups significantly impact the interaction with the aromatic ring and the molecule's oxo group(s). Previous studies have indicated that the active sites of TiO_2 are strictly linked to the contact with the water, favouring the direct deoxygenation mechanism of phenolic compounds due to the cleavage of the C−OH bond.[117, 118]

Upon hydroxylation, *β-SiO_2 (100)* leads to the formation of germinal silanol groups, Si-$(OH)_2$, providing new sites responsible for the adsorption of the compounds, which reduces the acid character ($\Delta\varepsilon_{VB}$ = −0.19 eV).[87] The most favourable interaction between the surface and lignols is at 0°, exposing the phenyl ring to the hydroxyl groups. For example, the highest adsorption energy in catechol is at 0° with an E_{ads} = −0.42 eV, while the weaker interaction is through the OH groups, E_{ads} = −0.21 eV. The hydroxyl groups act as new active sites that create long-range hydrogen bonds with the π-system of the model compounds.[119] *MgO (100)* is the only oxide examined that, upon hydroxylation, reduces its affinity to interact with the phenolic compounds between 9% and 46%. Catechol is the most notorious case among all the compounds studied. These results can be explained because the clean MgO basicity *(100)* is lower than the hydroxylated surface ($\Delta\varepsilon_{VB}$ = −1.87 eV).[120, 121]

Figure 4.12 shows the relation of the adsorption energies with the valence (ε_{VB}) and conduction (ε_{CB}) band centres, i.e. the oxides' acid-base properties. As expected, no clear trend can be seen between the acid site (Mg cation) and the compounds rather than the base site (O^{2-} site), meaning that the Lewis basicity controls the interaction with the compounds.

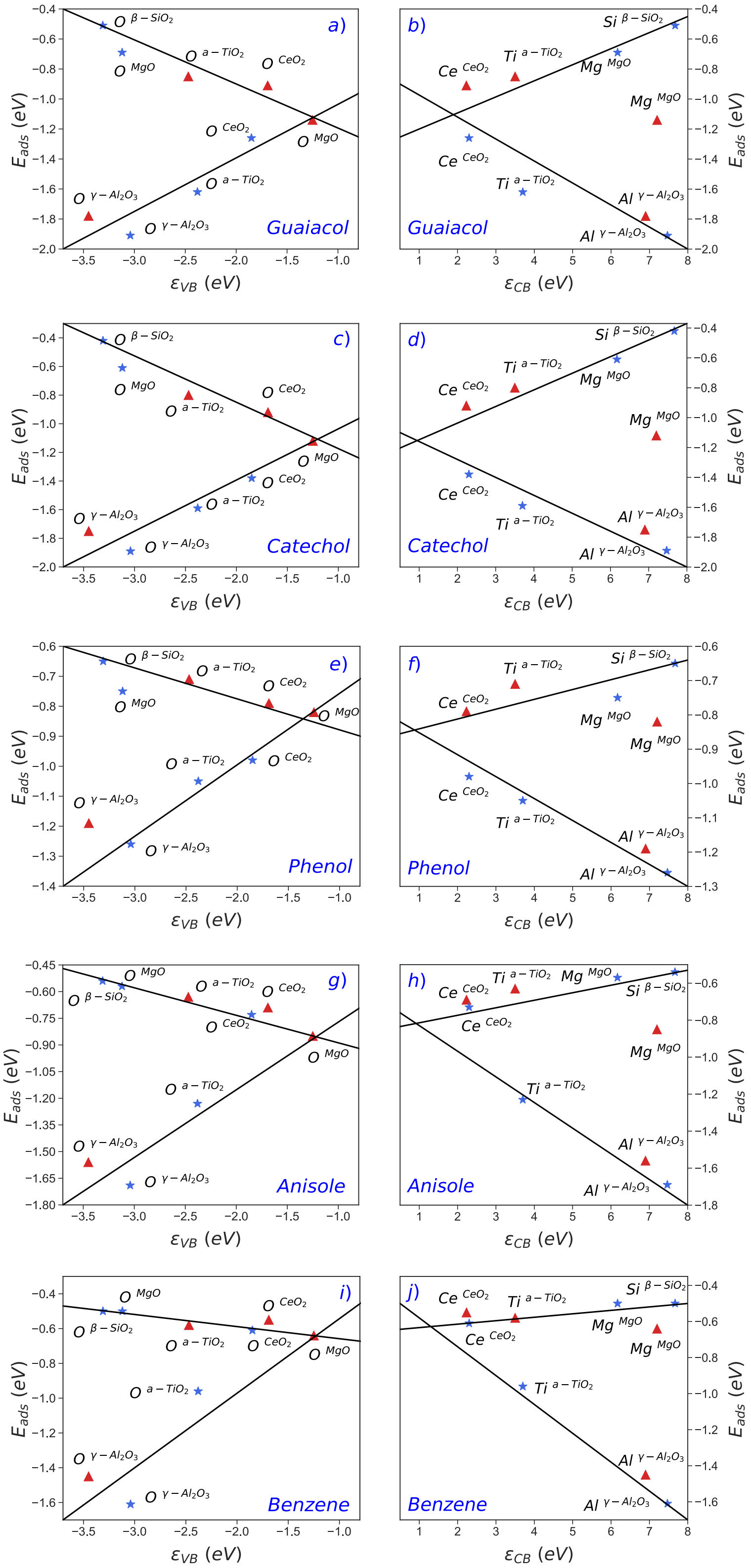

Figure 4.12. *Adsorption energies for (a-b) guaiacol, (c-d) catechol, (e-f) phenol, (g-h) anisole and (i-j) benzene versus band centres (ε_{VB} and ε_{CB}) for the five oxide surfaces (clean and hydroxylated). Colour code: red triangle (▲) and blue star (★) represents the clean and the hydroxylated oxide surfaces, respectively. Black trend lines are inset to guide the eye.*

The results confirm that the hydroxyl groups shield the adsorption sites of the surface (base site), which weakens their adsorption capabilities. The ε_{VB} linear trend, related to the occupied *O-2p* orbitals of the surface, is a good descriptor based on the Lewis basicity properties. The trends confirm that a decrease in basicity character strengthens the interaction with the phenolic compounds. Similarly, ε_{CB} is linearly related to the adsorption energy, although less reliable when including *d* and *f* orbitals, further modifying the oxides' ionic-covalent character.[110]

4.4 Chapter conclusion

This chapter studied the adsorption of five compounds derived from lignin, e.g. guaiacol, catechol, phenol, anisole, and benzene, on clean and hydroxylated oxide surfaces using a periodic DFT study (GGA-RPBE). The oxide surfaces, including acid−base and reducible properties, e.g. *γ-*Al_2O_3 *(110)*, CeO_2 *(111), MgO (100), β-*SiO_2 *(100)* and *a-*TiO_2 *(101)*, were selected for this study as candidates to support HDO catalysts.

The results confirm that clean *γ-*Al_2O_3 *(110)* is the support with the highest affinity to oxygen and all the oxygen compounds due to its high Lewis acidity. The hydroxylation of the surfaces was introduced to simulate more realistic scenarios. The effect of the surface hydroxylation process slightly increases the adsorption strength with all the compounds studied. The molecules generally adopt a parallel orientation with the surface, maximising the interaction between the molecular π-system and the dangling orbitals at the surface. These results confirm that the interaction with the oxy compounds behaves differently for clean and hydroxylated oxide surfaces. Conduction and valence band centres as a Lewis descriptor were introduced to study the Lewis acid-base properties in clean and hydroxylated surfaces. The results clarified the acid, amphoteric and base behaviours of the oxides. Besides, the electronic structure provided insights into the surface's ionic/covalent character. Although the *p* oxides results, e.g. γ-Al_2O_3, β-SiO_2 and MgO, are not comparable with CeO_2 and a-TiO_2 as the participating band is formed by *d* and *f* bands.

The hydroxylation process makes a significant impact on *γ-Al_2O_3 (110), β-SiO_2 (100)* and *CeO_2 (111)*, while a considerable improvement was seen on *a-TiO_2 (101)*. On *MgO (100)*, incorporating hydroxyl groups did not increase the interaction with oxy compounds. On the contrary, the hydroxylation process reduces oxygen compounds' affinity by 46%. This indicates that the basic site (O^{2-}) is responsible for the adsorption of oxygen compounds. For *CeO_2 (111), β-SiO_2 (100)* and *γ-Al_2O_3 (110)*, the effect of the surface hydroxylation process slightly increases the interaction strength with all the compounds studied. The main interaction with the molecules and the π-system at the molecule ring is through the metal on the surface. For *γ-Al_2O_3 (110)*, the Lewis acid-base descriptors show that the acidity decreases upon hydroxylation, proving that the Al_{3C} site exists at a moderate hydroxyl coverage.

For *a-TiO_2 (101)*, the OH groups from the hydroxylated process create stronger bonds with the aromatic ring of the compounds (π-hydrogen bonds). This increases the adsorption energy due to the strength of the π-hydrogen bonds compared to the interaction of the coordinated oxygen atoms of the clean surface (anion-π bonds). These results confirm that the interaction with the oxy compounds behaves differently for clean and hydroxylated oxide surfaces. An oxide-support interaction that is neither too weak nor too strong will avoid high activation barriers and low reactivity. Although weak Lewis acidity supports are favourable to avoid coke formation, there are limitations between the surface bonding and the studied descriptors to predict the reaction rate for undesired reactions.

4.5 References

1. F. Morteo-Flores, J. Engel and A. Roldan, *Philosophical Transactions of the Royal Society A*, 2020, **378**, 20200056.
2. J. Engel, S. Francis and A. Roldan, *Physical Chemistry Chemical Physics*, 2019, **21**, 19011-19025.
3. J. W. M. Crawley, et al., *Chemical Reviews*, 2022, **122 (6)**, 6795-6849.
4. G. Hernández Cedeño, R. Silva-Rodrigo, A. Guevara-Lara, J. A. Melo-Banda, A. Torre, F. Morteo and A. Castillo-Mares, *Catalysis Today*, 2015, **271**.
5. T. Samadhi, S. Subagjo, K. R. Lismana and K. Fuadi, *Journal of Engineering and Technological Sciences* 2011, **43**, 113-126.
6. E.-M. Ryymin, M. L. Honkela, T.-R. Viljava and A. O. I. Krause, *Applied Catalysis A: General*, 2010, **389**, 114-121.

7. A. Y. Bunch and U. S. Ozkan, *Journal of catalysis*, 2002, **206**, 177-187.
8. T.-R. Viljava, S. Komulainen, T. Selvam and A. Krause, in *Studies in surface science and catalysis*, Elsevier, 1999, vol. 127, pp. 145-152.
9. T.-R. Viljava, R. Komulainen and A. Krause, *Catalysis Today*, 2000, **60**, 83-92.
10. E. Laurent and B. Delmon, *Journal of Catalysis*, 1994, **146**, 281-291.
11. O. Şenol, T.-R. Viljava and A. Krause, *Catalysis Today*, 2005, **106**, 186-189.
12. X. Zhang, W. Tang, Q. Zhang, T. Wang and L. Ma, *Energy Procedia*, 2017, **105**, 518-523.
13. S. Mahamulkar, K. Yin, M. T. Claure, R. J. Davis, L. Li, H. Shibata, A. Malek, C. W. Jones and P. K. Agrawal, *Fuel*, 2018, **218**, 357-365.
14. Y. Yang, A. Gilbert and C. C. Xu, *Applied Catalysis A: General*, 2009, **360**, 242-249.
15. J. Zhang, C. Li, X. Chen, W. Guan and C. Liang, *Catalysis Today*, 2019, **319**, 155-163.
16. T. Nimmanwudipong, R. C. Runnebaum, K. Brodwater, J. Heelan, D. E. Block and B. C. Gates, *Energy & Fuels*, 2014, **28(2)**, 1090-1096.
17. P. Natewong, Y. Murakami, H. Tani and K. Asami, *American Scientific Research Journal for Engineering, Technology, and Sciences (ASRJETS)*, 2016, **22**, 153-165.
18. W. Wang, K. Wu, P. Liu, L. Li, Y. Yang and Y. Wang, *Industrial & Engineering Chemistry Research*, 2016, **55**, 7598-7603.
19. D. Chen, Q. Ma, L. Wei, N. Li, Q. Shen, W. Tian, J. Zhou and J. Long, *Journal of Analytical and Applied Pyrolysis*, 2018, **130**, 169-180.
20. C. Alvarez, K. Cruces, R. Garcia, C. Sepulveda, J. Fierro, I. Ghampson and N. Escalona, *Applied Catalysis A: General*, 2017, **547**, 256-264.
21. P. Shen, R. Wei, M. Y. Zhu, D. Pan, S. Xu, L. Gao and G. Xiao, *ChemistrySelect*, 2018, **3**, 4786-4796.
22. H. Shafaghat, Y. F. Tsang, J.-K. Jeon, J. M. Kim, Y. Kim, S. Kim and Y.-K. Park, *Chemical Engineering Journal*, 2020, **382**, 122912.
23. S. Cheng, L. Wei, J. Julson and M. Rabnawaz, *Energy conversion and management*, 2017, **150**, 331-342.
24. J.-S. Moon, E.-G. Kim and Y.-K. Lee, *Journal of catalysis*, 2014, **311**, 144-152.
25. X. Zhang, T. Wang, L. Ma, Q. Zhang, Y. Yu and Q. Liu, *Catalysis Communications*, 2013, **33**, 15-19.
26. J. Yang, et al., *Applied Catalysis B: Environmental*, 2017, **201**, 266-277.
27. L. Nie and D. E. Resasco, *Journal of catalysis*, 2014, **317**, 22-29.
28. M. B. Griffin, G. A. Ferguson, D. A. Ruddy, M. J. Biddy, G. T. Beckham and J. A. Schaidle, *ACS Catalysis*, 2016, **6**, 2715-2727.
29. S. Boonyasuwat, T. Omotoso, D. E. Resasco and S. P. Crossley, *Catalysis letters*, 2013, **143**, 783-791.
30. X. Zhang, P. Yan, B. Zhao, K. Liu, M. C. Kung, H. H. Kung, S. Chen and Z. C. Zhang, *ACS Catalysis*, 2019, **9**, 3551-3563.
31. H. Tamura, K. Mita, A. Tanaka and M. Ito, *Journal of colloid and interface science*, 2001, **243**, 202-207.
32. H. Boehm, *Discussions of the Faraday Society*, 1971, **52**, 264-275.
33. G. Kresse and J. Furthmüller, *Computational materials science*, 1996, **6**, 15-50.

34. P. E. Blöchl, *Physical review B*, 1994, **50**, 17953.
35. S. Grimme, S. Ehrlich and L. Goerigk, *Journal of computational chemistry*, 2011, **32**, 1456-1465.
36. D. A. Andersson, S. I. Simak, B. Johansson, I. A. Abrikosov and N. V. Skorodumova, *Physical Review B*, 2007, **75**, 035109.
37. E. S. Ziambaras, Elsebeth, *Physical Review B*, 2003, **68**, 064112.
38. J. P. Perdew, K. Burke and M. Ernzerhof, *Physical review letters*, 1996, **77**, 3865.
39. N. Aaron Deskins, D. Mei and M. Dupuis, *Surface Science*, 2009, **603**, 2793-2807.
40. M. Nolan, S. Grigoleit, D. C. Sayle, S. C. Parker and G. W. Watson, *Surface Science*, 2005, **576**, 217-229.
41. R. Evarestov and A. Bandura, *International journal of quantum chemistry*, 2004, **100**, 452-459.
42. D.-N. Zhang, L. Zhao, J.-F. Wang and Y.-L. Li, *Surface Review and Letters*, 2015, **22**, 1550037.
43. T. Demuth, Y. Jeanvoine, J. Hafner and J. Angyan, *Journal of Physics: Condensed Matter*, 1999, **11**, 3833.
44. C. Arasa, P. Gamallo and R. Sayós, *The Journal of Physical Chemistry B*, 2005, **109**, 14954-14964.
45. S. Singh and M. N. Tripathi, *Pramana*, 2017, **89**, 5.
46. Y.-H. Lu and H.-T. Chen, *Physical Chemistry Chemical Physics*, 2015, **17**, 6834-6843.
47. M. Digne, P. Sautet, P. Raybaud, P. Euzen and H. Toulhoat, *Journal of Catalysis*, 2004, **226**, 54-68.
48. G. Gutiérrez, A. Taga and B. Johansson, *Physical Review B*, 2001, **65**, 012101.
49. B. Huang, R. Gillen and J. Robertson, *The Journal of Physical Chemistry C*, 2014, **118(42)**, 24248-24256.
50. P. Quaino, O. Syzgantseva, L. Siffert, F. Tielens, C. Minot and M. Calatayud, *Chemical Physics Letters*, 2012, **519-520**, 69-72.
51. T. Bredow and A. R. Gerson, *Physical Review B*, 2000, **61**, 5194.
52. A. Del Vitto, G. Pacchioni, F. Delbecq and P. Sautet, *The Journal of Physical Chemistry B*, 2005, **109**, 8040-8048.
53. E. Finazzi, C. Di Valentin, G. Pacchioni and A. Selloni, *The Journal of chemical physics*, 2008, **129**, 154113.
54. A. H. Larsen, et al., *Journal of Physics: Condensed Matter*, 2017, **29**, 273002.
55. J. Gu, J. Wang and J. Leszczynski, *ACS Omega*, 2018, **3**, 1881-1888.
56. P. Nortier, P. Fourre, A. M. Saad, O. Saur and J. Lavalley, *Applied Catalysis*, 1990, **61**, 141-160.
57. R. Wischert, C. Copéret, F. Delbecq and P. Sautet, *Angewandte Chemie*, 2011, **123**, 3260-3263.
58. M. Nolan, S. C. Parker and G. W. Watson, *Surface Science*, 2005, **595**, 223-232.
59. J. P. Allen, S. C. Parker and D. W. Price, *The Journal of Physical Chemistry C*, 2009, **113**, 8320-8328.

60. Z. Zhao, Z. Li and Z. Zou, *Journal of Physics: Condensed Matter*, 2010, **22**, 175008.
61. O. D. Feya, Q. Wang, S. V. Lepeshkin, V. S. Baturin, Y. A. Uspenskii and A. R. Oganov, *Scientific reports*, 2018, **8**, 1-9.
62. J. Yang, H. Wang, X. Zhao, Y. Li and W. Fan, *RSC Advances*, 2016, **6**, 40459-40473.
63. K. Sohlberg, S. J. Pennycook and S. T. Pantelides, *Journal of the American Chemical Society*, 1999, **121**, 10999-11001.
64. G. Spezzati, et al., *Applied Catalysis B: Environmental*, 2019, **243**, 36-46.
65. C. Downing, A. Sokol and C. Catlow, *Physical Chemistry Chemical Physics*, 2014, **16**, 184-195.
66. M. Yazdanmehr, S. J. Asadabadi, A. Nourmohammadi, M. Ghasemzadeh and M. Rezvanian, *Nanoscale research letters*, 2012, **7**, 1-10.
67. M. El Khalifi, F. Picaud and M. Bizi, *Analytical Methods*, 2016, **8**, 5045-5052.
68. M. Fernandez-Garcia, A. Martinez-Arias, J. Hanson and J. Rodriguez, *Chemical reviews*, 2004, **104**, 4063-4104.
69. S. Heo, E. Cho, H.-I. Lee, G. S. Park, H. J. Kang, T. Nagatomi, P. Choi and B.-D. Choi, *AIP Advances*, 2015, **5**, 077167.
70. S. Kohiki, M. Arai, H. Yoshikawa and S. Fukushima, *The Journal of Physical Chemistry B*, 1999, **103**, 5296-5299.
71. R. Asahi, Y. Taga, W. Mannstadt and A. J. Freeman, *Physical Review B*, 2000, **61**, 7459.
72. H. P. Pinto, R. M. Nieminen and S. D. Elliott, *Physical review b*, 2004, **70**, 125402.
73. N. Martsinovich, D. R. Jones and A. Troisi, *The Journal of Physical Chemistry C*, 2010, **114**, 22659-22670.
74. Y. Xu, W.-K. Chen, S.-H. Liu, M.-J. Cao and J.-Q. Li, *Chemical physics*, 2007, **331**, 275-282.
75. A. Jain, et al., *Apl Materials*, 2013, **1**, 011002.
76. N. Kamarulzaman, D. Mustaffa, N. Chayed, N. Badar, M. Taib and A. Ibrahim, *Applied Nanoscience*, 2018, **8**, 1621-1628.
77. Y. Irokawa and M. Usami, *Sensors*, 2015, **15**, 14757-14765.
78. G. Zhang, X. Wang, Y. Xiong, Y. Shi, J. Song and D. Luo, *International journal of hydrogen energy*, 2013, **38**, 1157-1165.
79. M. A. Christiansen, G. Mpourmpakis and D. G. Vlachos, *ACS Catalysis*, 2013, **3**, 1965-1975.
80. Z. Chafi, N. Keghouche and C. Minot, *Physics Procedia*, 2009, **2**, 673-676.
81. O. Matz and M. Calatayud, *ACS omega*, 2018, **3**, 16063-16073.
82. D. Mei, N. A. Deskins, M. Dupuis and Q. Ge, *The Journal of Physical Chemistry C*, 2007, **111**, 10514-10522.
83. I. A. Pašti, M. Baljozović and N. V. Skorodumova, *Surface Science*, 2015, **632**, 39-49.
84. I. E. Castelli, S. G. Soriga and I. C. Man, *The Journal of chemical physics*, 2018, **149**, 034704.
85. L. Kantorovich, M. Gillan and J. White, *Journal of the Chemical Society, Faraday Transactions*, 1996, **92**, 2075-2080.

86. G. Geneste, J. Morillo and F. Finocchi, *The Journal of chemical physics*, 2005, **122**, 174707.
87. J. Yang, S. Meng, L. Xu and E. Wang, *Physical Review B*, 2005, **71**, 035413.
88. M. M. Islam, M. Calatayud and G. Pacchioni, *The Journal of Physical Chemistry C*, 2011, **115**, 6809-6814.
89. A. Hussain, J. Gracia, B. E. Nieuwenhuys and J. H. Niemantsverdriet, *ChemPhysChem*, 2010, **11**, 2375-2382.
90. W. Zeng, T. Liu, Z. Wang, S. Tsukimoto, M. Saito and Y. Ikuhara, *Materials transactions*, 2010, **51**, 171-175.
91. Z. He and X. Wang, *Catalysis for sustainable energy*, 2012, **1**, 28-52.
92. P. M. Kowalski, B. Meyer and D. Marx, *Physical Review B*, 2009, **79**, 115410.
93. J. Scaranto and S. Giorgianni, *Molecular Physics*, 2009, **107**, 1997-2003.
94. S. Iarlori, D. Ceresoli, M. Bernasconi, D. Donadio and M. Parrinello, *The Journal of Physical Chemistry B*, 2001, **105**, 8007-8013.
95. M. Digne, P. Sautet, P. Raybaud, P. Euzen and H. Toulhoat, *Journal of Catalysis*, 2002, **211**, 1-5.
96. R. Wischert, P. Laurent, C. Copéret, F. Delbecq and P. Sautet, *Journal of the American Chemical Society*, 2012, **134**, 14430-14449.
97. R.-P. Ren, X.-W. Liu, Z.-J. Zuo and Y.-K. Lv, *RSC Advances*, 2015, **5**, 55372-55382.
98. M. Corral Valero, P. Raybaud and P. Sautet, *The Journal of Physical Chemistry B*, 2006, **110**, 1759-1767.
99. H.-L. Chen and H.-T. Chen, *Chemical Physics Letters*, 2010, **493**, 269-272.
100. M. Stirniman, C. Huang, R. Scott Smith, S. Joyce and B. D. Kay, *The Journal of chemical physics*, 1996, **105**, 1295-1298.
101. X. Rozanska, F. Delbecq and P. Sautet, *Physical Chemistry Chemical Physics*, 2010, **12**, 14930-14940.
102. C. Arrouvel, M. Digne, M. Breysse, H. Toulhoat and P. Raybaud, *Journal of Catalysis*, 2004, **222**, 152-166.
103. D. Zhang, M. Yang and S. Dong, *The Journal of Physical Chemistry C*, 2015, **119**, 1451-1456.
104. R. Salomão, C. Arruda and M. L. Antunes, *Interceram-International Ceramic Review*, 2020, **69**, 52-62.
105. S. Chatterji, *Cement and Concrete Research*, 1995, **25**, 51-56.
106. G.-M. Rignanese, A. De Vita, J.-C. Charlier, X. Gonze and R. Car, *Physical Review B*, 2000, **61**, 13250.
107. J. A. Duffy, *Journal of Chemical Education*, 1996, **73**, 1138.
108. P. Hirunsit, T. Toyao, S. H. Siddiki, K. Shimizu and M. Ehara, *ChemPhysChem*, 2018, **19**, 2848-2857.
109. G. R. Jenness, M. A. Christiansen, S. Caratzoulas, D. G. Vlachos and R. J. Gorte, *The Journal of Physical Chemistry C*, 2014, **118**, 12899-12907.
110. E. Bordes-Richard and P. Courtine, in *Metal Oxides*, CRC Press, 2005, pp. 341-374.
111. O. Matz and M. Calatayud, *The Journal of Physical Chemistry C*, 2017, **121**, 13135-13143.

112. F. Allegretti, S. O'brien, M. Polcik, D. I. Sayago and D. P. Woodruff, *Physical review letters*, 2005, **95**, 226104.
113. J. Saiz-Poseu, J. Mancebo-Aracil, F. Nador, F. Busqué and D. Ruiz-Molina, *Angewandte Chemie International Edition*, 2019, **58**, 696-714.
114. M. B. McBride and L. G. Wesselink, *Environmental science & technology*, 1988, **22**, 703-708.
115. S. Roy, G. Mpourmpakis, D.-Y. Hong, D. G. Vlachos, A. Bhan and R. Gorte, *ACS Catalysis*, 2012, **2**, 1846-1853.
116. H. Yuzawa, M. Aoki, K. Otake, T. Hattori, H. Itoh and H. Yoshida, *The Journal of Physical Chemistry C*, 2012, **116**, 25376-25387.
117. J. Mao, et al., *ACS Catalysis*, 2017, **7**, 695-705.
118. R. C. Nelson, B. Baek, P. Ruiz, B. Goundie, A. Brooks, M. C. Wheeler, B. G. Frederick, L. C. Grabow and R. N. Austin, *ACS Catalysis*, 2015, **5**, 6509-6523.
119. S. Shylesh, D. Hanna, J. Gomes, C. G. Canlas, M. Head-Gordon and A. T. Bell, *ChemSusChem*, 2015, **8**, 466-472.
120. C. Chizallet, G. Costentin, H. Lauron-Pernot, J. M. Krafft, P. Bazin, J. Saussey, F. Delbecq, P. Sautet and M. Che, *Oil & Gas Science and Technology-Revue de l'IFP*, 2006, **61**, 479-488.
121. T. Iizuka, H. Hattori, Y. Ohno, J. Sohma and K. Tanabe, *Journal of Catalysis*, 1971, **22**, 130-139.

5

Mechanism and trends of Guaiacol HDO on transition metal catalysts

5.1 Introduction

As discussed in Chapter 1, transition metals (TMs) such as Ni and Co have emerged as alternative candidates due to their abundance and performance in hydrogenation reactions, showing different selectivity depending on the reaction temperature, supports and H_2 partial pressure.[1, 2] Based on the results from Chapter 3, six metal surfaces, Fe, Co, Ni, Cu, Pd, and Pt, were chosen to study the guaiacol adsorption. Their selection is based on their hydrogen and oxygen intermediate affinity (neither too weak nor too strong), which will overcome the activation barrier and desorb the oxygen-free products.[3]

Among the many species resulting from the pyrolytic treatment, guaiacol (1-hydroxy-2-methoxy benzene) has been used as a primary model compound for HDO investigations. The guaiacol HDO mechanism takes place through three different main pathways to form anisole, phenol and catechol compounds: dehydroxylation ($C_{aryl}-OH$), demethylation ($C_{alkyl}–O$) and demethoxylation ($C_{aryl}-OCH_3$).[4-7] Different HDO experiments on TMs have also highlighted the presence of methane, water, and methanol in the products mixture.[8] Sun *et al*. studied the HDO of guaiacol on TM catalysts supported on carbon, e.g. Cu, Fe, Pd, Pt, and Ru. They found that catechol is the major product, followed by phenol.[9] According to DFT-based simulations on *Pt (111)* [10], the three C−O bonds have different dissociation energies, $C_{aryl}-OH$ (4.97 eV), $C_{aryl}-OCH_3$ (4.44 eV) and $C_{alkyl}–O$ (2.58 eV), being the demethylation route to catechol the most feasible pathway, also in agreement with previous publications.[4, 11, 12] Despite these results, the direct deoxygenation pathway is kinetically hindered [10, 13-16], and co-adsorbed hydrogen on the catalysts is required to facilitate the C−O bond cleavage of oxy−compounds through the activation of the aromatic ring and the deoxygenation reaction.[17, 18]

Chapter 5 provides provide atomistic details on the guaiacol HDO mechanisms on six TM surfaces, *Fe (110), Co (0001), Ni (111), Cu (111), Pd (111) and Pt (111)*. Moreover, reaction schemes based on the guaiacol C−O bond scission are proposed, i.e. (i) C_{aryl}−OH, (ii) C_{aryl}−OCH_3, (iii) C_{alkyl}−O, as the first stage of the hydrogenation process until producing benzene. The different C−O cleave energies are linked through the reaction energy profile, which allows rationalising the catalyst's performances and accelerating the design of new catalysts.

5.2 Computational details

Spin-polarised density functional theory (DFT) calculations on transition metal slab models using the Vienna Ab initio Software Package (VASP).[19] The exchange-correlation contributions were calculated using the generalised gradient approximation (GGA) with the revised functional of Perdew-Burke-Ernzerhof (RPBE).[3] The core electrons were described using the Projected Augmented Wave (PAW) formalism [20], and a kinetic energy cut-off of 550 eV was chosen for the valence electron plane-wave basis set. The zero-damping Grimme’s empirical correction (DFT-D3) accounted for the long-range dispersion interactions.[21] Appropriate dipole correction was used perpendicular to the surfaces upon molecular adsorptions, and the Brillouin zone was sampled with a Monkhorst-Pack 3 x 3 x 1 k-point grid. The convergence criteria were set to −0.03 eV $Å^{-1}$ for the ionic and 10^{-5} eV for the electronic threshold. Slab models were generated with the atomic simulation environment (ASE) based on the optimised bulk lattice parameters.[22] See Chapter 3 for more information about the slab details.

The adsorption energies (E_{ads}) were calculated using *Eq. 5.1* based on the HDO reaction $R{-}OH + H_2 \rightarrow R{-}H + H_2O$ *(Eq. 1.1),* where the E_{system} is the energy of the adsorbate on the slab, the E_{slab} and the $E_{molecule}$ are the energies of the clean surface and the isolated adsorbate, respectively. E_{H_2} is the energy of an isolated H_2 molecule. The half energy of the molecule refers to one H atom, and n is the number of H atoms used in the particular HDO route. For adsorption steps without H_2, $n = 0$.

$$\Delta E = E_{system} - E_{slab} - E_{molecule} - {}^{n}/_{2}\, E_{H_2} \qquad \text{Eq. 5.1}$$

The reaction energy of each reaction step (*E_r; Eq. 5.2*) is given by the difference between the final (*E_{FS}*) and the initial (*E_{IS}*) state energies. The climbing-image nudged elastic band (CI-NEB) [23, 24] and the improved dimer method (DM) were combined to find the saddle points of the transition states (TS) structures, linking the minima across the reaction profile.[25] All transition states have been characterized using vibrational analysis to confirm one imaginary frequency along the reaction coordinate. Activation barrier (*E_a; Eq. 5.3*) is defined as the energy difference between the initial state and the transition state (*E_{TS}*) energies.

$$E_r = E_{FS} - E_{IS} \qquad \text{Eq. 5.2}$$

$$E_a = E_{TS} - E_{IS} \qquad \text{Eq. 5.3}$$

5.3 Results and discussion

5.3.1 Guaiacol adsorption

Fe (110), Co (0001), Ni (111), Cu (111), Pd (111) and *Pt (111)* were investigated using the most stable surfaces according to their intermediate adsorption energies of H, and O. The guaiacol molecule was placed at different adsorption positions (0°, 45° and 90°) on the TMs selected as seen in ***Figure 5.1.***

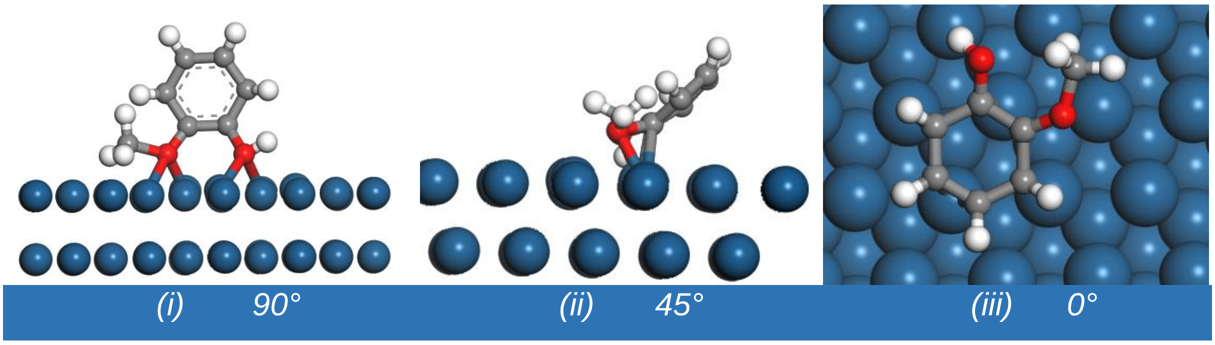

Figure 5.1. *Schematic view of the different guaiacol adsorption on Pt (111) when the molecule is adsorbed in i) parallel (0°), ii) 45° and iii) perpendicular (90°) mode.*

As shown in ***Figure 5.2***, the weakest adsorption is at 90° angle between the surface and the aromatic ring of the substrate, while the strongest is at 0°. This is because a cloud of π−electrons characterises the aromatic ring in the guaiacol; these electrons interact strongly with the surfaces increasing the selectivity and the adsorption energy.

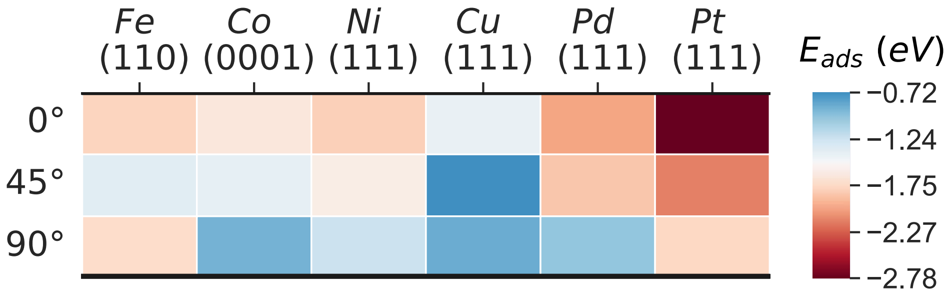

Figure 5.2. *Guaiacol adsorption on metal surfaces at different positions*

After three different guaiacol adsorption modes were investigated on the six transition metal surfaces selected, the parallel configuration was the most favourable in agreement with previous works, ***Figure 5.3***.[10, 26-31] The adsorption sites with the strongest affinity for oxo-groups, i.e. −OH and $-OCH_3$, are seen at the hollow sites. At the same time, the C−C bonds of the aromatic ring prefer the bridge position between metals atoms.[32] In all the cases, the molecule's surface bonding occurs through the ring π-electrons, tilting the H atoms and the oxo groups away from the surface.

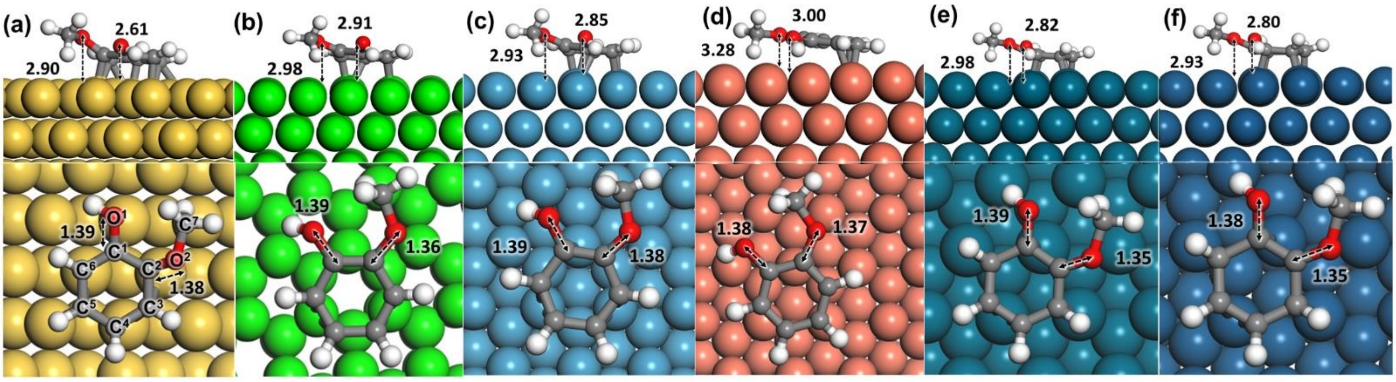

Figure 5.3. *Top and side views of guaiacol adsorbed on (a) Fe (110), (b) Co (0001), (c) Ni (111), (d) Cu (111), (e) Pd (111), and (f) Pt (111); the metal atoms are represented in yellow, light green, blue, orange, dark green, and dark blue colour code, respectively. Red, white, and grey represent oxygen, hydrogen, and carbon. Inset distances are given in Å.*

Table 5.1 shows the guaiacol adsorption energies on the most stable configurations. The most favourable adsorption is on Pt *(111)*, followed by *Pd (111) > Ni (111) > Fe (110) > Co (0001) > Cu (111)*. The guaiacol adsorption energy on *Pt (111)* is 0.37 eV stronger than previously reported [27] because of the different molecular coverage and different GGA pseudopotentials used. The most stable configurations were taken as the initial guaiacol position to study the HDO reaction mechanism towards phenol, anisole, and catechol, in which adsorptions follow the same metal preference as guaiacol. These results compare very well with different works, proving the validity of the selected methodology.[13, 14, 16, 27, 29, 30, 33, 34]

Table 5.1. *Adsorption energy (in eV) for guaiacol, phenol, anisole, and catechol on the TM surfaces obtained in the present work with available theoretical values.*

	Guaiacol		*Phenol*		*Anisole*		*Catechol*	
	This work	*Other theor. works*	*This work*	*Other theor. works*	*This work*	*Other theor. works*	*This work*	*Other theor. works*
Fe (110)	−1.79	−2.01 [26]	−1.84	−1.99 [35]	−1.82	---- *	−1.74	---- *
Co (0001)	−1.64	---- *	−1.57	---- *	−1.67	---- *	−1.68	---- *
Ni (111)	−1.80	−1.76 [29]	−1.70	−1.83 [29]	−1.99	−1.82 [29]	−1.78	−1.83 [29]
Cu (111)	−1.44	−1.90 [30]	−1.21	---- *	−1.31	−0.72 [30]	−1.49	−2.18 [30]
Pd (111)	−2.02	−2.27 [26]	−1.85	−2.23 [35]	−1.75	−1.45 [36]	−2.05	−1.46 [36]
Pt (111)	−2.78	−2.41 [27]	−2.54	−2.26 [37]	−2.67	−2.33 [37]	−2.79	−2.35 [37]

----* = Not available

Note: Calculations from Refs [27, 29, and 37] were conducted at the GGA-PBE level of theory
Calculation from Ref [26] was conducted at the GGA-PW91 level of theory
Calculation from Ref [36] was conducted at the GGA-B3PW91 level of theory
Calculation from Ref [30] was conducted at the GGA-PBE-D2 level of theory
Calculation from Ref [35] was conducted at the GGA-OptB88-vdW level of theory

The interaction between the O atoms in guaiacol and the metal weakens the C−O bonds, indicating the bond activation.[28, 38, 39] The bond lengths within the molecule and the metal surface (M−O) were also examined, proving a clear relationship between the oxophilic nature of the metals with the M−O distances, ***Table 5.2.*** Fe (110) has the shortest M−O distances, d(Fe−OH) = 2.61 Å and d(Fe−OCH$_3$) = 2.90 Å, whereas Cu (111) presents the largest one in the series with a d(Cu−OH) and d(Cu−OCH$_3$) = 3.00 Å and 3.28 Å, respectively. Both metals, Fe and Cu, demonstrated their strong and weak interactions with the oxo-groups. These metals can limit the deoxygenation reaction with an endothermic behaviour and substantial activation barriers according to Sabatier's principle.[29]

Table 5.2. *Bond-length (Å) between the metal surface and carbon (C) and oxygen (O) atoms from the guaiacol molecule. The enumeration of each atom is based on Figure 5.3 (a).*

	Fe (110)	*Co (0001)*	*Ni (111)*	*Cu (111)*	*Pd (111)*	*Pt (111)*
C^1	2.17	2.38	2.13	2.69	2.27	2.12
C^2	2.18	2.46	2.17	2.95	2.43	2.13
C^3	1.95	2.18	2.01	2.81	2.20	2.24
C^4	1.99	2.05	2.03	2.63	2.14	2.14
C^5	1.83	2.04	2.04	2.58	2.14	2.36
C^6	2.07	2.13	2.04	2.69	2.14	2.14
C^7	3.18	3.15	3.11	3.28	3.14	3.22
O^1	2.61	2.91	2.85	3.00	2.82	2.80
O^2	2.90	2.98	2.93	3.28	2.98	2.93

** M = metal surface; C, O = carbon and oxygen from the guaiacol molecule.

Many publications have considered the C−O bond elongation upon the guaiacol adsorption as a descriptor for the deoxygenation activity.[14, 29] The bond activation concept was extended across the oxo−groups in guaiacol, phenol, anisole, and catechol compounds, i.e. (i) $C_{aryl}-OH$, (ii) $C_{aryl}-OCH_3$, and (iii) $C_{alkyl}-O$. The results are found in ***Table 5.3.*** In all cases, $C_{alkyl}-O$ presented the most notorious elongation meaning that, in adsorbed guaiacol, it weakens more than the $C_{aryl}-OCH_3$, which showed little change. These trends agree with the reported $C_{alkyl}-O$ and $C_{aryl}-OCH_3$ dissociation bond energies of 2.58 eV and 4.44 eV, respectively.[4, 40, 41] Namely, the demethylation route producing catechol is the most favourable reaction in all the metals. The results in this work are similar to Liu et al.[14], who studied the guaiacol HDO mechanism over Ni, Pt and Fe-alloyed. They found that $C_{aryl}-OH$ shows the shortest bond elongation (between 1.36 Å – 1.39 Å) compared to $C_{aryl}-OCH_3$ (1.41 Å) on *NiFe (111)* and *PtFe (111)*. These results agree that the bond elongation is related to the dissociation bond energy, where $C_{aryl}-OH$ is the most challenging bond to break (bond dissociation energy = 4.97 eV).[41]

Table 5.3. *Bond distance (in Å) between carbon (C) and the molecular functional groups (i) hydroxyl group (C_{aryl}−OH), (ii) methoxy group (C_{aryl}−OCH_3) and (iii) methyl group (C_{alkyl}−O)*

	Guaiacol*	Fe (110)	Co (0001)	Ni (111)	Cu (111)	Pd (111)	Pt (111)
(i) C_{aryl}−OH	1.383	1.390	1.388	1.389	1.380	1.386	1.383
(ii) C_{aryl}−OCH_3	1.340	1.387	1.363	1.382	1.365	1.351	1.345
(iii) C_{alkyl}−O	1.437	1.444	1.451	1.453	1.453	1.457	1.461

* Guaiacol bond distances as a free molecule.

5.3.2 HDO energy profile

The guaiacol HDO reaction to form benzene may proceed through seven different pathways: the first three pathways are P1: dehydroxylation (DHY), P2: demethoxylation (DMO) and P3: demethylation (DME) pathway, which leads to anisole, phenol, and catechol, respectively. Pathways 4 and 5, denominated as direct deoxygenation (DDO) and demethylation (DME) pathways, convert catechol and anisole into phenol. Finally, pathways 6 and 7 produce benzene as a final product from anisole and phenol through the demethoxylation (DMO) and hydrogenolysis (HGL) routes, respectively, ***Scheme 5.1.***

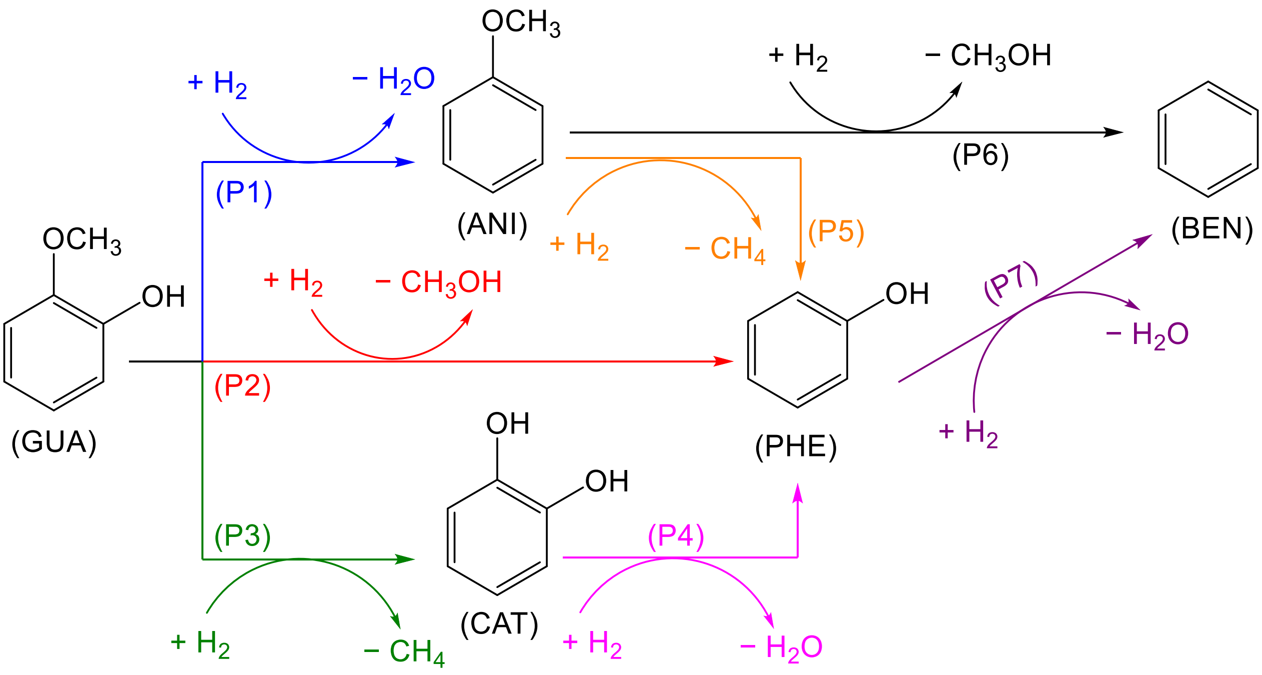

Scheme 5.1. *Proposed reaction network of the guaiacol HDO.*

Table 5.4. Reactions (R) involved in each pathway (P) of the guaiacol conversion. Each reaction presents initial and final states, where the transition state is located between these states.

Pathways (P)	*Reactions (R)*	*Description*
P1 (DHY)	(R1): $C_6H_4(OH)(OCH_3)^* + H^* \rightarrow C_6H_4(OCH_3)^* + OH^* + H^*$	$C_{aryl}-OH$ bond cleavage
	(R2): $C_6H_4(OCH_3)^* + OH^* + H^* \rightarrow C_6H_5(OCH_3)^* + OH^*$	$C_{aryl}-H$ bond formation
	(R3): $C_6H_5(OCH_3)^* + OH^* + H^* \rightarrow C_6H_5\ (OCH_3)^* + H_2O^*$	$O-H$ (H_2O) bond formation
P2 (DMO)	(R4): $C_6H_4(OH)(OCH_3)\ ^* + H^* \rightarrow C_6H_4(OH)^* + OCH_3^* + H^*$	$C_{aryl}-OCH_3$ bond cleavage
	(R5) $C_6H_4(OH)^* + OCH_3^* + H^* \rightarrow C_6H_5(OH)^* + OCH_3^*$	$C_{aryl}-H$ bond formation
	(R6) $C_6H_5(OH)^* + OCH_3^* + H^* \rightarrow C_6H_5(OH)^* + HOCH_3^*$	$O-H$ (CH_3OH) bond formation
P3 (DME)	(R7): $C_6H_4(OH)(OCH_3)^* + H^* \rightarrow C_6H_4(OH)(O)^* + CH_3^* + H^*$	$C_{alkyl}-O$ bond cleavage
	(R8): $C_6H_4(OH)(O)^* + CH_3^* + H^* \rightarrow C_6H_4(OH)(O)^* + CH_4^*$	$C-H$ (CH_4) bond formation
	(R9): $C_6H_4(OH)(O)^* + CH_4^* + H^* \rightarrow C_6H_4(OH)(OH)^*$	$O-H$ (catechol) bond formation
P4 (DDO)	(R10): $C_6H_4(OH)(OH)^* + H^* \rightarrow C_6H_4(OH)^* + OH^* + H^*$	$C_{aryl}-OH$ bond cleavage
	(R11): $C_6H_4(OH)^* + OH^* + H^* \rightarrow C_6H_5(OH)^* + OH^*$	$C_{aryl}-H$ bond formation
	(R12): $C_6H_5(OH)^* + OH^* + H^* \rightarrow C_6H_5(OH)^* + H_2O^*$	$O-H$ (H_2O) bond formation
P5 (DME)	(R13): $C_6H_5(OCH_3)^* + H^* \rightarrow C_6H_5(O)^* + CH_3^* + H^*$	$C_{alkyl}-O$ bond cleavage
	(R14): $C_6H_5(O)^* + CH_3^* + H^* \rightarrow C_6H_5(O)^* + CH_4^*$	$C-H$ (CH_4) bond formation
	(R15): $C_6H_5(O)^* + CH_4^* + H^* \rightarrow C_6H_5(OH)^* + CH_4^*$	$O-H$ (catechol) bond formation
P6 (DMO)	(R16): $C_6H_5(OCH_3)^* + H^* \rightarrow C_6H_5^* + OCH_3^* + H^*$	$C_{aryl}-OCH_3$ bond cleavage
	(R17): $C_6H_5^* + OCH_3^* + H^* \rightarrow C_6H_6^* + OCH_3^*$	$C_{aryl}-H$ bond formation
	(R18): $C_6H_6^* + OCH_3^* + H^* \rightarrow C_6H_6^* + HOCH_3^*$	$O-H$ (CH_3OH) bond formation
P7 (HGL)	(R19): $C_6H_5(OH)^* + H^* \rightarrow C_6H_5^* + OH^* + H^*$	$C_{aryl}-OH$ bond cleavage
	(R20): $C_6H_5^* + OH^* + H^* \rightarrow C_6H_6^* + OH^*$	$C_{aryl}-H$ bond formation
	(R21): $C_6H_6^* + OH^* + H^* \rightarrow C_6H_6^* + H_2O^*$	$O-H$ (H_2O) bond formation

The reaction mechanism starts with the guaiacol molecule adsorption and its partial hydrogenation, activating the phenyl ring. The molecular hydrogen spontaneously dissociates into atoms with transition metals due to its low energy barrier (< 0.1 eV).[42] The co-adsorbed H* (* denotes adsorbed species) promotes the C−O bond scission and saturates the ring dangling bonds. ***Table 5.4*** explains the reactions (R) involved in each of the seven pathways (P) in ***Scheme 5.1***, including the type of reaction, either scission or formation in the guaiacol HDO mechanism.

The first three pathways (P1, P2, P3) were examined on the six transition metal surfaces to identify the most favourable routes and continued the hydrogenation process to yield benzene, ***Figure 5.4***. Upon C–O bond cleavage, H* may prefer to hydrogenate the ring or the cleavage groups forming CH_3OH, CH_4 and H_2O (e.g. $-CH_3$ or $-OH$); ***Table 5.4*** summarise the results on the different alternatives.

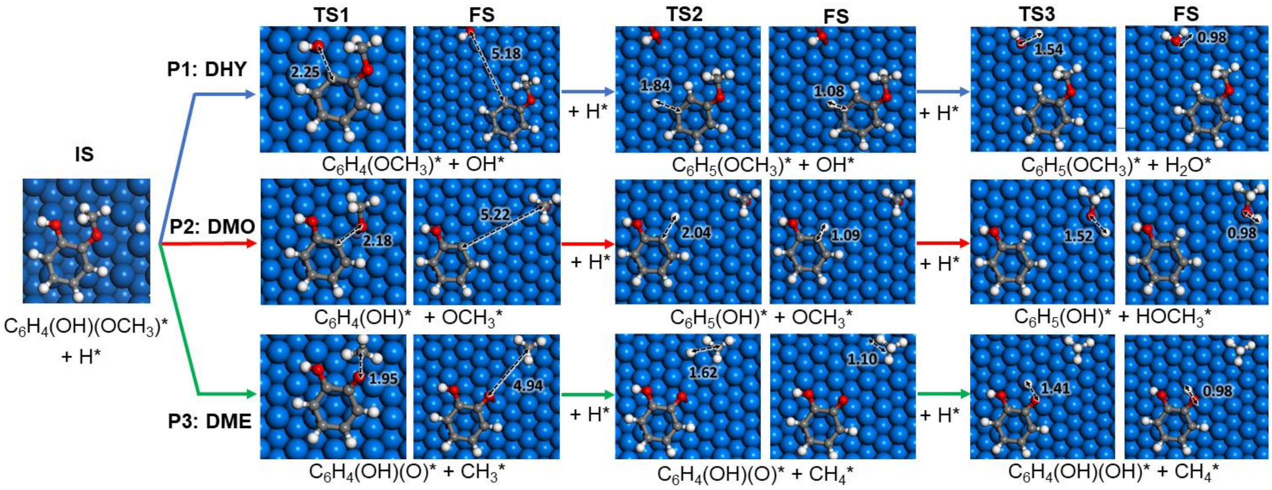

Figure 5.4. *Proposed reaction pathways for the hydrodeoxygenation of guaiacol on Ni (111). Colour scheme: Oxygen, red; hydrogen, white; carbon, grey and nickel, blue. The asterisk (*) denotes adsorbed surface species. Functional groups are denoted in parenthesis.*

5.3.2.1 *Guaiacol dehydroxylation pathway*

The dehydroxylation (DHY) energy profile to produce anisole (P1) is shown in ***Figure 5.5.*** The reaction is initiated with the co-adsorption of H*, which activates the ring, with an electron charge transfer (from 0.37 e^- to 0.09 e^-). This disrupts the aromaticity and weakens the metal-phenolic interaction, provoking the C_{aryl}−OH bond scission, ***Figure 5.4***. The results show that breaking the C_{aryl}−OH bond is exothermic and more likely on oxophilic catalysts. The activation barrier on *Fe (110)* is 1.13 eV, followed by Co > Ni > Pt > Cu > Pd. Indeed, guaiacol dehydroxylation is only exothermic on Fe and Co (E_r = −0.83 eV and −0.18 eV, respectively). The C_{aryl}−OH bond scission creates two co−adsorbed species: 2−methoxyphenyl and hydroxide, ***Table 5.5***.

Table 5.5. *Adsorption energy (in eV) of the formation of a) anisole, phenol, and catechol, or b) water, methanol, and methane for the first three pathways of the guaiacol HDO mechanism.*

Pathways (P)		*Fe (110)*	*Co (0001)*	*Ni (111)*	*Cu (111)*	*Pd (111)*	*Pt (111)*
(P1)	**a:** $C_6H_5(OCH_3)^* + OH^*$	−3.53	−2.92	−2.64	−2.11	−2.17	−2.96
DHY	**b:** $C_6H_4(OCH_3)^* + H_2O^*$	−1.71	−1.82	−1.76	−1.02	−1.54	−1.88
(P2)	**a:** $C_6H_5(OH)^* + OCH_3^*$	−3.61	−2.41	−2.79	−2.16	−2.09	−2.94
DMO	**b:** $C_6H_4(OH)^* + {}^*HOCH_3^*$	−2.22	−1.78	−1.68	−1.22	−1.49	−1.67
(P3)	**a:** $C_6H_4(OH)(OH)^* + CH_3^*$	−2.80	−2.59	−2.33	−1.93	−2.72	−3.38
DME	**b:** $C_6H_4(OH)(O)^* + CH_4^*$	−3.17	−2.73	−2.50	−2.29	−2.81	−3.84

The formation of anisole is more feasible on *Fe (110)*, which activation barrier is only 0.10 eV, followed by Pt, Ni, Pd, Cu, and Co. Finally, the last step is the formation of water as a subproduct. On *Fe (110)*, it is endothermic (E_r = +1.20 eV) and has a considerable activation barrier (E_a = 1.73 eV), thus, becoming the limiting step of the reaction.

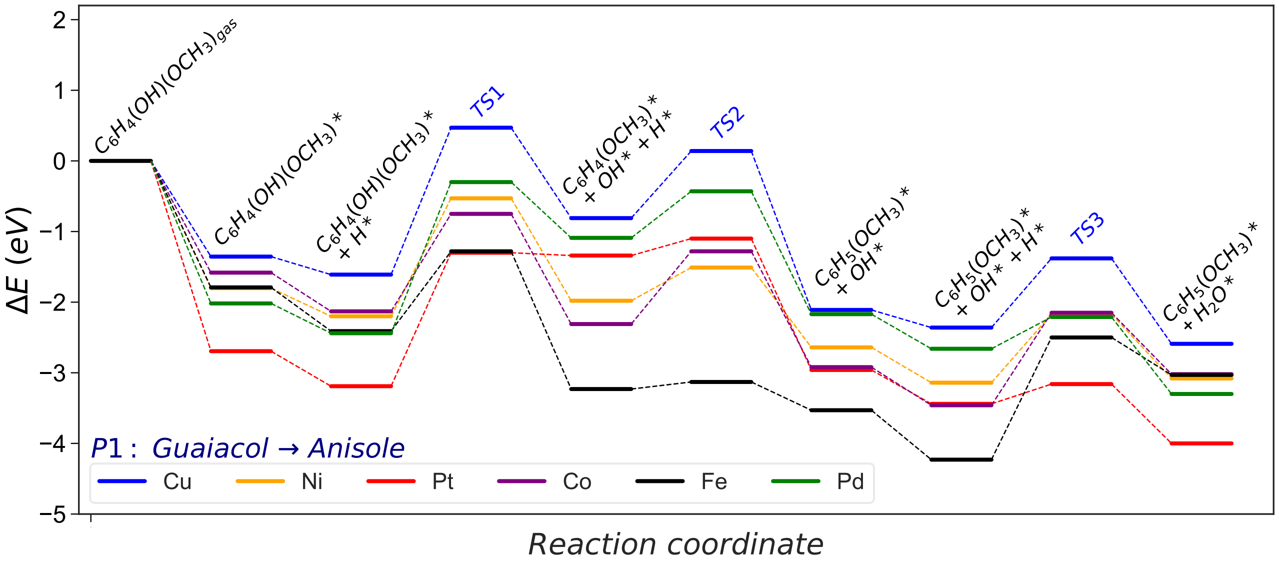

Figure 5.5. *Energy profile of the dehydroxylation (DHY) pathway converting guaiacol into anisole and water. The asterisk (*) represents adsorbed surface species. Molecular functional groups are denoted in parenthesis.*

5.3.2.2 Guaiacol demethoxylation pathway

Pathway 2 (P2) is the demethoxylation reaction (DMO) consisting of the guaiacol conversion to produce phenol and methanol. The energetic profile is shown in ***Figure 5.6***. The reaction pathway starts with the hydrogenation of guaiacol, provoking the C_{aryl}−OCH_3 scission, ***Figure 5.4***. All the selected metals exhibit an endothermic behaviour except Fe (110), which shows an E_r = −0.96 eV and the lowest activation energy (E_a = 1.28 eV) followed by *Co (0001) > Ni (111) > Pt (111) > Pd (111)*, and *Cu (111).*

The breaking of the bond creates two species: 2-hydroxyphenyl and methoxide, ***Table 5.5***. The formation of phenol is less energetically demanding for Ni with an activation barrier of 0.12 eV, followed by Co > Pt > Pd > Fe and Cu. However, the formation of methanol on Fe is also endothermic and kinetically unfavourable (E_r = +1.15 eV and E_a = 1.78 eV). Accordingly, none of the metals explored promotes the demethoxylation pathway due to the high barrier to cleave the $C_{aryl}-OCH_3$ bond and the efficient CH_3OH desorption.

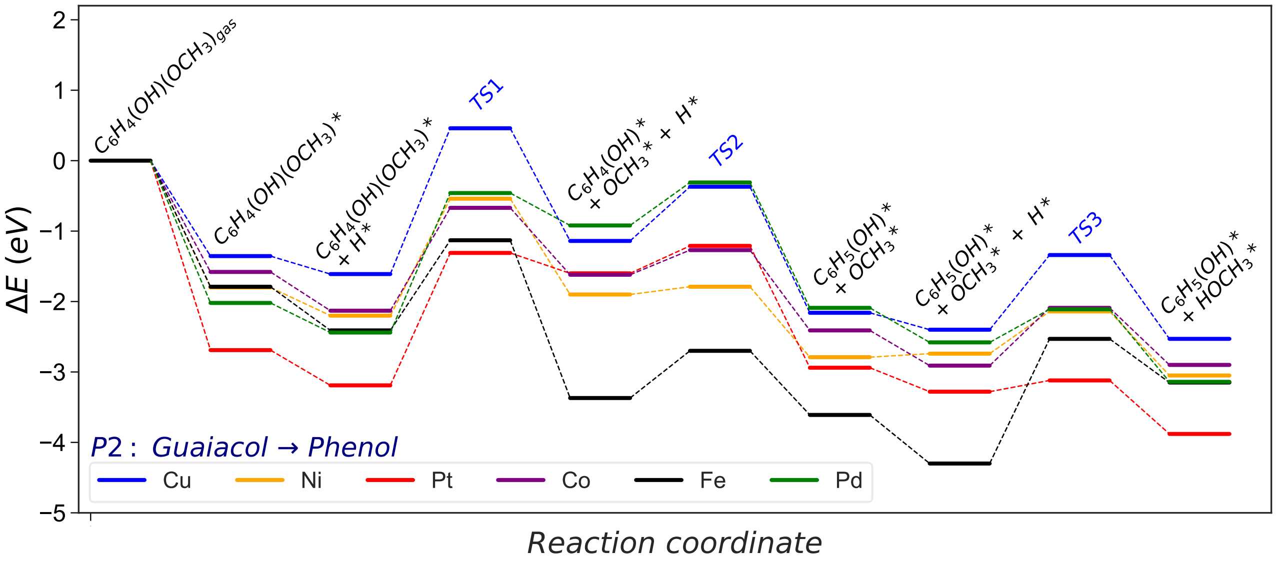

***Figure 5.6**. Energy profile of the demethoxylation (DMO) pathway converting guaiacol into phenol and methanol. The asterisk (*) represents adsorbed surface species. Molecular functional groups are denoted in parenthesis.*

5.3.2.3 Guaiacol demethylation pathway

The demethylation (DME) pathway (P3) converts guaiacol into catechol and methane. The pathway follows the scission of the $C_{alkyl}-O$, as shown in ***Figure 5.7***. ***Figure 5.4*** shows the DME energy profile. All the surfaces exhibit an exothermic behaviour except *Cu (111)* (E_r = +0.04 eV). Indeed, *Co (0001)* and *Ni (111)* present the lowest activation energies (E_a = 1.23 eV and 1.21 eV) for the guaiacol demethylation. The breaking of the bond creates two species: 2-hydroxyphenolate and methyl, ***Table 5.5.*** The results show the most accessible methane formation on *Pt (111)* (E_a = 0.36 eV) followed by Ni > Pd > Cu > Co and Fe; this is due to its good affinity with hydrogen.

The catechol formation dominates the subsequent hydrogenation step, where Ni and Pd present the lowest activation barrier (E_a = 0.62 eV and 0.70 eV). Based on the DME results, metals with an average oxophilic character, like Ni, promote the cleavage of C_{alkyl}−O.

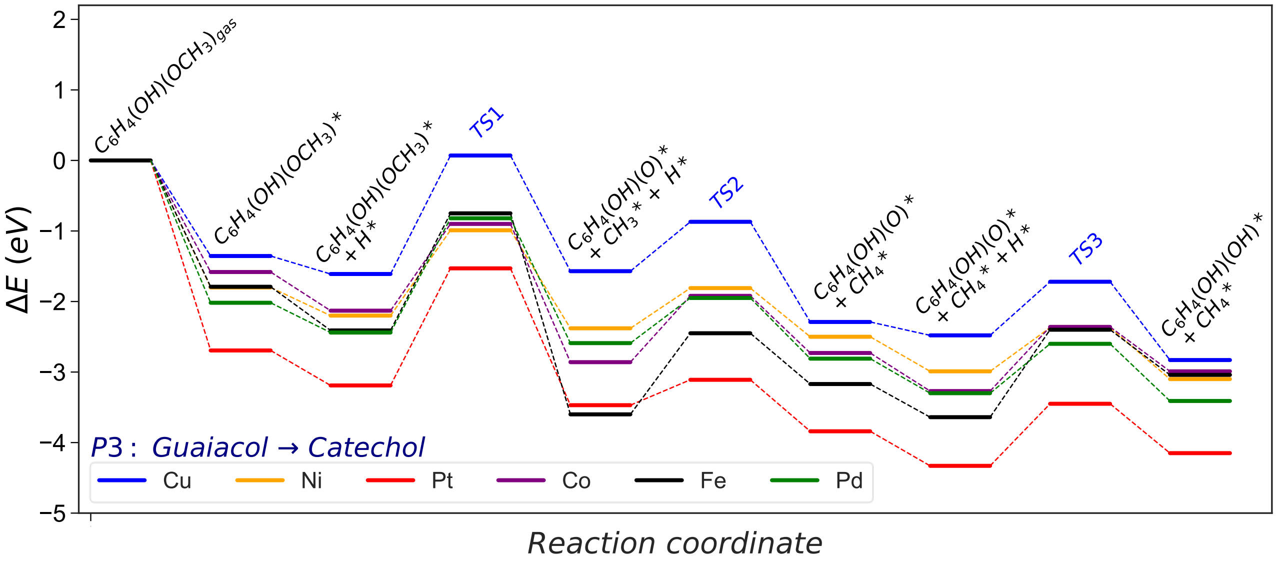

Figure 5.7. *Energy profile of the demethylation (DME) pathway converting guaiacol into catechol and methane. The asterisk (*) represents adsorbed surface species. Molecular functional groups are denoted in parenthesis.*

The energy profiles (***Figure 5.5 − 5.7***) and the results in ***Figure 5.8*** show that guaiacol demethylation (DME) is the most likely pathway on Co, Ni, Cu, Pt, and Pd. It agrees with experimental data in which catechol is the main product of guaiacol partial deoxygenation.[9, 43, 44] Still, it diverges from previous studies suggesting catalysts with optimal oxophilicity and hydrogen affinity will follow the DMO pathway to obtain phenol as a main product [37, 45]. Although *Fe (110)* has the lowest activation barrier and exothermic behaviour, one of the disadvantages of using a highly oxophilic metal is its difficulty desorbing small molecular products, e.g. HO−CH_3, CH_4, and H_2O, which hinders the overall reaction rate. ***Table 5.6*** exhibits the reaction and activation energy for the most favourable pathway for the TM studied.

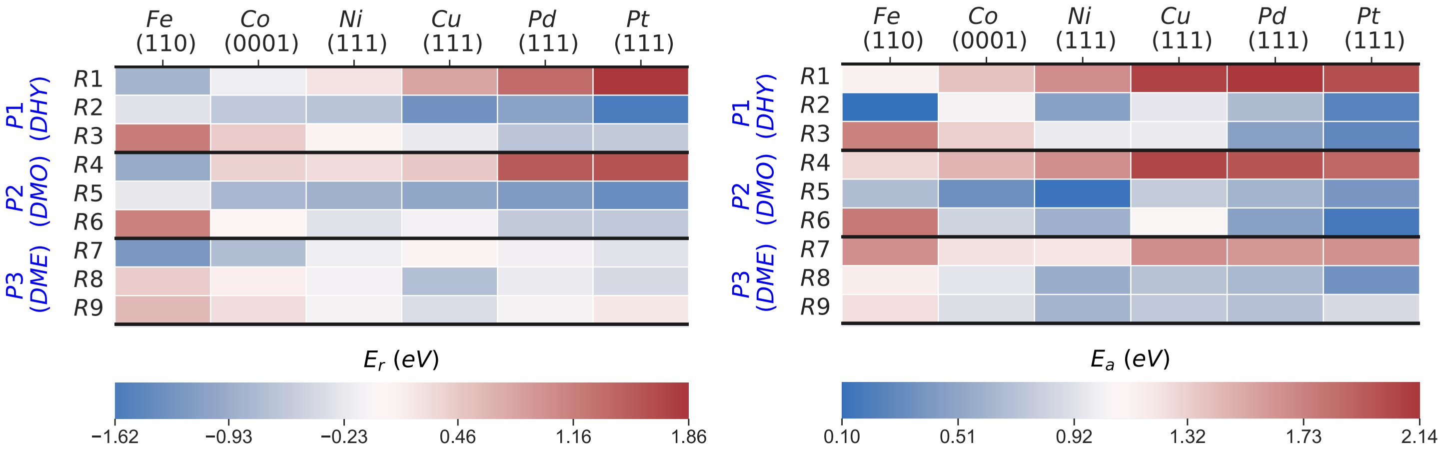

Figure 5.8. *Reaction (E_r, left) and activation energies (E_a, right) in eV of the P1, P2, and P3 for the guaiacol HDO reaction mechanism on the six transition metal surfaces*

Table 5.6. *Reaction (E_r) and activation (E_a) energies (in eV) for the most feasible pathways on the six transition metal surfaces included in this work. DHY and DME stand for dehydroxylation and demethylation pathways, respectively.*

Surface	*Preferred pathway*	*E_r (eV)*			*E_a (eV)*		
		(1)	*(2)*	*(3)*	*(1)*	*(2)*	*(3)*
Fe (110)	P1: DHY	−0.83	−0.29	1.20	1.13	0.10	1.73
Co (0001)	P3: DME	−0.73	0.13	0.28	1.23	0.94	0.90
Ni (111)	P3: DME	−0.18	−0.12	−0.11	1.21	0.57	0.62
Cu (111)	P3: DME	0.04	−0.71	−0.36	1.67	0.71	0.76
Pd (111)	P3: DME	−0.15	−0.21	−0.11	1.62	0.65	0.70
Pt (111)	P3: DME	−0.28	−0.38	0.18	1.65	0.36	0.88

5.3.2.4 Anisole pathway

According to ***Table 5.6***, on *Fe (110),* dehydroxylation is the preferable route to convert guaiacol into anisole. From this point, the following hydrogenation reactions may take two possible routes: (i) anisole to phenol via demethylation (P5, DME) and (ii) anisole to benzene (P6, DMO) via demethoxylation, ***Figure 5.9.***

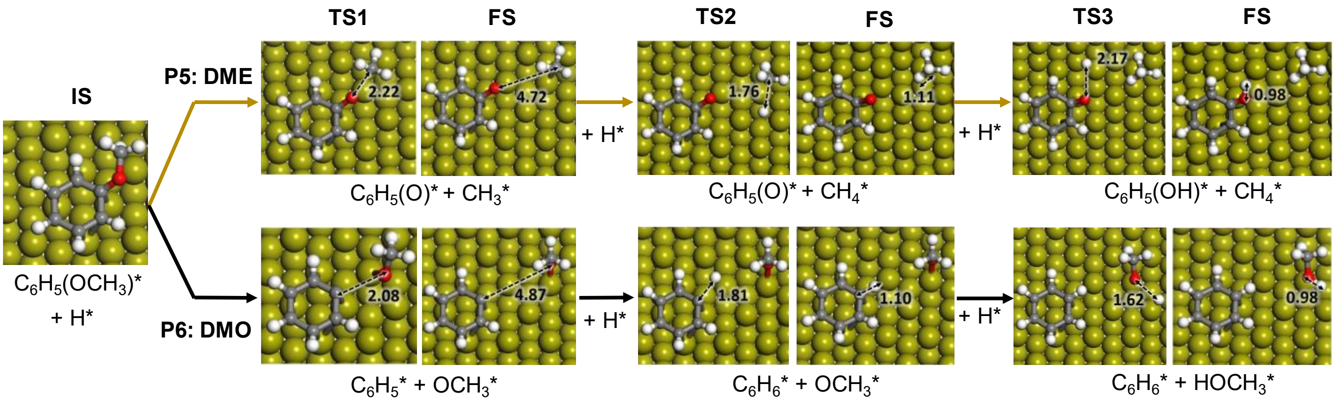

Figure 5.9. *Proposed reaction scheme for the hydrodeoxygenation of anisole on Fe (110). Colour scheme: Oxygen, red; hydrogen, white; carbon, grey and Fe, dark yellow.*

The demethylation reaction (P5) converts anisole into phenol and methane; ***Figure 5.9***. The energetic profile diagram is shown in ***Figure 5.10***. The reaction mechanism starts with the co-adsorption of H* next to the phenyl ring, provoking the C_{alkyl}−O bond activation. The process is exothermic (E_r = −1.12 eV) with an activation energy of 1.76 eV, where the breaking of the bond creates two surface species: phenolate and methyl, ***Table 5.7.*** The results show that the methane formation is an endothermic reaction (E_r = 0.35 eV) with an activation energy of 0.67 eV. The subsequent step is the phenol formation, which is also unfavourable (E_r = 0.71 eV and E_a = 1.22 eV).

Table 5.7. *Adsorption energy (in eV) of the formation of a) phenol and benzene, or b) water, methane, and methanol for the P4, P5, P6 and P7 pathways of the guaiacol HDO mechanism.*

Pathways		*Fe (110)*	*Co (0001)*	*Ni (111)*	*Cu (111)*	*Pd (111)*	*Pt (111)*
(P4)	a: $C_6H_5(OH)$* + OH*	----*	−2.86	−2.55	−2.13	−2.24	−2.66
DDO	**b:** $C_6H_4(OH)$* + H_2O*	----*	−1.75	−1.76	−1.19	−1.62	−2.15
(P5)	**a:** $C_6H_5(OH)$* + CH_3*	−2.57	----*	----*	----*	----*	----*
DME	**b:** $C_6H_4(O)$* + CH_4*	−3.29	----*	----*	----*	----*	----*
(P6)	**a:** C_6H_6* + OCH_3*	−2.89	----*	----*	----*	----*	----*
DMO	**b:** C_6H_5* + $HOCH_3$*	−1.97	----*	----*	----*	----*	----*
(P7)	**a:** C_6H_6* + OH*	----*	−2.71	−2.56	−1.77	−1.90	−2.57
HGL	**b:** C_6H_5* + H_2O*	----*	−1.58	−1.58	−0.88	−1.40	−1.02

* = Not available

On the other hand, the demethoxylation reaction (P6) converts anisole into benzene and methanol (DMO). The H* co-adsorption reaction provokes the activation of the C_{aryl}−OCH_3, ***Figure 5.9.*** The scission step is endothermic with a relatively small activation energy (E_r = 0.16 eV and E_a = 0.98 eV). The breaking of the bond creates two species: phenyl and methoxide, ***Table 5.7***. The formation of benzene is an exothermic reaction (E_r = −0.52 eV) with a small activation barrier (E_a = 0.42 eV). However, the formation of methanol is an endothermic and kinetically hindered process (E_r = 0.49 eV and E_a = 1.12 eV). The results demonstrate that *Fe (110)* preferentially breaks C_{aryl}−OCH_3 over C_{alkyl}−O. This behaviour is also explained by the Fe high oxophilicity, which anchors on its surface the O species, e.g. −OCH_3.

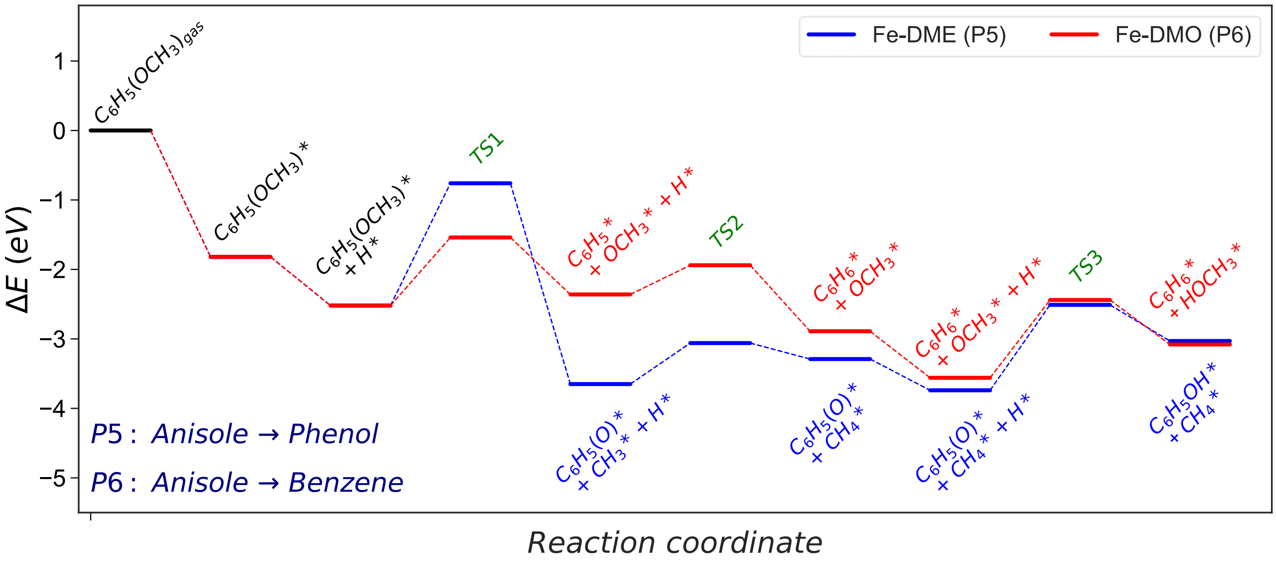

Figure 5.10. *Energy profile of the demethylation (DME) and demethoxylation (DMO) pathways converting anisole into phenol and benzene on Fe (110). The asterisk (*) represents adsorbed surface species. Molecular functional groups are denoted in parenthesis.*

5.3.2.5 Catechol direct deoxygenation pathway

The direct deoxygenation (DDO) pathway is the second step in the guaiacol reduction process, ***Figure 5.11***. It consists of the catechol conversion into phenol (P4), i.e. reducing one hydroxyl group. *Co (0001)* presented the most favourable process for the C_{aryl}−OH scission (E_r = +0.02 eV, E_a = 1.23 eV). In contrast, the C_{aryl}−OH bond requires more energy to break on *Ni (111)*; still, it is kinetically more accessible than on *Pd (111)* and *Pt (111)* (E_a = 2.36 eV and 2.11 eV, respectively).

The DDO results on the metals are very similar to those presented by Zhou *et al*. on *NiFe (111)*.[13] The bond scission creates two surface species: 2-hydroxyphenyl hydroxide, ***Table 5.7.*** Upon phenol formation, the evolution of water is less favourable in terms of reaction and activation energies; on *Co (0001)*, it presents reaction and activation energies of +0.55 eV and 1.36 eV, respectively. In contrast, the −OH hydrogenation on *Ni (111)* has a favourable behaviour (E_r = 0.02 eV and E_a = 0.82 eV, respectively). Nevertheless, the reducing conditions during the HDO process should shift the reaction towards H_2O formation.

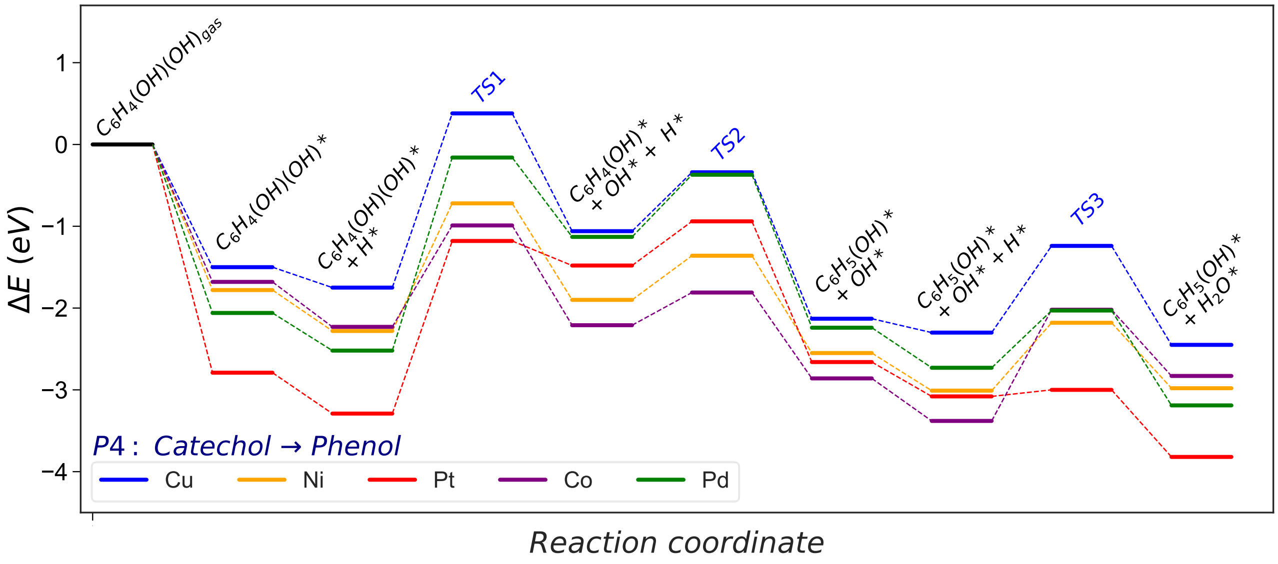

Figure 5.11. *Energy profile of the direct deoxygenation (DDO) converting catechol into phenol and water. The asterisk (*) represents adsorbed surface species. Molecular functional groups are denoted in parenthesis.*

5.3.2.6 Phenol hydrogenolysis pathway

The hydrogenolysis (HGL) pathway is part of the second hydrogenation stage and forms benzene and water molecules from phenol. In this reaction, the cleavage of the phenol C_{aryl}−OH is endothermic on all the metal catalysts studied, ***Figure 5.12.*** *Co (0001)* and *Ni (111)* are the metal surfaces that require less energy to break the C_{aryl}−OH (E_a = 1.41 eV and 1.55 eV, respectively), although the energy barrier is still substantial, ***Figure 5.13***.

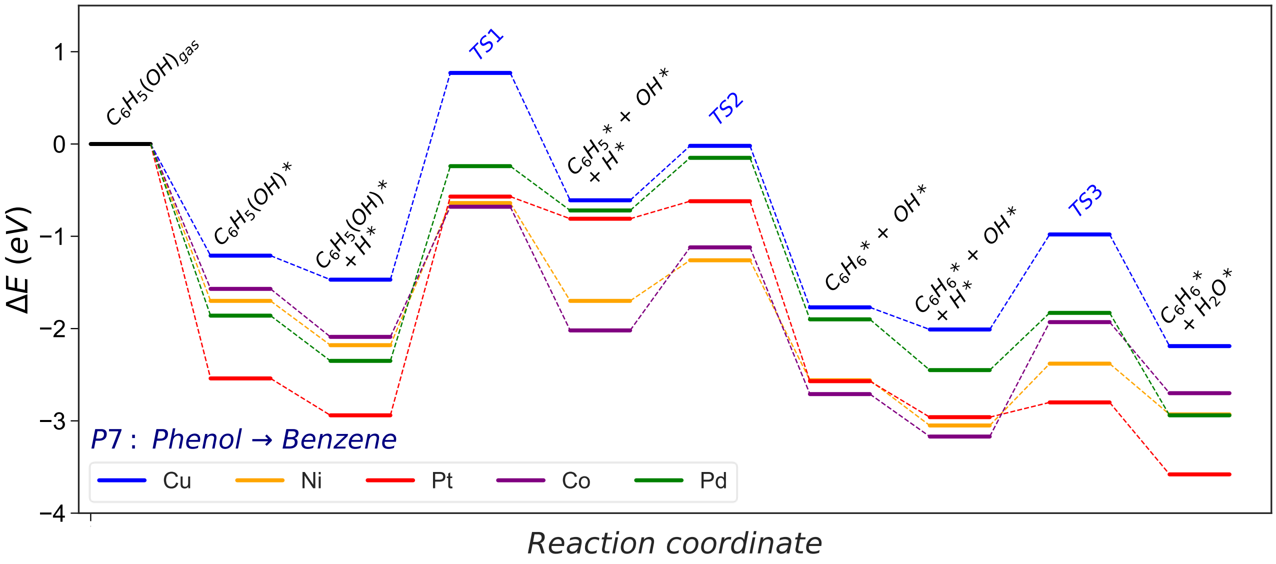

Figure 5.12. *Energy profile of the hydrogenolysis (HGL) pathway converting phenol into benzene and water. The asterisk (*) represents adsorbed surface species. Molecular functional groups are denoted in parenthesis.*

The noble metals, i.e. Pt and Pd, present the most hindered path, agreeing with previous experiments.[36] The C_{aryl}−OH scission creates phenyl and hydroxide species, ***Table 5.7***. The phenyl hydrogenation is exothermic on all the surfaces investigated. *Pt (111)* shows the most feasible process (E_r = −1.76 eV and E_a = 0.20 eV), although it is obstructed by the significant energy barrier to break C_{aryl}−OH (E_a = 2.36 eV). *Ni (111)* is the most suitable catalyst for this pathway (P7) due to the relatively low energy required to break the C_{aryl}−OH bond and hydrogenate the intermediates. Reaction and activation energies for the pathways P4 and P7 are illustrated in ***Figure 5.13.***

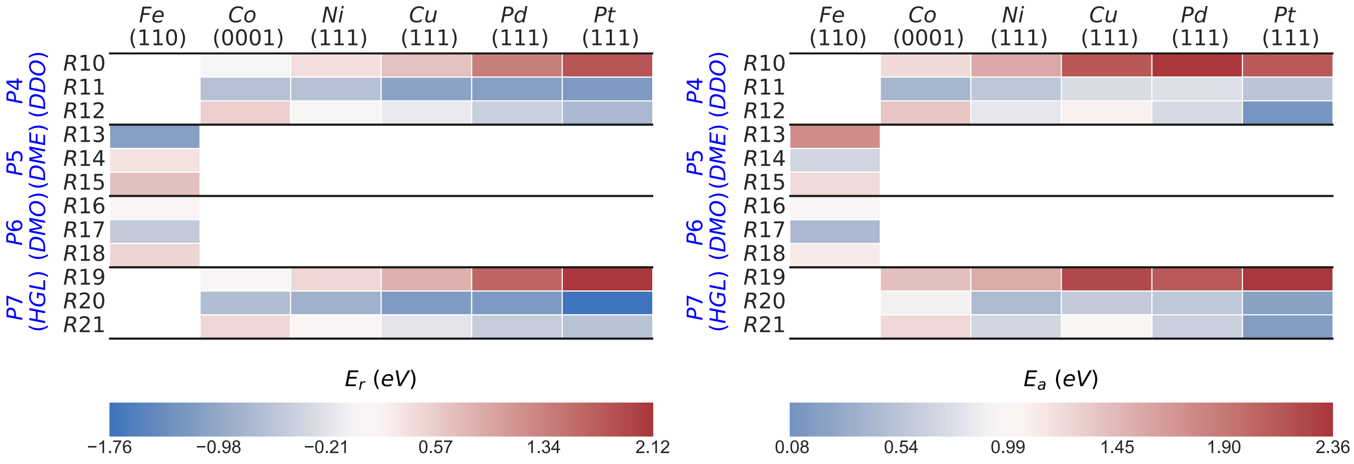

Figure 5.13. *Reaction (E_r, left) and activation energies (E_a, right) in eV of the P4, P5, P6 and P7 for the guaiacol HDO reaction mechanism on the six transition metal surfaces.*

5.3.3 BEP and TSS scaling relations.

Trends from the analysis performed on the different metal catalysts help developing eco-efficient catalysts; for instance, by unravelling the scaling relation between reaction and activation energies. These trends describe crucial properties for engineering new catalysts of superior HDO activity towards the desired product. A sounded trend is represented by Brønsted-Evans-Polanyi (BEP), which shows a linear correlation between the reaction's thermodynamics and kinetics.[46-50] This relationship covers many essential reactions such as bond breaking and hydrogenations. An alternative method, which correlates the initial (E_{IS}) or final state (E_{FS}) energies with the transition state energy (E_{TS}), is known as the transition state scaling (TSS), ***Figure 5.14***. Nevertheless, several publications have claimed these methods' low accuracy trends.[48, 51]

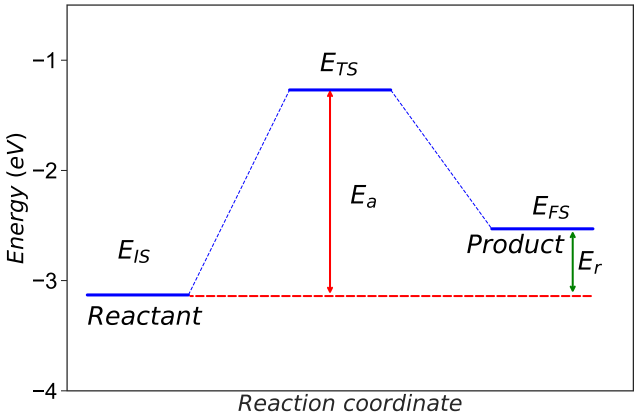

Figure 5.14. *Energies used in the TSS-IS, TSS-FS and BEP correlations in Eq. 5.2 and Eq. 5.3. The energies in the reaction are the initial state (E_{IS}), final state (E_{FS}), reaction (E_r) and activation (E_a) energies.*

The heterogeneity of the processes, e.g. C−O scissions and hydrogenation, leads to a substantial mean absolute error (MAE) using BEP, TSS-IS or TSS-FS. Similarly, Wang *et al.* investigated the BEP and TSS models over different bond-breaking reactions occurring on the functional groups of furans on *Pd (111)* and found that the combination of all reactions decreases the accuracy.[51] Using these relationships to**.** Using these relationships to obtain activation barriers of C−O scissions and hydrogenations may lead to 1.70 eV errors. The results combining all the steps are summarised in ***Table 5.8*** and ***Figure 5.15***.

Table 5.8. *TSS-IS, TSS-FS, and BEP relationships of the combined, bond scission and hydrogenation reactions for the six transition metal surfaces studied in this work.*

		Reactions	No.		m	b	MAE	M_iAE	RMSE	R^2
	--	Combined	87	**IS**	0.91	0.82	0.48	1.30	0.59	0.61
				FS	1.00	1.15	0.41	1.70	0.51	0.71
				BEP	0.57	1.12	0.29	1.22	0.37	0.61
(A) *Bond scission reactions*	(1)	C_{aryl}−OH	16	**IS**	0.91	1.62	0.34	0.72	0.40	0.56
				FS	0.59	−0.41	0.31	0.93	0.42	0.47
				BEP	0.42	1.51	0.16	0.39	0.20	0.72
	(2)	C_{aryl}−OCH_3	7	**IS**	1.13	1.93	0.32	0.61	0.36	0.66
				FS	0.48	0.15	0.41	0.86	0.50	0.36
				BEP	0.30	1.47	0.21	0.54	0.28	0.43
	(3)	C_{alkyl}−O	6	**IS**	0.91	1.29	0.16	0.29	0.19	0.82
				FS	0.51	0.59	0.23	0.51	0.29	0.55
				BEP	0.02	1.52	0.17	0.31	0.19	0.00
(B) *Hydrogenation reactions*	(4)	C_{aryl}−H	23	**IS**	1.07	0.65	0.19	0.54	0.25	0.91
				FS	1.63	3.10	0.30	0.62	0.33	0.84
				BEP	0.05	0.59	0.20	0.47	0.25	0.01
	(5)	CH_3O–H	7	**IS**	0.52	−0.64	0.28	0.78	0.39	0.40
				FS	1.25	1.63	0.15	0.22	0.17	0.89
				BEP	0.80	0.85	0.11	0.31	0.15	0.90
	(6)	H_3C–H	6	**IS**	0.92	0.51	0.18	0.43	0.23	0.86
				FS	1.28	1.67	0.14	0.38	0.19	0.90
				BEP	0.51	0.80	0.13	0.27	0.16	0.52
	(7)	$C_{aryl}O$–H	6	**IS**	0.84	0.31	0.13	0.34	0.16	0.88
				FS	1.11	1.13	0.11	0.30	0.15	0.90
				BEP	0.57	0.80	0.07	0.16	0.09	0.77
	(8)	HO−H	16	**IS**	0.74	0.08	0.35	0.79	0.42	0.46
				FS	1.18	1.46	0.17	0.39	0.20	0.88
				BEP	0.78	0.90	0.15	0.32	0.18	0.83

To improve the accuracy of these models, the reaction data was divided into two groups: (**A**) C−O bond cleavage and (**B**) hydrogenation reactions. **A** includes: (1) C_{aryl}−OH, (2) C_{aryl}−OCH_3 and (3) C_{alkyl}−O. The **B** group consists of five hydrogenations: (4) C_{aryl}−H, (5) CH_3O−H, (6) H_3C−H, (7) $C_{aryl}O$−H and (8) HO−H. The root-mean-square deviation method (RMSE) and maximum absolute error (M_iAE) were used to validate the accuracy of the methods.

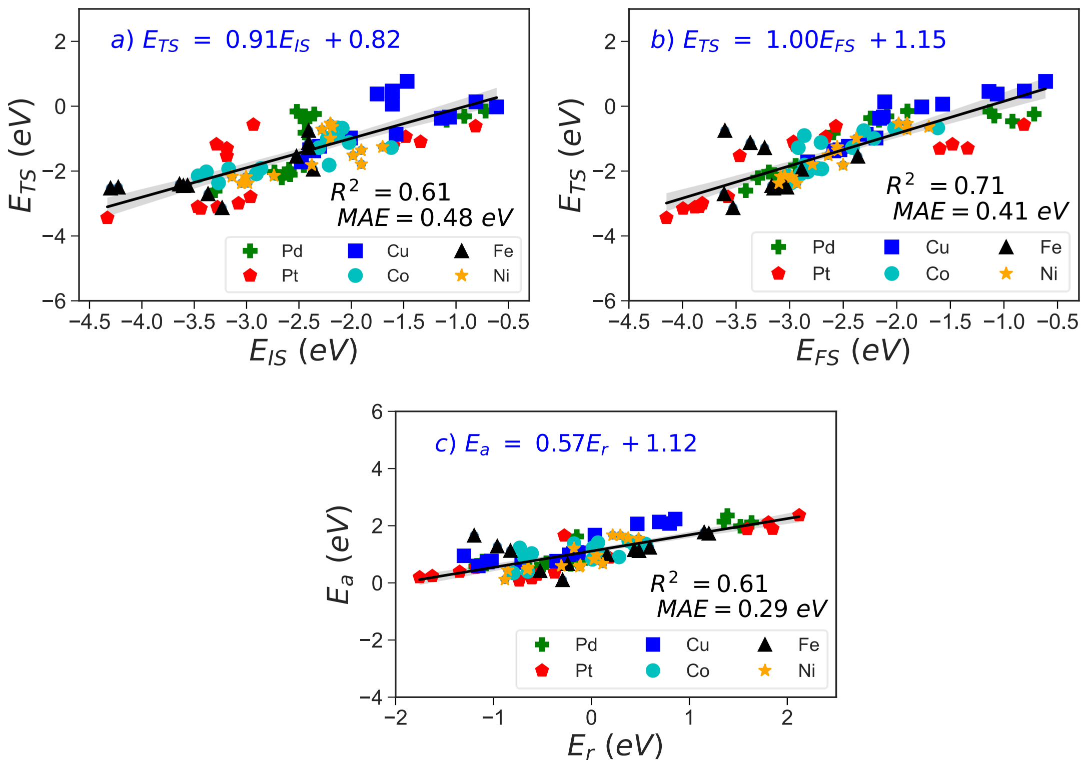

Figure 5.15. *Combined relations for (a) TSS-IS, b) TSS-FS, and c) BEP relationships, including bond scission and hydrogenation reactions.*

Table 5.8 contains these trend series's MAE, M$_i$AE, RMSE and R^2. The BEP relationship shows the lowest MAE for group **A** cleavages, where the C$_{aryl}$−OH and C$_{aryl}$−OCH$_3$ scissions reactions have the lowest mean error (0.16 and 0.21 eV, respectively).

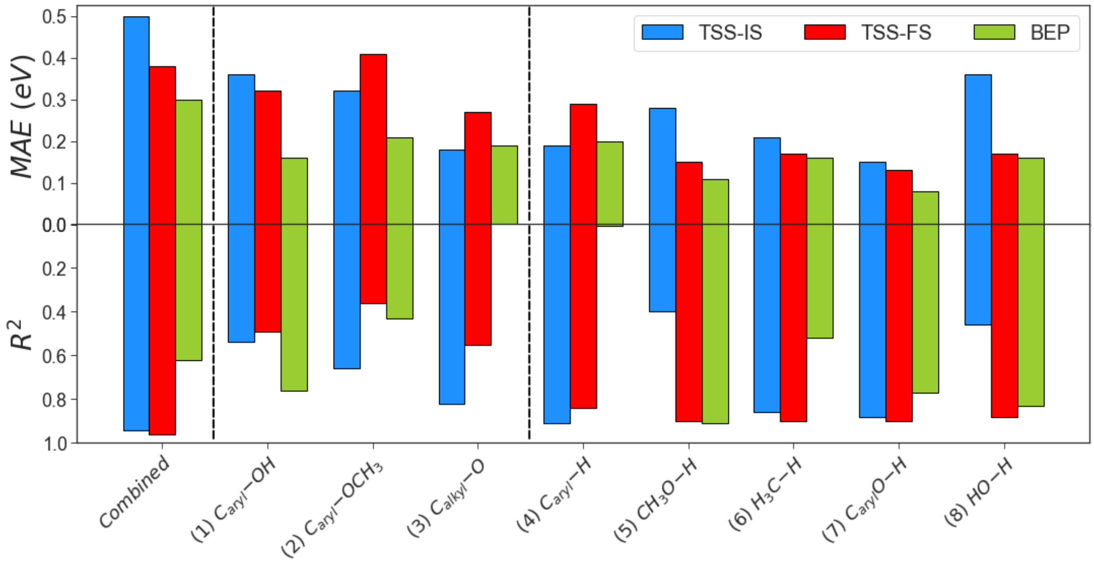

Figure 5.16. *Mean absolute error (MAE) and R^2 of the (1) combined, (2) scission of group **A** and (3) hydrogenation in group **B** for the TSS-IS, TSS-FS, and BEP relationships.*

Although the MAE difference between TSS−IS and TSS−FS is considerable (≈ 0.09 eV), it is worth noting that C_{alkyl}−O shows the lowest MAE for TSS-IS compared to the BEP relationship (0.16 eV). The BEP relationship again presents the lowest *MAE* (< 0.20 eV) for group **B**, whereas the MAE is up to 0.35 eV for TSS−IS and FS models, ***Figure 5.16.***

Table 5.9. *TSS-IS, TSS-FS, and BEP relationships of the combined bond scission and hydrogenation reactions for fcc metals, excluding Fe (110) and Co (0001), studied in this work.*

		Reactions	No.		m	b	MAE	M_iAE	RMSE	R^2
	--	Combined	60	**IS**	0.93	0.88	0.38	1.31	0.54	0.56
				FS	1.00	1.18	0.26	1.14	0.40	0.77
				BEP	0.63	1.12	0.20	0.71	0.29	0.72
(A) *Bond scission reactions*	(1)	C_{aryl}−OH	11	**IS**	0.97	1.95	0.17	0.47	0.24	0.80
				FS	0.83	0.68	0.29	0.87	0.40	0.37
				BEP	0.29	1.69	0.13	0.34	0.17	0.42
	(2)	C_{aryl}−OCH_3	4	**IS**	1.07	2.07	0.07	0.25	0.11	0.95
				FS	0.75	0.59	0.30	0.73	0.42	0.21
				BEP	0.08	1.82	0.07	0.21	0.11	0.09
	(3)	C_{alkyl}−O	5	**IS**	0.96	1.44	0.09	0.33	0.14	0.89
				FS	0.82	1.23	0.08	0.27	0.12	0.92
				BEP	0.38	1.59	0.09	0.32	0.14	0.05
(B) *Hydrogenation reactions*	(4)	C_{aryl}−H	16	**IS**	1.22	0.81	0.11	0.44	0.16	0.88
				FS	1.36	2.52	0.18	0.52	0.25	0.72
				BEP	0.16	0.71	0.12	0.46	0.18	0.04
	(5)	CH_3O–H	4	**IS**	1.86	2.94	0.07	0.24	0.11	0.94
				FS	1.30	1.90	0.03	0.10	0.05	0.99
				BEP	1.57	1.20	0.06	0.15	0.08	0.88
	(6)	H_3C–H	5	**IS**	1.18	1.01	0.03	0.09	0.04	1.00
				FS	1.27	1.69	0.12	0.34	0.18	0.91
				BEP	−0.17	0.51	0.06	0.21	0.09	0.09
	(7)	C_{aryl}O−H	5	**IS**	0.91	0.44	0.04	0.10	0.06	0.99
				FS	1.23	1.62	0.06	0.17	0.09	0.96
				BEP	0.26	0.77	0.05	0.12	0.06	0.25
	(8)	HO−H	11	**IS**	1.49	2.01	0.16	0.50	0.23	0.84
				FS	1.23	1.67	0.10	0.45	0.16	0.93
				BEP	0.89	0.94	0.13	0.37	0.17	0.60

The BEP model does not correlate well with the bond scission data, provoking a low description of the activation energies for C−O cleavage. In general, TSS-IS and TSS-

FS show a low linearity ($R^2 < 0.82$) due to the variable nature of the transition state in group **A**. The TSS-FS model presents a good correlation factor for group **B**, i.e. the hydrogenation series ($R^2 > 0.84$). The group **A** and **B** were narrowed down by considering only the fcc metals, i.e. excluding *Fe (110)* and *Co (0001),* ***Table 5.9***.

The BEP did not improve its predictability, contrarily to TSS-IS for $C_{aryl}-OCH_3$ and $C_{alkyl}-O$ ($R^2 = 0.95$ and 0.89, respectively). The MAE also decreased considerably in the TSS models, making them more reliable to describe the C−O dissociation reactions. The same consideration in group **B**, i.e. only fcc metals, led to an accurate description between the initial and the transition state energies for the H_3C-H and $C_{aryl}O-H$ hydrogenation ($R^2 = 1.00$ and 0.99, respectively). BEP shows acceptable accuracy only for forming small molecules such as CH_3OH and H_2O ($R^2 = 0.88$ and 0.60, respectively).

Figure 5.17 shows the most accurate scaling models for each reaction (group A and B) for all the metals considered in this work. ***Figures 5.17 (a − c)*** show the scaling models for the C−O bond scission, where the TSS−IS model helps visualise the binding strength between lignin-derivate compounds and metals surfaces. For instance, Pt shows difficulties catalysing the C−O bond scission due to its substantial activation energies and endothermic behaviour, ***Figure 5.17 (b)*** and ***(c)***. In contrast, *Fe (110), Ni (111)* and *Co (0001)* demonstrated exothermic C−O bond scissions with accessible energy barriers.

Figures 5.17 (d − h) show the most robust scaling models for the hydrogenation reactions of small molecules and aromatic compounds. *Fe (110)* stands out due to its endothermic behaviour and a substantial energy barrier on the hydrogenation of $C_{aryl}-H$ bonds. *Co (0001)* displays good performance in the C−O bond scission but fails in the hydrogenation of small molecules such as CH_3O-H. Whereas *Ni (111)* only shows acceptable energies for hydrogenation reactions. However, it is the most suitable for the C−O bond scission, both kinetically and thermodynamically, making it the most attractive catalysts candidate for the HDO of phenolic compounds.

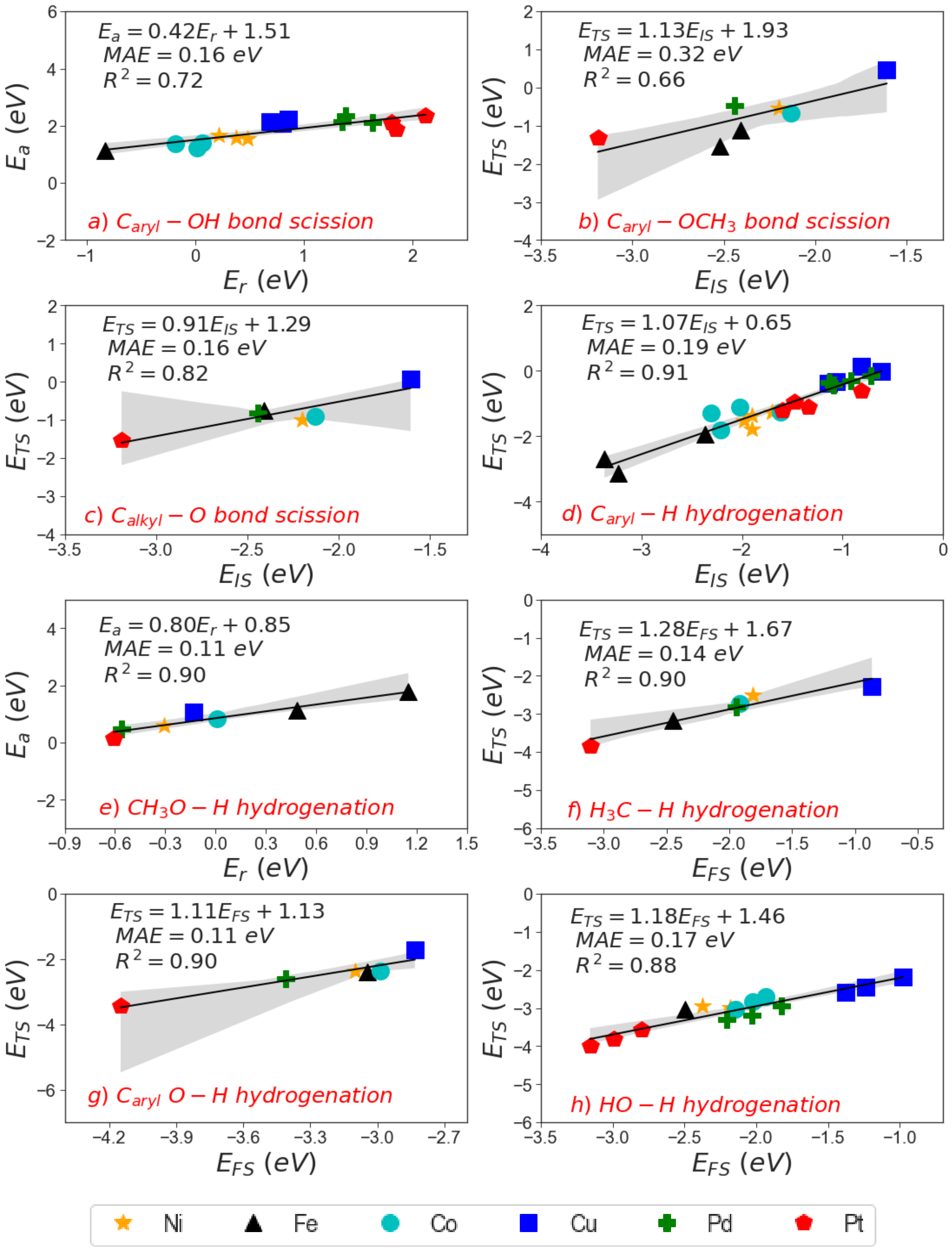

Figure 5.17. *BEP, TSS-IS and TSS-FS of the most accurate reactions (C−O bond scission and hydrogenation). Information of the linear equation, MAE and R^2 are included in each graph*

5.4 Chapter conclusion

Six transition metal surfaces, *Fe (110), Co (0001), Ni (111), Cu (111), Pd (111)* and *Pt (111)*, were investigated as catalysts for the HDO of lignin derivates to benzene. Guaiacol, as a model compound derived from lignin, strongly interacts with Pt followed by Pd > Ni > Fe > Co > Cu. The adsorption energies are directly related to the metal-molecule distance and the metal oxophilicity for the functional groups such as −OH and $-OCH_3$. The C−O bond elongation was evaluated as a descriptor to measure the C−O bond's weakening ($C_{aryl}-OH$, $C_{aryl}-OCH_3$ and $C_{alkyl}-O$). These agreed with the guaiacol conversion into catechol as the most likely pathway. Three pathways were scrutinised in the first guaiacol reduction step (dihydroxylation, demethylation and demethoxylation). The results validated that the demethylation pathway (DME) to convert guaiacol into catechol is the most accessible mechanism on Co, Ni, Cu, Pd, and Pt follow the route guaiacol → catechol → phenol → benzene. In contrast, Fe (110) preferred producing anisole through the dehydroxylation (DHY) reaction pathway, following the route guaiacol → anisole → benzene.

Moving forward to design superior catalysts for the HDO process, scaling models were generated to evaluate the overall catalytic activity, i.e. Bronsted-Evans-Polanyi and transition state scaling (TSS). These trends correlate positively with grouping fcc metals and reaction types, C−O scission, and hydrogenation. The scaling models exhibited the main trends in the studied catalysts where *Ni (111)* and *Co (0001)* displayed an accessible activation barrier for C−O scissions. The latter, however, fails to hydrogenate small oxygenated compounds, leaving Ni as the most feasible transition-metal catalyst for the HDO of phenolic compounds.

5.5 References

1. H. Fang, J. Zheng, X. Luo, J. Du, A. Roldan, S. Leoni and Y. Yuan, *Applied Catalysis A: General*, 2017, **529**, 20-31.
2. W. Song, Y. Liu, E. Baráth, C. Zhao and J. A. Lercher, *Green Chemistry*, 2015, **17**, 1204-1218.
3. F. Morteo-Flores, J. Engel and A. Roldan, *Philosophical Transactions of the Royal Society A*, 2020, **378**, 20200056.
4. V. N. Bui, D. Laurenti, P. Afanasiev and C. Geantet, *Applied Catalysis B: Environmental*, 2011, **101**, 239-245.
5. D.-P. Phan, T. K. Vo, J. Kim and E. Y. Lee, *Journal of Industrial and Engineering Chemistry*, 2020, **83**, 351-358.
6. C. A. Teles, P. M. de Souza, R. C. Rabelo-Neto, M. B. Griffin, C. Mukarakate, K. A. Orton, D. E. Resasco and F. B. Noronha, *Applied Catalysis B: Environmental*, 2018, **238**, 38-50.
7. A. Infantes-Molina, B. Pawelec, J. L. G. Fierro, C. V. Loricera, A. Jiménez-López and E. Rodríguez-Castellón, *Topics in Catalysis*, 2015, **58**, 247-257.

8. N. T. T. Tran, Y. Uemura and A. Ramli, *Procedia Engineering*, 2016, **148**, 1252-1258.
9. J. Sun, A. M. Karim, H. Zhang, L. Kovarik, X. S. Li, A. J. Hensley, J.-S. McEwen and Y. Wang, *Journal of Catalysis*, 2013, **306**, 47-57.
10. J. Lu, S. Behtash, O. Mamun and A. Heyden, *ACS Catalysis*, 2015, **5**, 2423-2435.
11. X. Lan, E. J. M. Hensen and T. Weber, *Applied Catalysis A: General*, 2018, **550**, 57-66.
12. M. Á. González-Borja and D. E. Resasco, *Energy & Fuels*, 2011, **25**, 4155-4162.
13. J. Zhou and W. An, *Catalysis Science & Technology*, 2020, **10**, 6849-6859.
14. J. Zhou, W. An, Z. Wang and X. Jia, *Catalysis Science & Technology*, 2019, **9**, 4314-4326.
15. J. Lu and A. Heyden, *Journal of Catalysis*, 2015, **321**, 39-50.
16. A. J. R. Hensley, Y. Wang and J.-S. McEwen, *Surface Science*, 2016, **648**, 227-235.
17. J. Zhang, J. Sun and Y. Wang, *Green Chemistry*, 2020, **22**, 1072-1098.
18. G. Zhu, W. Wang, K. Wu, S. Tan, L. Tan and Y. Yang, *Industrial & Engineering Chemistry Research*, 2016, **55**, 12173-12182.
19. G. Kresse and J. Furthmüller, *Computational materials science*, 1996, **6**, 15-50.
20. P. E. Blöchl, *Physical review B*, 1994, **50**, 17953.
21. S. Grimme, S. Ehrlich and L. Goerigk, *Journal of computational chemistry*, 2011, **32**, 1456-1465.
22. A. H. Larsen, et al., *Journal of Physics: Condensed Matter*, 2017, **29**, 273002.
23. G. Henkelman and H. Jónsson, *The Journal of chemical physics*, 2000, **113**, 9978-9985.
24. G. Henkelman, B. P. Uberuaga and H. Jónsson, *The Journal of chemical physics*, 2000, **113**, 9901-9904.
25. G. Henkelman and H. Jónsson, *The Journal of chemical physics*, 1999, **111**, 7010-7022.
26. A. J. Hensley, Y. Wang and J.-S. McEwen, *Surface Science*, 2016, **648**, 227-235.
27. K. Lee, G. H. Gu, C. A. Mullen, A. A. Boateng and D. G. Vlachos, *ChemSusChem*, 2015, **8**, 315-322.
28. X. Liu, W. An, C. H. Turner and D. E. Resasco, *Journal of Catalysis*, 2018, **359**, 272-286.
29. X. Liu, W. An, Y. Wang, C. H. Turner and D. E. Resasco, *Catalysis Science & Technology*, 2018, **8**, 2146-2158.
30. D. Konadu, C. R. Kwawu, R. Tia, E. Adei and N. H. de Leeuw, *Catalysts*, 2021, **11**, 523.
31. A. M. Verma and N. Kishore, *Journal of Molecular Modeling*, 2018, **24**, 1-16.
32. W. Liu, V. G. Ruiz, G.-X. Zhang, B. Santra, X. Ren, M. Scheffler and A. Tkatchenko, *New Journal of Physics*, 2013, **15**, 053046.
33. G. Porwal, S. Gupta, S. Sreedhala, J. Elizabeth, T. S. Khan, M. A. Haider and C. P. Vinod, *ACS Sustainable Chemistry & Engineering*, 2019, **7**, 17126-17136.
34. M. L. Honkela, J. Björk and M. Persson, *Physical Chemistry Chemical Physics*, 2012, **14**, 5849-5854.

35. A. J. Hensley, Y. Wang and J.-S. McEwen, *Surface science*, 2014, **630**, 244-253.
36. A. M. Verma and N. Kishore, *Physical Chemistry Chemical Physics*, 2017, **19**, 25582-25597.
37. Q. Tan, G. Wang, A. Long, A. Dinse, C. Buda, J. Shabaker and D. E. Resasco, *Journal of Catalysis*, 2017, **347**, 102-115.
38. D. Gao, Y. Xiao and A. Varma, *Industrial & Engineering Chemistry Research*, 2015, **54**, 10638-10644.
39. D. Shi and J. M. Vohs, *Journal of Physics: Energy*, 2018, **1**, 015003.
40. X. Jia, W. An, Z. Wang and J. Zhou, *The Journal of Physical Chemistry C*, 2019, **123**, 16873-16882.
41. K. Agrawal, A. M. Verma and N. Kishore, *ChemistrySelect*, 2019, **4**, 6013-6025.
42. K. Christmann, in *Encyclopedia of Interfacial Chemistry*, Elsevier, Oxford, 2018, pp. 213-220.
43. M. Bykova, O. Bulavchenko, D. Y. Ermakov, M. Y. Lebedev, V. Yakovlev and V. Parmon, *Catalysis in industry*, 2011, **3**, 15-22.
44. Y.-C. Lin, C.-L. Li, H.-P. Wan, H.-T. Lee and C.-F. Liu, *Energy & Fuels*, 2011, **25**, 890-896.
45. C.-c. Chiu, A. Genest, A. Borgna and N. Rösch, *ACS Catalysis*, 2014, **4**, 4178-4188.
46. A. Logadottir, T. H. Rod, J. K. Nørskov, B. Hammer, S. Dahl and C. J. H. Jacobsen, *Journal of Catalysis*, 2001, **197**, 229-231.
47. R. Alcala, M. Mavrikakis and J. A. Dumesic, *Journal of Catalysis*, 2003, **218**, 178-190.
48. S. Wang, et al., *Physical Chemistry Chemical Physics*, 2011, **13**, 20760-20765.
49. J. E. Sutton and D. G. Vlachos, *ACS Catalysis*, 2012, **2**, 1624-1634.
50. S. Wang, et al., *Catalysis Letters*, 2011, **141**, 370-373.
51. S. Wang, V. Vorotnikov, J. E. Sutton and D. G. Vlachos, *Acs Catalysis*, 2014, **4**, 604-612.

6

Microkinetic study of Guaiacol HDO on transition metal catalysts

6.1 Introduction

The catalytic HDO process is formed by an extensive network of reactions, including several elementary steps where the reaction occurs over a catalyst surface. In these reactions, the reactants are adsorbed on the surface, react forming products, and desorb. Therefore, a kinetic model will help to understand the basic surface chemistry and the catalyst's behaviour under different HDO conditions (time, pressure, and temperature). Indeed, a microkinetic model is a convenient tool for consolidating essential information about the catalytic process, intermediates, and products, closing the gap between simulation and experiments. This allows estimating the contribution of each elementary step to the overall rate under realistic reaction conditions.[1] However, the microkinetic model's main drawback is that the energy barriers of each elementary step must be known. This challenge can be solved by computational methods, which offer a good agreement with experiments.[2] On the other hand, complex reaction networks are challenging to rationalise only from DFT reaction profiles, and its coupling with the microkinetic model leads to a multiscale tool providing a robust understanding of the process.[3]

Microkinetic modelling plays an essential role in predicting and describing the HDO system's behaviour of biomass-derived components using different catalytic materials.[4] For example, Nimmanwudipong *et al.*[5] studied the guaiacol conversion on Pt / γ-Al_2O_3 in the presence of H_2 at 573 K. In this study, data analysis was used to determine a reaction network and identify the kinetics of significant reactions for the guaiacol conversion into phenol and anisole. The same authors confirmed the HDO selectivity based on the increase of H_2 partial pressure and temperature decrease.

Different studies have used DFT and the information of the guaiacol hydrodeoxygenation kinetic experiments using Pt over different supports to propose different reaction pathways.[6, 7] Moreover, temperature-programmed reaction (TPR) was incorporated as a technique to study the catalytic reactions under a range of temperatures. TPR studies are mainly used for catalysts to explain the reaction mechanism and as a fast method for catalyst screening.[8]

Chapter 6 summarises the DFT calculations used to develop a microkinetic model and reveals the most likely reaction paths. It includes thermodynamics and kinetics parameters of the guaiacol HDO mechanism on five transition metal catalysts (TMs), Co (0001), Ni (111), Cu (111), Pd (111) and Pt (111). Moreover, the microkinetic model was used to simulate the TPR from the guaiacol HDO conversion under a temperature range from 273 K to 1073 K.

6.2 Computational details

6.2.1 DFT calculations

Vienna Ab initio Simulation Package (VASP) was employed to model the guaiacol HDO on five transition metals (TMs) as described in *Chapter 5*. The reaction (E_r) and activation (E_a) energies were determined using *Eq.* 5.2 and *Eq. 5.3*, respectively. The transition states (TS) were obtained by combining the climbing-image nudged elastic band (CI-NEB) [9, 10] and the improved dimer method [11] to find the saddle points, which were verified with vibrational analyses.

6.2.2 Microkinetic modelling

A batch reactor microkinetic model was employed using an in-house code.[12] Translation, rotation and vibration modes were used to calculate thermodynamic parameters, such as enthalpy, entropy and Gibbs free energy as a function of the temperature. The partition functions to describe the thermodynamic properties are described in *Eq. 2.22 − 2.33*. Each surface elementary step's constant rate (k) was computed, employing the Eyring, Evans and Polanyi approximations in the transition-state theory (TST) framework, *Eq. 2.21*.

The microkinetic model assumes that each site on the surface is identical, where the species are adsorbed randomly and do not interact laterally. For adsorption reactions, the rate of adsorption of a gas (r_{ads}) on a surface is determined by the rate of collision between the gas and the surface and by the sticking coefficient (*Eq. 6.1*), where P_A is the pressure of the species in the reaction system and θ_* is the fraction of free sites on the surface. The reaction rate described for each step and the ordinary differential equations (ODEs) system were calculated to obtain a steady-state solution.[13]

$$r_{ads} = k_{ads} * P_A * \theta_* \qquad \textit{Eq. 6.1}$$

$$k_{ads} = A_o * S_o = \frac{A_{cat}}{\sqrt{2 * \pi * m_A * k_B * T}} * S_o(T) \qquad \textit{Eq. 6.2}$$

$$S_o(T) = \frac{q_{vib}^{TS}}{q_{trans}^{2D} * q_{rot}^{gas} * q_{vib}^{gas}} * \mathrm{e}\left(-\frac{\Delta E}{k_B T}\right) \qquad \textit{Eq. 6.3}$$

The rate constants were calculated using the Hertz-Knudsen equations (*Eq. 6.2)*, where $S_o(T)$ is the sticking coefficient, A_{cat} is the area of a free site, being 1.94 x 10^{-18} m^2 (Co), 1.90 x 10^{-18} m^2 (Ni), 1.99 x 10^{-18} (Cu), 2.41 x 10^{-18} (Pd) and 2.43 x 10^{-18} (Pt), m_A is the mass of a single molecule **(*Table 6.1*)**, k_B is the Boltzmann constant and T is the absolute temperature.[14]

Table 6.1. *Optimised gas molecule information*

Species	*Pressure (Pa)*	*Mass (Kg)*	*Symmetry*	*Inertia (Kg * m²)*
H_2	101325	3.35 x 10^{-27}	2	4.67 x 10^{-48}
Anisole	101325	1.79 x 10^{-25}	1	6.53 x 10^{-134}
Benzene	101325	1.29 x 10^{-25}	6	1.49 x 10^{-45}
Guaiacol	101325	2.06 x 10^{-25}	1	1.59 x 10^{-133}
H_2O	101325	2.99 x 10^{-26}	2	6.39 x 10^{-141}
Phenol	101325	1.56 x 10^{-25}	1	2.34 x 10^{-134}
Catechol	101325	1.82 x 10^{-25}	1	6.17 x 10^{-134}
CH_3OH	101325	5.32 x 10^{-26}	1	8.39 x 10^{-138}
CH_4	101325	2.66 x 10^{-26}	3	5.44 x 10^{-47}

The sticking coefficient describes the probability that an incident molecule becomes adsorbed upon collision with the surface *(Eq. 6.3)*. As the molecule moves perpendicular to the surface towards a transition state (TS), the translation and rotation are frustrated. Therefore, its partition function includes only vibration, q_{vib}^{TS}.

6.3 Results and discussion

6.3.1 Sticking coefficient (S_o)

The guaiacol HDO mechanism to form benzene proceeds through seven different pathways, ***Scheme 5.1***. The reaction mechanism starts with the guaiacol molecule adsorption and partial hydrogenation, activating the phenyl ring; ***Section 5.3.1*** studied the guaiacol adsorption energies on the TMs. To confirm the observations in *Chapter 5* about the oxy-molecule adsorption, the sticking coefficient (S_o) was studied on the five TMs, *Eq. 6.3*. ***Figure 6.1*** shows the S_o for the guaiacol in a temperature range from 273 K to 1073 K. Results indicate that the guaiacol adsorption process is accessible at low temperatures (273 K), whereas at a temperature higher than 600 K, S_o keeps constant.

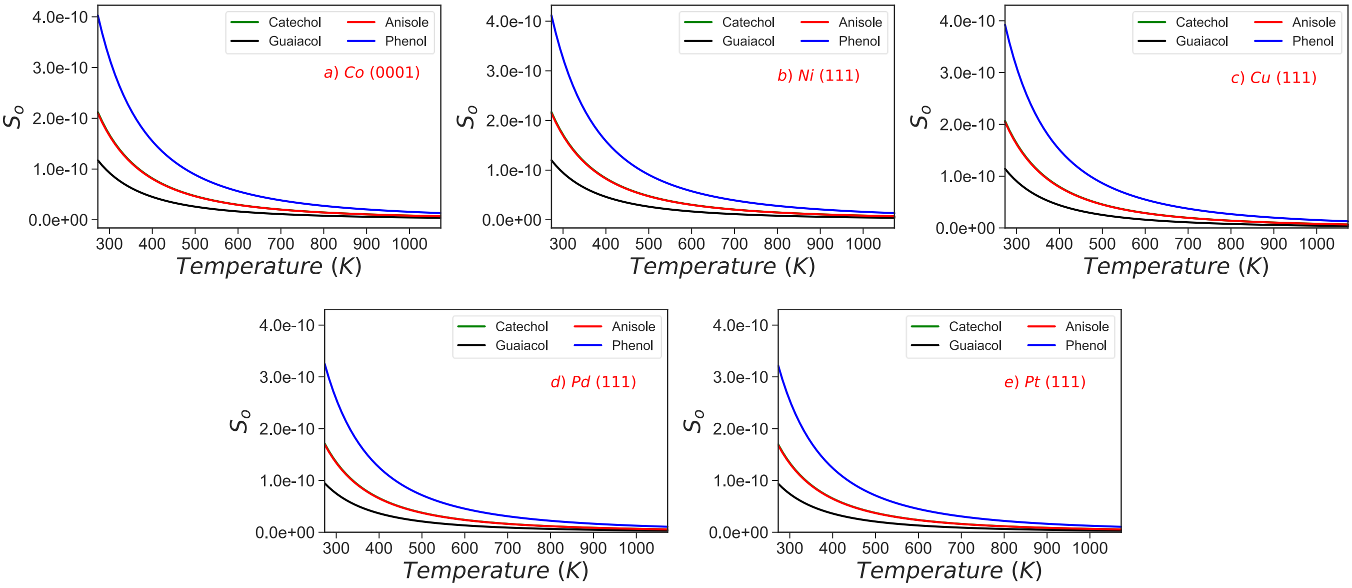

Figure 6.1. *Calculated sticking coefficient (S_o) as a function of the temperature for model compounds' adsorption reaction on a) Co (0001), b) Ni (111), c) Cu (111), d) Pd (111) and e) Pt (111). Notice that anisole and catechol are very similar.*

While at high temperatures, the energetic interaction between the surface and the molecule reduces. This can be seen in the change of S_o, which decreases exponentially with the temperature increase in all TMs studied, with similar results found in ref [15]. The sticking coefficient of molecules such as guaiacol, catechol, phenol, and anisole on TMs depends on the temperature. The S_o decrease can be considered an entropy change occurring in the adsorption process due to the entropy restrictions imposed on the adsorbate. This means that the adsorbate freedom is related to the entropy change. At low temperatures, the entropy change reaches a small transition state, favouring the adsorption. Whereas the transition state of the adsorption is substantial at high temperatures, resulting in a low sticking coefficient.[16] Therefore, an increase in temperature results in a small molecule interaction to the surface, which results in a low HDO activity. An optimised temperature is essential for the interaction of reactants and the bond scission during the HDO process.[17, 18] Experimental sticking coefficient studies for guaiacol are not available. However, similar results have been found for phenol on Ni and Pt, where low temperatures favour the adsorption due to the small entropy change.[19]

6.3.2 Thermochemistry analysis

To understand the HDO process at different temperatures, reaction (ΔG_r) and activation (ΔG_a) free energies for each reaction step in the guaiacol conversion have been calculated within a temperature range from 573 K to 1073 K. The free energies were obtained as the difference between products and reactants and TS and reactants, respectively, *Eq. 2.29, 2.32 and 2.33.*

6.3.2.1 Guaiacol dehydroxylation pathway

The calculated reaction energies for the dehydroxylation pathway (DHY) show that the breaking of the C_{aryl}−OH bond is exothermic only on Co (0001), and the process becomes more endothermic with increasing the temperature (*S4,* reaction steps in ***Table 6.2***). Meanwhile, the activation free energy is 1.39 eV for Co followed by Ni > Pt > Cu > Pd at 573 K (300 °C), the characteristic experimental temperature for the guaiacol HDO process [20, 21], ***Figure 6.2***. The hydrogenation process to form anisole *(S5)* is more feasible on *Pt (111)* with a ΔG_r = −1.38 eV than on other metals. *Pd (111)* shows a ΔG_r = −1.04 eV with an ΔG_a = 0.49 eV at 573 K, and its activation free energy decreases to 0.21 eV at 1073 K. In contrast, the activation free energies for *Co (0001)*, *Ni (111)* and *Cu (111)* do not show any significant change with the temperature. Finally, the last step in the dehydroxylation mechanism is water formation (*S7*). *Cu (111), Pt (111)*, and *Pd (111)* present an exothermic reaction at 573 K with a ΔG_r = −0.36 eV, −0.55 eV, −0.56 eV, respectively. Still, only Pd and *Pt (111)* show viable activation free energies of 0.46 eV and 0.28 eV at the same temperature, ***Figure 6.2***. The results found are similar to previous studies where the guaiacol HDO conversion on Ni, Co and Pt−supported catalysts did not show a selectivity to the dehydroxylation pathway at 573 K.[20, 22] This can be explained due to the high bond dissociation of the C_{aryl}-OH bond compared to C_{aryl}−OCH_3; therefore, the phenol and catechol production is more predominant than anisole.

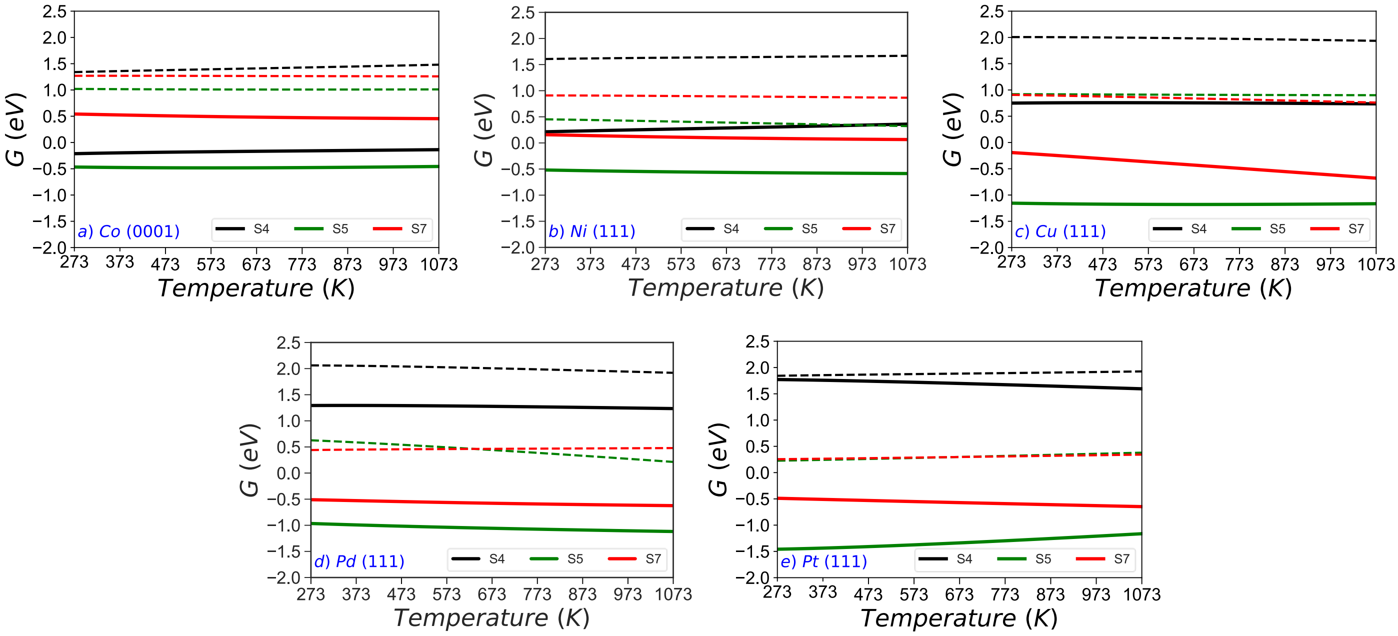

Figure 6.2. *Reaction (ΔG_r) and activation (ΔG_a) free energies as a function of the temperature of elementary steps for the dehydroxylation pathway (guaiacol → anisole) (S4) including the hydrogenation reaction to anisole (S5) and water (S7) formation. Bold and dashed lines correspond to ΔG_r and ΔG_a, respectively.*

6.3.2.2 Guaiacol demethoxylation pathway

The demethoxylation (DMO) pathway is characterised by the C_{aryl}−OCH_3 bond scission to form phenol (*S12,* reaction steps in ***Table 6.2***), ***Figure 6.3***. All the metals exhibit an endothermic reaction and activation free energies higher than 1.5 eV even at temperatures higher than 573 K. At 573 K, the phenol formation (*S13*) is favourable for *Pt (111)* and *Pd (111)* with an ΔG_r = −1.31 eV and −0.98 eV and low activation free energies (ΔG_a = 0.36 eV and 0.65 eV, respectively), ***Figure 6.3***. The same results are seen in the methanol formation step (*S15*) with exothermic behaviours and low activation free energies for Pt and Pd. However, the substantial activation free energy and endothermic behaviour of the C_{aryl}−OCH_3 bond scission limits the reaction on all the metals sampled. Several authors have shown similar results on Ni, Pt, and Co-based catalysts for the guaiacol HDO, where the phenol formation has a positive impact at high temperatures (> 573 K).[5, 22-25] Moreover, its selectivity improves with increasing the guaiacol weight.[20] Although high temperatures can decrease the HDO and hydrogenation rates.[26]

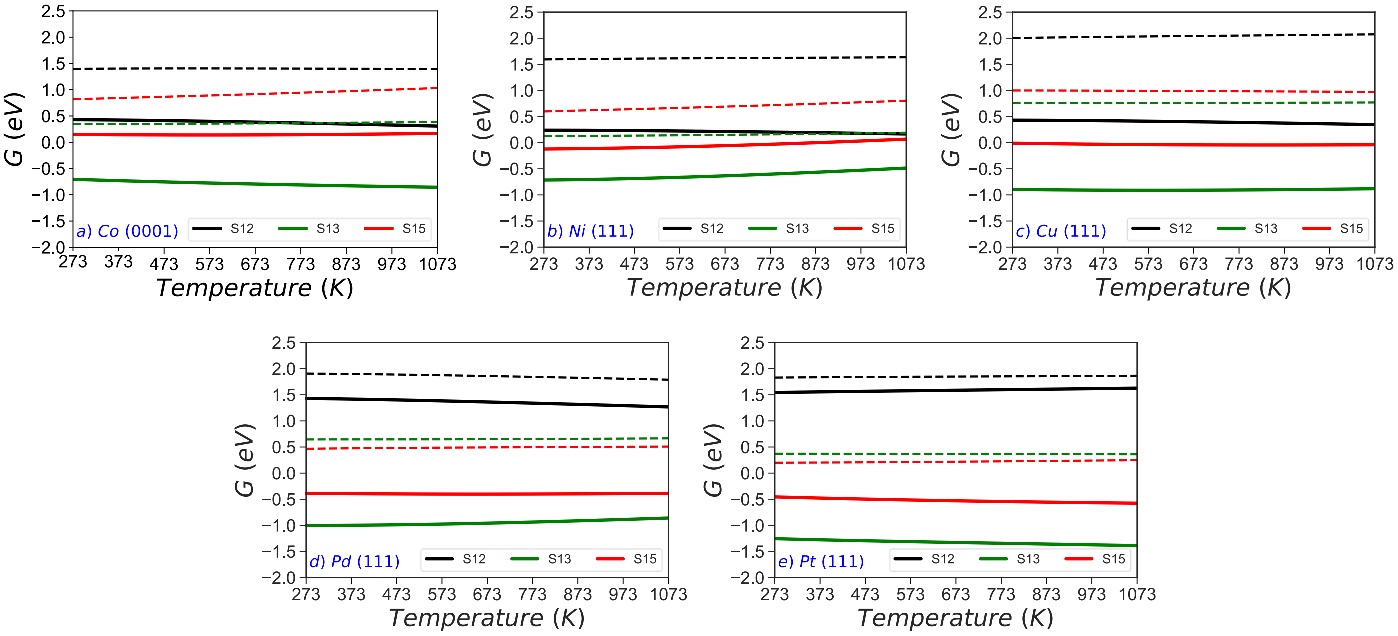

Figure 6.3. *Energy reaction (ΔG_r) and activation free energies (ΔG_a) as a function of the temperature of elementary steps for the demethoxylation pathway (guaiacol → phenol) (S12) including the hydrogenation reaction to phenol (S13) and methanol (S15) formation. Bold and dashed lines correspond to ΔG_r and ΔG_a, respectively.*

6.3.2.3 *Guaiacol demethylation pathway*

The demethylation (DME) pathway follows the C_{alkyl}–O scission mechanism, ***Figure 6.4***. All the metals show an exothermic step at 573 K, where *Co (0001)* is the only metal which stands out with an ΔG_r = −0.84 eV, followed by Pd > Ni > Pt > Cu (*S20,* reaction steps in ***Table 6.2***). However, *Pd (111)* presents a considerable increase in its exothermic nature, reaching a reaction free energy of −0.95 eV at 1073 K. *Ni (111)* and *Co (0001)* show the lowest activation free energies at 573 K (ΔG_a = 1.19 eV and 1.26 eV), which slightly increase with the temperature. *Pt (111)* and *Ni (111)* are the most feasible for methane formation (*S21*) with a ΔG_a = 0.44 eV and 0.71 eV at 573 K, respectively. Finally, for the catechol formation (*S23*), *Ni (111)* presents an exothermic behaviour with the lowest activation energy at 573 K (ΔG_a = 0.40 eV), which decreases up to 0.17 eV at 1073 K. Based on these results, *Ni (111)* is the most accessible metal to promote the C_{alkyl}–O bond scission. *Pt (111)* and *Pd (111)* exhibited poor deoxygenation activity with high activation barriers and endothermic behaviour; this can be attributed to the strong guaiacol adsorption energy on the metals, ***Figure 6.4***.[27]

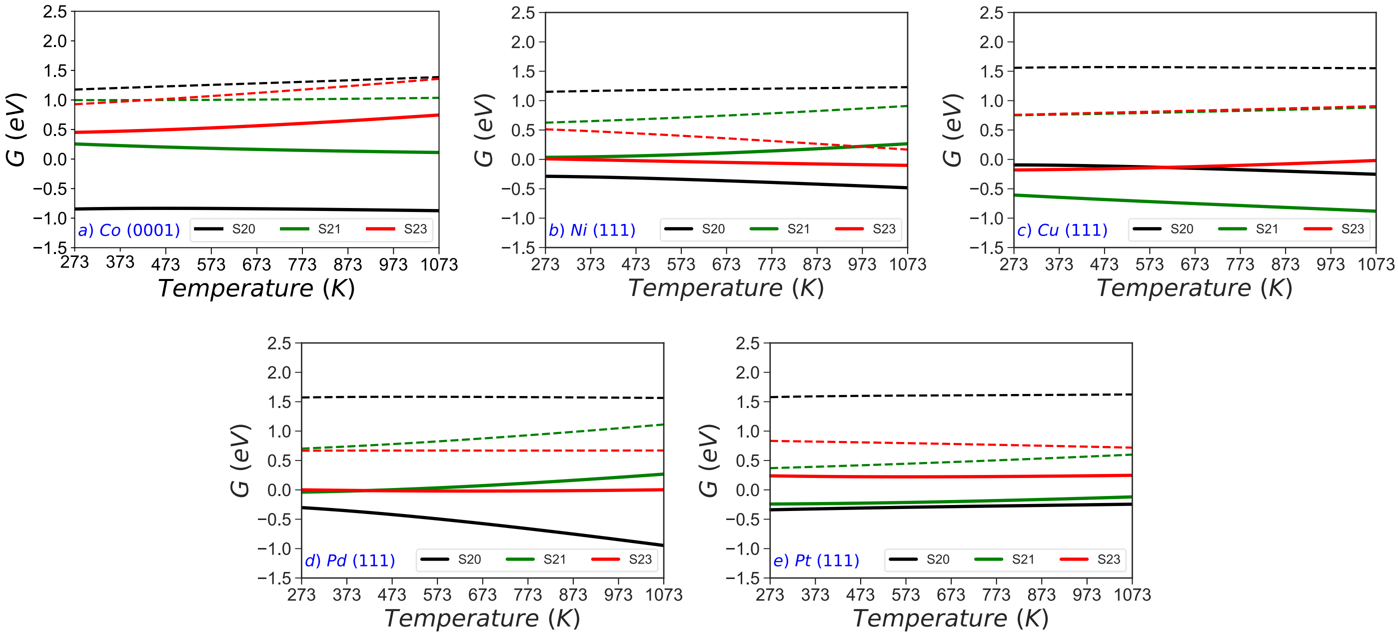

Figure 6.4. *Reaction (ΔG_r) and activation (ΔG_a) free energy (ΔG_a) as a function of the temperature of elementary steps for the demethylation pathway (guaiacol → catechol) (S20) including the hydrogenation reaction to methane (S21) and catechol (S23) formation. Bold and dashed lines correspond to ΔG_r and ΔG_a, respectively.*

ΔG_r and ΔG_a results show that guaiacol demethylation (DME) is the most favourable pathway in the HDO process, ***Figure 6.2***. This agrees with experimental data where catechol is found as the main product from guaiacol at 300 °C (573 K) on different supported catalysts.[28-30] Different authors have demonstrated the presence of phenol at the same temperatures with catechol traces, suggesting subsequent hydrogenation reactions from catechol to produce phenol via direct deoxygenation pathway.[23, 31]

6.3.2.4 Catechol direct deoxygenation pathway

All the metals screened show a preferred route to convert guaiacol into catechol. The following hydrogenation reaction is the direct deoxygenation (DDO) pathway resulting from the cleavage of one C_{aryl}−OH bond (*S31*), ***Figure 6.5***. Co (0001) shows the most favourable C_{aryl}−OH scission conditions with a ΔG_r = −0.06 eV and a low activation barrier (ΔG_a = 1.22 eV) at 573 K. In contrast, the C_{aryl}−OH scission is inaccessible on *Pt (111)* at the same temperature (ΔG_r = 1.77 eV and ΔG_a = 2.06 eV). In the next hydrogenation step (*S32*), *Cu (111)*, *Pt (111)*, and *Pd (111)* yield phenol with an exothermic behaviour (ΔG_r = −1.09 eV, −1.13 eV, and −1.02 eV, respectively). Small activation free energies are seen on *Pd (111)* and *Pt (111)*, which are invariable with respect to the temperature increase. The results agree with previous works, which describe that Pt and Pd catalysts have a low deoxygenation performance. They use more hydrogen for the aromatic ring saturation instead of the oxygen scission.[32, 33]

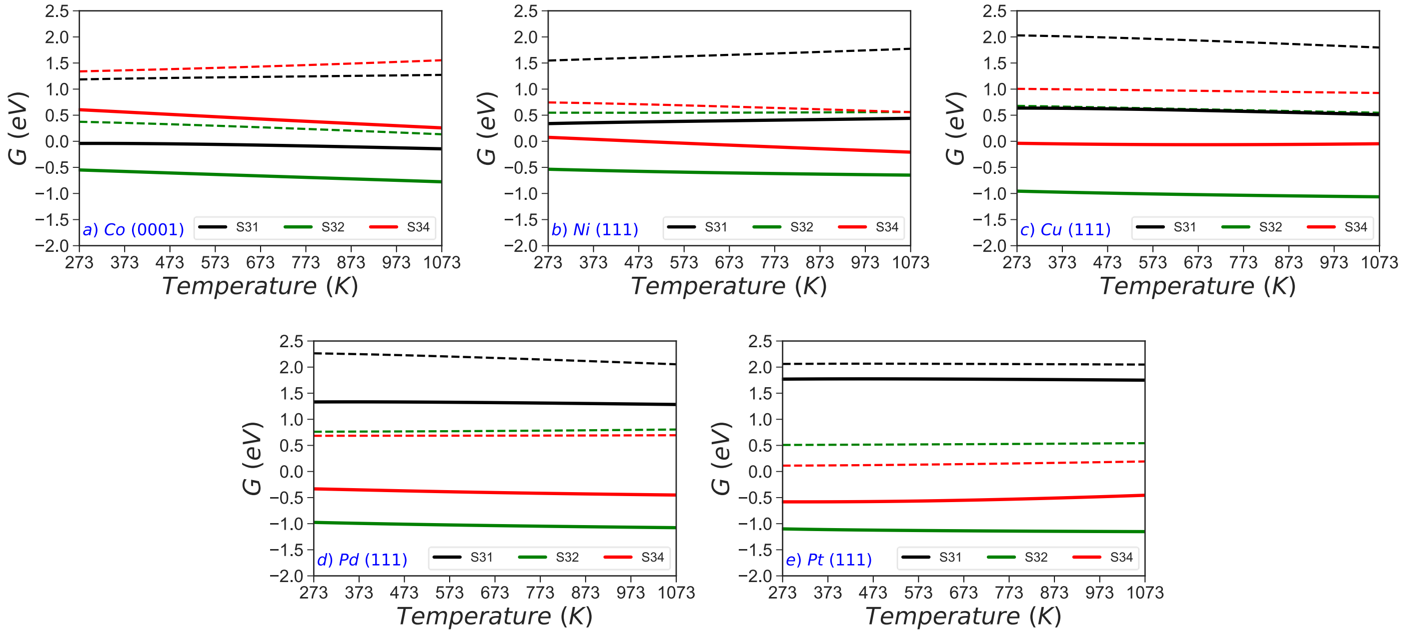

Figure 6.5. *Reaction (ΔG_r) and activation (ΔG_a) free energies as a function of the temperature of elementary steps for the direct deoxygenation pathway (catechol → phenol) (S31), including the hydrogenation reaction to phenol (S32) and water (S34) formation. Bold and dashed lines correspond to ΔG_r and ΔG_a, respectively.*

6.3.2.5 Phenol hydrogenolysis pathway

The hydrogenolysis pathway (HGL) represents the second stage of the guaiacol hydrogenation to form benzene through the C_{aryl}−OH scission (*S61*), ***Figure 6.6***. The results indicate that all the metals have a considerable activation barrier (ΔG_a > 1.30 eV) at 573 K, where Co (0001) is the only metal that presents an exothermic behaviour with a ΔG_r = −0.23 eV, which becomes more favourable with respect to the temperature. Upon oxygen bond scission, *Pd (111)* and *Pt (111)* present the most favourable conditions for the intermediate hydrogenation forming benzene (*S62*) (ΔG_r = −1.05 eV and −1.63 eV) and relatively low activation energies (ΔG_a = 0.53 eV and 0.17 eV). Various authors have reported the outstanding hydrogenation activity of noble metals, favouring the hydrogenation of the aromatic ring in the phenol conversion into cyclohexanone instead of benzene.[34, 35] However, catalysts such as Ni and CoMo supported catalysts have demonstrated a good deoxygenation performance in the phenol conversion into benzene at high temperatures, similar results found in this work.[36, 37]

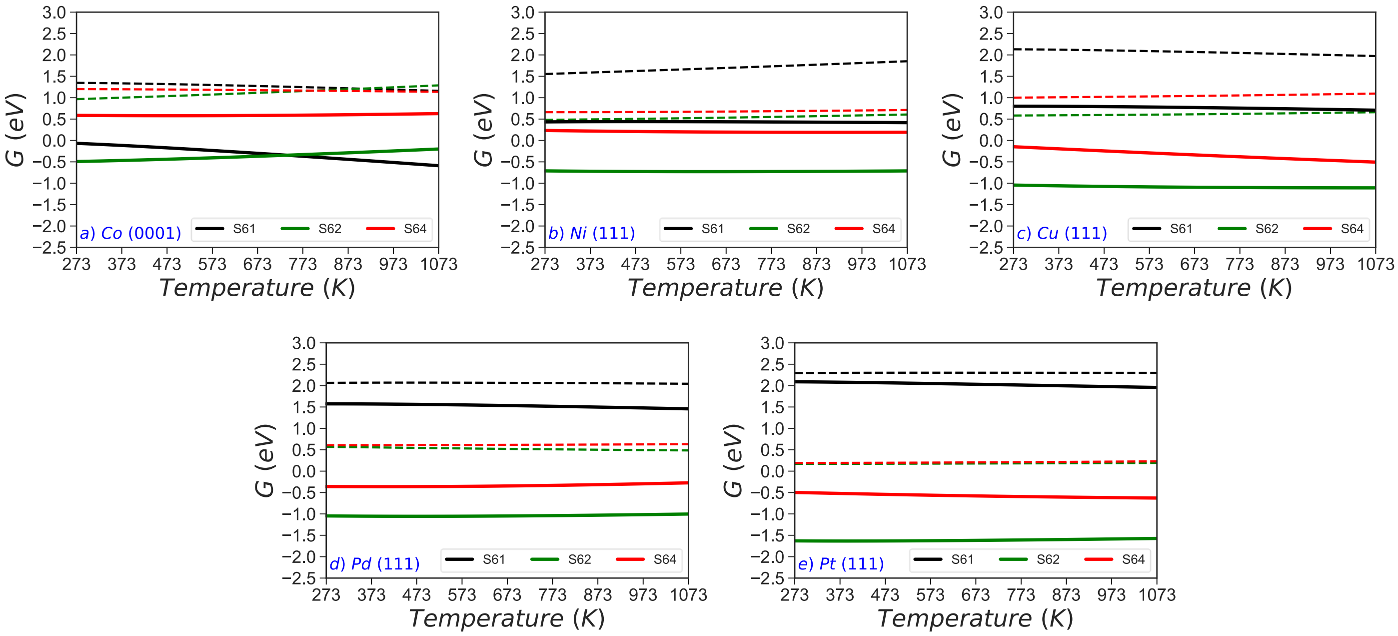

Figure 6.6. *Reaction (ΔG_r) and activation (ΔG_a) free energies as a function of the temperature of elementary steps for the hydrogenolysis pathway (phenol → benzene) (S61), including the hydrogenation reaction to benzene (S62) and water (S64) formation. Bold and dashed lines correspond to ΔG_r and ΔG_a, respectively.*

6.3.3 Reaction orders

The reaction network of guaiacol HDO forming benzene involves 68 reactions steps, including adsorption, desorption, and three significant elementary steps on the surface, i.e. (i) bond scission of the guaiacol adsorbed, (ii) hydrogenation step of the adsorbed aromatic species, and (iii) hydrogenation step of the sub-product. The rate constants were calculated at selected temperatures, 273 K, 573 K, 673 K and 1073 K (***Table A2 − A6*** in the Appendix section). The partial pressures for the reactants (guaiacol) and H_2 were set in a 1 to 5 ratio. The rate law's pre-exponential factor and rate constant for each step of the guaiacol conversion at 573 K are summarised in ***Table 6.2***.

The adsorption constants of the oxygenated compounds are compared for the TMs studied at 573 K. The results confirm that guaiacol shows a low rate (k = 3.53 x 10^{-7} s^{-1}), followed by catechol > anisole > phenol (k = 1.39 x 10^{-6} s^{-1}). This confirms that the reaction constant is affected by the type of functional groups, where phenol reactions are faster than molecules with $C-OCH_3$ bonds such as anisole.[38] The guaiacol bond scission rate constants are analysed on the metals studied. The $C_{aryl}-OH$ scission rate constant (*S4*) is low for the dehydroxylation pathway at 573 K. *Co (0001)* presents the highest rate with a k = 2.00 s^{-1} followed by Ni > Pt > Pd > Cu, suggesting that this reaction may limit the overall reaction path. Higher rates are exhibited in the hydrogenation reactions compared to the dissociation reactions, reaching up to 10 orders of magnitude for *Ni (111)* and *Pd (111)* (k = 2.43 x 10^{10} s^{-1} and k = 8.49 x 10^{10} s^{-1}, respectively). The same trends are seen in the demethoxylation pathway, where the reaction rates for the $C_{aryl}-OCH_3$ (*S12*); *Co (0001)* shows the highest rate constant (k = 1.06 x 10^{1} s^{-1}).

In contrast, the C_{alkyl}–O bond scission rate for the demethylation pathway (*S20*) is kinetically favoured in the range of temperatures considered here. In this pathway, *Ni (111)* exhibits a k = 2.31 x 10^{2} s^{-1}, which is three orders of magnitude greater than for the other pathways, followed by Co > Cu > Pd > Pt. The subsequent hydrogenation steps to form catechol (*S23*) have a rate constant of k = 5.53 x 10^{11} s^{-1} for *Ni (111)* faster than on the other metals. The analysis of rate constants confirms that guaiacol conversion into catechol is the most feasible pathway at 573 K, and Ni is a good candidate to catalyse it. These results agree with Lu *et al*.[39] studies on *Pt (111).* They found that catechol is the major product of the guaiacol HDO reaction, where phenol is four orders of magnitude slower than catechol. The pre-exponential factor, which expresses the fraction of reactant molecules that possess enough kinetic energy to react, for the different C_{alkyl}–O bond scission are in a range of 10^{12} - 10^{13} order of magnitude at 573 K. These orders of magnitude are similar to different HDO microkinetic studies, which study the guaiacol and anisole molecules under the same conditions (T= 573 K).[40, 41] This will give high accuracy to the microkinetic model developed and the results provided in this study.

The HDO reaction continues from catechol to form phenol and benzene as the final product. *Co (0001)* presents the highest rate constant for the C_{aryl}−OH scission (*S31*), which is five orders of magnitude higher than the other metal with a $k = 9.22 \times 10^{1}\ s^{-1}$, followed by Ni > Cu > Pt and Pd. In the subsequent phenol hydrogenation step (*S32*), *Pt (111)* presents a rate, $k = 3.89 \times 10^{8}\ s^{-1}$, which is 13 orders of magnitude higher than the deoxygenation steps. The same effect is seen in water production, where Pt exhibits the highest rate with a $k = 3.44 \times 10^{11}\ s^{-1}$. These predictions agree with experimental studies where Pt demonstrated its good hydrogenation performance but a poor deoxygenation activity at 573 K.[26, 42, 43]

The benzene yield occurs via the hydrogenolysis pathway. The reaction constant shows a low benzene production rate hindered by the C_{aryl}−OH bond scission (*S61*). *Co (0001)* exhibits the highest rate constant ($k = 6.49 \times 10^{2}\ s^{-1}$) followed by Ni > Cu > Pd and Pt. However, Ni presents a rate constant of $k = 6.16 \times 10^{7}\ s^{-1}$ for the phenyl hydrogenation (*S62*), which is six orders of magnitudes faster than *Co (0001)* for the same reaction ($k = 8.51 \times 10^{1}\ s^{-1}$). Pt and Pd generally shows favourable hydrogenation abilities (*S62*) ($k = 4.73 \times 10^{11}\ s^{-1}$ and $1.58 \times 10^{9}\ s^{-1}$, respectively) but very poor deoxygenation performance ($k = 1.06 \times 10^{-7}\ s^{-1}$ and $1.14 \times 10^{-5}\ s^{-1}$). These results are similar to previous computational studies, where *Pt (111)* and *Pd (111)* show high rates for the phenyl hydrogenation ($k = 3.16 \times 10^{7}\ s^{-1}$ and $6.34 \times 10^{8}\ s^{-1}$).[39, 44] Although the O removal rate is too slow ($k = 5.71 \times 10^{-8}\ s^{-1}$ and $1.02 \times 10^{-13}\ s^{-1}$) in the range of temperatures considered here, limiting the reaction on both metals. Therefore, *Ni (111)* is the only catalyst candidate that presents a high-rate constant for product formation.

Table 6.2. *Pre-exponential factor (A_o) and forward rate constant (k) for the elementary reactions for the guaiacol conversion into benzene at 573 K. The notation to the structures used in each step (S) is explained in Table A1 (Appendix section), where GUA, CAT, ANI, PHE and BEN represent guaiacol, catechol, anisole, phenol and benzene.*

			Co (0001)		Ni (111)		Cu (111)		Pd (111)		Pt (111)	
	Step	**Reactions**	A_o	$k\ (s^{-1})$	A_o	$k\ (s^{-1})$	A_o	$k\ (s^{-1})$	A_o	$k\ (s^{-1})$	A_o	$k\ (s^{-1})$
	S1	GUA + * >> GUA*	1.92 x 10^{4}	3.53 x 10^{-7}	1.88 x 10^{4}	3.53 x 10^{-7}	1.97 x 10^{4}	3.53 x 10^{-7}	2.38 x 10^{4}	3.53 x 10^{-7}	2.41 x 10^{4}	3.53 x 10^{-7}
	S2	H_2 + * >> H_2*	1.50 x 10^{5}	6.16 x 10^{1}	1.48 x 10^{5}	6.16 x 10^{1}	1.54 x 10^{5}	6.15 x 10^{1}	1.87 x 10^{5}	6.16 x 10^{1}	1.89 x 10^{5}	6.16 x 10^{1}
	S3	GUA* + H* >> R11 + *	7.52 x 10^{13}	3.61 x 10^{14}	5.58 x 10^{13}	1.36 x 10^{14}	1.89 x 10^{13}	1.87 x 10^{13}	1.63 x 10^{13}	5.18 x 10^{13}	6.23 x 10^{12}	2.14 x 10^{13}
Guaiacol → Anisole	**S4**	R11 > TS11 > R12	3.65 x 10^{12}	2.00 x 10^{0}	1.49x 10^{13}	6.41 x 10^{-2}	3.96 x 10^{13}	1.19 x 10^{-4}	1.42 x 10^{14}	2.20 x 10^{-4}	9.67 x 10^{12}	3.10 x 10^{-4}
	S5	R12 > TS12 > R13	2.40 x 10^{13}	3.18 x 10^{4}	9.15 x 10^{13}	2.43 x 10^{10}	2.87 x 10^{13}	2.78 x 10^{5}	1.84 x 10^{15}	8.49 x 10^{10}	2.02 x 10^{12}	7.18 x 10^{9}
	S6	R13 + H* >> R14 + *	2.01 x 10^{13}	3.38 x 10^{13}	8.50 x 10^{12}	5.97 x 10^{12}	8.52 x 10^{12}	4.15 x 10^{12}	1.64 x 10^{13}	4.07 x 10^{13}	3.90 x 10^{13}	3.69 x 10^{14}
	S7	R14 > TS13 > R15	2.89 x 10^{13}	2.06 x 10^{2}	4.77 x 10^{13}	6.11 x 10^{5}	2.56 x 10^{14}	7.37 x 10^{6}	5.99 x 10^{12}	5.44 x 10^{8}	6.30 x 10^{12}	1.93 x 10^{10}
	S8	R15 >> H_2O* + ANI	1.24 x 10^{12}	7.14 x 10^{10}	6.09 x 10^{10}	2.21 x 10^{8}	1.28 x 10^{9}	4.50 x 10^{9}	3.92 x 10^{10}	3.99 x 10^{5}	4.07 x 10^{11}	2.62 x 10^{1}
	S9	H_2O* >> H_2O + *	1.06 x 10^{10}	3.59 x 10^{13}	1.42 x 10^{12}	9.53 x 10^{16}	6.19 x 10^{10}	1.16 x 10^{15}	7.08 x 10^{10}	1.73 x 10^{15}	2.14 x 10^{10}	1.67 x 10^{14}
	S10	R15 >> H_2O + ANI*	1.18 x 10^{11}	1.15 x 10^{15}	3.61 x 10^{11}	1.24 x 10^{16}	3.08 x 10^{10}	5.90 x 10^{14}	2.92 x 10^{10}	3.31 x 10^{14}	2.84 x 10^{10}	2.16 x 10^{14}
	S11	ANI* >> ANI + *	1.12 x 10^{11}	2.24 x 10^{9}	2.39 x 10^{11}	1.70 x 10^{9}	2.57 x 10^{9}	8.83 x 10^{9}	9.49 x 10^{10}	2.08 x 10^{6}	3.06 x 10^{11}	2.03 x 10^{1}
Guaiacol → Phenol	**S12**	R21 > TS21 > R22	2.42 x 10^{13}	1.06 x 10^{1}	1.33 x 10^{13}	8.41 x 10^{-2}	7.85 x 10^{12}	1.05 x 10^{-5}	9.91 x 10^{13}	3.24 x 10^{-3}	1.39 x 10^{13}	8.24 x 10^{-4}
	S13	R22 > TS22 > R23	9.47 x 10^{12}	7.16 x 10^{9}	6.88 x 10^{12}	3.87 x 10^{11}	1.73 x 10^{13}	3.54 x 10^{6}	6.70 x 10^{12}	1.34 x 10^{7}	1.55 x 10^{13}	8.78 x 10^{9}
	S14	R23 + H* >> R24 + *	1.90 x 10^{12}	1.88 x 10^{11}	3.75 x 10^{14}	9.34 x 10^{10}	2.04 x 10^{13}	1.57 x 10^{13}	4.55 x 10^{14}	1.38 x 10^{16}	2.02 x 10^{12}	2.65 x 10^{11}
	S15	R24 > TS23 > R25	1.05 x 10^{12}	1.55 x 10^{4}	1.11 x 10^{12}	1.54 x 10^{6}	4.09 x 10^{13}	7.66 x 10^{4}	6.27 x 10^{12}	3.21 x 10^{8}	4.88 x 10^{12}	6.59 x 10^{10}
	S16	R25 >> PHE + $HOCH_3$*	4.12 x 10^{10}	1.37 x 10^{9}	2.61 x 10^{11}	4.75 x 10^{9}	2.64 x 10^{10}	1.89 x 10^{12}	8.08 x 10^{9}	5.25 x 10^{5}	2.89 x 10^{11}	3.78 x 10^{2}
	S17	$HOCH_3$* >> $HOCH_3$ + *	1.32 x 10^{10}	9.04 x 10^{14}	8.53 x 10^{10}	1.01 x 10^{16}	4.80 x 10^{10}	1.46 x 10^{16}	1.40 x 10^{11}	9.44 x 10^{16}	2.20 x 10^{10}	8.01 x 10^{14}
	S18	R25 >> $HOCH_3$ + PHE*	6.07 x 10^{9}	3.55 x 10^{14}	2.03 x 10^{12}	5.43 x 10^{18}	9.68 x 10^{10}	5.14 x 10^{16}	7.66 x 10^{9}	1.48 x 10^{15}	1.14 x 10^{11}	4.62 x 10^{16}
	S19	PHE* >> PHE + *	8.99 x 10^{10}	3.48 x 10^{9}	1.10 x 10^{10}	8.80 x 10^{6}	1.31 x 10^{10}	5.35 x 10^{11}	1.48 x 10^{11}	3.35 x 10^{7}	5.55 x 10^{10}	6.57 x 10^{00}

Guaiacol → Catechol	**S20**	R31 >TS31 > R32	1.37 x 10^{12}	1.26 x 10^{1}	6.39 x 10^{12}	2.31 x 10^{2}	4.09 x 10^{13}	6.32 x 10^{-1}	1.37 x 10^{13}	1.61 x 10^{-1}	1.75 x 10^{13}	1.36 x 10^{-1}
	S21	R32 > TS32 > R33	9.14 x 10^{12}	1.42 x 10^{4}	2.81 x 10^{11}	1.54 x 10^{5}	2.24 x 10^{12}	2.44 x 10^{5}	1.06 x 10^{11}	5.93 x 10^{3}	8.39 x 10^{11}	1.03 x 10^{8}
	S22	R33 + H* >> R34 + *	1.35 x 10^{14}	7.95 x 10^{14}	2.84 x 10^{14}	1.99 x 10^{15}	9.88 x 10^{12}	1.69 x 10^{12}	1.03 x 10^{13}	1.84 x 10^{13}	6.66 x 10^{13}	1.14 x 10^{15}
	S23	R34 > TS33 > R35	9.66 x 10^{10}	4.05 x 10^{1}	1.91 x 10^{15}	5.53 x 10^{11}	2.03 x 10^{12}	1.47 x 10^{5}	1.96 x 10^{13}	2.58 x 10^{7}	9.21 x 10^{13}	9.34 x 10^{6}
	S24	R35 >> CAT + CH_4*	3.74 x 10^{10}	1.06 x 10^{8}	1.51 x 10^{10}	6.43 x 10^{6}	2.38 x 10^{12}	9.59 x 10^{9}	1.58 x 10^{11}	1.14 x 10^{6}	1.27 x 10^{13}	5.74 x 10^{2}
	S25	CH_4* >> CH_4 + *	3.97 x 10^{10}	1.39 x 10^{16}	9.97 x 10^{9}	4.72 x 10^{14}	2.63 x 10^{10}	1.73 x 10^{15}	4.24 x 10^{9}	6.28 x 10^{13}	1.87 x 10^{9}	1.81 x 10^{13}
	S26	R35* >> CH_4 + CAT*	3.19 x 10^{9}	1.18 x 10^{14}	2.82 x 10^{10}	3.46 x 10^{15}	3.62 x 10^{10}	3.83 x 10^{15}	1.31 x 10^{10}	5.22 x 10^{14}	1.79 x 10^{11}	4.55 x 10^{16}
	S27	CAT* >> CAT + *	4.65 x 10^{11}	1.25 x 10^{10}	5.35 x 10^{9}	8.77 x 10^{5}	1.73 x 10^{10}	4.33 x 10^{9}	5.11 x 10^{10}	1.38 x 10^{5}	1.33 x 10^{11}	2.28 x 10^{-1}
Catechol → Phenol	**S28**	CAT + * >> CAT*	2.04 x 10^{4}	6.78 x 10^{-7}	1.99 x 10^{4}	6.78 x 10^{-7}	2.09 x 10^{14}	6.78 x 10^{-7}	2.53 x 10^{4}	6.78 x 10^{-7}	2.55 x 10^{4}	6.78 x 10^{-7}
	S29	H_2 + * >> H_2*	1.50 x 10^{5}	6.16 x 10^{1}	1.48 x 10^{5}	6.16 x 10^{1}	1.54 x 10^{5}	6.15 x 10^{1}	1.87 x 10^{5}	6.16 x 10^{1}	1.89 x 10^{5}	6.16 x 10^{1}
	S30	CAT* + H* >> R41 + *	1.14 x 10^{14}	6.21 x 10^{14}	2.07 x 10^{12}	4.95 x 10^{11}	2.76 x 10^{12}	7.78 x 10^{11}	5.99 x 10^{12}	3.48 x 10^{12}	7.89 x 10^{12}	3.23 x 10^{13}
	S31	R41 > TS41 > R42	5.42 x 10^{12}	9.22 x 10^{1}	8.63 x 10^{11}	4.07 x 10^{-3}	6.40 x 10^{14}	3.57 x 10^{-3}	4.18 x 10^{14}	1.77 x 10^{-5}	2.71 x 10^{13}	1.89 x 10^{-5}
	S32	R42 > TS42 > R43	1.73 x 10^{14}	4.10 x 10^{11}	1.49 x 10^{13}	2.29 x 10^{8}	1.80 x 10^{14}	5.08 x 10^{8}	9.46 x 10^{12}	1.54 x 10^{6}	1.42 x 10^{13}	3.89 x 10^{8}
	S33	R43 + H* >> R44 + *	4.60 x 10^{12}	1.60 x 10^{12}	1.49 x 10^{12}	1.12 x 10^{11}	8.39 x 10^{12}	9.66 x 10^{11}	1.26 x 10^{13}	2.42 x 10^{13}	1.15 x 10^{13}	2.62 x 10^{13}
	S34	R44 > TS43 > R45	2.11 x 10^{12}	8.98 x 10^{-1}	2.87 x 10^{14}	2.54 x 10^{8}	8.06 x 10^{13}	2.04 x 10^{5}	1.78 x 10^{13}	1.65 x 10^{7}	4.92 x 10^{12}	3.44 x 10^{11}
	S35	R45 >> H_2O* + PHE	3.09 x 10^{9}	3.85 x 10^{7}	1.28 x 10^{9}	1.07 x 10^{6}	4.67 x 10^{10}	1.66 x 10^{13}	1.02 x 10^{11}	7.99 x 10^{6}	5.59 x 10^{12}	4.50 x 10^{4}
	S36	R45 >> H_2O + PHE*	3.63 x 10^{8}	3.97 x 10^{11}	1.65 x 10^{11}	1.16 x 10^{16}	2.21 x 10^{11}	3.61 x 10^{16}	4.88 x 10^{10}	4.13 x 10^{14}	2.16 x 10^{12}	1.15 x 10^{18}
	S37	PHE* >> PHE + *	8.99 x 10^{10}	3.48 x 10^{9}	1.10 x 10^{10}	8.79 x 10^{6}	1.31 x 10^{10}	5.35 x 10^{11}	1.48 x 10^{11}	3.35 x 10^{7}	5.55 x 10^{10}	6.57 x 10^{0}
Anisole → Phenol	**S38**	ANI + * > ANI*	2.06 x 10^{4}	6.77 x 10^{-7}	2.01 x 10^{4}	6.77 x 10^{-7}	2.11 x 10^{4}	6.77 x 10^{-7}	2.55 x 10^{4}	6.77 x 10^{-7}	2.58 x 10^{4}	6.77 x 10^{-7}
	S39	H_2 + * >> H_2*	1.50 x 10^{5}	6.16 x 10^{1}	1.48 x 10^{5}	6.16 x 10^{1}	1.54 x 10^{5}	6.15 x 10^{1}	1.87 x 10^{5}	6.16 x 10^{1}	1.89 x 10^{5}	6.16 x 10^{1}
	S40	ANI* + H* >> R51 + *	2.19 x 10^{12}	7.45 x 10^{11}	1.29 x 10^{13}	1.26 x 10^{13}	6.13 x 10^{11}	5.07 x 10^{10}	2.55 x 10^{13}	9.34 x 10^{13}	1.78 x 10^{13}	6.80 x 10^{13}
	S41	R51 > TS51 > R52	2.76 x 10^{14}	6.98 x 10^{2}	3.74 x 10^{14}	1.74 x 10^{2}	4.71 x 10^{13}	1.48 x 10^{-1}	6.22 x 10^{12}	1.43 x 10^{-2}	7.64 x 10^{12}	2.47 x 10^{-3}
	S42	R52 > TS52 > R53	2.19 x 10^{12}	6.70 x 10^{2}	2.47 x 10^{15}	3.07 x 10^{11}	1.14 x 10^{12}	2.55 x 10^{4}	4.63 x 10^{13}	1.91 x 10^{8}	4.99 x 10^{12}	1.12 x 10^{9}
	S43	R53 + H* >> R54 + *	2.74 x 10^{13}	1.43 x 10^{13}	6.11 x 10^{13}	1.86 x 10^{14}	4.05 x 10^{11}	2.52 x 10^{10}	2.14 x 10^{12}	1.43 x 10^{12}	3.64 x 10^{11}	5.54 x 10^{10}
	S44	R54 > TS53 > R54	2.80 x 10^{14}	7.91 x 10^{5}	4.28 x 10^{12}	8.47 x 10^{5}	5.73 x 10^{14}	1.21 x 10^{14}	9.27 x 10^{12}	1.35 x 10^{7}	4.76 x 10^{14}	4.04 x 10^{8}
	S45	R55 > PHE + CH_4*	2.26 x 10^{9}	7.92 x 10^{6}	7.30 x 10^{9}	1.73 x 10^{9}	8.37 x 10^{7}	9.91 x 10^{7}	4.46 x 10^{10}	1.92 x 10^{6}	2.73 x 10^{13}	3.23 x 10^{5}

	S46	R55 > CH_4 + PHE*	9.99 x 10^{8}	3.17 x 10^{13}	6.63 x 10^{9}	9.29 x 10^{14}	1.68 x 10^{8}	3.20 x 10^{11}	1.28 x 10^{9}	3.61 x 10^{12}	9.21 x 10^{11}	9.15 x 10^{17}
	S47	PHE* >> PHE + *	8.99 x 10^{10}	3.48 x 10^{9}	1.10 x 10^{10}	8.79 x 10^{6}	1.31 x 10^{10}	5.35 x 10^{11}	1.48 x 10^{11}	3.35 x 10^{7}	5.55 x 10^{10}	6.57 x 10^{0}
Anisole → Benzene	**S48**	ANI + * > ANI*	2.06 x 10^{4}	6.77 x 10^{-7}	2.01 x 10^{4}	6.77 x 10^{-7}	2.11 x 10^{4}	6.77 x 10^{-7}	2.55 x 10^{4}	6.77 x 10^{-7}	2.58 x 10^{4}	6.77 x 10^{-7}
	S49	H_2 + * >> H_2*	1.50 x 10^{5}	6.16 x 10^{1}	1.48 x 10^{5}	6.16 x 10^{1}	1.54 x 10^{5}	6.15 x 10^{1}	1.87 x 10^{5}	6.16 x 10^{1}	1.89 x 10^{5}	6.16 x 10^{1}
	S50	ANI* + H* >> R61 + *	2.19 x 10^{12}	7.45 x 10^{11}	1.29 x 10^{13}	1.26 x 10^{13}	1.14 x 10^{12}	1.58 x 10^{11}	2.64 x 10^{13}	9.89 x 10^{13}	1.84 x 10^{13}	7.16 x 10^{13}
	S51	R61 > TS61 > R62	3.94 x 10^{14}	1.00 x 10^{3}	3.40 x 10^{13}	7.47 x 10^{1}	2.44 x 10^{12}	7.65 x 10^{-7}	2.29 x 10^{12}	4.90x10^{-10}	1.43 x 10^{13}	3.55 x 10^{-8}
	S52	R62 > TS62 > R63	1.34 x 10^{13}	1.19 x 10^{10}	2.94 x 10^{12}	4.79 x 10^{8}	4.73 x 10^{12}	2.99 x 10^{6}	1.91 x 10^{15}	4.04 x 10^{11}	1.11 x 10^{12}	5.18 x 10^{6}
	S53	R63* + H* >> R64 + *	1.70 x 10^{11}	8.71 x 10^{9}	3.18 x 10^{14}	2.09 x 10^{15}	1.46 x 10^{14}	6.35 x 10^{14}	6.92 x 10^{12}	8.66 x 10^{12}	2.10 x 10^{13}	1.14 x 10^{14}
	S54	R64* > TS63 > R65	2.02 x 10^{14}	1.14 x 10^{3}	1.64 x 10^{11}	7.67 x 10^{1}	1.44 x 10^{11}	8.25 x 10^{1}	1.94 x 10^{12}	5.39 x 10^{7}	1.15 x 10^{12}	1.08 x 10^{9}
	S55	R65 >> BEN + $HOCH_3$*	8.29 x 10^{10}	5.60 x 10^{5}	1.89 x 10^{10}	2.08 x 10^{4}	1.34 x 10^{9}	8.28 x 10^{7}	3.40 x 10^{10}	2.68 x 10^{3}	2.07 x 10^{11}	1.72 x 10^{1}
	S56	R65 >> $HOCH_3$ + BEN*	2.23 x 10^{10}	6.54 x 10^{15}	3.83 x 10^{10}	7.27 x 10^{15}	1.22 x 10^{10}	1.31 x 10^{15}	1.24 x 10^{11}	1.18 x 10^{17}	1.54 x 10^{10}	4.26 x 10^{16}
	S57	BEN* >> BEN + *	4.92 x 10^{10}	7.74 x 10^{4}	4.21 x 10^{10}	2.87 x 10^{4}	5.29 x 10^{9}	9.21 x 10^{8}	3.85 x 10^{10}	2.14 x 10^{3}	2.95 x 10^{11}	3.22 x 10^{-1}
Phenol → Benzene	**S58**	PHE + * > PHE*	2.21 x 10^{4}	1.39 x 10^{-6}	2.16 x 10^{4}	1.39 x 10^{-6}	2.27 x 10^{4}	1.39x 10^{-6}	2.73 x 10^{4}	1.39 x 10^{-6}	2.76 x 10^{4}	1.39 x 10^{-6}
	S59	H_2 + * >> H_2*	1.50 x 10^{5}	6.16 x 10^{1}	1.48 x 10^{5}	6.16 x 10^{1}	1.54 x 10^{5}	6.15 x 10^{1}	1.87 x 10^{5}	6.16 x 10^{1}	1.89 x 10^{5}	6.16 x 10^{1}
	S60	PHE* + H* >> R71 + *	2.64 x 10^{12}	6.25 x 10^{11}	1.39 x 10^{13}	9.96 x 10^{12}	3.46 x 10^{12}	1.11 x 10^{12}	2.45 x 10^{13}	8.18 x 10^{13}	2.81 x 10^{12}	1.50 x 10^{12}
	S61	R71 > TS71 > R72	1.65 x 10^{14}	6.49 x 10^{2}	2.60 x 10^{11}	6.61 x 10^{-4}	1.78 x 10^{14}	7.48 x 10^{-5}	1.78 x 10^{13}	1.14 x 10^{-5}	1.86 x 10^{13}	1.06 x 10^{-7}
	S62	R72 > TS72 > R73	2.38 x 10^{11}	8.51 x 10^{1}	2.23 x 10^{12}	6.16 x 10^{7}	9.74 x 10^{12}	4.86 x 10^{7}	7.45 x 10^{13}	1.58 x 10^{9}	1.67 x 10^{13}	4.73 x 10^{11}
	S63	R73 + H* >> R74 + *	1.05 x 10^{13}	2.22 x 10^{12}	1.26 x 10^{13}	1.06 x 10^{13}	6.17 x 10^{13}	1.16 x 10^{14}	2.04 x 10^{13}	1.85 x 10^{14}	4.40 x 10^{12}	3.23 x 10^{12}
	S64	R74 > TS73 > R75	3.98 x 10^{13}	1.54 x 10^{3}	1.87 x 10^{13}	2.40 x 10^{7}	7.62 x 10^{12}	6.69 x 10^{3}	1.44 x 10^{13}	5.91 x 10^{7}	5.58 x 10^{12}	9.66 x 10^{10}
	S65	R75 >> BEN + H_2O*	3.22 x 10^{12}	2.81 x 10^{9}	3.78 x 10^{9}	5.31 x 10^{2}	4.88 x 10^{7}	4.99 x 10^{5}	4.01 x 10^{11}	4.42 x 10^{5}	7.69 x 10^{11}	6.05 x 10^{0}
	S66	R75 >> H_2O + BEN*	6.91 x 10^{11}	1.31 x 10^{18}	1.27 x 10^{11}	1.76 x 10^{15}	5.71 x 10^{8}	6.27 x 10^{11}	7.38 x 10^{11}	3.56 x 10^{17}	5.59 x 10^{10}	3.14 x 10^{15}
	S67	BEN* >> BEN + *	4.92 x 10^{10}	7.74 x 10^{4}	4.21 x 10^{10}	2.87 x 10^{4}	5.29 x 10^{9}	9.21 x 10^{8}	3.85 x 10^{10}	2.14 x 10^{3}	2.95 x 10^{11}	3.22 x 10^{-1}
	S68	GUA* >> GUA + *	8.58 x 10^{10}	1.04 x 10^{10}	1.22 x 10^{11}	1.61 x 10^{9}	6.18 x 10^{10}	1.30 x 10^{12}	2.71 x 10^{11}	5.31 x 10^{7}	3.95 x 10^{10}	4.43 x 10^{-1}

6.3.4 Influence of operating condition.

Figure 6.7 shows the evolution of the HDO products in the gas phase as a function of time at three different temperatures (273 K, 573 K and 1073 K). From 273 K, the generation of products is observed where the guaiacol conversion occurs before the first-time step, 0.02 s.

At 273 K, *Pd (111)* presents a high phenol concentration because of the fast guaiacol conversion upon its adsorption. This is due to the high-rate constant for the species conversion with a $k = 3.80 \times 10^{-11}$ s^{-1} (S19). On *Co (0001)*, the anisole formation reaches the steady state after 0.2 s, whereas the catechol concentration does not change after 0.02 s on *Cu (111)* and *Ni (111)*; this quick reaction is due to the catechol rate of formation (*S20*) compared to phenol and anisole. Meanwhile, benzene concentration is observed on *Pt (111)*, rising after 0.1 s, and keeping a steady state after that. This can be attributed to the hydrogenation catalytic performance on Pt (*S62*) with a high rate of 10^9 s^{-1}.

At 573 K, all metals exhibit a high catechol concentration, suggesting that guaiacol converts into catechol in a short time interval at this temperature; this quick reaction is due to the high rate in the C_{alkyl}−O dissociation compared to anisole and phenol (*S20*). Pd (111) is the only metal with a high phenol concentration compared to catechol. This is attributed to the high rate of phenol formation (*S19*) compared to catechol, suggesting that catechol is formed as an intermediate, similar result observed by Teles *et al*.[45] The guaiacol conversion is complete on Co, Ni, Pd and Pt at this temperature and when increasing the temperature.

At 1073 K, the concentration profile does change when increasing the temperature. Phenol dominates on Pd (111), whereas catechol is the main product on *Co (0001)*, *Ni (111)* and *Pt (111)*. *Cu (111)* is the only metal that presents a low conversion compared to the other metals, where anisole formation has the highest rate constant (*S11*) with a slight difference between phenol and catechol. A negligible increase in benzene production is observed on *Ni (111)* with respect to the time, showing a marginal increase after 0.4 s. This increase is proportional to the competitive rate with an order of 10^9 s^{-1} for the benzene hydrogenation (*S62*).

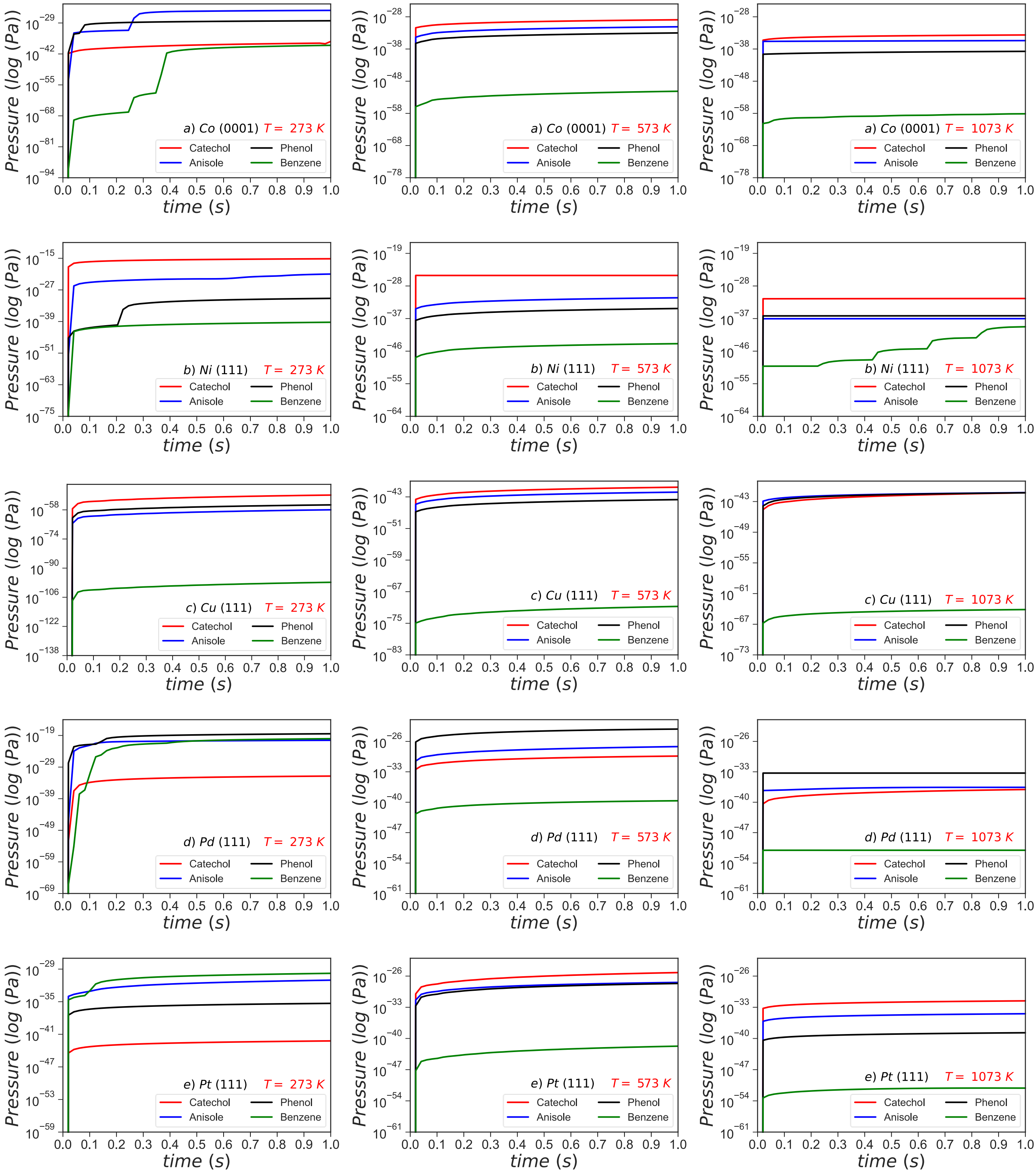

Figure 6.7. *Logarithmic graphs of the anisole, phenol, catechol, and benzene concentration in the gas-phase on the transition metal catalysts at 273 K, 573 K and 1073 K as a function of the time.*

6.3.5 Temperature-programmed reaction (TPR)

The temperature-programmed reaction (TPR) profiles of all the catalysts studied are displayed in ***Figure 6.8***, with a heating rate of 10 K s^{-1}. The TPR profiles exhibit the formation of the species as the temperature increases. These peaks were recorded in a temperature range from 273 K to 573 K for *Co (0001), Ni (111) and Pd (111)*. For *Cu (111)* and *Pt (111)*, the temperature range was from 273 K to 1073 K and 273 K to 673 K, respectively. All the profiles are normalised for direct comparison.

The results show that the peak for guaiacol desorption is proportional to the guaiacol adsorption energy, which follows this order Cu > Co > Ni > Pd > Pt (*More details in Chapter 5*), same results reported by Bjelić *et al.*[42] *Cu (111), Ni (111)* and *Co (0001)* exhibit the guaiacol desorption peaks at low temperatures, where the Cu desorption peak is seen at 293 K; this is due to the weakest adsorption strength of guaiacol on the metal. *Pt (111)* is the only metal that presents slow desorption (around 600 K) due to the strong strength shown with the compound. The slow guaiacol desorption on Pt is explained due to the endothermic behaviour and high activation barrier presented in the O−bond scission reactions. As a result, the guaiacol conversion takes place at high temperatures.

Catechol production is predominant in *Ni (111)*, where the peak reaches a maximum at 373 K. At the same time, phenol formation shows two peaks around 383 K and 413 K on the same metal. This can be attributed to the recombination of phenol on the surface due to the decomposition of catechol. On *Pd (111)* and *Co (0001)*, the anisole production takes place after 350 K, which is consistent with previous reports that indicate the anisole reaction takes place at 120 °C (393 K) on SiO_2.[46] Meanwhile, *Pt (111)* presents a broad phenol peak with a maximum peak at 593 K; this is similar to the results reported by Xu *et al*.[47] They reported that phenol molecule starts to form until 473 K from oxide surfaces; the same results were found for Ni and Pt in this study.

Finally, the TPR profile for Pt shows a broad peak for benzene production at 298 K, followed by Pd > Ni > Co > Cu. The fast benzene formation on Pt and Pd agrees with the low activation energies in the hydrogenation reaction and the high-rate constant for the benzene formation (*S67*). Experimental studies show that the benzene formation starts around 178 K with a broad peak at 320 K on *Pt (111)*, a similar effect seen in this study.[48] Although benzene reaction peak appears between 673 K and 773 K on SiO$_2$.[46, 49] *Cu (111)* is the only metal that fails in species production. The benzene reaction starts at 823 K with a low concentration, requiring high temperatures to form hydrocarbon products, concluding the low energy-efficient of the Cu catalyst HDO chemical reaction.

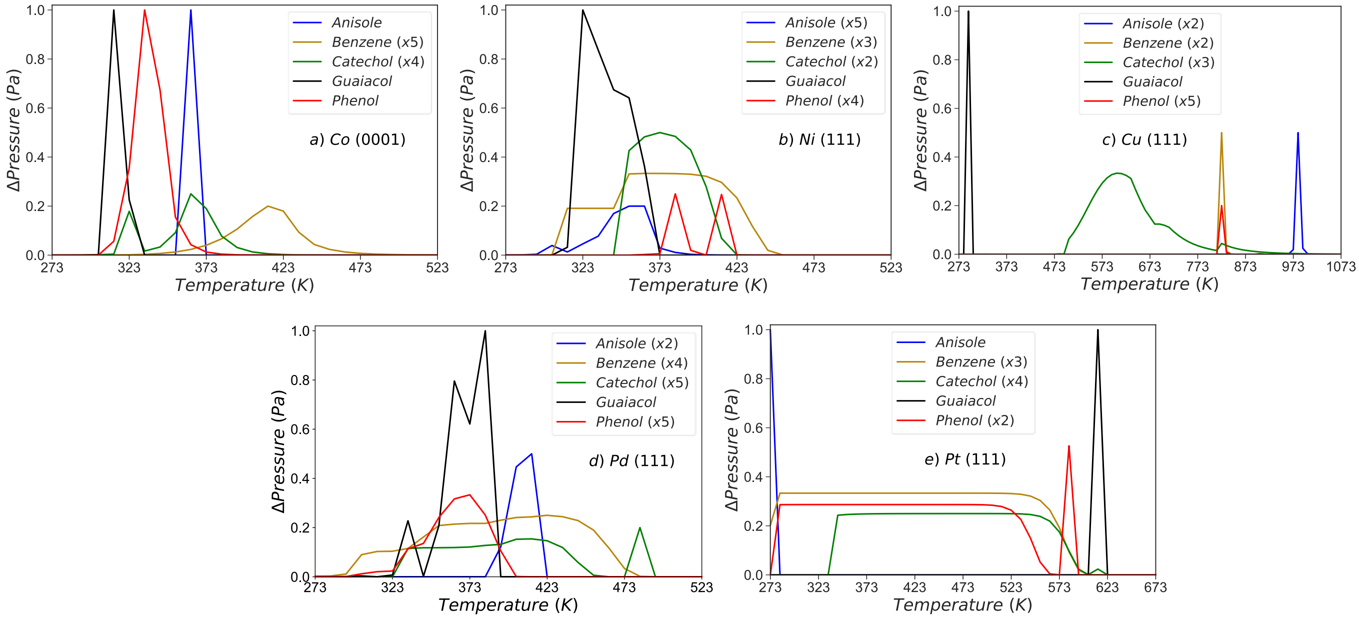

Figure 6.8. *Simulated Temperature-programmed reaction (TPR) profiles of the guaiacol conversion in the gas phase for a) Co (0001), Ni (111), c) Cu (111), d) Pd (111) and e) Pt (111). Indicated visibility's scaling factors have rescaled individual species' peaks.*

6.4 Chapter conclusion

A microkinetic analysis of the guaiacol HDO conversion using five transition metal catalysts, *Co (0001), Ni (111), Cu (111), Pd (111)*, and *Pt (111),* was performed using density functional theory (DFT) calculations. Reaction and activation free energies as a function of the temperature were studied in a range between 573 K to 1073 K; the results demonstrated that the demethylation pathway (DME) to convert guaiacol into catechol is the most accessible mechanism on *Co (0001)* and *Ni (111)* at 573 K.

In contrast, *Pd (111)* and *Pt (111)* showed a poor performance in the deoxygenation activity due to their high energy barriers and endothermic behaviour. This limits the scission of hydroxyl and methoxy groups from the aromatic ring. The previous results were confirmed with the kinetic rate analyses, where the hydrogenation reactions are faster than the deoxygenation reactions. In general, high temperatures favoured the deoxygenation reactions and increased the kinetic rate. TPR analysis was incorporated into the microkinetic model of the system to study the formation of the gas-phase products. The results demonstrated that the guaiacol adsorption strength is linked with the desorption temperature peak. *Pt (111)* presents the highest interaction with the oxy-molecule, giving a guaiacol slow desorption compared to the other metals.

Cu (111) presents the fastest desorption rate at 273 K for guaiacol, producing a low concentration of phenol and benzene at high temperatures (> 773 K). In contrast, Pt and Pd do not require high temperatures for product formation, such as catechol and phenol. This is due to their effectiveness in hydrogenation reactions. Although high temperatures are needed to favour the desorption of guaiacol, this is due to their endothermic behaviours, requiring more energy for the product's yield and decreasing the catalyst life. *Ni (111)* presents a guaiacol desorption at moderate temperatures (around 300 K), resulting in an increase in catechol, phenol, and benzene production at early stages (< 500 K). Moreover, Ni exhibits a fast-kinetic rate at 573 K and performs well in the deoxygenation and hydrogenation reactions, including a high concentration of hydrocarbon compounds, such as benzene. This makes it a good candidate for the guaiacol conversion at industrial temperatures for HDO processes. The results found in this study describe a better understanding of the HDO guaiacol process, giving insight into the catalyst design for active and selective materials.

6.5 References

1. J. K. Nørskov, F. Studt, F. Abild-Pedersen and T. Bligaard, *Fundamental concepts in heterogeneous catalysis*, John Wiley & Sons, 2014.
2. J. K. Nørskov, F. Abild-Pedersen, F. Studt and T. Bligaard, *Proceedings of the National Academy of Sciences*, 2011, **108**, 937-943.
3. M. Rellán-Piñeiro and N. r. López, *ACS Sustainable Chemistry & Engineering*, 2018, **6**, 16169-16178.
4. A. Bjelić, M. Grilc and B. Likozar, *Chemical Engineering Journal*, 2018, **333**, 240-259.
5. T. Nimmanwudipong, R. C. Runnebaum, D. E. Block and B. C. Gates, *Energy & fuels*, 2011, **25**, 3417-3427.

6. D. Gao, Y. Xiao and A. Varma, *Industrial & Engineering Chemistry Research*, 2015, **54**, 10638-10644.
7. R. C. Runnebaum, T. Nimmanwudipong, D. E. Block and B. C. Gates, *Catalysis Science & Technology*, 2012, **2**, 113-118.
8. F. Arena, F. Frusteri, A. Parmaliana and N. Giordano, *Applied Catalysis A: General*, 1995, **125**, 39-59.
9. G. Henkelman and H. Jónsson, *The Journal of chemical physics*, 2000, **113**, 9978-9985.
10. G. Henkelman, B. P. Uberuaga and H. Jónsson, *The Journal of chemical physics*, 2000, **113**, 9901-9904.
11. G. Henkelman and H. Jónsson, *The Journal of chemical physics*, 1999, **111**, 7010-7022.
12. X. Lu, J. Zhang, W.-K. Chen and A. Roldan, *Nanoscale Advances*, 2021, **3**, 1624-1632.
13. K. W. Kolasinski, *Surface science: foundations of catalysis and nanoscience*, John Wiley & Sons, 2012.
14. H. Ma and W. F. Schneider, *Journal of Catalysis*, 2020, **383**, 322-330.
15. S. M. Wetterer, *Helium atom reflectivity study of physisorption and chemisorption on single crystal metal surfaces*, Princeton University, 1998.
16. I. G. Pitt, R. G. Gilbert and K. R. Ryan, *The Journal of Physical Chemistry*, 1994, **98**, 13001-13010.
17. A. N. K. Lup, F. Abnisa, W. W. Daud and M. Aroua, presented in part at IOP Conference Series: Materials Science and Engineering, 2018
18. S. Derrouiche and D. Bianchi, *Langmuir*, 2004, **20**, 4489-4497.
19. S. J. Carey, W. Zhao, Z. Mao and C. T. Campbell, *The Journal of Physical Chemistry C*, 2018, **123**, 7627-7632.
20. D. Gao, C. Schweitzer, H. T. Hwang and A. Varma, *Industrial & Engineering Chemistry Research*, 2014, **53**, 18658-18667.
21. T. Mochizuki, S.-Y. Chen, M. Toba and Y. Yoshimura, *Applied Catalysis B: Environmental*, 2014, **146**, 237-243.
22. N. T. Tran, Y. Uemura, S. Chowdhury and A. Ramli, *Applied Catalysis A: General*, 2016, **512**, 93-100.
23. J. E. Peters, J. R. Carpenter and D. C. Dayton, *Energy & Fuels*, 2015, **29**, 909-916.
24. J.-s. Bredenberg, M. Huuska, J. Räty and M. Korpio, *Journal of Catalysis*, 1982, **77**, 242-247.
25. D. C. Elliott and T. R. Hart, *Energy & Fuels*, 2009, **23**, 631-637.
26. A. Gutierrez, R. K. Kaila, M. L. Honkela, R. Slioor and A. O. I. Krause, *Catalysis today*, 2009, **147**, 239-246.
27. Q. Tan, G. Wang, L. Nie, A. Dinse, C. Buda, J. Shabaker and D. E. Resasco, *ACS Catalysis*, 2015, **5**, 6271-6283.
28. M. Bykova, O. Bulavchenko, D. Y. Ermakov, M. Y. Lebedev, V. Yakovlev and V. Parmon, *Catalysis in industry*, 2011, **3**, 15-22.
29. Y.-C. Lin, C.-L. Li, H.-P. Wan, H.-T. Lee and C.-F. Liu, *Energy & Fuels*, 2011, **25**, 890-896.

30. J. Sun, A. M. Karim, H. Zhang, L. Kovarik, X. S. Li, A. J. Hensley, J.-S. McEwen and Y. Wang, *Journal of catalysis*, 2013, **306**, 47-57.
31. M. Á. González-Borja and D. E. Resasco, *Energy & Fuels*, 2011, **25**, 4155-4162.
32. J. Chang, T. Danuthai, S. Dewiyanti, C. Wang and A. Borgna, *ChemCatChem*, 2013, **5**, 3041-3049.
33. J. Wildschut, F. H. Mahfud, R. H. Venderbosch and H. J. Heeres, *Industrial & Engineering Chemistry Research*, 2009, **48**, 10324-10334.
34. J. Wildschut, I. Melián-Cabrera and H. Heeres, *Applied Catalysis B: Environmental*, 2010, **99**, 298-306.
35. S. Boullosa-Eiras, R. Lødeng, H. Bergem, M. Stöcker, L. Hannevold and E. A. Blekkan, *Catalysis Today*, 2014, **223**, 44-53.
36. E.-J. Shin and M. A. Keane, *Industrial & engineering chemistry research*, 2000, **39**, 883-892.
37. H. Weigold, *Fuel*, 1982, **61**, 1021-1026.
38. G. S. Foo, A. K. Rogers, M. M. Yung and C. Sievers, *ACS Catalysis*, 2016, **6**, 1292-1307.
39. J. Lu, S. Behtash, O. Mamun and A. Heyden, *ACS Catalysis*, 2015, **5**, 2423-2435.
40. K. Agrawal, A. Roldan, N. Kishore and A. J. Logsdail, *Catalysis Science & Technology*, 2022, **12**, 843-854.
41. D. Otyuskaya, J. W. Thybaut, R. Lødeng and G. B. Marin, *Energy & Fuels*, 2017, **31**, 7082-7092.
42. A. Bjelić, M. Grilc, M. Huš and B. Likozar, *Chemical Engineering Journal*, 2019, **359**, 305-320.
43. P. M. Mortensen, J.-D. Grunwaldt, P. A. Jensen and A. D. Jensen, *ACS Catalysis*, 2013, **3**, 1774-1785.
44. A. M. Verma and N. Kishore, *Physical Chemistry Chemical Physics*, 2017, **19**, 25582-25597.
45. C. A. Teles, et al., *Molecular Catalysis*, 2021, 111491.
46. X. Lan, E. J. M. Hensen and T. Weber, *Applied Catalysis A: General*, 2018, **550**, 57-66.
47. B. Q. Xu, T. Yamaguchi and K. Tanabe, *Materials Chemistry and Physics*, 1988, **19**, 291-297.
48. C. Xu, Y. L. Tsai and B. E. Koel, *The Journal of Physical Chemistry*, 1994, **98**, 585-593.
49. R. Reocreux, C. A. Ould Hamou, C. Michel, J. B. Giorgi and P. Sautet, *ACS Catalysis*, 2016, **6**, 8166-8178.

7

Conclusions and Future works

7.1 Conclusions

This thesis provides a study of catalytic materials, such as transition metals and oxide support, for the bio-oil upgrading through the hydrodeoxygenation (HDO) process using guaiacol as a main model compound. The electronic and geometrical properties of the catalytic materials were analysed using computational methods based on the density functional theory (DFT).

In Chapter 3, DFT calculations were carried out to explore the relationship between 13 transition metals (TMs) properties, Fe, Co, Ni, Cu, Mo, Ru, Rh, Pd, Ag, W, Ir, Pt and Au. Moreover, their affinity for hydrogen and oxygen was studied as critical species in the valorisation of biomass. The relation of these parameters defined the trends of the HDO process on biomass-derived compounds. It was found that the hydrogen and oxygen adsorption energies in the most stable sites have a linear relation with the electronic properties of these metals that will rationalise the surface's ability to bind the biomass-derived compounds and break the C–O bonds. This will accelerate the catalyst innovation for low temperature and efficient HDO processes on biomass derivates, e.g. guaiacol and anisole. Among the monometallic catalysts explored, the scaling relationship indicated that Ni has a favourable balance between hydrogen and oxygen affinities according to the d-band centre and d-band width models. Among all the descriptors used in the scaling relationship study, it was found that a linear combination of work function and d-band properties gives a significantly better correlation with H and O interaction with the TM studied.

In *Chapter 4*, the acid-base properties of five oxide surfaces, γ-Al_2O_3, CeO_2, MgO, β-SiO_2 and anatase-TiO_2, were investigated and their interaction with model compounds derived from lignin. DFT calculations were also used to understand the surface's hydroxylation role. The results showed that moderate hydroxyl coverage on the amphoteric *γ-*Al_2O_3 *(110)* slightly strengthens the oxy-compounds' adsorption due to increased Lewis acidity. Similarly, low hydroxyl coverage on the reducible *a-*TiO_2 *(101)* enlarges its adsorption capacity by up to 42 % compared with its clean surface. The higher affinity is attributed to the more favourable interaction between the surface-OH groups and the aromatic rings. Overall, the results indicate that hydroxyl coverage enhances the amphoteric and reducible adsorption capacity towards aromatic species.

In *Chapter 5*, a systematic examination of the guaiacol's HDO mechanism is reported to form benzene on six transition metal (TM) catalysts based on the results from *Chapter 3*, *Fe (110), Co (0001), Ni (111), Cu (111), Pd (111)* and *Pt (111)*, using density functional theory calculations. The results suggested a preferable C_{aryl}−O bond scission on *Ni (111)* and *Co (0001)*, whereas on *Fe (110)*, the C_{aryl}−OH bond scission is the most likely pathway. The C−O scission on *Pd (111)* and *Pt (111)* is not energetically feasible due to their high activation barriers and endothermic behaviour. *Fe (110)* also demonstrated its high oxophilic character by challenging the desorption of oxygenated products. A detailed analysis concluded that *Co (0001)* and *Ni (111)* are the most favourable in breaking phenolic compounds' C−O type bonds. Brønsted-Evans-Polanyi (BEP) and transition state scaling (TSS) models were implemented on the catalytic results to derive trends and accelerate the catalyst design and innovation. TSS demonstrated a reliable trend in defining dissociation and association reaction energies. The phenyl ring and oxo-groups; and the metal-molecule distances complement the catalysts' oxophilicity as selectivity descriptors in the HDO process.

In *Chapter 6*, a microkinetic analysis of the guaiacol HDO conversion was developed using five TM catalysts. The results showed that the demethylation pathway (DME) to convert guaiacol into catechol is the most accessible pathway on *Co (0001)* and *Ni (111)* at 573 K. Meanwhile, *Pd (111)* and *Pt (111)* showed a poor performance in the deoxygenation activity due to their high energy barriers and endothermic behaviour. The results were confirmed with the kinetic rate analyses, where the hydrogenation reactions are faster than the deoxygenation reactions. Temperature-programmed reaction (TPR) study was incorporated into the microkinetic model, revealing that guaiacol desorption presents desorption whose maximum peak is reached around 300

K on Ni. This increases the catechol, benzene, and phenol at 573 K, the experimental temperature used for the HDO process. Moreover, Ni exhibits a fast kinetic rate, performing well in deoxygenation and hydrogenation reactions than Pd and Pt. Therefore, Ni can be a good candidate for the guaiacol conversion under optimal and suitable conditions for the HDO guaiacol process.

7.2 Future work

7.2.1 Bimetallic alloys

Ni as a catalyst has demonstrated its good performance in the HDO guaiacol process. However, there are some challenges in the catalyst process development to reduce the running cost and H_2 consumption. The combination of different metals allows varying the geometrical and electronic properties of the catalyst surface, creating a promising alternative for the catalytic process that surpasses the monometallic catalysts. Bimetallic catalysts have been employed in HDO reactions due to the catalytic function of two metals. Metals, such as Ni and Pt, have a high hydrogenation activity, and oxophilic metals, e.g. Mo, W and Fe, are added to promote the C−OH and $C-OCH_3$ scission.

Different works have been carried out on the ideal surface alloying using Ni-M and Pt-M with another transition metal (M) to achieve oxygen adsorption, enhancing the C−O scission. Although experimental studies have been carried out to know the performance of bimetallic catalysts, a complete understanding of the role of bimetallic alloys in the HDO reactions at an atomic level is still needed. The design of bimetallic catalysts (Ni-M, Pt-M) requires active consideration of the actual surface state of the catalyst, which may differ from the bulk composition due to the spontaneous segregation of atoms in the surface layers. Two types of segregation need to be considered: segregation and antisegregation. The DFT studies allow the prediction of the segregation behaviour with metal (M) and Pt or Ni atoms.

7.2.2 Ni_n clusters supported on γ-Al_2O_3, and a-TiO_2

Many reactions are carried out at high temperatures; therefore, the study of the thermal stability of catalysts needs to be required. The metal-support interaction plays an essential role in heterogeneous catalysts. This interaction helps stabilise dispersed active metal nanoparticles on a support to avoid sintering and deactivation. Therefore, a strong metal-support interaction is crucial to prevent the sintering of metal nanoparticles. The strong interaction between the supports and dispersed species is strongly correlated to the catalytic activity of the surface, where the electronic properties of clusters and oxides are perturbed. Studies of selected materials such as γ-Al_2O_3 and a-TiO_2 (anatase form) supported nickel-based can be carried out.

The cluster size is another crucial element because depositing size-selected metal clusters onto a well-defined support surface provides a desirable way to control the cluster size and investigate the metal-support interaction. Therefore, a DFT study of the adsorption of small Ni clusters using different catalysts such as γ-Al_2O_3 and a-TiO_2 is needed in a range of 1-5 atoms. This is due to the catalytic activity of the surface is directly linked to the nature of the metal-support interaction.

A

Appendix

***Table A1**. Steps involved in the guaiacol HDO conversion based on Scheme 5.1*

	Guaiacol adsorption	
S1	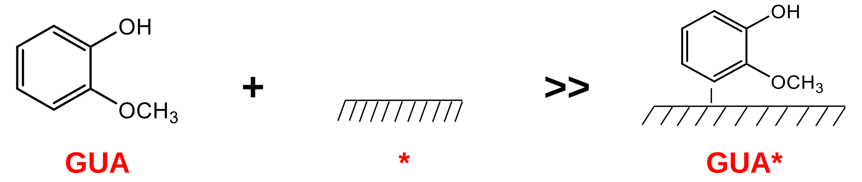	GUA + * >> GUA*
S2		H_2 + * >> H*
S3	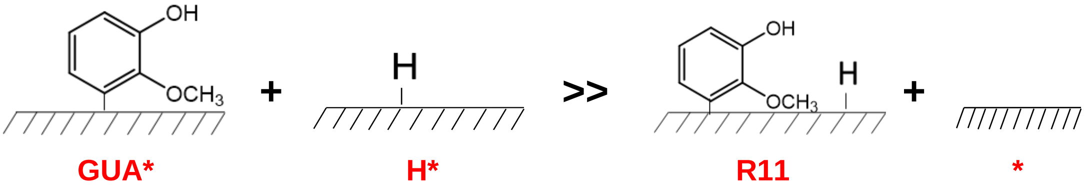	GUA* + H* >> R11 + *
	Guaiacol → Anisole	
S4	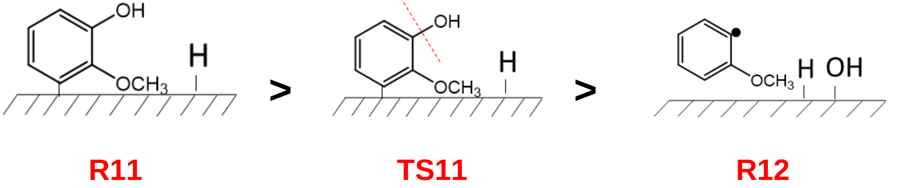	R11 > TS11 > R12
S5	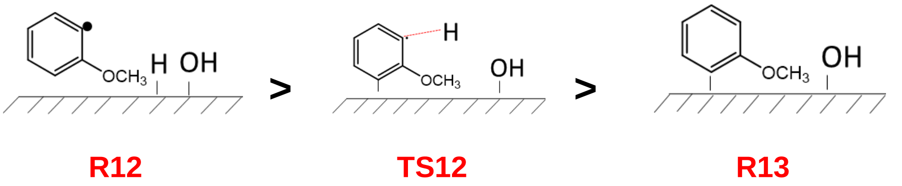	R12 > TS12 > R13
S6	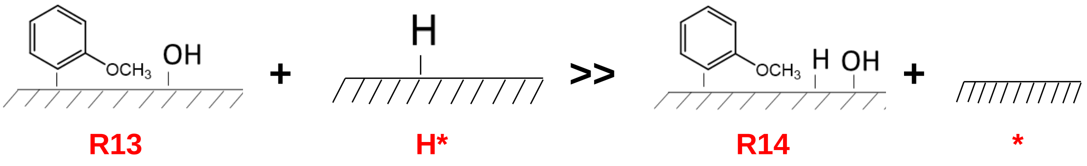	R13 + H* > R14 + *

S7	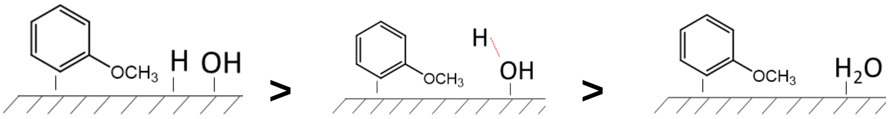 **R14** **TS13** **R15**	R14 > TS13 > R15
S8	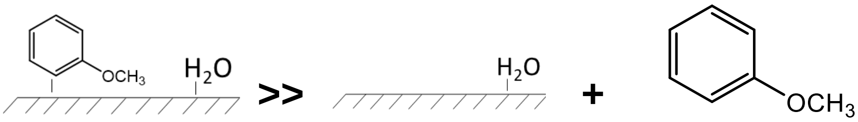 **R15** **H_2O*** **ANI**	R15 >> H_2O* + ANI
S9	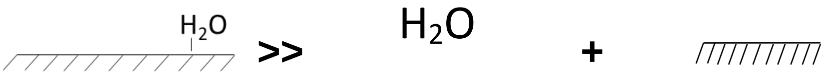 **H_2O *** **H_2O** *****	H_2O* >> H_2O + *
S10	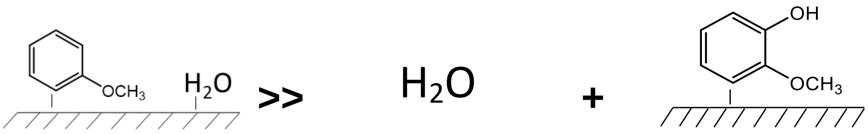 **R15** **H_2O** **ANI***	R15 >> H_2O + ANI*
S11	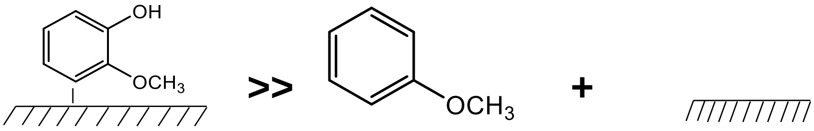 **ANI*** **ANI** *****	ANI* >> ANI + *
	Guaiacol → Phenol	
S12	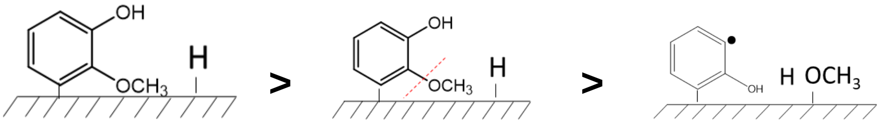 **R21** **TS21** **R22**	R21 > TS21 > R22
S13	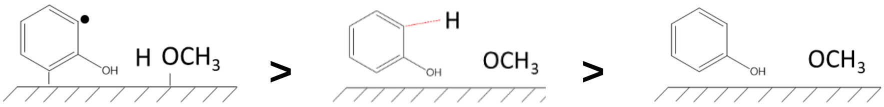 **R22** **TS22** **R23**	R22 > TS22 > R23
S14	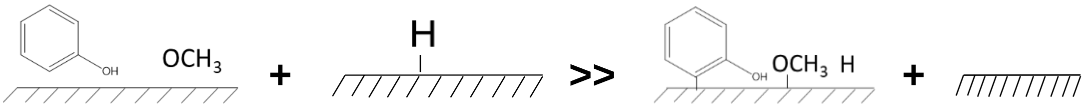 **R23** **H*** **R24** *****	R23 + H* >> R24 + *
S15	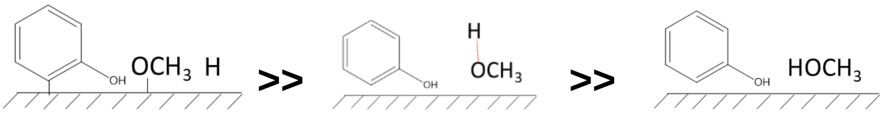 **R24** **TS23** **R25**	R24 > TS23 > R25

S16	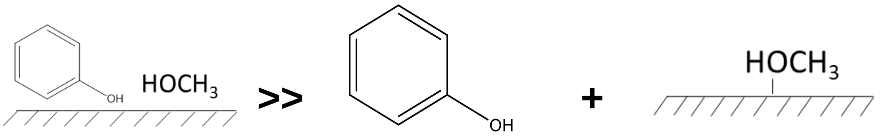 **R25** **PHE** **$HOCH_3$***	R25 >> PHE + $HOCH_3$*
S17	 **$HOCH_3$*** **$HOCH_3$** *****	$HOCH_3$* >> $HOCH_3$ + *
S18	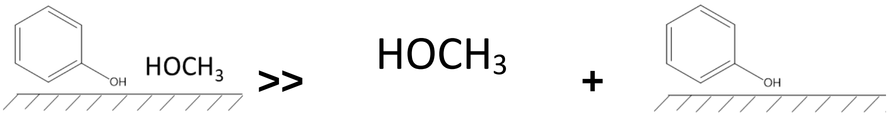 **R25** **$HOCH_3$** **PHE***	R25 >> $HOCH_3$ + PHE*
S19	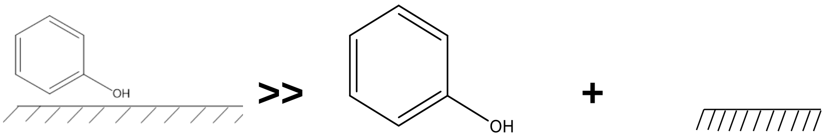 **PHE*** **PHE** *****	PHE* >> PHE + *

Guaiacol → Catechol

S20	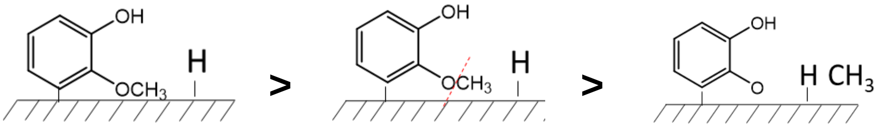 **R31** **TS31** **R32**	R31 > TS31 > R32
S21	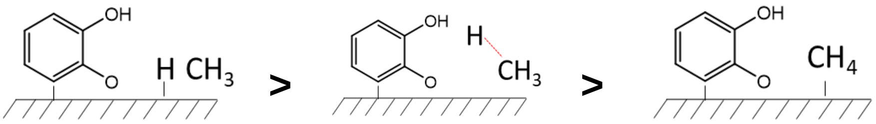 **R32** **TS32** **R33**	R32 > TS32 > R33
S22	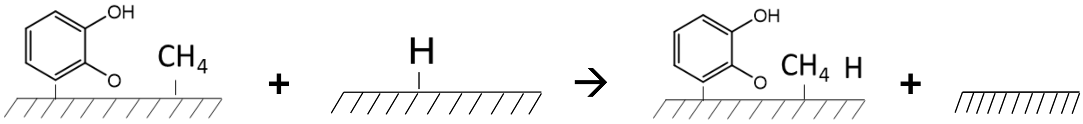 **R33** **H*** **R34** *****	R33 + H* >> R34 + *
S23	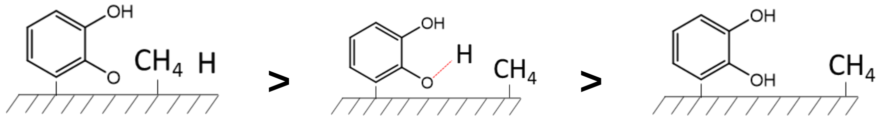 **R34** **TS33** **R35**	R34 > TS33 > R35
S24	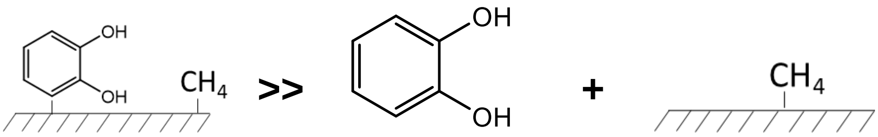 **R35** **CAT** **CH_4***	R35 >> CAT + CH_4*

S25

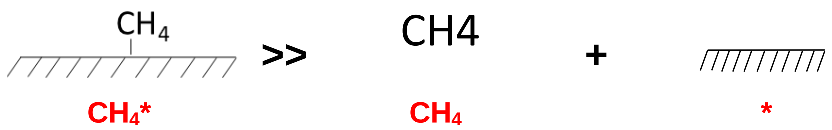

CH_4* >> CH_4 + *

S26

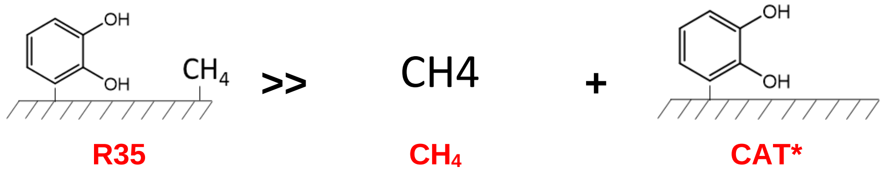

R35 >> CH_4 + CAT*

S27

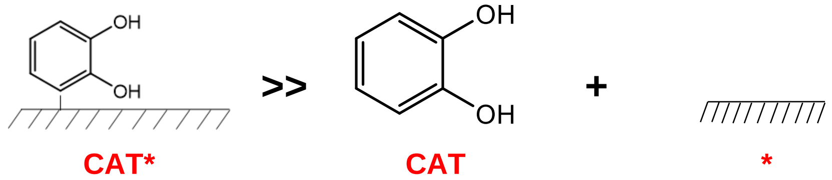

CAT* >> CAT + *

Catechol → Phenol

S28

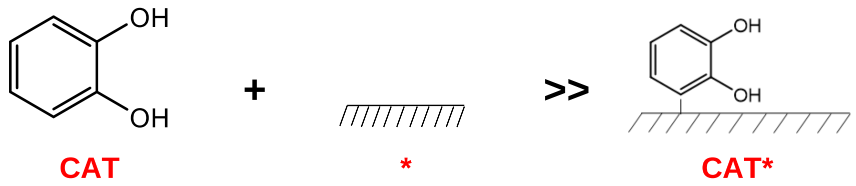

CAT + * >> CAT*

S29

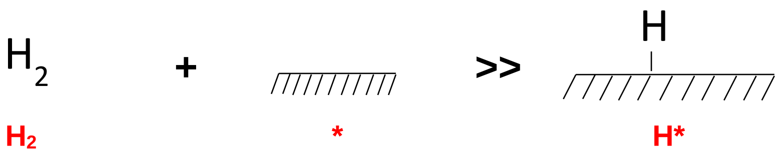

H_2 + * >> H*

S30

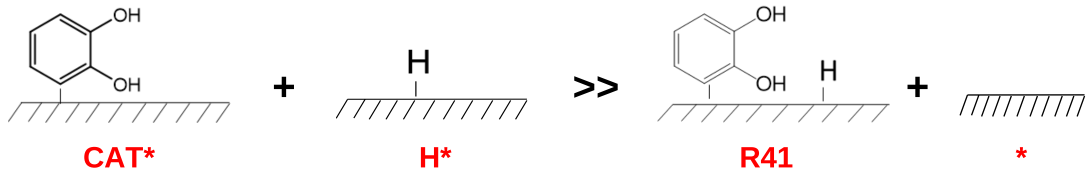

CAT* + H* >> R41 + *

S31

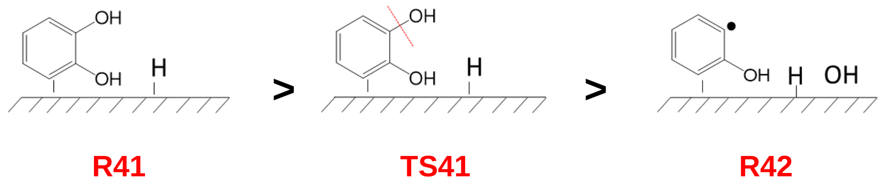

R41 > TS41 > R42

S32

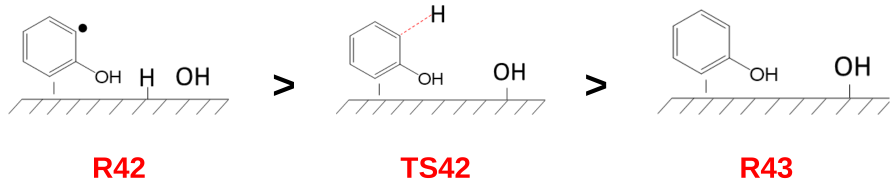

R42 > TS42 > R43

S33

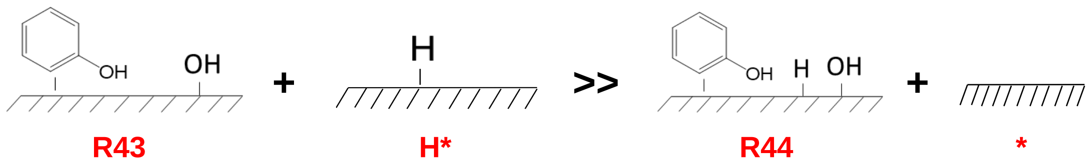

R43 + H* >> R44 + *

S34	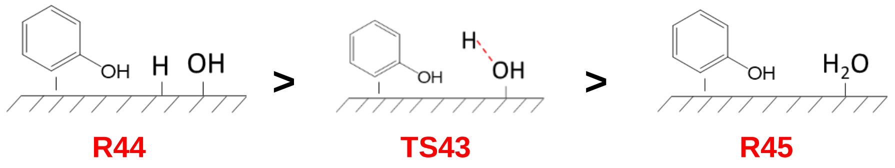	R44 > TS43 > R45
S35	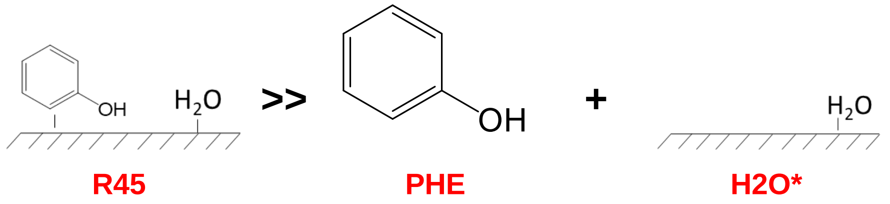	R45 >> PHE + H_2O*
S36	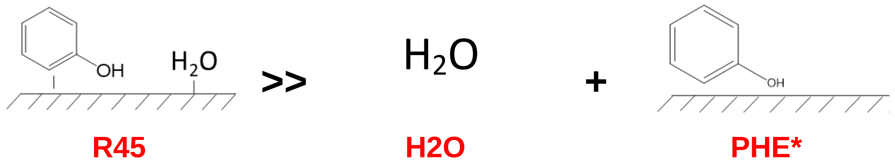	R45 >> H_2O + PHE*
S37	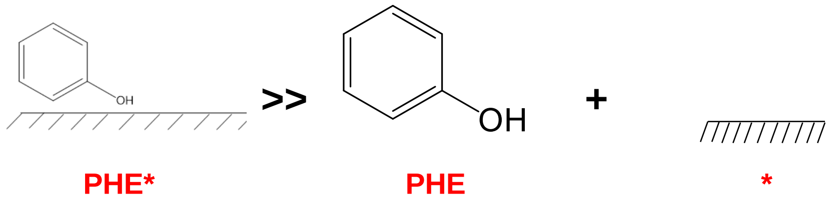	PHE* >> PHE + *

Anisole → Phenol

S38	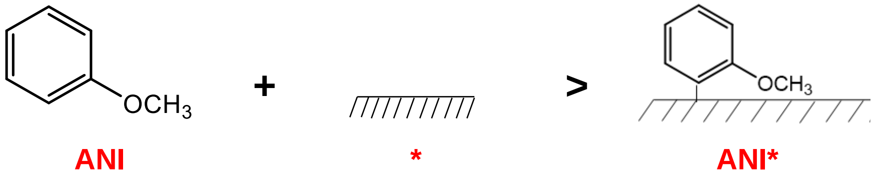	ANI + * > ANI*
S39	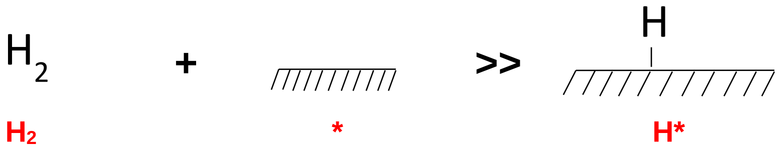	H_2 + * >> H*
S40	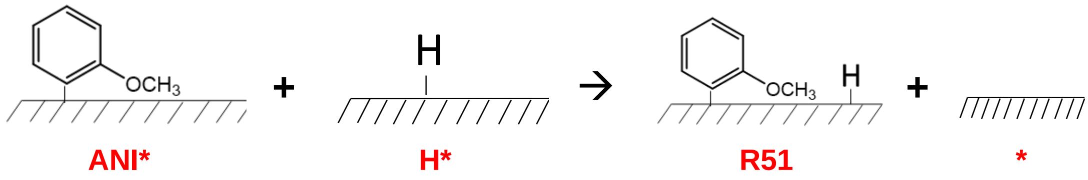	ANI* + H* >> R51 + *
S41	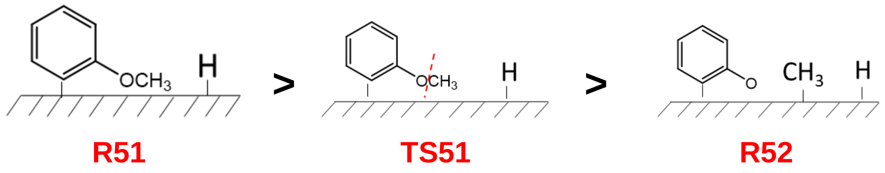	R51 > TS51 > R52
S42	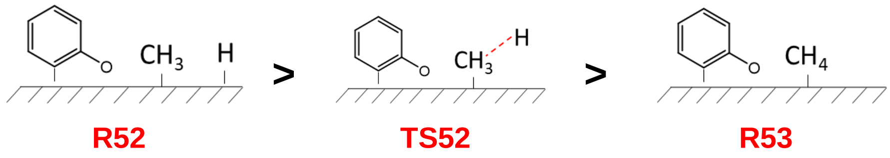	R52 > TS52 > R53

S43	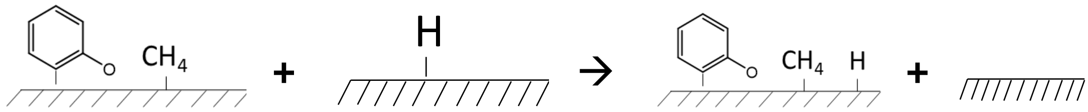 **R53** **H*** **R54** *****	R53 + H* >> R54 + *
S44	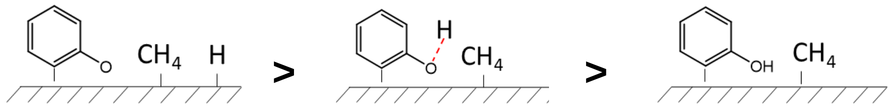 **R54** **TS53** **R55**	R54 > TS53 > R55
S45	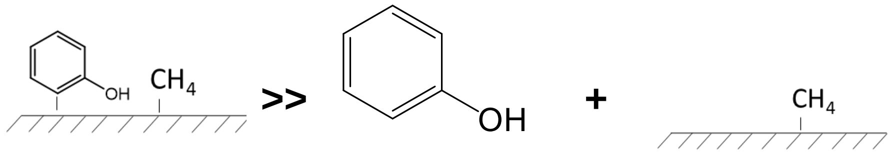 **R55** **PHE** **CH4***	R55 >> PHE + CH4*
S46	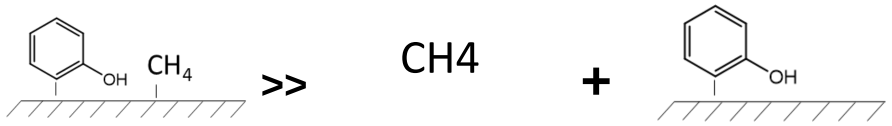 **R55** **CH4** **PHE***	R55 >> CH4 + PHE*
S47	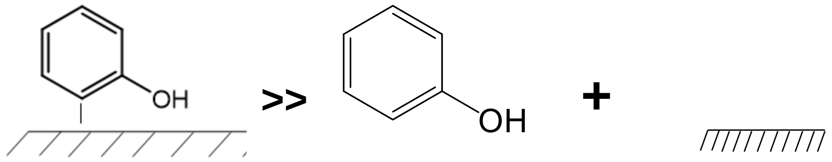 **PHE*** **PHE** *****	PHE* >> PHE + *

Anisole → Benzene

S48	 **ANI** ***** **ANI***	ANI + * > ANI*
S49	 **H_2** ***** **H***	H_2 + * >> H*
S50	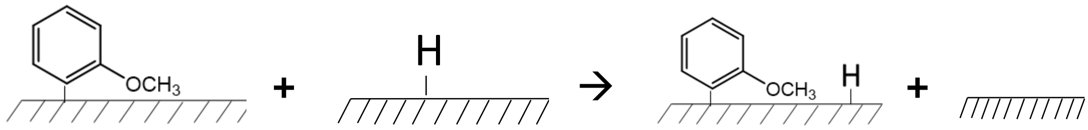 **ANI*** **H*** **R61** *****	ANI* + H* >> R51 + *
S51	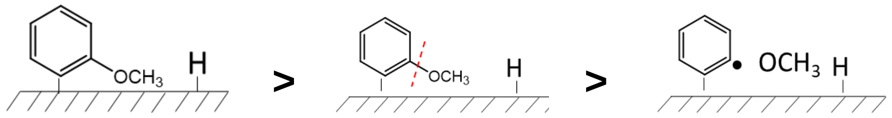 **R61** **TS61** **R62**	R61 > TS61 > R62

S52	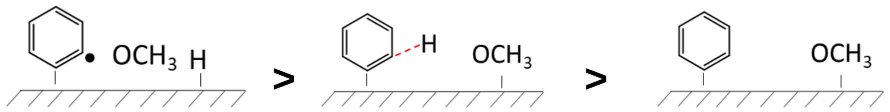 **R62** **TS62** **R63**	R62 > TS62 > R63
S53	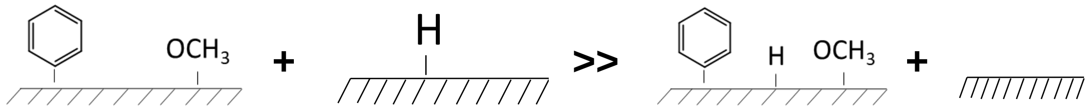 **R63** **H*** **R64** *****	R63 + H* >> R64 + *
S54	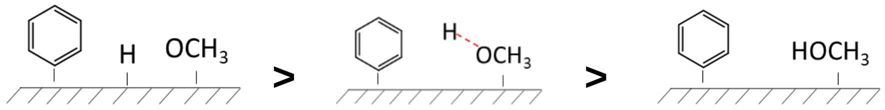 **R64** **TS63** **R65**	R64 > TS63 > R65
S55	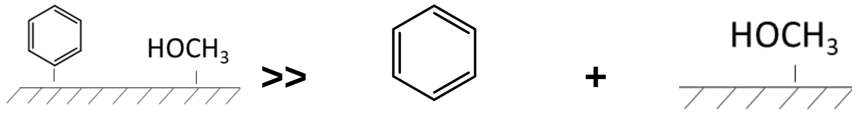 **R65** **BEN** **$HOCH_3$***	R65 >> BEN + $HOCH_3$*
S56	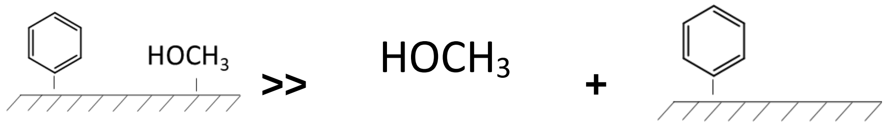 **R65** **HOCH3** **BEN***	R65 >> $HOCH_3$ + BEN*
S57	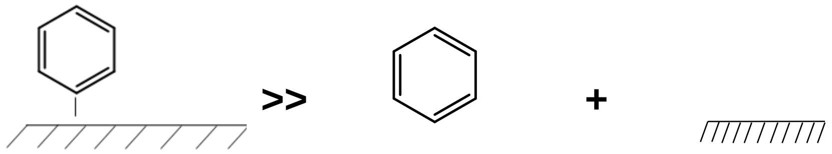 **BEN*** **BEN** *****	BEN* >> BEN + *
Phenol → Benzene		
S58	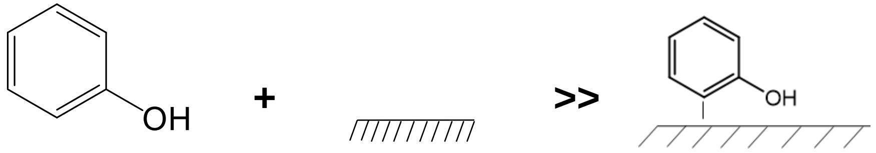 **PHE** ***** **PHE***	PHE + * >> PHE*
S59	 **H_2** ***** **H***	H_2 + * >> H*
S60	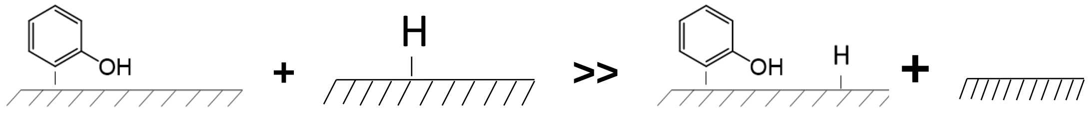 **PHE*** **H*** **R71** *****	PHE* + H* >> R71 + *

S61	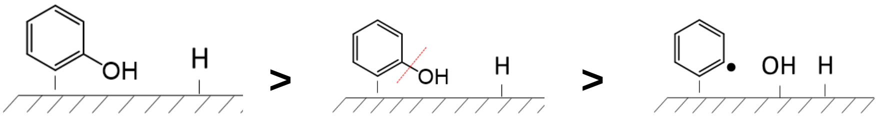 **R71** **TS71** **R72**	R71 > TS71 > R72
S62	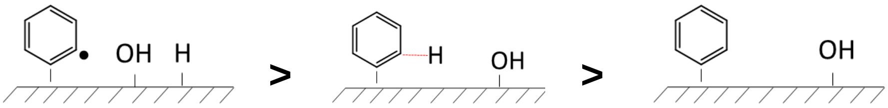 **R72** **TS72** **R73**	R72 > TS72 > R73
S63	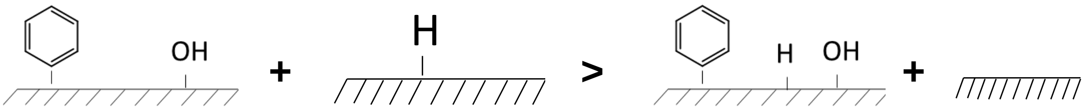 **R73** **H*** **R74** *	R73 + H* >> R74 + *
S64	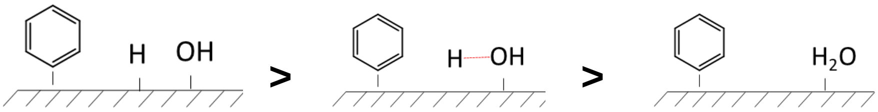 **R74** **TS73** **R75**	R74 > TS73 > R75
S65	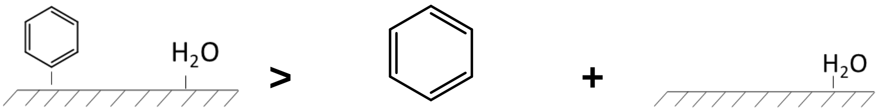 **R75** **BEN** **H_2O***	R75 >> BEN + H_2O*
S66	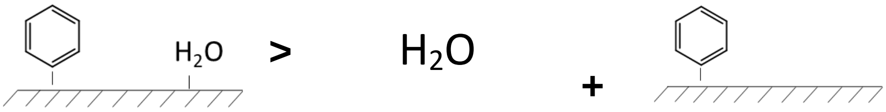 **R75** **H_2O** **BEN***	R75 >> H_2O + BEN
S67	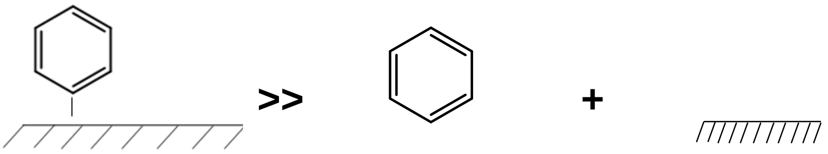 **BEN*** **BEN** *	BEN >> BEN + *
S68	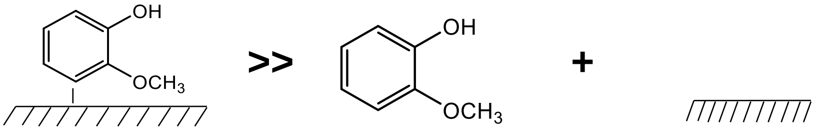 **GUA*** **GUA** *	GUA* >> GUA + *

Table A2*. Pre-exponential factor (A_o) and forward rate constant (k) for the elementary reactions for the guaiacol conversion into benzene at different temperatures (273 K, 573 K, 673 and 1073 K) for Co (0001). The notation of the structures used in each step (S) is explained* ***in Table A1****, where GUA, CAT, ANI, PHE and BEN represent guaiacol, catechol, anisole, phenol and benzene, respectively.*

					273 K		573 K		673 K		1073 K	
	Step	**Reactions**	E_a (eV)	E_r (eV)	A_o	k (s^{-1})	A_o	k (s^{-1})	A_o	k (s^{-1})	A_o	k (s^{-1})
	S1	GUA + * >> GUA*		−1.58	2.78 x 10^{4}	3.26 x 10^{-6}	1.92 x 10^{4}	3.53 x 10^{-7}	1.77 x 10^{4}	2.18 x 10^{-7}	1.40 x 10^{4}	5.38 x 10^{-8}
	S2	H_2 + * >> H_2*		−1.07	2.18 x 10^{5}	3.93 x 10^{2}	1.51 x 10^{5}	6.16 x 10^{1}	1.39 x 10^{5}	4.12 x 10^{1}	1.01 x 10^{5}	1.28 x 10^{1}
	S3	GUA* + H* >> R11 + *		−0.01	1.96 x 10^{13}	7.65 x 10^{13}	7.52 x 10^{13}	3.61 x 10^{14}	1.02 x 10^{14}	5.26 x 10^{14}	2.47 x 10^{14}	1.65 x 10^{15}
Guaiacol → Anisole	**S4**	R11 > TS11 > R12	1.38	−0.18	2.78 x 10^{12}	5.06 x 10^{-13}	3.65 x 10^{12}	2.00 x 10^{0}	3.82 x 10^{12}	1.05 x 10^{2}	4.06 x 10^{12}	4.48 x 10^{5}
	S5	R12 > TS12 > R13	1.03	−0.61	1.52 x 10^{13}	2.24 x 10^{-6}	2.40 x 10^{13}	3.18 x 10^{4}	2.55 x 10^{13}	7.16 x 10^{5}	2.84 x 10^{13}	5.08 x 10^{8}
	S6	R13 + H* >> R14 + *		−0.01	6.12 x 10^{12}	8.10 x 10^{12}	2.01 x 10^{13}	3.38 x 10^{13}	2.66 x 10^{13}	4.75 x 10^{13}	6.14 x 10^{13}	1.34 x 10^{14}
	S7	R14 > TS13 > R15	1.32	0.44	1.18 x 10^{13}	4.31 x 10^{-11}	2.89 x 10^{13}	2.06 x 10^{2}	3.38 x 10^{13}	1.13 x 10^{4}	4.91 x 10^{13}	5.99 x 10^{7}
	S8	R15 >> H_2O* + ANI		1.70	3.75 x 10^{12}	2.07 x 10^{-6}	1.24 x 10^{12}	7.14 x 10^{10}	8.66 x 10^{11}	1.11 x 10^{13}	2.52 x 10^{11}	3.81 x 10^{17}
	S9	H_2O* >> H_2O + *		0.43	9.51 x 10^{10}	1.46 x 10^{10}	1.06 x 10^{10}	3.59 x 10^{13}	5.93 x 10^{9}	7.96 x 10^{13}	9.55 x 10^{8}	2.37 x 10^{14}
	S10	R15 >> H_2O + ANI*		0.46	7.62 x 10^{11}	1.37 x 10^{11}	1.18 x 10^{11}	1.15 x 10^{15}	6.93 x 10^{10}	3.10 x 10^{15}	1.24 x 10^{10}	1.50 x 10^{16}
	S11	ANI* >> ANI + *		1.67	4.68 x 10^{11}	2.21 x 10^{-7}	1.12 x 10^{11}	2.24 x 10^{9}	7.42 x 10^{10}	2.84 x 10^{11}	1.94 x 10^{10}	6.02 x 10^{15}
Guaiacol → Phenol	**S12**	R21 > TS21 > R22	1.46	0.51	8.88 x 10^{12}	1.46 x 10^{-13}	2.42 x 10^{13}	1.06 x 10^{1}	2.97 x 10^{13}	9.09 x 10^{2}	5.04 x 10^{13}	1.41 x 10^{7}
	S13	R22 > TS22 > R23	0.34	−0.80	4.19 x 10^{12}	1.82 x 10^{6}	9.47 x 10^{12}	7.16 x 10^{9}	1.09 x 10^{13}	2.22 x 10^{10}	1.48 x 10^{13}	2.29 x 10^{11}
	S14	R23 + H* >> R24 + *		0.04	9.08 x 10^{11}	4.83 x 10^{10}	1.90 x 10^{12}	1.88 x 10^{11}	2.24 x $10^{!2}$	2.42 x 10^{11}	3.66 x 10^{12}	4.69 x 10^{11}
	S15	R24 > TS23 > R25	0.82	0.01	9.68 x 10^{11}	7.54 x 10^{-4}	1.05 x $10^{!2}$	1.55 x 10^{4}	1.04 x 10^{12}	1.43 x 10^{5}	9.51 x 10^{11}	1.35 x 10^{7}
	S16	R25 >> PHE + $HOCH_3$*		1.55	2.14 x 10^{11}	1.19 x 10^{-6}	4.12 x 10^{10}	1.37 x 10^{9}	2.61 x 10^{10}	1.23 x 10^{11}	5.98 x 10^{9}	1.13 x 10^{15}
	S17	$HOCH_3$* >> $HOCH_3$ + *		0.57	1.28 x 10^{11}	4.09 x 10^{10}	1.32 x 10^{10}	9.04 x 10^{14}	7.47 x 10^{9}	2.84 x 10^{15}	1.25 x 10^{9}	1.91 x 10^{16}
	S18	R25 >> $HOCH_3$ + PHE*		0.55	6.12 x 10^{10}	2.91 x 10^{10}	6.07 x 10^{9}	3.55 x 10^{14}	3.40 x 10^{9}	1.02 x 10^{15}	5.61 x 10^{8}	5.60 x 10^{15}
	S19	PHE* >> PHE + *		1.57	4.47 x 10^{11}	1.68 x 10^{-6}	8.99 x 10^{10}	3.48 x 10^{9}	5.74 x 10^{10}	3.40 x 10^{11}	1.33 x 10^{10}	3.85 x 10^{15}
Guaiacol → Catechol	**S20**	R31 >TS31 > R32	1.23	−0.73	1.30 x 10^{12}	2.54 x 10^{-10}	1.37 x 10^{12}	1.26 x 10^{1}	1.40 x 10^{12}	4.26 x 10^{3}	1.38 x 10^{12}	4.21 x 10^{5}
	S21	R32 > TS32 > R33	0.94	0.13	4.49 x 10^{12}	1.76 x 10^{-6}	9.14 x 10^{12}	1.42 x 10^{4}	1.01 x 10^{13}	2.95 x 10^{5}	1.21 x 10^{13}	1.65 x 10^{8}
	S22	R33 + H* >> R34 + *		0.00	3.54 x 10^{13}	1.13 x 10^{14}	1.35 x 10^{14}	7.95 x 10^{14}	1.82 x 10^{14}	1.22 x 10^{15}	4.41 x 10^{14}	4.32 x 10^{15}
	S23	R34 > TS33 > R35	0.90	0.28	2.38 x 10^{11}	1.82 x 10^{-6}	9.66 x 10^{10}	4.05 x 10^{1}	7.47 x 10^{10}	3.12 x 10^{2}	3.12 x 10^{10}	1.31 x 10^{4}
	S24	R35 >> CAT + CH_4*		1.71	1.76 x 10^{11}	3.23 x 10^{-9}	3.74 x 10^{10}	1.06 x 10^{8}	2.44 x 10^{10}	1.54 x 10^{10}	6.05 x 10^{9}	4.19 x 10^{14}
	S25	CH_4* >> CH_4 + *		0.19	1.98 x 10^{11}	8.85 x 10^{14}	3.97 x 10^{10}	1.39 x 10^{16}	2.70 x 10^{10}	1.83 x 10^{16}	8.35 x 10^{9}	2.52 x 10^{16}
	S26	R35* >> CH_4 + CAT*		0.21	3.06 x 10^{10}	1.65 x 10^{13}	3.19 x 10^{9}	1.18 x 10^{14}	1.87 x 10^{9}	1.24 x 10^{14}	3.73 x 10^{8}	8.57 x 10^{13}
	S27	CAT* >> CAT + *		1.69	1.13 x 10^{11}	1.73 x 10^{-7}	4.65 x 10^{11}	1.25 x 10^{10}	3.52 x 10^{11}	2.26 x 10^{12}	1.35 x 10^{11}	1.23 x 10^{17}
Catechol → Phenol	**S28**	CAT + * >> CAT*		−1.69	2.96 x 10^{4}	6.27 x 10^{-6}	2.04 x 10^{4}	6.78 x 10^{-7}	1.88 x 10^{4}	4.19 x 10^{-7}	1.49 x 10^{4}	1.03 x 10^{-7}
	S29	H_2 + * >> H_2*		−1.07	2.18 x 10^{5}	3.93 x 10^{2}	1.51 x 10^{5}	6.16 x 10^{1}	1.39 x 10^{5}	4.12 x 10^{1}	1.01 x 10^{5}	1.28 x 10^{1}
	S30	CAT* + H* >> R41 + *		0.00	2.69 x 10^{13}	9.76 x 10^{13}	1.14 x 10^{14}	6.21 x 10^{14}	1.56 x 10^{14}	9.48 x 10^{14}	3.93 x 10^{14}	3.35 x 10^{15}
	S31	R41 > TS41 > R42	1.23	0.02	2.99 x 10^{12}	3.92 x 10^{-10}	5.42 x 10^{12}	9.22 x 10^{1}	6.25 x 10^{12}	3.57 x 10^{3}	9.18 x 10^{12}	9.69 x 10^{6}
	S32	R42 > TS42 > R43	0.40	−0.65	1.69 x 10^{13}	2.14 x 10^{6}	1.73 x 10^{14}	4.10 x 10^{11}	2.90 x 10^{14}	2.85 x 10^{12}	1.28 x 10^{15}	2.99 x 10^{14}
	S33	R43 + H* >> R44 + *		0.01	5.17 x 10^{12}	2.69 x 10^{12}	4.60 x 10^{12}	1.60 x 10^{12}	4.29 x 10^{12}	1.33 x 10^{12}	3.27 x 10^{12}	6.97 x 10^{11}
	S34	R44 > TS43 > R45	1.36	0.55	2.74 x 10^{12}	5.14 x 10^{-13}	2.11 x 10^{12}	8.98 x 10^{-1}	1.87 x $10^{!2}$	3.51 x 10^{1}	1.18 x 10^{12}	6.01 x 10^{4}

	S35	R45 >> H_2O* + PHE		1.50	3.68 x 10^{10}	4.12 x 10^{-7}	3.09 x 10^{9}	3.85 x 10^{7}	1.64 x 10^{9}	2.20 x 10^{9}	2.29 x 10^{8}	6.27 x 10^{1}
	S36	R45 >> H_2O + PHE*		0.36	7.83 x 10^{9}	3.60 x 10^{9}	3.63 x 10^{8}	3.97 x 10^{11}	1.69 x 10^{8}	5.14 x 10^{11}	1.64 x 10^{7}	3.87 x 10^{11}
	S37	PHE* >> PHE + *		1.57	4.47 x 10^{11}	1.68 x 10^{-6}	8.99 x 10^{10}	3.48 x 10^{9}	5.74 x 10^{10}	3.41 x 10^{11}	1.33 x 10^{10}	3.86 x 10^{15}
Anisole → Phenol	**S38**	ANI + * > ANI*		−1.67	2.98 x 10^{4}	6.26 x 10^{-6}	2.06 x 10^{4}	6.77 x 10^{-7}	1.90 x 10^{4}	4.18 x 10^{-7}	1.50 x 10^{4}	1.03 x 10^{-7}
	S39	H_2 + * >> H_2*		−1.07	2.18 x 10^{5}	3.93 x 10^{2}	1.51 x 10^{5}	6.16 x 10^{1}	1.39 x 10^{5}	4.12 x 10^{1}	1.01 x 10^{5}	1.28 x 10^{1}
	S40	ANI* + H* >> R51 + *		−0.01	1.94 x 10^{12}	1.23 x 10^{12}	2.19 x 10^{12}	7.45 x 10^{11}	2.23 x 10^{12}	6.67 x 10^{11}	2.31 x 10^{12}	4.77 x 10^{11}
	S41	R51 > TS51 > R52	1.48	−0.65	3.58 x 10^{13}	2.86 x 10^{-12}	2.76 x 10^{14}	6.98 x 10^{2}	4.35 x 10^{14}	8.85 x 10^{4}	1.49 x 10^{15}	4.42 x 10^{9}
	S42	R52 > TS52 > R53	0.97	0.12	2.14 x 10^{12}	1.21 x 10^{-7}	2.19 x 10^{12}	6.70 x 10^{2}	2.07 x 10^{12}	1.19 x 10^{4}	1.57 x 10^{12}	3.79 x 10^{6}
	S43	R53 + H* >> R54 + *		0.06	8.26 x 10^{12}	6.99 x 10^{11}	2.74 x 10^{13}	1.43 x 10^{13}	3.60 x 10^{13}	2.47 x 10^{13}	8.17 x 10^{13}	1.07 x 10^{14}
	S44	R54 > TS53 > R54	1.10	0.37	5.44 x 10^{13}	4.75 x 10^{-6}	2.80 x 10^{14}	7.91 x 10^{5}	3.87 x 10^{14}	3.08 x 10^{7}	9.12 x 10^{14}	9.89 x 10^{10}
	S45	R55 > PHE + CH_4*		1.57	4.02 x 10^{10}	5.47 x 10^{-8}	2.26 x 10^{9}	7.92 x 10^{6}	1.08 x 10^{9}	4.44 x 10^{8}	1.08 x 10^{8}	1.01 x 10^{12}
	S46	R55 > CH_4 + PHE*		0.19	1.78 x 10^{10}	2.89 x 10^{13}	9.99 x 10^{8}	3.17 x 10^{13}	5.09 x 10^{8}	2.38 x 10^{13}	6.77 x 10^{7}	6.59 x 10^{12}
	S47	PHE* >> PHE + *		1.57	4.47 x 10^{11}	1.68 x 10^{-6}	8.99 x 10^{10}	3.48 x 10^{9}	5.74 x 10^{10}	3.41 x 10^{11}	1.33 x 10^{10}	3.86 x 10^{15}
Anisole → Benzene	**S48**	ANI + * > ANI*		−1.67	2.98 x 10^{4}	6.26 x 10^{-6}	2.06 x 10^{4}	6.77 x 10^{-7}	1.90 x 10^{4}	4.18 x 10^{-7}	1.50 x 10^{4}	1.03 x 10^{-7}
	S49	H_2 + * >> H_2*		−1.07	2.18 x 10^{5}	3.93 x 10^{2}	1.51 x 10^{5}	6.16 x 10^{1}	1.39 x 10^{5}	4.12 x 10^{1}	1.01 x 10^{5}	1.28 x 10^{1}
	S50	ANI* + H* >> R61 + *		−0.01	1.94 x 10^{12}	1.23 x 10^{12}	2.19 x 10^{12}	7.45 x 10^{11}	2.23 x 10^{12}	6.67 x 10^{11}	2.31 x 10^{12}	4.77 x 10^{11}
	S51	R61 > TS61 > R62	1.49	0.00	7.27 x 10^{13}	3.26 x 10^{-12}	3.94 x 10^{14}	1.00 x 10^{3}	5.61 x 10^{14}	1.16 x 10^{5}	1.47 x 10^{15}	4.37 x 10^{9}
	S52	R62 > TS62 > R63	0.35	−0.69	5.52 x 10^{12}	2.43 x 10^{6}	1.34 x 10^{13}	1.19 x 10^{10}	1.56 x 10^{13}	3.84 x 10^{10}	2.19 x 10^{13}	4.33 x 10^{11}
	S53	R63* + H* >> R64 + *		−0.00	3.22 x 10^{11}	4.67 x 10^{10}	1.70 x 10^{11}	8.71 x 10^{9}	1.47 x 10^{11}	5.93 x 10^{9}	9.54 x 10^{10}	1.85 x 10^{9}
	S54	R64* > TS63 > R65	1.41	0.58	3.98 x 10^{13}	1.38 x 10^{-11}	2.02 x 10^{14}	1.14 x 10^{3}	2.81 x 10^{14}	1.06 x 10^{5}	6.80 x 10^{14}	2.26 x 10^{9}
	S55	R65 >> BEN + $HOCH_3$*		1.65	4.16 x 10^{11}	1.33 x 10^{-10}	8.29 x 10^{10}	5.60 x 10^{5}	5.30 x 10^{10}	5.87 x 10^{7}	1.24 x 10^{10}	7.41 x 10^{11}
	S56	R65 >> $HOCH_3$ + BEN*		0.52	1.48 x 10^{11}	4.20 x 10^{11}	2.23 x 10^{10}	6.54 x 10^{15}	1.40 x 10^{10}	2.11 x 10^{16}	3.26 x 10^{9}	1.80 x 10^{17}
	S57	BEN* >> BEN + *		1.70	3.58 x 10^{11}	1.29 x 10^{-11}	4.92 x 10^{10}	7.74 x 10^{4}	2.83 x 10^{10}	7.89 x 10^{6}	4.77 x 10^{9}	7.85 x 10^{10}
Phenol → Benzene	**S58**	PHE + * > PHE*		−1.57	3.19 x 10^{4}	1.28 x 10^{-5}	2.21 x 10^{4}	1.39 x 10^{-6}	2.04 x 10^{4}	8.60 x 10^{-7}	1.61 x 10^{4}	2.12 x 10^{-7}
	S59	H_2 + * >> H_2*		−1.07	2.18 x 10^{5}	3.93 x 10^{2}	1.51 x 10^{5}	6.16 x 10^{1}	1.39 x 10^{5}	4.12 x 10^{1}	1.01 x 10^{5}	1.28 x 10^{1}
	S60	PHE* + H* >> R71 + *		0.02	2.21 x 10^{12}	5.70 x 10^{11}	2.64 x 10^{12}	6.25 x 10^{11}	2.73 x 10^{12}	6.15 x 10^{11}	2.93 x 10^{12}	5.48 x 10^{11}
	S61	R71 > TS71 > R72	1.41	0.07	2.53 x 10^{13}	3.43 x 10^{-12}	1.65 x 10^{14}	6.49 x 10^{2}	2.53 x 10^{14}	7.43 x 10^{4}	8.54 x 10^{14}	3.05 x 10^{9}
	S62	R72 > TS72 > R73	0.90	−0.69	1.65 x 10^{11}	2.46 x 10^{-7}	2.38 x 10^{11}	8.51 x 10^{1}	2.43 x 10^{11}	1.11 x 10^{3}	2.26 x 10^{11}	2.00 x 10^{5}
	S63	R73 + H* >> R74 + *		0.07	5.05 x 10^{12}	2.05 x 10^{11}	1.05 x 10^{13}	2.22 x 10^{12}	1.24 x 10^{13}	3.24 x 10^{12}	1.96 x 10^{13}	8.12 x 10^{12}
	S64	R74 > TS73 > R75	1.24	0.47	1.06 x 10^{13}	7.05 x 10^{-10}	3.98 x 10^{13}	1.54 x 10^{3}	5.19 x 10^{13}	8.15 x 10^{4}	1.07 x 10^{14}	4.88 x 10^{8}
	S65	R75 >> BEN + H_2O*		1.53	5.99 x 10^{12}	1.01 x 10^{-6}	3.22 x 10^{12}	2.81 x 10^{9}	2.61 x 10^{12}	3.38 x 10^{11}	1.28 x 10^{12}	8.67 x 10^{15}
	S66	R75 >> H_2O + BEN*		0.25	1.59 x 10^{12}	1.14 x 10^{15}	6.91 x 10^{11}	1.31 x 10^{18}	5.46 x 10^{11}	3.41 x 10^{18}	2.57 x 10^{11}	2.62 x 10^{19}
	S67	BEN* >> BEN + *		1.70	3.58 x 10^{11}	1.29 x 10^{-11}	4.92 x 10^{10}	7.74 x 10^{4}	2.83 x 10^{10}	7.89 x 10^{6}	4.77 x 10^{9}	7.85 x 10^{10}
	S68	GUA* >> GUA + *		1.58	4.22 x 10^{11}	4.32 x 10^{-6}	8.58 x 10^{10}	1.04 x 10^{10}	5.51 x 10^{10}	1.05 x 10^{12}	1.31 x 10^{10}	1.30 x 10^{16}

***Table A3**. Pre-exponential factor (A$_o$) and forward rate constant (k) for the elementary reactions for the guaiacol conversion into benzene at different temperatures (273 K, 573 K, 673 and 1073 K) for Ni (111). The notation of the structures used in each step (S) is explained **in Table A1**, where GUA, CAT, ANI, PHE and BEN represent guaiacol, catechol, anisole, phenol and benzene, respectively.*

					273 K		573 K		673 K		1073 K	
	Step	**Reactions**	E_a (eV)	E_r (eV)	A_o	k (s^{-1})	A_o	k (s^{-1})	A_o	k (s^{-1})	A_o	k (s^{-1})
	S1	GUA + * >> GUA*		−1.71	2.73×10^{4}	3.26×10^{-6}	1.88×10^{4}	3.53×10^{-7}	1.73×10^{4}	2.18×10^{-7}	1.37×10^{4}	5.38×10^{-8}
	S2	H_2 + * >> H_2*		−1.01	2.13×10^{5}	3.93×10^{2}	1.48×10^{5}	6.16×10^{1}	1.36×10^{5}	4.12×10^{1}	1.08×10^{5}	1.28×10^{1}
	S3	GUA* + H* >> R11 + *		0.01	1.44×10^{13}	1.76×10^{13}	5.58×10^{13}	1.36×10^{14}	7.56×10^{13}	2.11×10^{14}	1.85×10^{14}	7.61×10^{14}
Guaiacol → Anisole	**S4**	R11 > TS11 > R12	1.67	0.22	8.48×10^{12}	1.89×10^{-17}	1.49×10^{13}	6.41×10^{-2}	1.63×10^{13}	8.54×10^{0}	1.92×10^{13}	2.82×10^{5}
	S5	R12 > TS12 > R13	0.47	−0.66	2.09×10^{13}	9.39×10^{4}	9.15×10^{13}	2.43×10^{10}	1.22×10^{14}	1.46×10^{11}	2.53×10^{14}	7.74×10^{12}
	S6	R13 + H* >> R14 + *		0.00	4.38×10^{12}	2.69×10^{12}	8.50×10^{12}	5.97×10^{12}	9.86×10^{12}	7.01×10^{12}	1.52×10^{13}	1.10×10^{13}
	S7	R14 > TS13 > R15	0.97	0.06	1.33×10^{13}	2.22×10^{-4}	4.77×10^{13}	6.11×10^{5}	6.02×10^{13}	1.28×10^{7}	1.05×10^{14}	9.09×10^{9}
	S8	R15 >> H_2O* + ANI		1.73	5.14×10^{11}	2.56×10^{-8}	6.09×10^{10}	2.21×10^{8}	3.33×10^{10}	2.37×10^{10}	4.52×10^{9}	2.47×10^{14}
	S9	H_2O* >> H_2O + *		0.46	2.70×10^{12}	1.67×10^{12}	1.42×10^{12}	9.53×10^{16}	1.12×10^{12}	4.09×10^{17}	4.75×10^{11}	8.11×10^{18}
	S10	R15 >> H_2O + ANI*		0.44	1.28×10^{12}	8.70×10^{11}	3.61×10^{11}	1.24×10^{16}	2.46×10^{11}	3.99×10^{16}	6.78×10^{10}	3.45×10^{17}
	S11	ANI* >> ANI + *		1.75	1.08×10^{12}	4.93×10^{-8}	2.39×10^{11}	1.70×10^{9}	1.51×10^{11}	2.43×10^{11}	3.17×10^{10}	5.82×10^{15}
Guaiacol → Phenol	**S12**	R21 > TS21 > R22	1.66	0.30	5.92×10^{12}	2.21×10^{-17}	1.33×10^{13}	8.41×10^{-2}	1.57×10^{13}	1.18×10^{1}	2.37×10^{13}	4.94×10^{5}
	S13	R22 > TS22 > R23	0.12	−0.88	4.64×10^{12}	2.19×10^{10}	6.88×10^{12}	3.87×10^{11}	7.27×10^{12}	4.47×10^{11}	8.10×10^{12}	1.03×10^{12}
	S14	R23 + H* >> R24 + *		0.55	4.91×10^{13}	4.54×10^{4}	3.75×10^{14}	9.34×10^{10}	5.94×10^{14}	8.84×10^{11}	2.32×10^{15}	1.98×10^{14}
	S15	R24 > TS23 > R25	0.59	−0.31	1.09×10^{12}	9.92×10^{0}	1.11×10^{12}	1.54×10^{6}	1.09×10^{12}	7.31×10^{6}	9.64×10^{11}	1.62×10^{8}
	S16	R25 >> PHE + $HOCH_3$*		1.66	9.41×10^{11}	3.51×10^{-7}	2.61×10^{11}	4.75×10^{9}	1.77×10^{11}	6.28×10^{11}	4.79×10^{10}	1.45×10^{16}
	S17	$HOCH_3$* >> $HOCH_3$ + *		0.61	4.31×10^{11}	6.13×10^{10}	8.53×10^{10}	1.01×10^{16}	5.58×10^{10}	4.60×10^{16}	1.45×10^{10}	8.65×10^{17}
	S18	R25 >> $HOCH_3$ + PHE*		0.57	4.92×10^{12}	2.03×10^{13}	2.03×10^{12}	5.43×10^{18}	1.56×10^{12}	2.99×10^{19}	6.46×10^{11}	1.07×10^{21}
	S19	PHE* >> PHE + *		1.70	8.24×10^{10}	1.06×10^{-9}	1.10×10^{10}	8.80×10^{6}	6.34×10^{9}	9.64×10^{8}	1.07×10^{9}	1.17×10^{13}
Guaiacol → Catechol	**S20**	R31 >TS31 > R32	1.21	−0.18	3.55×10^{12}	2.10×10^{-9}	6.39×10^{12}	2.31×10^{2}	7.36×10^{12}	8.09×10^{3}	1.08×10^{13}	1.81×10^{7}
	S21	R32 > TS32 > R33	0.57	−0.12	3.40×10^{11}	9.61×10^{-1}	2.81×10^{11}	1.54×10^{5}	2.59×10^{11}	6.63×10^{5}	1.93×10^{11}	1.04×10^{7}
	S22	R33 + H* >> R34 + *		0.02	5.93×10^{13}	1.65×10^{14}	2.84×10^{14}	1.99×10^{15}	3.98×10^{14}	3.36×10^{15}	1.05×10^{15}	1.51×10^{16}
	S23	R34 > TS33 > R35	0.62	−0.11	2.22×10^{14}	7.93×10^{4}	1.91×10^{15}	5.53×10^{11}	3.04×10^{15}	6.25×10^{12}	1.09×10^{16}	1.80×10^{15}
	S24	R35 >> CAT + CH_4*		1.77	1.18×10^{11}	1.18×10^{-10}	1.51×10^{10}	6.43×10^{6}	8.73×10^{9}	9.16×10^{8}	1.48×10^{9}	1.95×10^{13}
	S25	CH_4* >> CH_4 + *		0.23	9.04×10^{10}	2.70×10^{13}	9.97×10^{9}	4.72×10^{14}	5.89×10^{9}	5.66×10^{14}	1.20×10^{9}	5.22×10^{14}
	S26	R35* >> CH_4 + CAT*		0.23	2.33×10^{11}	1.91×10^{14}	2.82×10^{10}	3.46×10^{15}	1.69×10^{10}	4.22×10^{15}	3.55×10^{9}	4.10×10^{15}
	S27	CAT* >> CAT + *		1.78	4.58×10^{10}	1.67×10^{-11}	5.35×10^{9}	8.77×10^{5}	3.04×10^{9}	1.23×10^{8}	4.97×10^{8}	2.48×10^{12}
Catechol → Phenol	**S28**	CAT + * >> CAT*		−1.78	2.89×10^{4}	6.27×10^{-6}	1.99×10^{4}	6.78×10^{-7}	1.84×10^{4}	4.19×10^{-7}	1.46×10^{4}	1.03×10^{-7}
	S29	H_2 + * >> H_2*		−1.01	2.13×10^{5}	3.93×10^{2}	1.48×10^{5}	6.16×10^{1}	1.36×10^{5}	4.12×10^{1}	1.08×10^{5}	1.28×10^{1}
	S30	CAT* + H* >> R41 + *		0.00	1.16×10^{12}	2.87×10^{11}	2.07×10^{12}	4.95×10^{11}	2.37×10^{12}	5.54×10^{11}	3.56×10^{12}	7.70×10^{11}
	S31	R41 > TS41 > R42	1.57	0.38	9.28×10^{11}	2.56×10^{-17}	8.63×10^{11}	4.07×10^{-3}	8.53×10^{11}	3.39×10^{-1}	7.96×10^{11}	3.75×10^{3}
	S32	R42 > TS42 > R43	0.55	−0.65	8.14×10^{12}	6.22×10^{2}	1.49×10^{13}	2.29×10^{8}	1.64×10^{13}	1.27×10^{9}	1.98×10^{13}	4.49×10^{10}
	S33	R43 + H* >> R44 + *		0.05	1.13×10^{12}	2.65×10^{10}	1.49×10^{12}	1.12×10^{11}	1.63×10^{12}	1.38×10^{11}	2.17×10^{12}	2.27×10^{11}
	S34	R44 > TS43 > R45	0.82	0.02	4.68×10^{13}	8.41×10^{-1}	2.87×10^{14}	2.54×10^{8}	4.13×10^{14}	4.36×10^{9}	1.08×10^{15}	2.55×10^{12}

	S35	R45 >> H_2O* + PHE		1.63	2.08 x 10^{10}	1.59 x 10^{-9}	1.28 x 10^{9}	1.07 x 10^{6}	6.50 x 10^{8}	7.92 x 10^{7}	8.29 x 10^{7}	3.84 x 10^{11}
	S36	R45 >> H_2O + PHE*		0.38	6.81 x 10^{11}	2.52 x 10^{12}	1.65 x 10^{11}	1.16 x 10^{16}	1.15 x 10^{11}	3.36 x 10^{16}	3.67 x 10^{10}	2.66 x 10^{17}
	S37	PHE* >> PHE + *		1.70	8.24 x 10^{10}	1.06 x 10^{-9}	1.10 x 10^{10}	8.79 x 10^{6}	6.34 x 10^{9}	9.64 x 10^{8}	1.07 x 10^{9}	1.17 x 10^{13}
Anisole → Phenol	**S38**	ANI + * > ANI*		−1.75	2.92 x 10^{4}	6.26 x 10^{-6}	2.01 x 10^{4}	6.77 x 10^{-7}	1.86 x 10^{4}	4.18 x 10^{-7}	1.47 x 10^{4}	1.03 x 10^{-7}
	S39	H_2 + * >> H_2*		−1.01	2.13 x 10^{5}	3.93 x 10^{2}	1.48 x 10^{5}	6.16 x 10^{1}	1.36 x 10^{5}	4.12 x 10^{1}	1.08 x 10^{5}	1.28 x 10^{1}
	S40	ANI* + H* >> R51 + *		0.00	5.99 x 10^{12}	5.33 x 10^{12}	1.29 x 10^{13}	1.26 x 10^{13}	1.52 x 10^{13}	1.50 x 10^{13}	2.43 x 10^{13}	2.48 x 10^{13}
	S41	R51 > TS51 > R52	1.58	−0.24	6.06 x 10^{13}	1.65x10^{-13}	3.74 x 10^{14}	1.74 x 10^{2}	5.43 x 10^{14}	2.54 x 10^{4}	1.41 x 10^{15}	1.47 x 10^{9}
	S42	R52 > TS52 > R53	0.61	−0.17	2.48 x 10^{14}	8.89 x 10^{3}	2.47 x 10^{15}	3.07 x 10^{11}	3.86 x 10^{15}	3.98 x 10^{12}	1.28 x 10^{16}	1.37 x 10^{15}
	S43	R53 + H* >> R54 + *		0.01	1.52 x 10^{13}	2.81 x 10^{13}	6.11 x 10^{13}	1.86 x 10^{14}	8.34 x 10^{13}	2.85 x 10^{14}	2.08 x 10^{14}	9.99 x 10^{14}
	S44	R54 > TS53 > R54	0.74	0.19	3.42 x 10^{12}	1.75 x 10^{-1}	4.28 x 10^{12}	8.47 x 10^{5}	4.34 x 10^{12}	6.55 x 10^{6}	4.13 x 10^{12}	4.26 x 10^{8}
	S45	R55 > PHE + CH_4*		1.64	1.03 x 10^{11}	2.46 x 10^{-8}	7.30 x 10^{9}	1.73 x 10^{9}	3.64 x 10^{9}	1.24 x 10^{9}	3.99 x 10^{8}	5.02 x 10^{12}
	S46	R55 > CH_4 + PHE*		0.17	1.13 x 10^{11}	6.29 x 10^{14}	6.63 x 10^{9}	9.29 x 10^{14}	3.38 x 10^{9}	7.30 x 10^{14}	4.44 x 10^{8}	2.24 x 10^{14}
	S47	PHE* >> PHE + *		1.70	8.24 x 10^{10}	1.06 x 10^{-9}	1.10 x 10^{10}	8.79 x 10^{6}	6.34 x 10^{9}	9.64 x 10^{8}	1.07 x 10^{9}	1.17 x 10^{13}
Anisole → Benzene	**S48**	ANI + * > ANI*		−1.75	2.92 x 10^{4}	6.26 x 10^{-6}	2.01 x 10^{4}	6.77 x 10^{-7}	1.86 x 10^{4}	4.18 x 10^{-7}	1.47 x 10^{4}	1.03 x 10^{-7}
	S49	H_2 + * >> H_2*		−1.01	2.13 x 10^{5}	3.93 x 10^{2}	1.48 x 10^{5}	6.16 x 10^{1}	1.36 x 10^{5}	4.12 x 10^{1}	1.08 x 10^{5}	1.28 x 10^{1}
	S50	ANI* + H* >> R61 + *		0.00	5.99 x 10^{12}	5.34 x 10^{12}	1.29 x 10^{13}	1.26 x 10^{13}	1.52 x 10^{13}	1.50 x 10^{13}	2.44 x 10^{13}	2.48 x 10^{13}
	S51	R61 > TS61 > R62	1.41	0.64	1.17 x 10^{13}	4.99x10^{-12}	3.40 x 10^{13}	7.47 x 10^{1}	4.22 x 10^{13}	5.21 x 10^{3}	7.32 x 10^{13}	5.30 x 10^{7}
	S52	R62 > TS62 > R63	0.36	−0.85	1.82 x 10^{12}	6.60 x 10^{4}	2.94 x 10^{12}	4.79 x 10^{8}	3.18 x 10^{12}	1.54 x 10^{9}	3.74 x 10^{12}	1.59 x 10^{10}
	S53	R63* + H* >> R64 + *		0.02	6.73 x 10^{13}	1.47 x 10^{14}	3.18 x 10^{14}	2.09 x 10^{15}	4.44 x 10^{14}	3.59 x 10^{15}	1.16 x 10^{15}	1.69 x 10^{16}
	S54	R64* > TS63 > R65	0.93	0.02	2.88 x 10^{11}	1.20 x 10^{-6}	1.64 x 10^{11}	7.67 x 10^{1}	1.40 x 10^{11}	7.46 x 10^{2}	8.32 x 10^{10}	6.26 x 10^{4}
	S55	R65 >> BEN + $HOCH_3$*		1.69	1.60 x 10^{11}	6.29 x 10^{-12}	1.89 x 10^{10}	2.08 x 10^{4}	1.07 x 10^{10}	1.94 x 10^{6}	1.73 x 10^{9}	1.57 x 10^{10}
	S56	R65 >> $HOCH_3$ + BEN*		0.56	2.16 x 10^{11}	1.61 x 10^{11}	3.83 x 10^{10}	7.27 x 10^{15}	2.46 x 10^{10}	2.75 x 10^{16}	6.14 x 10^{9}	3.36 x 10^{17}
	S57	BEN* >> BEN + *		1.75	3.19 x 10^{11}	2.39 x 10^{-12}	4.21 x 10^{10}	2.87 x 10^{4}	2.42 x 10^{10}	3.24 x 10^{6}	4.07 x 10^{9}	4.04 x 10^{10}
Phenol → Benzene	**S58**	PHE + * > PHE*		−1.70	3.13 x 10^{4}	1.29 x 10^{-5}	2.16 x 10^{4}	1.39 x 10^{-6}	1.99 x 10^{4}	8.60 x 10^{-7}	1.58 x 10^{4}	2.12 x 10^{-7}
	S59	H_2 + * >> H_2*		−1.01	2.13 x 10^{5}	3.93 x 10^{2}	1.48 x 10^{5}	6.16 x 10^{1}	1.36 x 10^{5}	4.12 x 10^{1}	1.08 x 10^{5}	1.28 x 10^{1}
	S60	PHE* + H* >> R71 + *		0.02	5.96 x 10^{12}	2.88 x 10^{12}	1.39 x 10^{13}	9.96 x 10^{12}	1.66 x 10^{13}	1.27 x 10^{13}	2.75 x 10^{13}	2.43 x 10^{13}
	S61	R71 > TS71 > R72	1.55	0.48	3.14 x 10^{11}	6.69 x 10^{-18}	2.60 x 10^{11}	6.61 x 10^{-4}	2.52 x 10^{11}	5.04 x 10^{-2}	2.23 x 10^{11}	4.43 x 10^{2}
	S62	R72 > TS72 > R73	0.44	−0.86	1.20 x 10^{12}	1.57 x 10^{3}	2.23 x 10^{12}	6.16 x 10^{7}	2.47 x 10^{12}	2.49 x 10^{8}	3.06 x 10^{12}	4.33 x 10^{9}
	S63	R73 + H* >> R74 + *		0.01	6.19 x 10^{12}	3.89 x 10^{12}	1.26 x 10^{13}	1.06 x 10^{13}	1.48 x 10^{13}	1.29 x 10^{13}	2.33 x 10^{13}	2.18 x 10^{13}
	S64	R74 > TS73 > R75	0.67	0.12	1.26 x 10^{13}	7.73 x 10^{0}	1.87 x 10^{13}	2.40 x 10^{7}	1.86 x 10^{13}	1.61 x 10^{8}	1.64 x 10^{13}	7.39 x 10^{9}
	S65	R75 >> BEN + H_2O*		1.73	6.59 x 10^{10}	1.84 x 10^{-13}	3.78 x 10^{9}	5.31 x 10^{2}	1.82 x 10^{9}	4.38 x 10^{4}	1.84 x 10^{8}	2.18 x 10^{8}
	S66	R75 >> H_2O + BEN*		0.45	5.59 x 10^{11}	1.29 x 10^{11}	1.27 x 10^{11}	1.76 x 10^{15}	8.39 x 10^{10}	5.53 x 10^{15}	2.15 x 10^{10}	4.37 x 10^{16}
	S67	BEN* >> BEN + *		1.75	3.19 x 10^{11}	2.39 x 10^{-12}	4.21 x 10^{10}	2.87 x 10^{4}	2.42 x 10^{10}	3.24 x 10^{6}	4.07 x 10^{9}	4.04 x 10^{10}
	S68	GUA* >> GUA + *		1.71	5.52 x 10^{11}	3.92 x 10^{-8}	1.22 x 10^{11}	1.61 x 10^{9}	7.95 x 10^{10}	2.39 x 10^{11}	1.94 x 10^{10}	6.82 x 10^{15}

Table A4*. Pre-exponential factor (A_o) and forward rate constant (k) for the elementary reactions for the guaiacol conversion into benzene at different temperatures (273 K, 573 K, 673 and 1073 K) for Cu (111). The notation of the structures used in each step (S) is explained* ***in Table A1****, where GUA, CAT, ANI, PHE and BEN represent guaiacol, catechol, anisole, phenol and benzene, respectively.*

					273 K		573 K		673 K		1073 K	
	Step	**Reactions**	E_a (eV)	E_r (eV)	A_o	k (s^{-1})	A_o	k (s^{-1})	A_o	k (s^{-1})	A_o	k (s^{-1})
	S1	GUA + * >> GUA*		−1.35	2.85 x 10^{4}	3.26 x 10^{-6}	1.97 x 10^{4}	3.53 x 10^{-7}	1.82 x 10^{4}	2.18 x 10^{-7}	1.44 x 10^{4}	5.37 x 10^{8}
	S2	H_2 + * >> H_2*		−0.54	2.24 x 10^{5}	3.92 x 10^{2}	1.54 x 10^{5}	6.15 x 10^{1}	1.42 x 10^{5}	4.12 x 10^{1}	1.13 x 10^{5}	1.28 x 10^{1}
	S3	GUA* + H* >> R11 + *		0.02	8.36 x 10^{12}	5.51 x 10^{12}	1.89 x 10^{13}	1.87 x 10^{13}	2.24 x 10^{13}	2.36 x 10^{13}	3.65 x 10^{13}	4.42 x 10^{13}
Guaiacol → Anisole	**S4**	R11 > TS11 > R12	2.08	0.80	1.10 x 10^{13}	9.91x10^{-25}	3.96 x 10^{13}	1.19 x 10^{-4}	5.28 x 10^{13}	7.54 x 10^{-2}	1.19 x 10^{14}	9.68 x 10^{4}
	S5	R12 > TS12 > R13	0.95	−1.30	1.12 x 10^{13}	1.19 x 10^{-4}	2.87 x 10^{13}	2.78 x 10^{13}	3.36 x 10^{13}	5.32 x 10^{6}	4.82 x 10^{13}	2.85 x 10^{9}
	S6	R13 + H* >> R14 + *		0.02	4.07 x 10^{12}	1.21 x 10^{12}	8.52 x 10^{12}	4.15 x 10^{12}	1.00 x 10^{13}	5.19 x 10^{12}	1.59 x 10^{13}	9.37 x 10^{12}
	S7	R14 > TS13 > R15	0.98	−0.23	8.16 x 10^{13}	1.51 x 10^{-3}	2.56 x 10^{14}	7.37 x 10^{6}	3.11 x 10^{14}	1.63 x 10^{8}	4.91 x 10^{14}	1.31 x 10^{11}
	S8	R15 >> H_2O* + ANI		1.29	1.71 x 10^{10}	4.26 x 10^{-2}	1.28 x 10^{9}	4.50 x 10^{9}	6.96 x 10^{8}	1.14 x 10^{11}	1.09 x 10^{8}	6.44 x 10^{13}
	S9	H_2O* >> H_2O + *		0.41	4.38 x 10^{11}	5.34 x 10^{11}	6.19 x 10^{10}	1.16 x 10^{15}	3.60 x 10^{10}	2.59 x 10^{15}	6.27 x 10^{9}	8.17 x 10^{15}
	S10	R15 >> H_2O + ANI*		0.38	3.24 x 10^{11}	7.04 x 10^{11}	3.08 x 10^{10}	5.90 x 10^{14}	1.68 x 10^{10}	1.13 x 10^{15}	2.49 x 10^{9}	2.48 x 10^{15}
	S11	ANI* >> ANI + *		1.32	2.31 x 10^{10}	3.23 x 10^{-2}	2.57 x 10^{9}	8.83 x 10^{9}	1.50 x 10^{9}	2.60 x 10^{11}	2.74 x 10^{8}	2.12 x 10^{14}
Guaiacol → Phenol	**S12**	R21 > TS21 > R22	2.06	0.47	3.76 x 10^{12}	3.97x10^{-25}	7.85 x 10^{12}	1.01 x 10^{-5}	9.16 x 10^{12}	4.64 x 10^{-3}	1.37 x 10^{13}	2.49 x 10^{3}
	S13	R22 > TS22 > R23	0.77	−1.02	8.99 x 10^{12}	7.56 x 10^{-2}	1.73 x 10^{13}	3.54 x 10^{6}	1.92 x 10^{13}	3.84 x 10^{7}	2.41 x 10^{13}	5.82 x 10^{9}
	S14	R23 + H* >> R24 + *		0.03	9.19 x 10^{12}	3.31 x 10^{12}	2.04 x 10^{13}	1.57 x 10^{13}	2.41 x 10^{13}	2.08 x 10^{13}	3.90 x 10^{13}	4.27 x 10^{13}
	S15	R24 > TS23 > R25	1.06	−0.13	1.47 x 10^{13}	5.21 x 10^{-6}	4.09 x 10^{13}	7.66 x 10^{4}	4.89 x 10^{13}	1.93 x 10^{6}	7.44 x 10^{13}	2.01 x 10^{9}
	S16	R25 >> PHE + $HOCH_3$*		1.21	1.34 x 10^{11}	1.98 x 10^{1}	2.64 x 10^{10}	1.89 x 10^{12}	1.78 x 10^{10}	5.29 x 10^{13}	4.74 x 10^{9}	4.76 x 10^{16}
	S17	$HOCH_3$* >> $HOCH_3$ + *		0.54	2.75 x 10^{11}	4.59 x 10^{11}	4.80 x 10^{10}	1.46 x 10^{16}	3.09 x 10^{10}	5.32 x 10^{16}	7.71 x 10^{9}	6.10 x 10^{17}
	S18	R25 >> $HOCH_3$ + PHE*		0.54	4.81 x 10^{11}	1.48 x 10^{12}	9.68 x 10^{10}	5.14 x 10^{16}	6.35 x 10^{10}	1.93 x 10^{17}	1.68 x 10^{10}	2.43 x 10^{18}
	S19	PHE* >> PHE + *		1.21	7.74 x 10^{10}	6.15 x 10^{0}	1.31 x 10^{10}	5.35 x 10^{11}	8.47 x 10^{9}	1.46 x 10^{13}	2.16 x 10^{9}	1.19 x 10^{16}
Guaiacol → Catechol	**S20**	R31 >TS31 > R32	1.67	0.03	1.47 x 10^{13}	2.51x10^{-16}	4.09 x 10^{13}	6.32 x 10^{-1}	5.02 x 10^{13}	9.21 x 10^{1}	8.03 x 10^{13}	4.14 x 10^{6}
	S21	R32 > TS32 > R33	0.71	−0.71	1.48 x 10^{12}	2.05 x 10^{-2}	2.24 x 10^{12}	2.44 x 10^{5}	2.38 x 10^{12}	2.11 x 10^{6}	2.67 x 10^{12}	1.88 x 10^{8}
	S22	R33 + H* >> R34 + *		0.08	1.13 x 10^{13}	6.02 x 10^{11}	9.88 x 10^{12}	1.69 x 10^{12}	9.18 x 10^{12}	1.75 x 10^{12}	6.96 x 10^{12}	1.45 x 10^{12}
	S23	R34 > TS33 > R35	0.76	−0.36	9.62 x 10^{11}	9.83 x 10^{-3}	2.03 x 10^{12}	1.47 x 10^{5}	2.35 x 10^{12}	1.44 x 10^{6}	3.34 x 10^{12}	1.86 x 10^{8}
	S24	R35 >> CAT + CH_4*		1.48	1.24 x 10^{11}	1.48 x 10^{-4}	2.38 x 10^{10}	9.59 x 10^{9}	1.57 x 10^{10}	6.46 x 10^{11}	4.21 x 10^{9}	3.69 x 10^{15}
	S25	CH_4* >> CH_4 + *		0.26	1.35 x 10^{11}	2.66 x 10^{13}	2.63 x 10^{10}	1.73 x 10^{15}	1.78 x 10^{10}	2.73 x 10^{15}	5.49 x 10^{9}	5.63 x 10^{15}
	S26	R35* >> CH_4 + CAT*		0.24	1.77 x 10^{11}	7.09 x 10^{13}	3.62 x 10^{10}	3.83 x 10^{15}	2.47 x 10^{10}	5.93 x 10^{15}	7.71 x 10^{9}	1.17 x 10^{16}
	S27	CAT* >> CAT + *		1.50	9.46 x 10^{10}	5.54 x 10^{-5}	1.73 x 10^{10}	4.33 x 10^{9}	1.14 x 10^{10}	2.98 x 10^{11}	2.99 x 10^{9}	1.77 x 10^{15}
Catechol → Phenol	**S28**	CAT + * >> CAT*		−1.50	3.04 x 10^{4}	6.27 x 10^{-6}	2.09 x 10^{4}	6.78 x 10^{-7}	1.93 x 10^{4}	4.19 x 10^{-7}	1.53 x 10^{4}	1.03 x 10^{-7}
	S29	H_2 + * >> H_2*		−0.54	2.24 x 10^{5}	3.92 x 10^{2}	1.54 x 10^{5}	6.15 x 10^{1}	1.42 x 10^{5}	4.12 x 10^{1}	1.13 x 10^{5}	1.28 x 10^{1}
	S30	CAT* + H* >> R41 + *		−0.01	1.71 x 10^{12}	3.93 x 10^{11}	2.76 x 10^{12}	7.78 x 10^{11}	3.11 x 10^{12}	8.81 x 10^{11}	4.49 x 10^{12}	1.24 x 10^{12}
	S31	R41 > TS41 > R42	2.13	0.69	1.11 x 10^{14}	3.82x10^{-24}	6.40 x 10^{14}	3.57 x 10^{-3}	9.20 x 10^{14}	3.15 x 10^{0}	2.45 x 10^{15}	8.96 x 10^{6}
	S32	R42 > TS42 > R43	0.73	−1.06	5.87 x 10^{13}	1.73 x 10^{1}	1.80 x 10^{14}	5.08 x 10^{8}	2.16 x 10^{14}	5.46 x 10^{9}	3.25 x 10^{14}	8.74 x 10^{11}
	S33	R43 + H* >> R44 + *		0.09	4.72 x 10^{12}	6.08 x 10^{10}	8.39 x 10^{12}	9.66 x 10^{11}	9.59 x 10^{12}	1.47 x 10^{12}	1.43 x 10^{13}	3.98 x 10^{12}
	S34	R44 > TS43 > R45	1.07	−0.15	3.36 x 10^{13}	9.48 x 10^{-6}	8.06 x 10^{13}	2.04 x 10^{5}	9.38 x 10^{13}	5.38 x 10^{6}	1.34 x 10^{14}	6.01 x 10^{9}

	S35	R45 >> H_2O* + PHE		1.15	1.97 x 10^{11}	3.51 x 10^{2}	4.67 x 10^{10}	1.66 x 10^{13}	3.32 x 10^{10}	4.56 x 10^{14}	1.16 x 10^{10}	4.63 x 10^{17}
	S36	R45 >> H_2O + PHE*		0.34	1.11 x 10^{12}	3.05 x 10^{13}	2.21 x 10^{11}	3.61 x 10^{16}	1.41 x 10^{11}	8.10 x 10^{16}	3.37 x 10^{10}	3.17 x 10^{17}
	S37	PHE* >> PHE + *		1.21	7.74 x 10^{10}	6.16 x 10^{0}	1.31 x 10^{10}	5.35 x 10^{11}	8.47 x 10^{9}	1.46 x 10^{13}	2.17 x 10^{9}	1.20 x 10^{16}
Anisole → Phenol	**S38**	ANI + * > ANI*		−1.32	3.06 x 10^{4}	6.26 x 10^{-6}	2.11 x 10^{4}	6.77 x 10^{-7}	1.95 x 10^{4}	4.18 x 10^{-7}	1.54 x 10^{4}	1.03 x 10^{-7}
	S39	H_2 + * >> H_2*		−0.54	2.24 x 10^{5}	3.92 x 10^{2}	1.54 x 10^{5}	6.15 x 10^{1}	1.42 x 10^{5}	4.12 x 10^{1}	1.13 x 10^{5}	1.28 x 10^{1}
	S40	ANI* + H* >> R51 + *		0.02	6.05 x 10^{11}	6.18 x 10^{10}	6.13 x 10^{11}	5.07 x 10^{10}	6.14 x 10^{11}	4.66 x 10^{10}	6.16 x 10^{11}	3.45 x 10^{10}
	S41	R51 > TS51 > R52	1.76	0.17	1.70 x 10^{13}	9.72 x 10^{-18}	4.71 x 10^{13}	1.48 x 10^{-1}	5.78 x 10^{13}	2.77 x 10^{1}	9.26 x 10^{13}	2.14 x 10^{6}
	S42	R52 > TS52 > R53	0.77	−0.71	1.23 x 10^{12}	1.36 x 10^{-3}	1.14 x 10^{12}	2.55 x 10^{4}	1.07 x 10^{12}	2.16 x 10^{5}	8.42 x 10^{11}	1.50 x 10^{7}
	S43	R53 + H* >> R54 + *		0.02	4.33 x 10^{11}	3.43 x 10^{10}	4.05 x 10^{11}	2.52 x 10^{10}	4.02 x 10^{11}	2.27 x 10^{10}	3.93 x 10^{11}	1.59 x 10^{10}
	S44	R54 > TS53 > R54	0.21	−0.18	1.29 x 10^{14}	1.52 x 10^{11}	5.73 x 10^{14}	1.21 x 10^{14}	7.54 x 10^{14}	3.32 x 10^{14}	1.54 x 10^{15}	3.46 x 10^{15}
	S45	R55 > PHE + CH_4*		1.20	1.81 x 10^{9}	1.59 x 10^{-2}	8.37 x 10^{7}	9.91 x 10^{7}	4.03 x 10^{7}	1.52 x 10^{9}	4.29 x 10^{6}	2.31 x 10^{11}
	S46	R55 > CH_4 + PHE*		0.24	3.17 x 10^{9}	6.93 x 10^{10}	1.68 x 10^{8}	3.20 x 10^{11}	8.48 x 10^{7}	2.85 x 10^{11}	1.09 x 10^{7}	1.08 x 10^{11}
	S47	PHE* >> PHE + *		1.21	7.74 x 10^{10}	6.16 x 10^{0}	1.31 x 10^{10}	5.35 x 10^{11}	8.47 x 10^{9}	1.46 x 10^{13}	2.17 x 10^{9}	1.20 x 10^{16}
Anisole → Benzene	**S48**	ANI + * > ANI*		−1.32	3.06 x 10^{4}	6.26 x 10^{-6}	2.11 x 10^{4}	6.77 x 10^{-7}	1.95 x 10^{4}	4.18 x 10^{-7}	1.54 x 10^{4}	1.03 x 10^{-7}
	S49	H_2 + * >> H_2*		−0.54	2.24 x 10^{5}	3.92 x 10^{2}	1.54 x 10^{5}	6.15 x 10^{1}	1.42 x 10^{5}	4.12 x 10^{1}	1.13 x 10^{5}	1.28 x 10^{1}
	S50	ANI* + H* >> R61 + *		0.01	1.05 x 10^{12}	1.82 x 10^{11}	1.14 x 10^{12}	1.58 x 10^{11}	1.16 x 10^{12}	1.48 x 10^{11}	1.19 x 10^{12}	1.15 x 10^{11}
	S51	R61 > TS61 > R62	2.09	0.81	1.74 x 10^{12}	3.92 x 10^{-26}	2.44 x 10^{12}	7.65 x 10^{-7}	2.55 x 10^{12}	3.09 x 10^{-4}	2.67 x 10^{12}	1.03 x 10^{2}
	S52	R62 > TS62 > R63	0.67	−1.08	3.77 x 10^{12}	1.65 x 10^{0}	4.73 x 10^{12}	2.99 x 10^{6}	4.73 x 10^{12}	1.94 x 10^{7}	4.26 x 10^{12}	8.24 x 10^{8}
	S53	R63* + H* >> R64 + *		0.02	2.42 x 10^{13}	2.89 x 10^{13}	1.46 x 10^{14}	6.35 x 10^{14}	2.21 x 10^{14}	1.24 x 10^{15}	7.77 x 10^{14}	8.72 x 10^{15}
	S54	R64* > TS63 > R65	0.92	−0.16	3.01 x 10^{11}	2.07 x 10^{-6}	1.44 x 10^{11}	8.25 x 10^{1}	1.19 x 10^{11}	7.35 x 10^{2}	6.48 x 10^{10}	5.04 x 10^{4}
	S55	R65 >> BEN + $HOCH_3$*		1.08	1.89 x 10^{10}	9.05 x 10^{-2}	1.34 x 10^{9}	8.28 x 10^{7}	7.29 x 10^{8}	1.05 x 10^{9}	1.10 x 10^{8}	1.24 x 10^{11}
	S56	R65 >> $HOCH_3$ + BEN*		0.54	1.54 x 10^{11}	1.06 x 10^{11}	1.22 x 10^{10}	1.31 x 10^{15}	6.61 x 10^{9}	3.77 x 10^{15}	1.01 x 10^{9}	2.04 x 10^{16}
	S57	BEN* >> BEN + *		1.09	3.38 x 10^{10}	3.93 x 10^{-1}	5.29 x 10^{9}	9.21 x 10^{8}	3.38 x 10^{9}	1.48 x 10^{10}	8.43 x 10^{8}	3.72 x 10^{12}
Phenol → Benzene	**S58**	PHE + * > PHE*		−1.21	3.28 x 10^{4}	1.29 x 10^{-5}	2.27 x 10^{4}	1.39 x 10^{-6}	1.95 x 10^{4}	5.67 x 10^{-7}	1.66 x 10^{4}	2.12 x 10^{-7}
	S59	H_2 + * >> H_2*		−0.54	2.24 x 10^{5}	3.92 x 10^{2}	1.54 x 10^{5}	6.15 x 10^{1}	1.42 x 10^{5}	4.12 x 10^{1}	1.13 x 10^{5}	1.28 x 10^{1}
	S60	PHE* + H* >> R71 + *		0.01	1.98 x 10^{12}	5.12 x 10^{11}	3.46 x 10^{12}	1.11 x 10^{12}	3.95 x 10^{12}	1.28 x 10^{12}	5.91 x 10^{12}	1.91 x 10^{12}
	S61	R71 > TS71 > R72	2.23	0.86	4.22 x 10^{13}	1.84 x 10^{-26}	1.78 x 10^{14}	7.48 x 10^{-5}	2.44 x 10^{14}	7.89 x 10^{-2}	5.92 x 10^{14}	3.19 x 10^{5}
	S62	R72 > TS72 > R73	0.59	−1.16	6.55 x $10^{!2}$	1.12 x 10^{2}	9.74 x 10^{12}	4.86 x 10^{7}	9.97 x 10^{12}	2.61 x 10^{8}	9.41 x 10^{12}	7.42 x 10^{9}
	S63	R73 + H* >> R74 + *		0.03	1.63 x 10^{13}	1.06 x 10^{13}	6.17 x 10^{13}	1.16 x 10^{14}	8.31 x 10^{13}	1.88 x 10^{14}	2.00 x 10^{14}	7.42 x 10^{14}
	S64	R74 > TS73 > R75	1.03	−0.19	5.91 x 10^{12}	1.98 x 10^{-6}	7.62 x $10^{!2}$	6.69 x 10^{3}	7.70 x 10^{12}	1.24 x 10^{5}	7.24 x 10^{12}	5.15 x 10^{7}
	S65	R75 >> BEN + H_2O*		1.04	6.24 x 10^{8}	1.34 x 10^{-3}	4.88 x 10^{7}	4.99 x 10^{5}	2.79 x 10^{7}	5.87 x 10^{6}	5.42 x 10^{6}	6.86 x 10^{8}
	S66	R75 >> H_2O + BEN*		0.36	8.08 x 10^{9}	1.83 x 10^{9}	5.71 x 10^{8}	6.27 x 10^{11}	2.98 x 10^{8}	1.03 x 10^{12}	4.03 x 10^{7}	1.15 x 10^{12}
	S67	BEN* >> BEN + *		1.09	3.38 x 10^{10}	3.93 x 10^{-1}	5.29 x 10^{9}	9.21 x 10^{8}	3.38 x 10^{9}	1.48 x 10^{10}	8.43 x 10^{8}	3.72 x 10^{12}
	S68	GUA* >> GUA + *		1.35	2.92 x 10^{11}	3.15 x 10^{-1}	6.18 x 10^{10}	1.30 x 10^{12}	4.11 x 10^{10}	6.03 x 10^{13}	1.11 x 10^{10}	1.56 x 10^{17}

***Table A5**. Pre-exponential factor (A_o) and forward rate constant (k) for the elementary reactions for the guaiacol conversion into benzene at different temperatures (273 K, 573 K, 673 and 1073 K) for Pd (111). The notation of the structures used in each step (S) is explained **in Table A1**, where GUA, CAT, ANI, PHE and BEN represent guaiacol, catechol, anisole, phenol and benzene, respectively.*

					273 K		573 K		673 K		1073 K	
	Step	Reactions	E_a (eV)	E_r (eV)	A_o	k (s^{-1})	A_o	k (s^{-1})	A_o	k (s^{-1})	A_o	k (s^{-1})
	S1	GUA + * >> GUA*		−1.94	3.44 x 10^{4}	3.26 x 10^{-6}	2.38 x 10^{4}	3.53 x 10^{-7}	2.20 x 10^{4}	2.18 x 10^{-7}	1.73 x 10^{4}	5.37 x 10^{-8}
	S2	H_2 + * >> H_2*		−0.92	2.65 x 10^{5}	3.59 x 10^{2}	1.87 x 10^{5}	6.16 x 10^{1}	1.72 x 10^{5}	4.12 x 10^{1}	1.36 x 10^{5}	1.28 x 10^{1}
	S3	GUA* + H* >> R11 + *		−0.04	7.21 x 10^{12}	6.33 x 10^{13}	1.63 x 10^{13}	5.18 x 10^{13}	1.95 x 10^{13}	5.38 x 10^{13}	3.18 x 10^{13}	6.68 x 10^{13}
Guaiacol → Anisole	**S4**	R11 > TS11 > R12	2.14	1.35	2.99 x 10^{13}	2.61x10^{-25}	1.42 x 10^{14}	2.20 x 10^{-4}	1.98 x 10^{14}	1.88 x 10^{-1}	4.96 x 10^{14}	4.81 x 10^{5}
	S5	R12 > TS12 > R13	0.66	−1.08	9.51 x 10^{13}	2.50 x 10^{2}	1.84 x 10^{15}	8.49 x 10^{10}	3.52 x 10^{15}	1.75 x 10^{12}	2.27 x 10^{16}	2.27 x 10^{15}
	S6	R13 + H* >> R14 + *		−0.04	7.33 x 10^{12}	3.73 x 10^{13}	1.64 x 10^{13}	4.07 x 10^{13}	1.94 x 10^{13}	4.36 x 10^{13}	3.12 x 10^{13}	5.72 x 10^{13}
	S7	R14 > TS13 > R15	0.46	−0.63	2.28 x 10^{12}	1.67 x 10^{4}	5.99 x 10^{12}	5.44 x 10^{8}	7.55 x 10^{12}	2.55 x 10^{9}	1.45 x 10^{13}	8.22 x 10^{10}
	S8	R15 >> H_2O* + ANI		2.00	2.58 x 10^{11}	4.96x10^{-14}	3.92 x 10^{10}	3.99 x 10^{5}	2.32 x 10^{10}	1.14 x 10^{8}	4.15 x 10^{9}	1.09 x 10^{13}
	S9	H_2O* >> H_2O + *		0.40	3.69 x 10^{11}	4.86 x 10^{11}	7.08 x 10^{10}	1.73 x 10^{15}	4.53 x 10^{10}	4.46 x 10^{15}	1.09 x 10^{10}	2.29 x 10^{16}
	S10	R15 >> H_2O + ANI*		0.41	1.71 x 10^{11}	9.64 x 10^{10}	2.92 x 10^{10}	3.31 x 10^{14}	1.84 x 10^{10}	8.40 x 10^{14}	4.24 x 10^{9}	4.09 x 10^{15}
	S11	ANI* >> ANI + *		1.99	5.58 x 10^{11}	2.51x10^{-13}	9.49 x 10^{10}	2.08 x 10^{6}	5.71 x 10^{10}	6.03 x 10^{8}	1.06 x 10^{10}	6.12 x 10^{13}
Guaiacol → Phenol	**S12**	R21 > TS21 > R22	1.98	1.52	2.30 x 10^{13}	1.52x10^{-22}	9.91 x 10^{13}	3.24 x 10^{-3}	1.34 x 10^{14}	1.60 x 10^{0}	3.08 x 10^{14}	1.22 x 10^{6}
	S13	R22 > TS22 > R23	0.61	−1.17	2.48 x 10^{12}	3.02 x 10^{0}	6.70 x 10^{12}	1.34 x 10^{7}	8.19 x 10^{12}	1.11 x 10^{8}	1.40 x 10^{13}	1.04 x 10^{10}
	S14	R23 + H* >> R24 + *		−0.03	9.55 x 10^{13}	3.29 x 10^{15}	4.55 x 10^{14}	1.38 x 10^{16}	6.37 x 10^{14}	2.02 x 10^{16}	1.68 x 10^{15}	6.64 x 10^{16}
	S15	R24 > TS23 > R25	0.47	−0.56	1.86 x 10^{12}	4.62 x 10^{3}	6.27 x 10^{12}	3.21 x 10^{8}	8.20 x 10^{12}	1.68 x 10^{9}	1.72 x 10^{13}	7.02 x 10^{10}
	S16	R25 >> PHE + $HOCH_3$*		1.81	1.12 x 10^{11}	1.17x10^{-11}	8.08 x 10^{9}	5.25 x 10^{5}	4.03 x 10^{9}	6.56 x 10^{7}	4.41 x 10^{8}	8.56 x 10^{11}
	S17	$HOCH_3$* >> $HOCH_3$ + *		0.55	4.75 x 10^{11}	1.25 x 10^{12}	1.40 x 10^{11}	9.44 x 10^{16}	1.03 x 10^{11}	4.26 x 10^{17}	3.82 x 10^{10}	9.45 x 10^{18}
	S18	R25 >> $HOCH_3$ + PHE*		0.50	8.57 x 10^{10}	3.84 x 10^{11}	7.66 x 10^{9}	1.48 x 10^{15}	4.23 x 10^{9}	3.64 x 10^{15}	6.74 x 10^{8}	1.43 x 10^{16}
	S19	PHE* >> PHE + *		1.86	6.18 x 10^{11}	3.80x10^{-11}	1.48 x 10^{11}	3.35 x 10^{7}	9.78 x 10^{10}	7.68 x 10^{9}	2.50 x 10^{10}	5.66 x 10^{14}
Guaiacol → Catechol	**S20**	R31 >TS31 > R32	1.62	−0.15	4.20 x 10^{12}	3.95x10^{-17}	1.37 x 10^{13}	1.61 x 10^{-1}	1.83 x 10^{13}	2.62 x 10^{1}	4.20 x 10^{13}	1.90 x 10^{6}
	S21	R32 > TS32 > R33	0.65	−0.21	3.27 x 10^{11}	3.62 x 10^{-2}	1.06 x 10^{11}	5.93 x 10^{3}	7.71 x 10^{10}	2.16 x 10^{4}	2.72 x 10^{10}	1.62 x 10^{5}
	S22	R33 + H* >> R34 + *		−0.04	4.98 x 10^{12}	1.90 x 10^{13}	1.03 x 10^{13}	1.84 x 10^{13}	1.20 x 10^{13}	1.94 x 10^{13}	1.90 x 10^{13}	2.42 x 10^{13}
	S23	R34 > TS33 > R35	0.70	−0.11	8.73 x 10^{12}	4.47 x 10^{0}	1.96 x 10^{13}	2.58 x 10^{7}	2.28 x 10^{13}	2.25 x 10^{8}	3.26 x 10^{13}	2.33 x 10^{10}
	S24	R35 >> CAT + CH_4*		2.06	4.65 x 10^{11}	5.38x10^{-15}	1.58 x 10^{11}	1.14 x 10^{6}	1.16 x 10^{11}	5.94 x 10^{8}	4.15 x 10^{10}	2.96 x 10^{14}
	S25	CH_4* >> CH_4 + *		0.26	6.18 x 10^{10}	5.15 x 10^{12}	4.24 x 10^{9}	6.28 x 10^{13}	2.22 x 10^{9}	6.58 x 10^{13}	3.08 x 10^{8}	3.75 x 10^{13}
	S26	R35* >> CH_4 + CAT*		0.26	1.19 x 10^{11}	1.93 x 10^{13}	1.31 x 10^{10}	5.22 x 10^{14}	7.75 x 10^{9}	6.66 x 10^{14}	1.57 x 10^{9}	7.06 x 10^{14}
	S27	CAT* >> CAT + *		2.06	2.41 x 10^{11}	1.43x10^{-15}	5.11 x 10^{10}	1.38 x 10^{5}	3.32 x 10^{10}	5.86 x 10^{7}	8.13 x 10^{9}	1.57 x 10^{13}
Catechol → Phenol	**S28**	CAT + * >> CAT*		−2.06	3.66 x 10^{4}	6.27 x 10^{-6}	2.53 x 10^{4}	6.78 x 10^{-7}	2.33 x 10^{4}	4.19 x 10^{-7}	1.85 x 10^{4}	1.03 x 10^{-7}
	S29	H_2 + * >> H_2*		−0.92	2.65 x 10^{5}	3.59 x 10^{2}	1.87 x 10^{5}	6.16 x 10^{1}	1.72 x 10^{5}	4.12 x 10^{1}	1.36 x 10^{5}	1.28 x 10^{1}
	S30	CAT* + H* >> R41 + *		0.00	2.97 x 10^{12}	1.83 x 10^{12}	5.99 x 10^{12}	3.48 x 10^{12}	7.00 x 10^{12}	3.99 x 10^{12}	1.10 x 10^{13}	6.06 x 10^{12}
	S31	R41 > TS41 > R42	2.36	1.39	7.94 x 10^{13}	1.28x10^{-28}	4.18 x 10^{14}	1.77 x 10^{-5}	5.91 x 10^{14}	3.02 x 10^{-2}	1.51 x 10^{15}	3.39 x 10^{5}
	S32	R42 > TS42 > R43	0.76	−1.11	5.14 x 10^{12}	4.52 x 10^{-2}	9.46 x 10^{12}	1.54 x 10^{6}	1.05 x 10^{13}	1.60 x 10^{7}	1.31 x 10^{13}	2.19 x 10^{9}
	S33	R43 + H* >> R44 + *		−0.03	6.18 x 10^{12}	2.27 x 10^{13}	1.26 x 10^{13}	2.42 x 10^{13}	1.47 x 10^{13}	2.58 x 10^{13}	2.30 x 10^{13}	3.32 x 10^{13}
	S34	R44 > TS43 > R45	0.71	−0.46	8.24 x 10^{12}	1.95 x 10^{0}	1.78 x 10^{13}	1.65 x 10^{7}	2.04 x 10^{13}	1.46 x 10^{8}	2.76 x 10^{13}	1.51 x 10^{10}

	S35	R45 >> H_2O* + PHE		1.89	8.41 x 10^{11}	1.73 x 10^{-11}	1.02 x 10^{11}	7.99 x 10^{6}	5.49 x 10^{10}	1.43 x 10^{9}	7.16 x 10^{9}	4.32 x 10^{13}
	S36	R45 >> H_2O + PHE*		0.44	5.03 x 10^{11}	2.21 x 10^{11}	4.88 x 10^{10}	4.13 x 10^{14}	2.54 x 10^{10}	8.30 x 10^{14}	3.11 x 10^{9}	1.75 x 10^{15}
	S37	PHE* >> PHE + *		1.86	6.18 x 10^{11}	3.80 x 10^{-11}	1.48 x 10^{11}	3.35 x 10^{7}	9.78 x 10^{10}	7.68 x 10^{9}	2.50 x 10^{10}	5.66 x 10^{14}
Anisole → Phenol	**S38**	ANI + * > ANI*		−1.99	3.69 x 10^{4}	6.26 x 10^{-6}	2.55 x 10^{4}	6.77 x 10^{-7}	2.35 x 10^{4}	4.18 x 10^{-7}	1.86 x 10^{4}	1.03 x 10^{-7}
	S39	H_2 + * >> H_2*		−0.92	2.65 x 10^{5}	3.59 x 10^{2}	1.87 x 10^{5}	6.16 x 10^{1}	1.72 x 10^{5}	4.12 x 10^{1}	1.36 x 10^{5}	1.28 x 10^{1}
	S40	ANI* + H* >> R51 + *		−0.04	1.15 x 10^{13}	8.78 x 10^{13}	2.55 x 10^{13}	9.34 x 10^{13}	3.01 x 10^{13}	1.00 x 10^{14}	4.85 x 10^{13}	1.33 x 10^{14}
	S41	R51 > TS51 > R52	1.68	−0.03	2.62 x 10^{12}	2.67 x 10^{-18}	6.22 x 10^{12}	1.43 x 10^{-2}	7.59 x 10^{12}	2.26 x 10^{0}	1.29 x 10^{13}	1.29 x 10^{5}
	S42	R52 > TS52 > R53	0.66	−0.20	1.23 x 10^{13}	1.59 x 10^{1}	4.63 x 10^{13}	1.91 x 10^{8}	5.99 x 10^{13}	1.89 x 10^{9}	1.18 x 10^{14}	2.88 x 10^{11}
	S43	R53 + H* >> R54 + *		−0.04	1.14 x 10^{12}	2.39 x 10^{12}	2.14 x 10^{12}	1.43 x 10^{12}	2.47 x 10^{12}	1.39 x 10^{12}	3.79 x 10^{12}	1.44 x 10^{12}
	S44	R54 > TS53 > R54	0.67	−0.03	4.57 x 10^{12}	5.45 x 10^{0}	9.27 x 10^{12}	1.35 x 10^{7}	1.06 x 10^{13}	1.04 x 10^{8}	1.47 x 10^{13}	8.06 x 10^{9}
	S45	R55 > PHE + CH_4*		1.90	3.02 x 10^{11}	2.23x10^{-12}	4.46 x 10^{10}	1.92 x 10^{6}	2.61 x 10^{10}	3.99 x 10^{8}	4.55 x 10^{9}	1.92 x 10^{13}
	S46	R55 > CH_4 + PHE*		0.30	3.02 x 10^{10}	3.02 x 10^{11}	1.28 x 10^{9}	3.61 x 10^{12}	5.91 x 10^{8}	3.42 x 10^{12}	5.60 x 10^{7}	1.27 x 10^{12}
	S47	PHE* >> PHE + *		1.86	6.18 x 10^{11}	3.80x10^{-11}	1.48 x 10^{11}	3.35 x 10^{7}	9.78 x 10^{10}	7.68 x 10^{9}	2.50 x 10^{10}	5.66 x 10^{14}
Anisole → Benzene	**S48**	ANI + * > ANI*		−1.99	3.69 x 10^{4}	6.26 x 10^{-6}	2.55 x 10^{4}	6.77 x 10^{-7}	2.35 x 10^{4}	4.18 x 10^{-7}	1.86 x 10^{4}	1.03 x 10^{-7}
	S49	H_2 + * >> H_2*		−0.92	2.65 x 10^{5}	3.59 x 10^{2}	1.87 x 10^{5}	6.16 x 10^{1}	1.72 x 10^{5}	4.12 x 10^{1}	1.36 x 10^{5}	1.28 x 10^{1}
	S50	ANI* + H* >> R61 + *		−0.04	1.18 x 10^{13}	9.23 x 10^{13}	2.64 x 10^{13}	9.89 x 10^{13}	3.12 x 10^{13}	1.06 x 10^{14}	5.02 x 10^{13}	1.42 x 10^{14}
	S51	R61 > TS61 > R62	2.45	1.61	1.76 x 10^{12}	9.49 x 10^{-33}	2.29 x 10^{12}	4.90 x 10^{-10}	2.38 x 10^{12}	5.82 x 10^{-7}	2.46 x 10^{12}	1.93 x 10^{0}
	S52	R62 > TS62 > R63	0.59	−1.06	2.29 x 10^{14}	2.22 x 10^{4}	1.91 x 10^{15}	4.04 x 10^{11}	2.93 x 10^{15}	4.72 x 10^{12}	9.19 x 10^{15}	1.25 x 10^{15}
	S53	R63* + H* >> R64 + *		−0.04	3.14 x 10^{12}	9.34 x 10^{12}	6.92 x 10^{12}	8.66 x 10^{12}	8.18 x 10^{12}	9.07 x 10^{12}	1.32 x 10^{13}	1.13 x 10^{13}
	S54	R64* > TS63 > R65	0.47	−0.58	1.12 x 10^{12}	2.49 x 10^{3}	1.94 x 10^{12}	5.39 x 10^{7}	2.18 x 10^{12}	2.16 x 10^{18}	2.89 x 10^{12}	4.06 x 10^{9}
	S55	R65 >> BEN + $HOCH_3$*		1.83	2.49 x 10^{11}	2.22 x 10^{-14}	3.40 x 10^{10}	2.68 x 10^{3}	1.97 x 10^{10}	4.12 x 10^{5}	3.34 x 10^{9}	9.78 x 10^{9}
	S56	R65 >> $HOCH_3$ + BEN*		0.52	4.16 x 10^{11}	2.44 x 10^{12}	1.24 x 10^{11}	1.18 x 10^{17}	9.08 x 10^{10}	5.01 x 10^{17}	3.39 x 10^{10}	9.72 x 10^{18}
	S57	BEN* >> BEN + *		1.86	2.84 x 10^{11}	1.13x10^{-14}	3.85 x 10^{10}	2.14 x 10^{3}	2.22 x 10^{10}	3.50 x 10^{5}	3.76 x 10^{9}	9.51 x 10^{9}
Phenol → Benzene	**S58**	PHE + * > PHE*		−0.04	3.96 x 10^{4}	1.29 x 10^{-5}	2.73 x 10^{4}	1.39 x 10^{-6}	2.52 x 10^{4}	8.60 x 10^{-7}	1.99 x 10^{4}	2.12 x 10^{-7}
	S59	H_2 + * >> H_2*		−0.92	2.65 x 10^{5}	3.59 x 10^{2}	1.87 x 10^{5}	6.16 x 10^{1}	1.72 x 10^{5}	4.12 x 10^{1}	1.36 x 10^{5}	1.28 x 10^{1}
	S60	PHE* + H* >> R71 + *		−0.04	1.05 x 10^{13}	7.16 x 10^{13}	2.45 x 10^{13}	8.18 x 10^{13}	2.92 x 10^{13}	8.91 x 10^{13}	4.79 x 10^{13}	1.23 x 10^{14}
	S61	R71 > TS71 > R72	2.11	1.64	4.98 x 10^{12}	3.85 x 10^{-26}	1.78 x 10^{13}	1.14 x 10^{-5}	2.38 x 10^{13}	8.15 x 10^{-3}	5.42 x 10^{13}	1.36 x 10^{4}
	S62	R72 > TS72 > R73	0.57	−1.18	2.34 x 10^{13}	7.42 x 10^{2}	7.45 x 10^{13}	1.58 x 10^{9}	8.86 x 10^{13}	1.13 x 10^{10}	1.26 x 10^{14}	6.70 x 10^{11}
	S63	R73 + H* >> R74 + *		−0.09	7.44 x 10^{12}	3.25 x 10^{14}	2.04 x 10^{13}	1.85 x 10^{14}	2.59 x 10^{13}	1.93 x 10^{14}	5.42 x 10^{13}	2.85 x 10^{14}
	S64	R74 > TS73 > R75	0.63	−0.49	7.16 x 10^{12}	4.72 x 10^{1}	1.44 x 10^{13}	5.91 x 10^{7}	1.62 x 10^{13}	4.01 x 10^{8}	2.14 x 10^{13}	2.34 x 10^{10}
	S65	R75 >> BEN + H_2O*		1.80	1.16 x 10^{12}	1.61 x 10^{-12}	4.01 x 10^{11}	4.42 x 10^{5}	2.94 x 10^{11}	9.19 x 10^{7}	1.05 x 10^{11}	6.30 x 10^{12}
	S66	R75 >> H_2O + BEN*		0.34	1.51 x 10^{12}	6.91 x 10^{13}	7.38 x 10^{11}	3.56 x 10^{17}	5.99 x 10^{11}	1.17 x 10^{18}	3.04 x 10^{11}	1.52 x 10^{19}
	S67	BEN* >> BEN + *		1.86	2.84 x 10^{11}	1.13x10^{-14}	3.85 x 10^{10}	2.14 x 10^{3}	2.22 x 10^{10}	3.50 x 10^{5}	3.76 x 10^{9}	9.51 x 10^{9}
	S68	GUA* >> GUA + *		1.94	1.06 x 10^{12}	5.56 x 10^{-12}	2.71 x 10^{11}	5.31 x 10^{7}	1.79 x 10^{11}	1.65 x 10^{10}	4.50 x 10^{10}	2.28 x 10^{15}

***Table A6**. Pre-exponential factor (A_o) and forward rate constant (k) for the elementary reactions for the guaiacol conversion into benzene at different temperatures (273 K, 573 K, 673 and 1073 K) for Pt (111). The notation of the structures used in each step (S) is explained **in Table A1**, where GUA, CAT, ANI, PHE and BEN represent guaiacol, catechol, anisole, phenol and benzene, respectively.*

					273 K		573 K		673 K		1073 K	
	Step	**Reactions**	E_a (eV)	E_r (eV)	A_o	k (s^{-1})	A_o	k (s^{-1})	A_o	k (s^{-1})	A_o	k (s^{-1})
	S1	GUA + * >> GUA*		−2.69	3.48 x 10^{4}	3.26 x 10^{-6}	2.41 x 10^{4}	3.53 x 10^{-7}	2.22 x 10^{4}	2.18 x 10^{-7}	1.76 x 10^{4}	5.37 x 10^{-8}
	S2	H_2 + * >> H_2*		−0.74	2.73 x 10^{5}	3.93 x 10^{2}	1.89 x 10^{5}	6.16 x 10^{1}	1.74 x 10^{5}	4.12 x 10^{1}	1.38 x 10^{5}	1.28 x 10^{1}
	S3	GUA* + H* >> R11 + *		−0.12	2.66 x 10^{12}	3.81 x 10^{13}	6.23 x 10^{12}	2.14 x 10^{13}	7.34 x 10^{12}	1.99 x 10^{13}	1.12 x 10^{13}	1.68 x 10^{13}
Guaiacol → Anisole	**S4**	R11 > TS11 > R12	1.89	1.85	7.32 x 10^{12}	6.93x10^{-22}	9.67 x 10^{12}	3.10 x 10^{-4}	1.00 x 10^{13}	7.72 x 10^{-2}	1.03 x 10^{13}	9.25 x 10^{3}
	S5	R12 > TS12 > R13	0.24	−1.63	1.76 x 10^{12}	1.12 x 10^{8}	2.02 x 10^{12}	7.18 x 10^{9}	2.07 x 10^{12}	1.22 x 10^{10}	2.24 x 10^{12}	3.70 x 10^{10}
	S6	R13 + H* >> R14 + *		−0.11	1.00 x 10^{13}	1.55 x 10^{14}	3.90 x 10^{13}	3.69 x 10^{14}	5.20 x 10^{13}	4.61 x 10^{14}	1.17 x 10^{14}	8.96 x 10^{14}
	S7	R14 > TS13 > R15	0.28	−0.56	5.52 x 10^{12}	1.06 x 10^{8}	6.30 x 10^{12}	1.93 x 10^{10}	6.42 x 10^{12}	3.84 x 10^{10}	6.86 x 10^{12}	1.69 x 10^{11}
	S8	R15 >> H_2O* + ANI		2.68	1.99 x 10^{12}	7.20x10^{-25}	4.07 x 10^{11}	2.62 x 10^{1}	2.53 x 10^{11}	6.29 x 10^{4}	5.14 x 10^{10}	6.17 x 10^{11}
	S9	H_2O* >> H_2O + *		0.42	1.68 x 10^{11}	8.62 x 10^{10}	2.14 x 10^{10}	1.67 x 10^{14}	1.23 x 10^{10}	3.65 x 10^{14}	2.08 x 10^{9}	1.08 x 10^{15}
	S10	R15 >> H_2O + ANI*		0.43	2.89 x 10^{11}	1.07 x 10^{11}	2.84 x 10^{10}	2.16 x 10^{14}	1.56 x 10^{10}	4.67 x 10^{14}	2.36 x 10^{9}	1.35 x 10^{15}
	S11	ANI* >> ANI + *		2.67	1.16 x 10^{12}	5.82x10^{-25}	3.06 x 10^{11}	2.03 x 10^{1}	2.00 x 10^{11}	4.91 x 10^{4}	4.54 x 10^{10}	4.92 x 10^{11}
Guaiacol → Phenol	**S12**	R21 > TS21 > R22	1.88	1.59	8.12 x 10^{12}	1.37x10^{-21}	1.39 x 10^{13}	8.24 x 10^{-4}	1.55 x 10^{13}	2.21 x 10^{-1}	2.03 x 10^{13}	3.57 x 10^{4}
	S13	R22 > TS22 > R23	0.39	−1.35	7.09 x 10^{12}	9.77 x 10^{5}	1.55 x 10^{13}	8.78 x 10^{9}	1.83 x 10^{13}	3.22 x 10^{10}	2.98 x 10^{13}	6.02 x 10^{11}
	S14	R23 + H* >> R24 + *		0.04	1.68 x 10^{12}	1.61 x 10^{11}	2.02 x 10^{12}	2.65 x 10^{11}	2.08 x 10^{12}	2.73 x 10^{11}	2.22 x 10^{12}	2.65 x 10^{11}
	S15	R24 > TS23 > R25	0.16	−0.61	2.39 x 10^{12}	4.90 x 10^{8}	4.88 x 10^{12}	6.59 x 10^{10}	5.65 x 10^{12}	1.30 x 10^{11}	8.53 x 10^{12}	5.80 x 10^{11}
	S16	R25 >> PHE + $HOCH_3$*		2.48	1.05 x 10^{12}	6.23x10^{-22}	2.89 x 10^{11}	3.78 x 10^{2}	1.89 x 10^{11}	5.23 x 10^{5}	4.30 x 10^{10}	1.58 x 10^{12}
	S17	$HOCH_3$* >> $HOCH_3$ + *		0.63	1.37 x 10^{11}	5.40 x 10^{9}	2.20 x 10^{10}	8.01 x 10^{14}	1.40 x 10^{10}	3.57 x 10^{15}	3.43 x 10^{9}	6.16 x 10^{16}
	S18	R25 >> $HOCH_3$ + PHE*		0.56	5.82 x 10^{11}	8.30 x 10^{11}	1.14 x 10^{11}	4.62 x 10^{16}	7.50 x 10^{10}	1.83 x 10^{17}	1.95 x 10^{10}	2.57 x 10^{18}
	S19	PHE* >> PHE + *		2.54	2.46 x 10^{11}	4.05x10^{-24}	5.55 x 10^{10}	6.57 x 10^{0}	3.53 x 10^{10}	1.02 x 10^{4}	7.55 x 10^{9}	3.79 x 10^{10}
Guaiacol → Catechol	**S20**	R31 >TS31 > R32	1.65	−0.28	7.64 x 10^{12}	5.63x10^{-17}	1.75 x 10^{13}	1.36 x 10^{-1}	2.06 x 10^{13}	1.86 x 10^{1}	2.88 x 10^{13}	6.84 x 10^{5}
	S21	R32 > TS32 > R33	0.36	−0.38	1.08 x 10^{12}	1.63 x 10^{5}	8.39 x 10^{11}	1.03 x 10^{8}	7.78 x 10^{11}	2.24 x 10^{8}	6.02 x 10^{11}	9.19 x 10^{8}
	S22	R33 + H* >> R34 + *		−0.12	1.52 x 10^{13}	5.26 x 10^{14}	6.66 x 10^{13}	1.14 x 10^{15}	9.06 x 10^{13}	1.42 x 10^{15}	2.13 x 10^{14}	2.77 x 10^{15}
	S23	R34 > TS33 > R35	0.88	0.18	3.21 x 10^{13}	1.34 x 10^{-2}	9.21 x 10^{13}	9.34 x 10^{6}	1.14 x 10^{14}	1.61 x 10^{8}	2.05 x 10^{14}	8.63 x 10^{10}
	S24	R35 >> CAT + CH_4*		2.80	1.36 x 10^{13}	4.57x10^{-26}	1.27 x 10^{13}	5.74 x 10^{2}	1.11 x 10^{13}	3.72 x 10^{6}	5.84 x 10^{12}	4.63 x 10^{14}
	S25	CH_4* >> CH_4 + *		0.26	1.99 x 10^{10}	9.95 x 10^{11}	1.87 x 10^{9}	1.81 x 10^{13}	1.08 x 10^{9}	2.15 x 10^{13}	2.10 x 10^{8}	1.90 x 10^{13}
	S26	R35* >> CH_4 + CAT*		0.26	4.61 x 10^{11}	2.14 x 10^{14}	1.79 x 10^{11}	4.55 x 10^{16}	1.42 x 10^{11}	9.43 x 10^{16}	6.90 x 10^{10}	4.36 x 10^{17}
	S27	CAT* >> CAT + *		2.80	5.90 x 10^{11}	2.13x10^{-28}	1.33 x 10^{11}	2.28 x 10^{-1}	8.45 x 10^{10}	8.47 x 10^{2}	1.78 x 10^{10}	2.01 x 10^{10}
Catechol → Phenol	**S28**	CAT + * >> CAT*		−2.80	3.70 x 10^{4}	6.27 x 10^{-6}	2.55 x 10^{4}	6.78 x 10^{-7}	2.36 x 10^{4}	4.19 x 10^{-7}	1.87 x 10^{4}	1.03 x 10^{-7}
	S29	H_2 + * >> H_2*		−0.74	2.73 x 10^{5}	3.93 x 10^{2}	1.89 x 10^{5}	6.16 x 10^{1}	1.74 x 10^{5}	4.12 x 10^{1}	1.38 x 10^{5}	1.28 x 10^{1}
	S30	CAT* + H* >> R41 + *		−0.12	3.86 x 10^{12}	5.71 x 10^{13}	7.89 x 10^{12}	3.23 x 10^{13}	9.09 x 10^{12}	2.99 x 10^{13}	1.33 x 10^{13}	2.49 x 10^{13}
	S31	R41 > TS41 > R42	2.11	1.81	9.65 x 10^{12}	8.79x10^{-26}	2.71 x 10^{13}	1.89 x 10^{-5}	3.33 x 10^{13}	1.21 x 10^{-2}	5.57 x 10^{13}	1.33 x 10^{4}
	S32	R42 > TS42 > R43	0.54	1.18	7.92 x 10^{12}	3.26 x 10^{3}	1.42 x 10^{13}	3.89 x 10^{8}	1.55 x 10^{13}	1.89 x 10^{9}	1.93 x 10^{13}	5.45 x 10^{10}
	S33	R43 + H* >> R44 + *		−0.05	5.67 x 10^{12}	3.33 x 10^{13}	1.15 x 10^{13}	2.62 x 10^{13}	1.34 x 10^{13}	2.67 x 10^{13}	2.08 x 10^{13}	3.13 x 10^{13}
	S34	R44 > TS43 > R45	0.08	−0.74	3.78 x 10^{12}	3.27 x 10^{10}	4.92 x 10^{12}	3.44 x 10^{11}	5.06 x 10^{12}	4.43 x 10^{11}	5.26 x 10^{12}	6.58 x 10^{11}

	S35	R45 >> H_2O* + PHE		2.50	6.19 x 10^{12}	3.97 x 10^{-21}	5.59 x 10^{12}	4.50 x 10^{4}	5.05 x 10^{12}	1.20 x 10^{8}	3.23 x 10^{12}	2.62 x 10^{15}
	S36	R45 >> H_2O + PHE*		0.38	4.25 x 10^{12}	8.45 x 10^{13}	2.16 x 10^{12}	1.15 x 10^{18}	1.76 x 10^{12}	4.29 x 10^{18}	8.94 x 10^{11}	7.45 x 10^{19}
	S37	PHE* >> PHE + *		2.54	2.46 x 10^{11}	4.05 x 10^{-24}	5.55 x 10^{10}	6.57 x 10^{0}	3.53 x 10^{10}	1.02 x 10^{4}	7.55 x 10^{9}	3.79 x 10^{10}
Anisole → Phenol	**S38**	ANI + * > ANI*		−2.67	3.73 x 10^{4}	6.26 x 10^{-6}	2.58 x 10^{4}	6.77 x 10^{-7}	2.38 x 10^{4}	4.18 x 10^{-7}	1.88 x 10^{4}	1.03 x 10^{-7}
	S39	H_2 + * >> H_2*		−0.74	2.73 x 10^{5}	3.93 x 10^{2}	1.89 x 10^{5}	6.16 x 10^{1}	1.74 x 10^{5}	4.12 x 10^{1}	1.38 x 10^{5}	1.28 x 10^{1}
	S40	ANI* + H* >> R51 + *		−0.05	8.87 x 10^{12}	1.03 x 10^{14}	1.78 x 10^{13}	6.80 x 10^{13}	2.06 x 10^{13}	6.78 x 10^{13}	3.18 x 10^{13}	7.62 x 10^{13}
	S41	R51 > TS51 > R52	1.78	−0.34	4.64 x 10^{12}	1.42 x 10^{-19}	7.64 x 10^{12}	2.47 x 10^{-3}	8.13 x 10^{12}	4.08 x 10^{-1}	8.27 x 10^{12}	1.86 x 10^{4}
	S42	R52 > TS52 > R53	0.42	−0.16	3.85 x 10^{12}	4.82 x 10^{5}	4.99 x 10^{12}	1.12 x 10^{9}	5.26 x 10^{12}	3.26 x 10^{9}	6.21 x 10^{12}	3.42 x 10^{10}
	S43	R53 + H* >> R54 + *		−0.04	4.51 x 10^{11}	2.45 x 10^{11}	3.64 x 10^{11}	5.54 x 10^{10}	3.49 x 10^{11}	4.17 x 10^{10}	3.17 x 10^{11}	1.95 x 10^{10}
	S44	R54 > TS53 > R54	0.80	0.11	9.65 x 10^{13}	5.46 x 10^{-1}	4.76 x 10^{14}	4.04 x 10^{8}	6.32 x 10^{14}	6.97 x 10^{9}	1.29 x 10^{15}	3.50 x 10^{12}
	S45	R55 > PHE + CH_4*		2.54	2.61 x 10^{13}	1.57 x 10^{-20}	2.73 x 10^{13}	3.23 x 10^{5}	2.41 x 10^{13}	9.22 x 10^{8}	1.33 x 10^{13}	1.95 x 10^{16}
	S46	R55 > CH_4 + PHE*		0.26	2.13 x 10^{12}	3.86 x 10^{15}	9.21 x 10^{11}	9.15 x 10^{17}	7.39 x 10^{11}	1.95 x 10^{18}	3.70 x 10^{11}	9.75 x 10^{18}
	S47	PHE* >> PHE + *		2.54	2.46 x 10^{11}	4.05 x 10^{-24}	5.55 x 10^{10}	6.57 x 10^{0}	3.53 x 10^{10}	1.02 x 10^{4}	7.55 x 10^{9}	3.79 x 10^{10}
Anisole → Benzene	**S48**	ANI + * > ANI*		−2.67	3.73 x 10^{4}	6.26 x 10^{-6}	2.58 x 10^{4}	6.77 x 10^{-7}	2.38 x 10^{4}	4.18 x 10^{-7}	1.88 x 10^{4}	1.03 x 10^{-7}
	S49	H_2 + * >> H_2*		−0.74	2.73 x 10^{5}	3.93 x 10^{2}	1.89 x 10^{5}	6.16 x 10^{1}	1.74 x 10^{5}	4.12 x 10^{1}	1.38 x 10^{5}	1.28 x 10^{1}
	S50	ANI* + H* >> R61 + *		−0.05	9.21 x 10^{12}	1.07 x 10^{14}	1.84 x 10^{13}	7.16 x 10^{13}	2.13 x 10^{13}	7.14 x 10^{13}	3.27 x 10^{13}	8.02 x 10^{13}
	S51	R61 > TS61 > R62	2.36	1.47	5.02 x 10^{12}	4.11 x 10^{-31}	1.43 x 10^{13}	3.55 x 10^{-8}	1.73 x 10^{13}	4.85 x 10^{-5}	2.75 x 10^{13}	2.41 x 10^{2}
	S52	R62 > TS62 > R63	0.53	−1.12	6.89 x 10^{11}	3.86 x 10^{1}	1.11 x 10^{12}	5.18 x 10^{6}	1.26 x 10^{12}	2.62 x 10^{7}	1.84 x 10^{12}	9.19 x 10^{8}
	S53	R63* + H* >> R64 + *		−0.10	8.54 x 10^{12}	1.02 x 10^{14}	2.10 x 10^{13}	1.14 x 10^{14}	2.48 x 10^{13}	1.18 x 10^{14}	3.83 x 10^{13}	1.25 x 10^{14}
	S54	R64* > TS63 > R65	0.27	−0.28	1.68 x 10^{12}	1.46 x 10^{7}	1.15 x 10^{12}	1.08 x 10^{9}	1.04 x 10^{12}	1.71 x 10^{9}	7.46 x 10^{11}	3.65 x 10^{9}
	S55	R65 >> BEN + $HOCH_3$*		2.24	1.37 x 10^{12}	2.49 x 10^{-20}	2.07 x 10^{11}	1.72 x 10^{1}	1.17 x 10^{11}	8.34 x 10^{3}	1.71 x 10^{10}	2.09 x 10^{9}
	S56	R65 >> $HOCH_3$ + BEN*		0.39	1.61 x 10^{11}	1.09 x 10^{14}	1.54 x 10^{10}	4.26 x 10^{16}	8.60 x 10^{9}	7.77 x 10^{16}	1.40 x 10^{9}	1.64 x 10^{17}
	S57	BEN* >> BEN + *		2.47	1.16 x 10^{12}	1.24 x 10^{-24}	2.95 x 10^{11}	3.22 x 10^{-1}	1.90 x 10^{11}	3.83 x 10^{2}	4.19 x 10^{10}	7.84 x 10^{8}
Phenol → Benzene	**S58**	PHE + * > PHE*		−2.54	4.00 x 10^{4}	1.29 x 10^{-5}	2.76 x 10^{4}	1.39 x 10^{-6}	2.55 x 10^{4}	8.60 x 10^{-7}	2.02 x 10^{4}	2.12 x 10^{-7}
	S59	H_2 + * >> H_2*		−0.74	2.73 x 10^{5}	3.93 x 10^{2}	1.89 x 10^{5}	6.16 x 10^{1}	1.74 x 10^{5}	4.12 x 10^{1}	1.38 x 10^{5}	1.28 x 10^{1}
	S60	PHE* + H* >> R71 + *		−0.03	1.56 x 10^{12}	1.57 x 10^{12}	2.81 x 10^{12}	1.50 x 10^{12}	3.22 x 10^{12}	1.54 x 10^{12}	4.81 x 10^{12}	1.81 x 10^{12}
	S61	R71 > TS71 > R72	2.36	2.12	8.43 x 10^{12}	3.96 x 10^{-30}	1.86 x 10^{13}	1.06 x 10^{-7}	2.22 x 10^{13}	1.29 x 10^{-4}	3.48 x 10^{13}	5.56 x 10^{2}
	S62	R72 > TS72 > R73	0.20	−1.76	9.64 x 10^{12}	6.93 x 10^{9}	1.67 x 10^{13}	4.73 x 10^{11}	1.82 x 10^{13}	8.33 x 10^{11}	2.22 x 10^{13}	2.76 x 10^{12}
	S63	R73 + H* >> R74 + *		−0.02	3.63 x 10^{12}	6.34 x 10^{12}	4.40 x 10^{12}	3.23 x 10^{12}	4.51 x 10^{12}	2.82 x 10^{12}	4.73 x 10^{12}	1.95 x 10^{12}
	S64	R74 > TS73 > R75	0.16	−0.61	3.20 x 10^{12}	9.46 x 10^{8}	5.58 x 10^{12}	9.66 x 10^{10}	6.31 x 10^{12}	1.84 x 10^{11}	9.07 x 10^{12}	7.58 x 10^{11}
	S65	R75 >> BEN + H_2O*		2.41	1.71 x 10^{12}	2.29 x 10^{-23}	7.69 x 10^{11}	6.05 x 10^{0}	5.94 x 10^{11}	8.41 x 10^{3}	2.41 x 10^{11}	3.47 x 10^{10}
	S66	R75 >> H_2O + BEN*		0.36	2.49 x 10^{11}	1.59 x 10^{12}	5.59 x 10^{10}	3.14 x 10^{15}	3.84 x 10^{10}	8.01 x 10^{15}	1.99 x 10^{10}	4.76 x 10^{16}
	S67	BEN* >> BEN + *		2.47	1.16 x 10^{12}	1.24 x 10^{-24}	2.95 x 10^{11}	3.22 x 10^{-1}	1.90 x 10^{11}	3.83 x 10^{2}	4.19 x 10^{10}	7.84 x 10^{8}
	S68	GUA* >> GUA + *		2.69	2.24 x 10^{11}	6.34 x 10^{-27}	3.95 x 10^{10}	4.43 x 10^{-1}	2.38 x 10^{10}	1.09 x 10^{3}	4.42 x 10^{9}	1.03 x 10^{10}